INTELLIGENT OPERATION AND CONTROL IN NEXT GENERATION URBAN POWER GRID

EDITED BY: Ke-Jun Li, Shutang You, Kaiqi Sun, Xingpeng Li,
Huangqing Xiao and Zhaohao Ding

PUBLISHED IN: Frontiers in Energy Research

frontiers Research Topics

ISSN 1664-8714
ISBN 978-2-83250-310-2
DOI 10.3389/978-2-83250-310-2

About Frontiers

Frontiers is more than just an open-access publisher of scholarly articles: it is a pioneering approach to the world of academia, radically improving the way scholarly research is managed. The grand vision of Frontiers is a world where all people have an equal opportunity to seek, share and generate knowledge. Frontiers provides immediate and permanent online open access to all its publications, but this alone is not enough to realize our grand goals.

Frontiers Journal Series

The Frontiers Journal Series is a multi-tier and interdisciplinary set of open-access, online journals, promising a paradigm shift from the current review, selection and dissemination processes in academic publishing. All Frontiers journals are driven by researchers for researchers; therefore, they constitute a service to the scholarly community. At the same time, the Frontiers Journal Series operates on a revolutionary invention, the tiered publishing system, initially addressing specific communities of scholars, and gradually climbing up to broader public understanding, thus serving the interests of the lay society, too.

Dedication to Quality

Each Frontiers article is a landmark of the highest quality, thanks to genuinely collaborative interactions between authors and review editors, who include some of the world's best academicians. Research must be certified by peers before entering a stream of knowledge that may eventually reach the public - and shape society; therefore, Frontiers only applies the most rigorous and unbiased reviews.
Frontiers revolutionizes research publishing by freely delivering the most outstanding research, evaluated with no bias from both the academic and social point of view. By applying the most advanced information technologies, Frontiers is catapulting scholarly publishing into a new generation.

What are Frontiers Research Topics?

Frontiers Research Topics are very popular trademarks of the Frontiers Journals Series: they are collections of at least ten articles, all centered on a particular subject. With their unique mix of varied contributions from Original Research to Review Articles, Frontiers Research Topics unify the most influential researchers, the latest key findings and historical advances in a hot research area! Find out more on how to host your own Frontiers Research Topic or contribute to one as an author by contacting the Frontiers Editorial Office: frontiersin.org/about/contact

INTELLIGENT OPERATION AND CONTROL IN NEXT GENERATION URBAN POWER GRID

Topic Editors:
Ke-Jun Li, Shandong University, China
Shutang You, The University of Tennessee, Knoxville, United States
Kaiqi Sun, Shandong University, China
Xingpeng Li, University of Houston, United States
Huangqing Xiao, South China University of Technology, China
Zhaohao Ding, North China Electric Power University, China

Citation: Li, K.-J., You, S., Sun, K., Li, X., Xiao, H., Ding, Z., eds. (2022). Intelligent Operation and Control in Next Generation Urban Power Grid. Lausanne: Frontiers Media SA. doi: 10.3389/978-2-83250-310-2

Table of Contents

frontiers | Frontiers in Energy Research

TYPE Editorial
PUBLISHED 14 September 2022
DOI 10.3389/fenrg.2022.1001300

Editorial: Intelligent operation and control in next generation urban power grid

Jingshan Wang[1], Ke-Jun Li[1]*, Kaiqi Sun[1], Shutang You[2], Xingpeng Li[3], Huangqing Xiao[4] and Zhaohao Ding[5]

[1]School of Electrical Engineering, Shandong University, Jinan, China, [2]The University of Tennessee, Knoxville, TN, United States, [3]University of Houston, Houston, TX, United States, [4]School of Electric Power Engineering, South China University of Technology, Guangzhou, China, [5]School of Electrical and Electronic Engineering, North China Electric Power University, Beijing, China

OPEN ACCESS

EDITED AND REVIEWED BY
ZhaoYang Dong,
Nanyang Technological University,
Singapore

*CORRESPONDENCE
Ke-Jun Li,
lkjun@sdu.edu.cn

SPECIALTY SECTION
This article was submitted
to Smart Grids,
a section of the journal
Frontiers in Energy Research

RECEIVED 23 July 2022
ACCEPTED 01 August 2022
PUBLISHED 14 September 2022

CITATION
Wang J, Li K-J, Sun K, You S, Li X, Xiao H and Ding Z (2022), Editorial: Intelligent operation and control in next generation urban power grid.
Front. Energy Res. 10:1001300.
doi: 10.3389/fenrg.2022.1001300

KEYWORDS

urban power grid, renewable energy, flexible load, energy storage, operation and control

Editorial on the Research Topic
Intelligent operation and control in next generation urban power grid

With the rapid development of the economy and the rapid growth of population over the decades, urbanization has today become a prevailing trend all around the world. With world urbanization, there is a great increase in electrical energy demand for urban activities. Urban power grids are facing many expansion and operational challenges. On the other hand, with the ever-increasing double pressure from the energy crisis and environmental protection, the need to accommodate the rising urban demand in a sustainable way is therefore of high priority. In order to confront the challenges above, some key technologies related to urban power systems have been developed rapidly, such as voltage source converter-based high voltage direct current transmission technology, flexible DC transmission/distribution grid technology, and large-scale new energy such as renewables and energy storage integration in urban areas, that would be of great importance as efficient and sustainable development options in both meeting the increasing urban power demand and reducing greenhouse gas emissions. It can be predicted that the next-generation urban power grid is characterized by high penetrations of renewable energies and high penetrations of power electronic converter devices. Moreover, the rapid integration of flexible loads with the characteristics of source and load, such as electric vehicles, further brings more uncertainties into the urban power system. These factors subsequently enable the rapid development of urban power grids into novel and complex forms. There is a significant change in "generation-grid-load" for next-generation urban power systems, particularly the high penetrations of renewable energies and high penetrations of power electronic devices into the generation, transmission, and distribution areas have great impacts on urban power systems control, operation, and stability. While facing more challenges and risks in system control, stability, and operation, the next generation urban power grids have better controllability with the increasing penetration of power converter interfaced devices. Therefore, the innovation of the technology and control strategy for the next urban power grids becomes essential.

This Frontiers in Energy Research special issue aims to promote theoretical and practical studies in the control and operation of the Next Generation Urban Power Grid so as to improve operating stability and flexibility and increase the affable integration of renewable energies and flexible loads. All original contributions covering a variety of topics related to the theme of the special issue are encouraged. There are in total 13 papers accepted for this research topic after the rigorous review process, and they cover the following four categories:1) Intelligent control for reliable operation in urban power grids; 2) Modelling theory and simulation methodologies for next-generation urban power systems; 3) Data-driven approaches to improve the operation quality of urban power grids; 4) Medium and low voltage level DC technology application in urban power grids. The papers accepted in this special issue are summarized below.

1) Intelligent control for reliable operation in urban power grids

With the increasing penetrations of renewable energies and power converter devices, the dynamic characteristics of the urban power system undergo a significant change; for instance, inertia in the urban power system becomes low, which can directly and negatively impact the urban power system operation in terms of stability and reliability. Hence, it is essential to develop intelligent control strategies to support the stable and reliable operation of the urban power grid. Li Q et al. propose a virtual inertia control strategy based on the fuzzy logic method for wind turbines to enhance the frequency stability of the power system. Xiao H et al. present a synchronous generator imitation control and dynamic power sharing method for the distributed power generation system based on voltage source converter (VSC) stations. High power density high-efficiency converter-interfaced devices such as modular multilevel converters (MMC) have played and will continue to play a significant role in urban power grids by providing efficient, clean electrical power conversion, transmission, and distribution. Qian J et al. describe an MMC-based wind energy conversion system and propose a constant capacitor voltage ripple (CCVR) control method in order to reduce the capacitance of the submodule capacitor of the MMC-based wind power converter, which improves MMC system economy and reliable operation.

2) Modeling theory and simulation methodologies for next-generation urban power systems

Modeling and simulation methodologies to analyze the static and dynamic characteristics of the urban power system with high penetrations of renewables and converters are the basis of operation, planning, control, and decision optimization in next-generation urban power grids. Zhu L et al. propose a dynamic equivalence method applicable to multiple wind farms with different wind turbine models in an urban power grid for analyses of the system operation. Xie X et al. propose a unified MMC modeling scheme in a synchronous reference frame for simulating the MMC-based flexible hybrid AC/DC power grids and analyzing the small-signal stability of the grid. Zhu L et al. propose a generic user-defined modeling (UDM) method applicable to various model objects in PSS/E and implement the detailed UDM of a modular multilevel converter high-voltage direct current (MMC-HVDC) transmission system following the proposed method.

3) Data-driven approaches to improve the operation quality of urban power grids

As the complexity of urban power grid operation progressively increases, advanced measurement and data-driven based artificial intelligence approaches are needed to improve the operation quality of urban power grids. She B et al. propose a data-driven approach to compensate for the time delay in voltage source converter-based high voltage direct current (VSC-HVDC) damping control based on synchronous phasor measurement unit (PMU) measurements, which leverages the modern recurrent neural network LSTM. Bai X et al. propose an event-triggered dual set-membership state estimation for power distribution networks (PDNs) to realize the online state monitoring and improve the perception ability of the PDNs, thereinto, the synchronous PMU provides an important measured data source for the PDNs estimation. The core of urban power grid operation is to keep electric power and energy balanced between supply and demand, where accurate load forecasting is a crucial aspect of properly balancing electricity supply and demand on the urban power grid, Xin J et al. propose a long short-term memory recurrent neural network and fully connected neural network (LSTM-RNN-FNN) model based on the assemblage perspective for electrical load forecasting. To facilitate urban power system operation, planning, and control in the context of high renewable energy sources penetration, Kim J et al. propose a probabilistic spectral clustering method applicable to large-scale power systems, including variable renewable energy sources. Meng X et al. present a method for generating grid operation databases based on a weighted elimination algorithm to improve the solving efficiency of data-driven power flow calculation problems in large-scale urban power grids.

4) Medium and low voltage level DC technology application in urban power grids

Medium and low voltage level direct current (DC) power distribution systems operating as a parallel path or an alternative option to the existing urban alternating current (AC) distribution networks is becoming a trend and the way of the future. Li L et al. present a novel isolated modular multilevel converter (I-M^{2}C) topology with symmetrical wiring and its bipolar balance control method for achieving reliable and efficient interconnecting architectures and power flow control among the low-voltage DC (LVDC), medium-voltage DC (MVDC), and medium-voltage AC (MVAC) distribution systems. Wang F et al. propose a comprehensive decision-making method for DC transformation priority of multiple AC distribution networks in urban distribution power grid upgrading, aiming to guide the planning department of the urban power grid to arrange the priority scheme of DC transformation objects reasonably.

In summary, the papers in this Frontiers Special Issue covered a variety of topics related to the operation and control of urban power grids. Renewables and new grid networking technologies pave the way for urban power grid transformation and upgrading. Still, there are many challenges and opportunities with the acceleration of the urban power grid transition process, and the application of advancing technologies and their related theory in the urban power grid need to be further investigated. It is hoped that this special issue will provide beneficial ideas and references for further theoretical and practical research related to next-generation urban power grids.

Finally, we would like to sincerely acknowledge the journal editors and editorial office of Frontiers in Energy Research for their valuable support during the elaboration of this special issue. We especially thank all the contributing authors and all the reviewers for their diligence and hard work in making this special issue possible.

Author contributions

All authors listed have made a substantial, direct, and intellectual contribution to the work and approved it for publication.

Conflict of interest

The authors declare that the research was conducted in the absence of any commercial or financial relationships that could be construed as a potential conflict of interest.

Publisher's note

frontiers
in Energy Research

ORIGINAL RESEARCH
published: 22 February 2022
doi: 10.3389/fenrg.2022.809481

LVDC Bipolar Balance Control of I-M^{2}C in Urban AC/DC Hybrid Distribution System

*Liangzi Li, Kaiqi Sun, Zhijie Liu, Wenning Wang and Ke-Jun Li**

School of Electrical Engineering, Shandong University, Jinan, China

With the high proportional renewable energy integration and rapid increase in the DC loads, such as the electric vehicle and distributed energy storage, the DC distribution system becomes a prospective solution for the urban power grid enhancement for its high-efficiency and eco-friendly nature. In most DC distribution systems, power interfaces are applied to connect low-voltage DC (LVDC) distribution systems with multiple medium-voltage (MV) systems in order to improve the operating reliability and economy. Compared to other types of multiports power interfaces, the three-port-isolated modular multilevel converter (I-M^{2}C) has shown many advantages, including low cost, high power density, and low control complexity. However, the I-M^{2}C cannot handle the power imbalance at the bipolar LVDC port like the other MMC-based three-port power interfaces, which limits the operating range and decreases the stability of the I-M^{2}C in bipolar LVDC application. In order to solve the bipolar imbalance problems, a novel balance control method is proposed in this article. The proposed balance control method is based on symmetrical decomposition. By decoupling the MV power control and the LV bipolar power compensation control, the proposed method can eliminate the bipolar voltage deviation under different working conditions. The simulation results prove the validity and good control performance of the proposed method.

Keywords: urban power system, DC distribution system, solid-state transformer, isolated modular multilevel converter, bipolar balance

Edited by:
Yuvaraja Teekaraman,
Vrije University Brussel, Belgium

Reviewed by:
Jlanwen Zhang,
Shanghai Jiao Tong University, China
Yushuai Li,
University of Oslo, Norway

****Correspondence:***
Ke-Jun Li
lkjun@sdu.edu.cn

Specialty section:
This article was submitted to Smart Grids,
a section of the journal
Frontiers in Energy Research

Received: *05 November 2021*
Accepted: *27 January 2022*
Published: *22 February 2022*

Citation:
Li L, Sun K, Liu Z, Wang W and Li K-J (2022) LVDC Bipolar Balance Control of I-M^{2}C in Urban AC/DC Hybrid Distribution System.
Front. Energy Res. 10:809481.
doi: 10.3389/fenrg.2022.809481

1 INTRODUCTION

With the global-scale urbanization in the past few decades, the urban power grid has met many operating challenges (Sun et al., 2021a; Zhang et al., 2021). In recent years, the DC system has been proved as a prospective selection for urban power grid enhancement (Hakala et al., 2015). Compared to AC power supply technology, DC power supply technology provides many benefits, including asynchronous operation, DC load/source affinity, and larger supply capacity (Sun et al., 2021a; Sun et al., 2021b). For the medium-voltage (MV) level like 10 kV, the MVDC distribution network can increase the efficiency and reliability with large-scale centralized RESs like photovoltaic plants or offshore wind turbines (Zhao et al., 2016). For low voltage (LV) level like ±750V, the LVDC distribution system has many advantages including high power quality, control convenience, and fault ride through capability (Li B et al., 2021; Xiao et al., 2021). With the rapid penetration of renewable energy and the continuous increase of DC loads, such as electric vehicles and distributed energy storage, DC power supply technology will meet unprecedented development opportunities in the urban power grid (Agrawal et al., 2019).

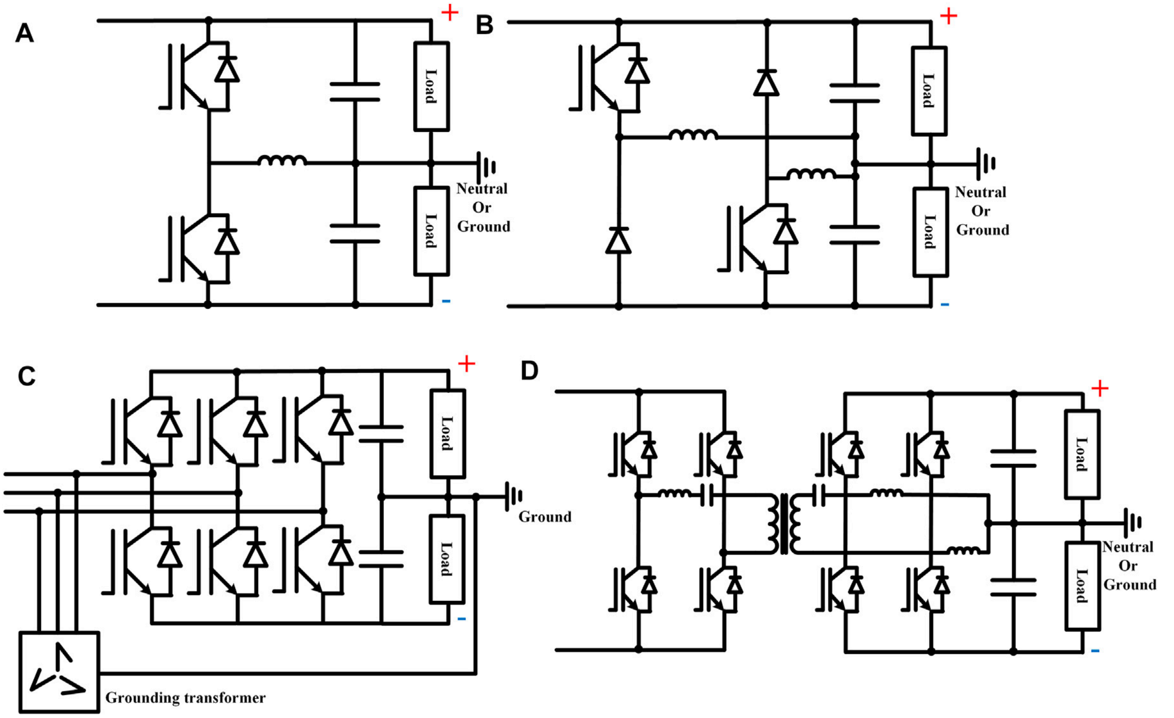

FIGURE 1 | (A) Buck/boost type in Rivera et al. (2021). **(B)** Dual-buck type in Rivera et al. (2021). **(C)** Utilization of Grounding transformer in Li et al. (2018). **(D)** Enhanced CLLC with bipolar balance in Li Y et al. (2021).

In most of the urban DC application scenarios, the LVDC distribution system is linked to MV distribution systems for increasing the power supply reliability and efficiency. Thus, reliable power interfaces like power converters or solid-state transformers (SSTs) are necessary for the grid integration of an LVDC system (Sun et al., 2021c; Zheng et al., 2021). Unlike classical two-port power interfaces, the MMC-based three-port SSTs can connect the LVDC system to both the MVAC and MVDC systems. Most of the MMC-based SSTs require large quantity of submodule capacitors, which brings high cost and control difficulty (Ma et al., 2020; Ma et al., 2021; Zhou et al., 2021). A novel kind of MMC-based SSTs, isolated MMC (I-M^{2}C), decreases the capacitor number to one by sharing a single capacitor among all the submodules (Liu et al., 2020). I-M^{2}C is proved appropriate for three-port AC/DC hybrid SST application due to its high efficiency and low control complexity.

In order to increase the power capacity, bipolar topology is adopted in many LVDC distribution systems (Rivera et al., 2021). The bipolar topology has a positive pole and a negative pole, and the pole-to-ground voltages are equal. The equivalent line voltage of a bipolar DC system is twice as much as the bus voltage of a unipolar system with the same voltage insulation level. However, the bipolar DC system is required to maintain the balance between the positive side and the negative side.

Bipolar imbalance is caused by the power inequality between the positive pole and the negative pole. In recent years, many research studies have focused on the mitigation of LVDC bipolar imbalance. The LVDC bipolar balance solutions can be classified into two categories: the power balance and the voltage balance (Gu et al., 2016; Lee et al., 2021). The power balance solutions aim at decreasing the bipolar power imbalance by optimization of the system's inner power flow (Chew et al., 2019; Liao et al., 2021a). The voltage balance method eliminates the bus voltage deviation by regulating the bipolar power inputs from the outer systems with the assist of power interfaces (Cui et al., 2019).

In the previous research, a power interface cannot balance the bipolar voltage unless special topology improvements and corresponding control frames are implemented. Additional transformers or power switches are required to satisfy the power deviation between the positive pole and the negative pole (Li et al., 2018; Li Y et al., 2021; Liao et al., 2021b) (Li Y et al., 2021). Four existing topologies with bipolar voltage balance capability are illustrated in **Figures 1A–D**. The buck/boost-type voltage balancer and the dual-buck-type voltage balancer in Rivera et al. (2021) regenerate the positive and negative voltages to control the power imbalance. The three-phase rectifier with the utilization of grounding transformer in Li et al. (2018) achieves the bipolar voltage balance by injecting extra zero-sequence current to the LVDC neutral point. The enhanced CLLC converter in Li Y et al. (2021) eliminates the bipolar voltage difference by the regulation of the duty cycle of IGBTs. All the previously existing bipolar schemes add extra voltage balancers in the LVDC systems with extra cost, power loss, and response time. Since the MMC-based three-port SSTs have multiple power submodules, the voltage balance of the LVDC port can be achieved by controlling the LVDC power

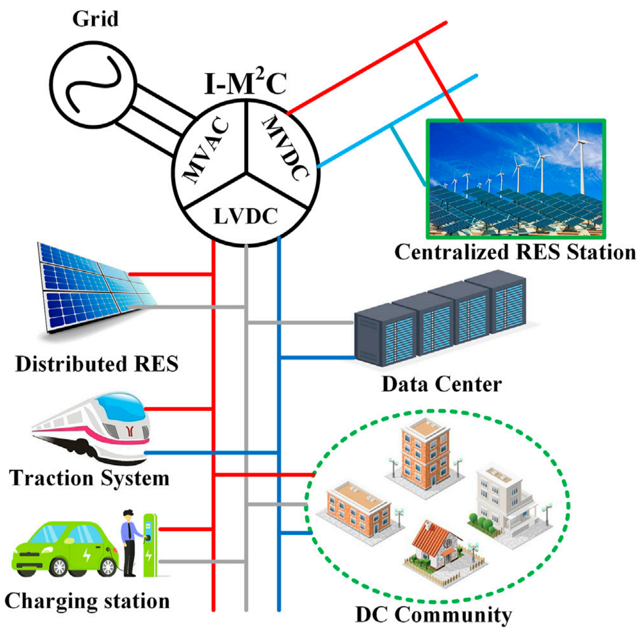

FIGURE 2 | Example of the I-M^{2}C in the urban power system.

flows of submodules without adding new power conversion stages, which has been rarely studied in the existing research.

In this article, a bipolar balancing method for the I-M^{2}C is proposed. The contribution of the proposed method is summarized as follows:

1) A symmetrical wiring topology of the I-M^{2}C is proposed, which does not add extra power devices but only changes the wiring layout.
2) An LVDC bipolar balance control method based on symmetrical decomposition is proposed to control the bipolar differential power without changing the power distribution on the MV side.
3) With the assist of the proposed control method, the I-M^{2}C with the bipolar LVDC port can maintain bus voltage balance under large bipolar power imbalance.

The rest of this article is organized as follows: the I-M^{2}C topology with symmetrical wiring is described in **Section 2**. The mathematical model of LVDC bipolar balance is analyzed in **Section 3**. **Section 4** introduced the symmetrical balance control method of the hybrid I-M^{2}C. The simulation results are presented in **Section 5**. The article is concluded in **Section 6**.

2 I-M^{2}C TOPOLOGY WITH SYMMETRICAL WIRING

In the urban power system, an isolated modular multilevel converter (I-M^{2}C) is applied as a three-port solid-state transformer between MVDC, MVAC, and LVDC distribution systems, as illustrated in **Figure 2**. The topology diagram of a three-phase I-M^{2}C is shown in **Figure 3A**. The three-phase I-M^{2}C has six arms, and each arm is formed by N ISMs. The topology diagram of an upper arm is illustrated in **Figure 3B**. The submodule of the I-M^{2}C, ISM, can be seen as a phase shift full bridge converter with 8 IGBTs/MOSFETs and a high frequency transformer. As demonstrated in **Figure 3A**, the ISMs in one arm series are connected at the HV side. In order to achieve the symmetry power balance at the bipolar LVDC port, half of the ISMs are parallelly connected to the positive LVDC link capacitor and the other half are parallelly connected to the negative LVDC link capacitor.

2.1 Basic Operation Principle of I-M^{2}C

The operation principle of the I-M^{2}C is similar with the carrier wave phase shift modulation control in a classical MMC. The output voltage of an ISM, as illustrated in **Figure 3B**, is modulated by the duty cycle regulation of the high-frequency waves using the high-frequency transformer, as shown in **Figure 4**. Two modulation freedoms, one in DC and one in working frequency AC, are utilized in the modulation to generate both the DC voltage and the AC voltage. By the series connected to the ISMs, the arm voltage modulation can be derived as follows:

$$\begin{cases} u_{\text{armju}} = 0.5NkU_{dcL}\left(D + d_j\right), \\ u_{\text{armjl}} = 0.5NkU_{dcL}\left(D + d_j\right), \\ U_{\text{dcM}} = u_{\text{armju}} + u_{\text{armjl}}, \\ u_{\text{vj}} = u_{\text{armju}} - u_{\text{armjl}}. \end{cases} j = a, b, c, \tag{1}$$

where u_{armju} and u_{armjl} are the upper and lower voltages of the phase unit j, N is the submodule number per arm, k is the ratio of high-frequency ratio, U_{dcL} are the pole-to-pole voltage of the LVDC bipolar port, D is the DC modulation freedom, d_{j} is the AC modulation freedom of phase j, U_{dcM} is the MVDC voltage, and u_{j} is the MVAC voltage of phase unit j.

The MVDC power flow is controlled by DC modulation D with the regulation of difference between the MVDC common bus voltage and U_{dcM}. The MVAC power flow is controlled by d_{j} with the control of dq-axis control of the AC phase currents. When the MVAC power is not sent to the MVDC port, the rest active power flows through the ISMs and supply the power consumption of the LVDC system.

2.2 Modulation With the Symmetrical Wiring

Considering the convenience for design and construction, the wiring between the ISMs and the LVDC port is symmetrically connected. As demonstrated in **Figure 1B**, the top half ISMs in the upper arm and the bottom half in the lower arm are connected to the positive side for each phase unit. Symmetrically, the bottom half ISMs in the upper arm and the top half in the lower arm are linked to the negative side. The proposed symmetry wiring guarantees that the arm voltage modulation should not be affected by the voltage imbalance of the bipolar LVDC system. The modulation of a submodule in the I-M^{2}C can be derived as follows:

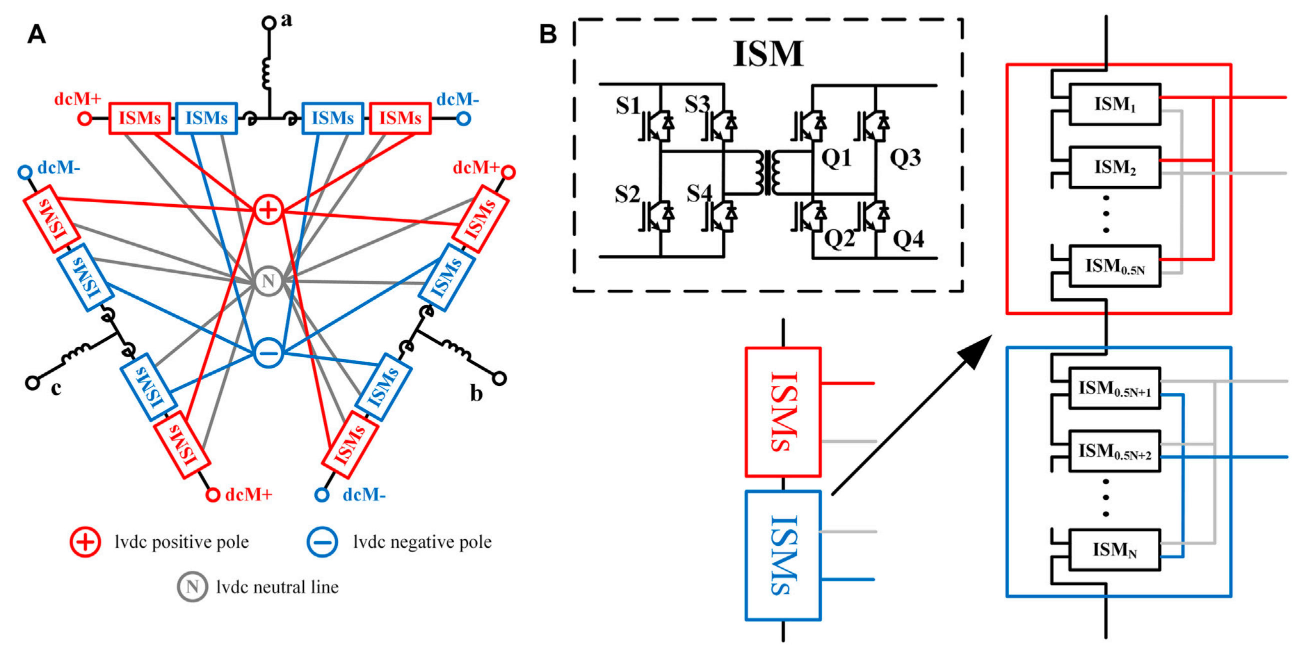

FIGURE 3 | (A) Topology diagram of the I-M^{2}C. **(B)** Topology diagram of an upper arm.

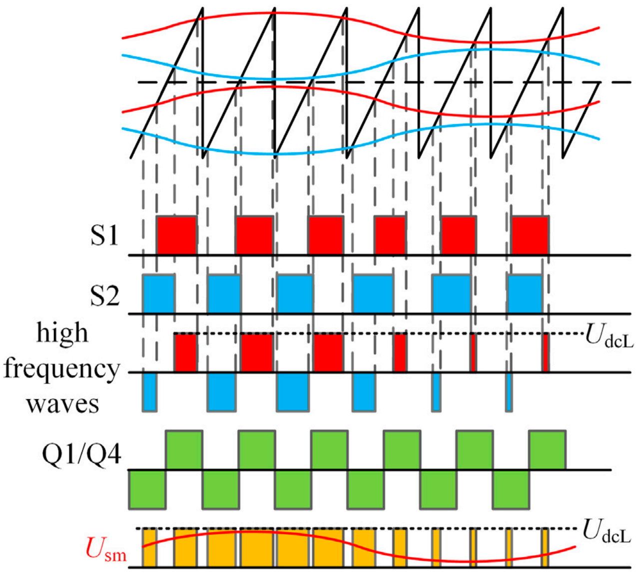

FIGURE 4 | Modulation of the ISM output voltage $U_{\rm sm}$ by regulating the duty cycle of the high frequency waves with AC and DC modulation freedoms.

$$\begin{cases} u_{\rm smpu} = kU_{dcLp}\left(D_p + d_{jp}\right), \\ u_{\rm smnu} = kU_{dcLn}\left(D_n + d_{jn}\right), \\ u_{\rm smpl} = kU_{dcLp}\left(D_p - d_{jp}\right), \\ u_{\rm smnl} = kU_{dcLn}\left(D_n - d_{jn}\right). \end{cases} j = a, b, c, \tag{2}$$

where $u_{\rm smpu}$, $u_{\rm smpu}$, $u_{\rm smpl}$, and $u_{\rm smnl}$ are, respectively, the output voltages of the submodules on the upper arms linked to the LVDC-positive pole, on the upper arms linked to the negative pole, on the lower arms linked to the positive pole, on the lower arms linked to the negative pole. $U_{\rm dcLp}$ and $U_{\rm dcLn}$ are, respectively, the positive voltage and negative voltage at the LVDC port. $D_{\rm p}$ *and* $D_{\rm n}$ are the DC modulations for the positive-linked and negative-linked ISMs. $d_{\rm jp}$ and $d_{\rm jn}$ are the AC modulations of phase j for positive ISMs and negative ISMs.

The arm voltage modulation can be derived as follows:

$$\begin{cases} u_{\rm armju} = 0.5Nk\left[U_{\rm dcLp}\left(D_p + d_{\rm jp}\right) + U_{\rm dcLn}\left(D_n + d_{\rm jn}\right)\right] \\ = 0.5Nk\left[\left(U_{\rm dcLp}D_p + U_{\rm dcLn}D_n\right) + \left(U_{\rm dcLp}d_{\rm jp} + U_{\rm dcLn}d_{\rm jn}\right)\right], \\ u_{\rm armjl} = 0.5Nk\left[U_{\rm dcLp}\left(D_p - d_{\rm jp}\right) + U_{\rm dcLn}\left(D_n - d_{\rm jn}\right)\right] \\ = 0.5Nk\left[\left(U_{\rm dcLp}D_p + U_{\rm dcLn}D_n\right) - \left(U_{\rm dcLp}d_{\rm jp} + U_{\rm dcLn}d_{\rm jn}\right)\right], \\ U_{dcM} = u_{\rm armju} + u_{\rm armjl} = Nk\left(U_{\rm dcLp}D_p + U_{\rm dcLn}D_n\right), \\ u_{vj} = u_{\rm armju} - u_{\rm armjl} = Nk\left(U_{\rm dcLp}d_{\rm jp} + U_{\rm dcLn}d_{\rm jn}\right). \end{cases} \mathbf{j} = \mathbf{a}, \mathbf{b}, \mathbf{c}. \tag{3}$$

According to **(3)**, the fundamental AC components of the arm voltages keep symmetrical with the LVDC bipolar voltage difference. Thus, the voltage imbalance at the LVDC port cannot influence the normal operation of the MVDC and MVAC distribution systems. However, the bipolar power imbalance is not controlled by the symmetrical wiring.

3 MATHEMATICAL MODEL OF LVDC BIPOLAR BALANCE

In the LVDC distribution system, the bipolar imbalance is shown as the deviation between the positive voltage $U_{\rm dcLp}$ and the negative voltage $U_{\rm dcLn}$. The intrinsic reason for the voltage imbalance is the power difference between the positive side and the negative side. The mathematical relation between the bipolar voltage deviation and the power imbalance can be obtained as follows:

$$\begin{cases} C_{\mathrm{dcL}} \dfrac{dU_{\mathrm{dcLp}}}{dt} = \dfrac{P_{\mathrm{dcLp}} - P_{\mathrm{conp}}\left(U_{\mathrm{dcLp}}\right)}{U_{\mathrm{dcLp}}} \\ C_{\mathrm{dcL}} \dfrac{dU_{\mathrm{dcLn}}}{dt} = \dfrac{P_{\mathrm{dcLn}} - P_{\mathrm{conn}}\left(U_{\mathrm{dcLn}}\right)}{U_{\mathrm{dcLn}}}, \end{cases} \tag{4}$$

where C_{dcL} is the capacitance of the LVDC link capacitors. P_{conp} and P_{conn} are, respectively, the power consumption of the positive LVDC and the negative LVDC, which are the function of the corresponding voltage.

As demonstrated in **(4)**, the balance control is dependent on the power flow of the positive and negative poles.

3.1 Power Flow Model

As a three-port power electronic transformer (PET), the I-M^{2}C is able to control the active power distribution among the three ports. The active power control is achieved by changing the six-arm voltages' DC and fundamental AC components. The active power distribution of the I-M^{2}C with a unipolar LVDC port can be obtained as follows:

$$\begin{cases} P_{\mathrm{dcM}} = U_{\mathrm{dcM}} \cdot I_{\mathrm{dcM}}, \\ P_{\mathrm{acM}} = \dfrac{3}{2} u_{\mathrm{vd}} i_{\mathrm{vd}} + \dfrac{3}{2} u_{\mathrm{vq}} i_{\mathrm{vq}}, \\ P_{\mathrm{dcL}} = P_{\mathrm{dcM}} + P_{\mathrm{acM}}. \end{cases} \tag{5}$$

where I_{dcM} is the MVDC current. u_{vd}, u_{vq} and i_{vd}, i_{vq} are, respectively, the dq-axis components of the three-phase AC source voltages and AC line currents.

Take a positive-linked ISM on the upper arm of phase A as an example, the active power flow through the ISM P_{smpua} can be obtained as follows:

$$\begin{aligned} P_{\mathrm{smpu}a} &= u_{\mathrm{smpu}} \left(\frac{I_{\mathrm{dcM}}}{3} + \frac{i_a}{2} \right) \\ &= kU_{\mathrm{dcLp}} \left(\frac{D_p I_{\mathrm{dcM}}}{3} + \frac{d_{ap} i_a \cos \theta_{va}}{2} \right), \end{aligned} \tag{6}$$

where θ_{va} is the angle between phasor d_{ap} and i_{a}.

Extended to the other ISMs and sum, the power flows of the positive pole and the negative pole from the I-M^{2}C can be derived as follows:

$$\begin{cases} P_{\mathrm{dcLp}} = NkU_{\mathrm{dcLp}} \left(D_{\mathrm{p}} I_{\mathrm{dcM}} + \dfrac{3}{2} d_{\mathrm{pd}} i_{\mathrm{vd}} + \dfrac{3}{2} d_{\mathrm{pq}} i_{\mathrm{vq}} \right) \\ P_{\mathrm{dcLp}} = NkU_{\mathrm{dcLn}} \left(D_{\mathrm{n}} I_{\mathrm{dcM}} + \dfrac{3}{2} d_{\mathrm{nd}} i_{\mathrm{vd}} + \dfrac{3}{2} d_{\mathrm{nq}} i_{\mathrm{vq}} \right) \end{cases}, \tag{7}$$

where d_{pd} and d_{pq} are dq-axis components of d_{jp}, d_{nd}, and d_{nq} are dq-axis components of d_{jn}.

The equivalent circuit of the bipolar power flow is illustrated in **Figure 5**. The arm of the I-M^{2}C can be seen as the DC and AC voltage-controlled voltage source controlled by the bipolar voltages. And the bipolar power flows received from the MVDC and MVAC systems can be equivalent as the DC and AC current-controlled current source controlled by the MVDC current I_{dcM} and MVAC currents i_{vd} and i_{vq}.

It can be seen from **Figure 5** that the bipolar power flows are decided by the MVDC/MVAC power and the DC/AC modulations. If the voltage difference is eliminated at steady state, the relationship between the LVDC power and the MVAC/MVDC power can be calculated as follows:

$$\begin{cases} P_{\mathrm{dcLp}} = \dfrac{D_p}{D_p + D_n} P_{\mathrm{dcM}} + \dfrac{d_{\mathrm{pd}} i_{\mathrm{vd}} + d_{\mathrm{pq}} i_{\mathrm{vq}}}{d_{\mathrm{pd}} i_{\mathrm{vd}} + d_{\mathrm{pq}} i_{\mathrm{vq}} + d_{\mathrm{nd}} i_{\mathrm{vd}} + d_{\mathrm{nq}} i_{\mathrm{vq}}} P_{\mathrm{acM}} \\ P_{\mathrm{dcLp}} = \dfrac{D_n}{D_p + D_n} P_{\mathrm{dcM}} + \dfrac{d_{\mathrm{nd}} i_{\mathrm{vd}} + d_{\mathrm{nq}} i_{\mathrm{vq}}}{d_{\mathrm{pd}} i_{\mathrm{vd}} + d_{\mathrm{pq}} i_{\mathrm{vq}} + d_{\mathrm{nd}} i_{\mathrm{vd}} + d_{\mathrm{nq}} i_{\mathrm{vq}}} P_{\mathrm{acM}}. \end{cases} \tag{8}$$

It can be seen from **(8)**, the control of the bipolar power flow lies on the regulation of the DC/AC modulations. However, it can be seen from the variation of DC and AC modulations will change the MVDC and MVAC power as well. The two modulation freedoms should be decomposed into common modulations and differential modulations in order to separate the control of MV power flows and the LVDC bipolar power deviation.

3.2 Common/Differential Decomposition

For decoupling the control of MV side power flows and LV side power imbalance, symmetrical decomposition is utilized. As shown in **(9)**, the bipolar elements are divided into common/differential mode elements.

$$\begin{cases} D_{\mathrm{com}} = \left(D_p + D_n\right)/2, \\ D_{\mathrm{dif}} = \left(D_p + D_n\right)/2, \\ d_{\mathrm{jcom}} = \left(d_{\mathrm{jp}} + d_{\mathrm{jn}}\right)/2, \\ d_{\mathrm{jdif}} = \left(d_{\mathrm{jp}} + d_{\mathrm{jn}}\right)/2. \end{cases} j = a, b, c. \tag{9}$$

The arm voltage modulation and with common/differential mode can be obtained as follows:

$$\begin{cases} U_{\mathrm{dcM}} = 2Nk\left(D_{\mathrm{com}} \cdot U_{\mathrm{com}} + D_{\mathrm{dif}} U_{\mathrm{dif}}\right), \\ u_{\mathrm{vj}} = 2Nk\left(d_{\mathrm{jcom}} \cdot U_{\mathrm{com}} + d_{\mathrm{jdif}} \cdot U_{\mathrm{dif}}\right), \\ U_{\mathrm{com}} = \left(U_{\mathrm{dcLp}} + U_{\mathrm{dcLn}}\right)/2, \\ U_{\mathrm{dif}} = \left(U_{\mathrm{dcLp}} - U_{\mathrm{dcLn}}\right)/2. \end{cases} j = a, b, c, \tag{10}$$

where U_{com} and U_{dif} represent the common mode voltage and differential mode voltage of LVDC bipolar voltage, respectively.

The equivalent circuit of the virtual power flow of the common and differential voltage is demonstrated in **Figure 6**.

The active power distribution based on common/differential mode can be derived as follows:

$$\begin{cases} P_{\mathrm{dcLp}} = 2Nk\left(D_{\mathrm{com}} + D_{\mathrm{dif}}\right)U_{\mathrm{dcLp}} \cdot I_{\mathrm{dcM}} + 3Nk\left(d_{\mathrm{com}d} + d_{\mathrm{dif}d}\right)U_{\mathrm{dcLp}} \cdot i_{\mathrm{vd}} \\ \qquad -3Nk\left(d_{\mathrm{com}q} + d_{\mathrm{dif}q}\right)U_{\mathrm{dcLp}} \cdot i_{\mathrm{vq}}, \\ P_{\mathrm{dcLn}} = 2Nk\left(D_{\mathrm{com}} - D_{\mathrm{dif}}\right)U_{\mathrm{dcLn}} \cdot I_{\mathrm{dcM}} + 3Nk\left(d_{\mathrm{com}d} - d_{\mathrm{dif}d}\right)U_{\mathrm{dcLn}} \cdot i_{\mathrm{vd}} \\ \qquad -3Nk\left(d_{\mathrm{com}q} - d_{\mathrm{dif}q}\right)U_{\mathrm{dcLn}} \cdot i_{\mathrm{vq}}, \\ P_{\mathrm{dcM}} = 2Nk\left(D_{\mathrm{com}} \cdot U_{\mathrm{com}} + D_{\mathrm{dif}} \cdot U_{\mathrm{dif}}\right) \cdot I_{\mathrm{dcM}}, \\ P_{\mathrm{acM}} = 3NkU_{\mathrm{com}}\left[\left(d_{\mathrm{com}d} \cdot i_{\mathrm{vd}} - d_{\mathrm{com}q} \cdot i_{\mathrm{vq}}\right) + \left(d_{\mathrm{dif}d} \cdot i_{\mathrm{vd}} - d_{\mathrm{dif}q} \cdot i_{\mathrm{vq}}\right)\right]. \end{cases} j = a, b, c, \tag{11}$$

where d_{comd}, d_{comq}, d_{difd}, and d_{difq} are the d-axis and q-axis components of AC freedom d_{j}.

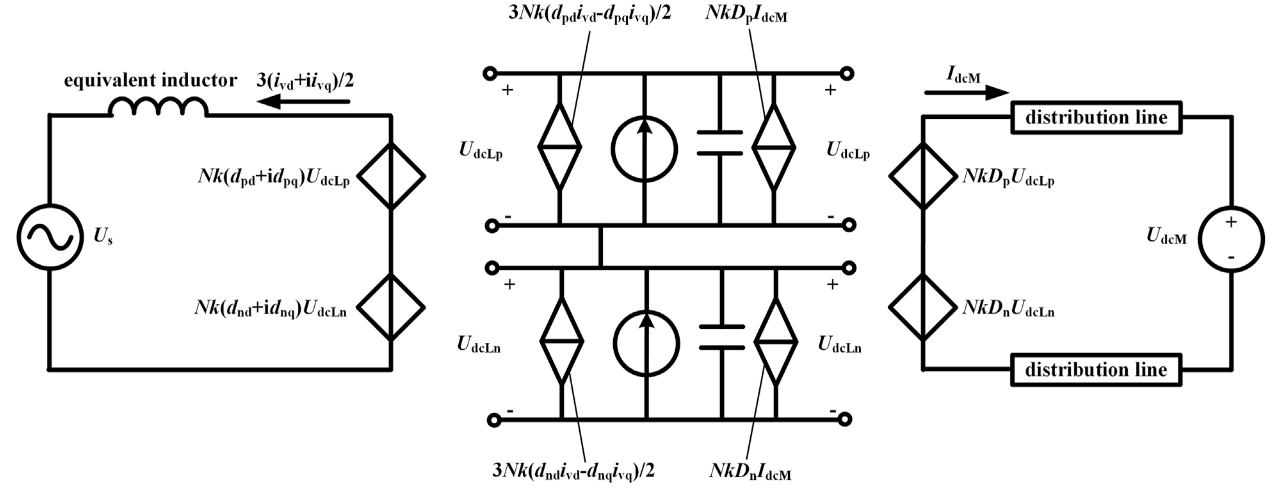

FIGURE 5 | Equivalent circuit of LVDC bipolar power flows.

According to **Figure 6** and **(11)**, in a steady state when $U_{\mathrm{dif}} = 0$, the MVAC/MVAC power is only decided by U_{com} and common modulations. In the dynamic state when $U_{\mathrm{dif}} << U_{\mathrm{com}}$, the influence on MV power flow of common modulations D_{com} and $d_{j\mathrm{com}}$ is always much larger than the influence of differential modulations. On the other hand, the differential current is directly controlled by D_{dif}. Therefore, the common modulations can be utilized to control MV power flows independently, while the elimination of U_{dif} can be directly controlled by differential modulations D_{dif} and $d_{j\mathrm{dif}}$.

4 SYMMETRICAL BIPOLAR BALANCE CONTROL METHOD

Based on the mathematical analysis of LVDC bipolar balance, a symmetrical bipolar balance control method is proposed. The common/differential mode decomposition and composition are utilized in the proposed method.

4.1 DC Modulation Freedom Control

According to **(9)**, the DC modulation freedom can be decomposed into D_{com} and D_{dif}. With the common/differential decomposition, the DC modulation freedom control is divided into common mode voltage control and differential mode voltage control.

As discussed in **Section 3.2**, the common voltage control is implemented to regulate the total power exchange of the LVDC port with the MVDC port. Double-loop control is applied. The negative feedback control of U_{com} is the outer loop, and the inner loop controls the MVDC current I_{dcM}.

The differential voltage controller regulates D_{dif} to eliminate the voltage deviation between the positive side and the negative side. It can be inferred from **Figure 5** that the relation between U_{dif} and D_{dif} is linearly influenced by the MVDC current I_{dcM}.

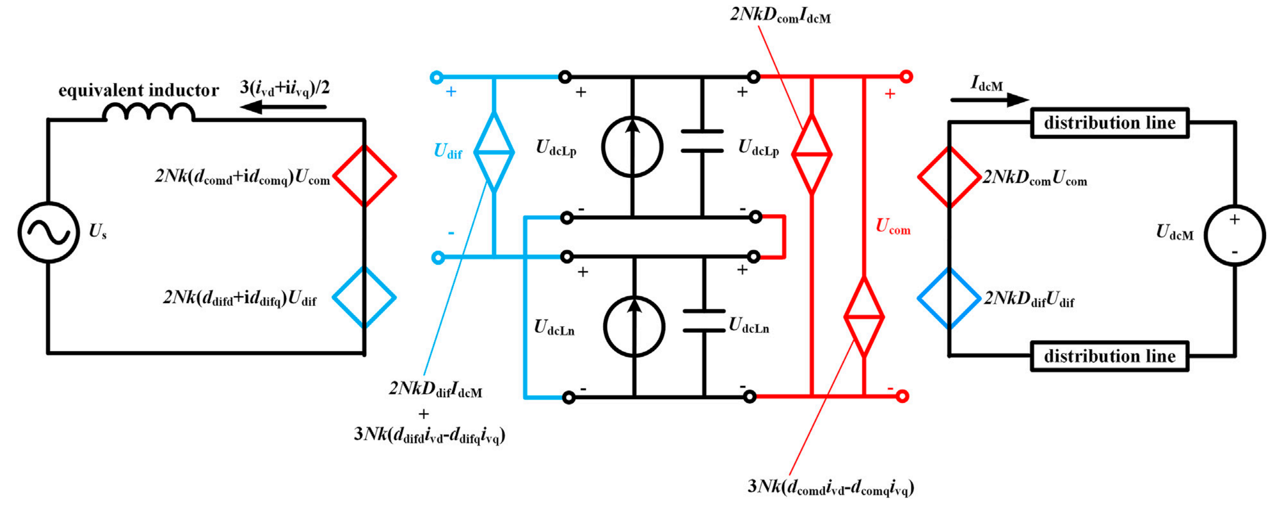

FIGURE 6 | Equivalent circuit of the virtual power flows on U_{com} and U_{dif}.

Therefore, the output of the differential mode controller should be multiplied with I_{dcM} or its positive/negative sign. Taking the coordination with AC modulation freedom control into consideration, the multiply coefficient is set to I_{dcM}.

The double-loop control architecture is also introduced in the differential controllers. After the common/differential controllers calculate D_{com} and D_{dif}, the two DC modulation freedoms are composed to form the direct DC modulation reference waves D_{p} and D_{n} for the ISMs. Four PI regulators are used. Theoretically, the transfer functions of U_{com} and U_{dif} are mirror symmetrical. Therefore, the inner loop controllers should be numerically equivalent and the outer loop controllers.

4.2 AC Modulation Freedom Control

Similar to the DC control, d_{j} is decomposed into d_{com} and d_{dif}. In addition to the common/differential decomposition, the dq-axis decomposition is applied to further divide the AC modulation freedom into d_{comd}, d_{comq}, d_{difd}, and d_{difq}.

In the classical MMC dq-axis power control theory, the active power is only related to the control of i_{vd}. This inference is valid in the common modulation freedom control. Since the LVDC common voltage U_{com} is controlled by the DC control. The AC common control can be occupied to regulate the AC active/reactive power. The classical double-loop dq-axis is utilized for the common control.

When the dq-axis is applied in AC differential control, the inference that i_{vd} independently controls active power is wrong. For the classical MMC dq-axis power control, the AC source voltage u_{sd} and u_{sq} are utilized. u_{sq} is naturally 0 when PLL is successfully achieved and the active power contribution from i_{vq} is 0 as a result. However, the differential control has to utilize the AC components in the arm voltages u_{vd} and u_{vq}. Since u_{vq} is always non-zero, the active power contribution from i_{vq} cannot be neglected.

For analyzing the mathematical relation between the AC currents and the differential control, the phasor diagram of the I-M^{2}C AC voltage in the steady state is illustrated in **Figure 7**. In a steady state, the bipolar voltage deviation should be eliminated; thus, the common components of u_{vp} and u_{vn} are equal. For the side with more power consumption, its voltage projection on the direction of current i_{va} is required to be larger than the voltage projection on the other side. Therefore, the direction of differential voltage increment u_{adif} should be the same as i_{va}. In the contrary, the phasor voltage of the other side should add an increment to the opposite direction of i_{va}.

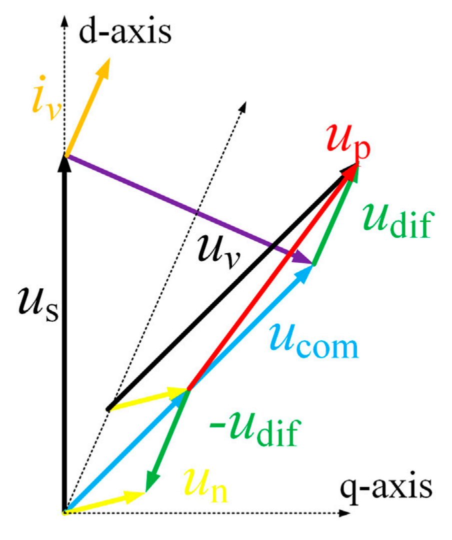

FIGURE 7 | Phasor diagram of the I-M^{2}C AC voltage.

Based on the earlier analysis, the dq-decoupling AC differential modulation freedom controller adds two multipliers before output and the multiply coefficients are i_{vd} and i_{vq}.

The diagrams of the DC control and AC differential modulation freedom control are shown in **Figure 8**. The outer loop of the AC differential controller is the same as the DC controller. Thus, only the inner loop is necessary. The AC controller outputs are composed of d_{jp} and d_{jn}. According to (2), the reference waves for LVDC positive-connected ISMs should be $D_{\mathrm{p}} \pm d_{\mathrm{jp}}$. Similarly, $D_{\mathrm{n}} \pm d_{\mathrm{jn}}$ is the modulation reference for LVDC negative-connected ISMs.

4.3 Operation Range With the Restriction of the Modulation Range

As introduced in **Section 2**, the modulation of the ISMs is based on the duty cycle regulation. Considering the turn on/turn off time and the dead zone of the IGBTs, the modulation range of the submodules is restricted to [0.02, 0.98]. Since the bipolar balance control is dependent on the variation of the modulations, the operation range of the power imbalance is naturally limited within the modulation range.

If the bipolar voltage balance is achieved, the relation between the power imbalance and the modulations can be obtained as **(12)** according to **(11)**:

$$\frac{P_{\mathrm{dcLp}}-P_{\mathrm{dcLn}}}{P_{\mathrm{dcL}}}=\frac{D_{\mathrm{dif}}P_{\mathrm{dcM}}}{D_{\mathrm{com}}P_{\mathrm{dcL}}}+\frac{\left(d_{\mathrm{difd}}i_{\mathrm{vd}}+d_{\mathrm{difq}}i_{\mathrm{vq}}\right)P_{\mathrm{acM}}}{\left(d_{\mathrm{comd}}i_{\mathrm{vd}}+d_{\mathrm{comq}}i_{\mathrm{vq}}\right)P_{\mathrm{dcL}}}. \tag{12}$$

The level of power imbalance can be represented by $\lambda=(P_{\mathrm{dcLp}}\text{-}P_{\mathrm{dcLn}})/P_{\mathrm{dcL}}$ Then **(12)** can be transformed to the following equation:

$$1-\frac{2}{\lambda+1}=\frac{D_{\mathrm{dif}}P_{\mathrm{dcM}}}{D_{\mathrm{com}}P_{\mathrm{dcL}}}+\frac{\left(d_{\mathrm{difd}}i_{\mathrm{vd}}+d_{\mathrm{difq}}i_{\mathrm{vq}}\right)P_{\mathrm{acM}}}{\left(d_{\mathrm{comd}}i_{\mathrm{vd}}+d_{\mathrm{comq}}i_{\mathrm{vq}}\right)P_{\mathrm{dcL}}}. \tag{13}$$

It can be deduced from **(13)** that the range of λ is not only decided by the modulation range but also variable with the ratio of the system power flows $P_{\mathrm{dcM}}/P_{\mathrm{dcL}}$ and $P_{\mathrm{acM}}/P_{\mathrm{dcL}}$. When $P_{\mathrm{acM}} = 0$, $d_{\mathrm{jdif}} = 0$, $P_{\mathrm{dcM}} = P_{\mathrm{dcL}}$, and $D_{\mathrm{dif}} = 0.9$, the upper limitation of λ reaches its minimum:

$$1-\frac{2}{\lambda_{\mathbf{max}}+1}\geq 0.16\Rightarrow\lambda_{\mathbf{max}}\geq\frac{29}{21}\approx 1.38. \tag{14}$$

According to **(13)**, the upper limit of λ becomes higher when $P_{\mathrm{dcM}}/P_{\mathrm{dcL}}$ and $P_{\mathrm{acM}}/P_{\mathrm{dcL}}$ becomes larger. Not considering the influence of reactive power, if the MVAC

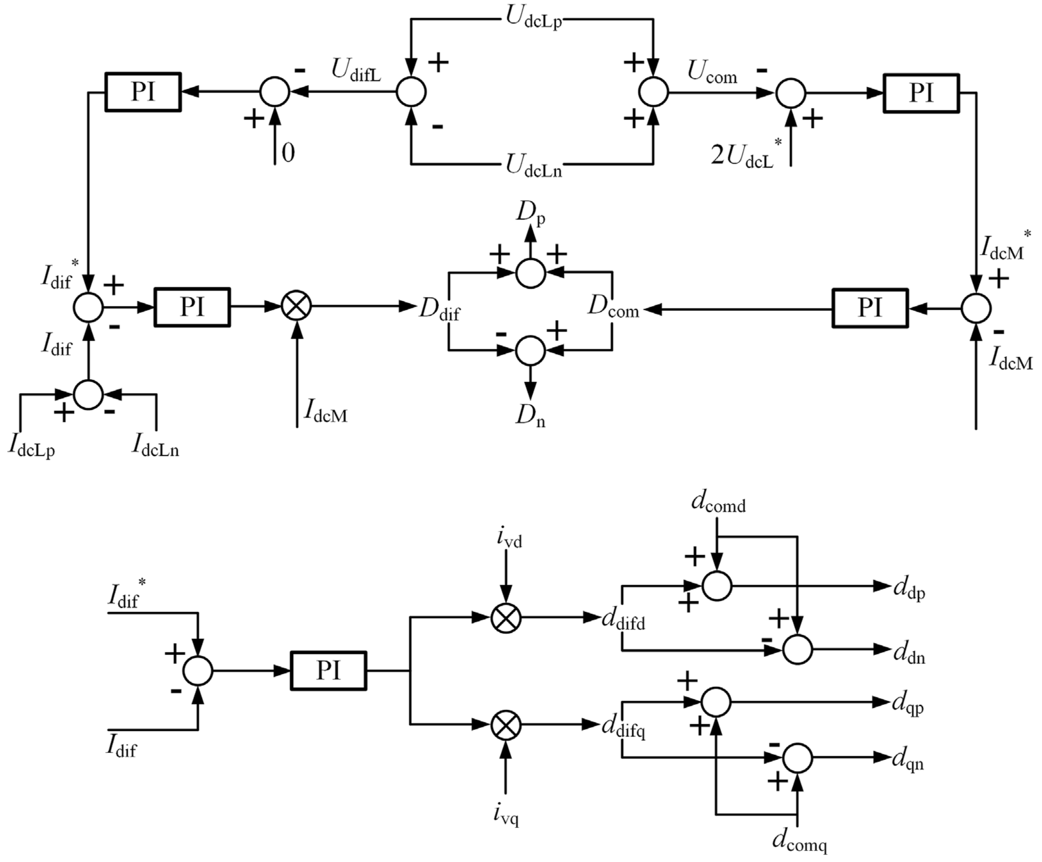

FIGURE 8 | Control diagram of AC differential modulation and DC modulation.

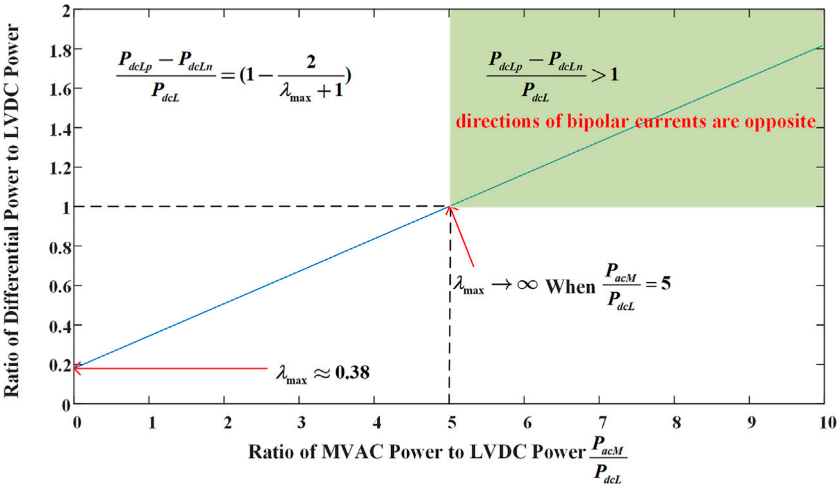

FIGURE 9 | Relationship between $\lambda_{\max}$ and $P_{\mathrm{acM}}/P_{\mathrm{dcL}}$.

power is five times larger than the LVDC power, 100% power loss on one pole is controllable. A linear-approximate function of the relationship between $\lambda_{\max}$ and $P_{\mathrm{acM}}/P_{\mathrm{dcL}}$ is demonstrated in **Figure 9**.

Although the controllable imbalance range of the proposed method is limited by the modulation range and the power flow ratio, power imbalances under 38% are always controllable. It should be noticed that even if a high-power high-deviation

TABLE 1 | Parameters of the Simulated I-M^{2}C system.

Parameter	Value
MVDC rated voltage (kV)	±6
MVAC rated voltage L–L rms (kV)	6
LVDC rated voltage (V)	±750
MVAC equivalent inductor (mH)	12.5
LVDC link capacitor C_{dcL} (mF)	4
Switching frequency (kHz)	10

bipolar imbalance is controlled at the LVDC port, the large current difference between the positive and negative lines will cause the rest busses of the LVDC system to suffer large voltage imbalances. Therefore, a wide range of controllable power imbalance is not necessary for a PET with bipolar balance control capability. On the other hand, the rated capacity of the MVDC/MVAC system is much larger than the eight times of the LVDC system capacity, considering the rated voltage ratio of the MVDC system to the LVDC system. Even if the LVDC system is under full load, the proposed balance control method of the I-M^{2}C is able to stabilize 100% power imbalance under most conditions.

5 SIMULATION

To verify the validity of the proposed method, a detailed simulation of the I-M^{2}C with the bipolar LVDC port was conducted in MATLAB/Simulink. The main parameters of the I-M^{2}C system for simulation are listed in **Table 1**. The MVDC port of the I-M^{2}C is assumed to be connected to one of

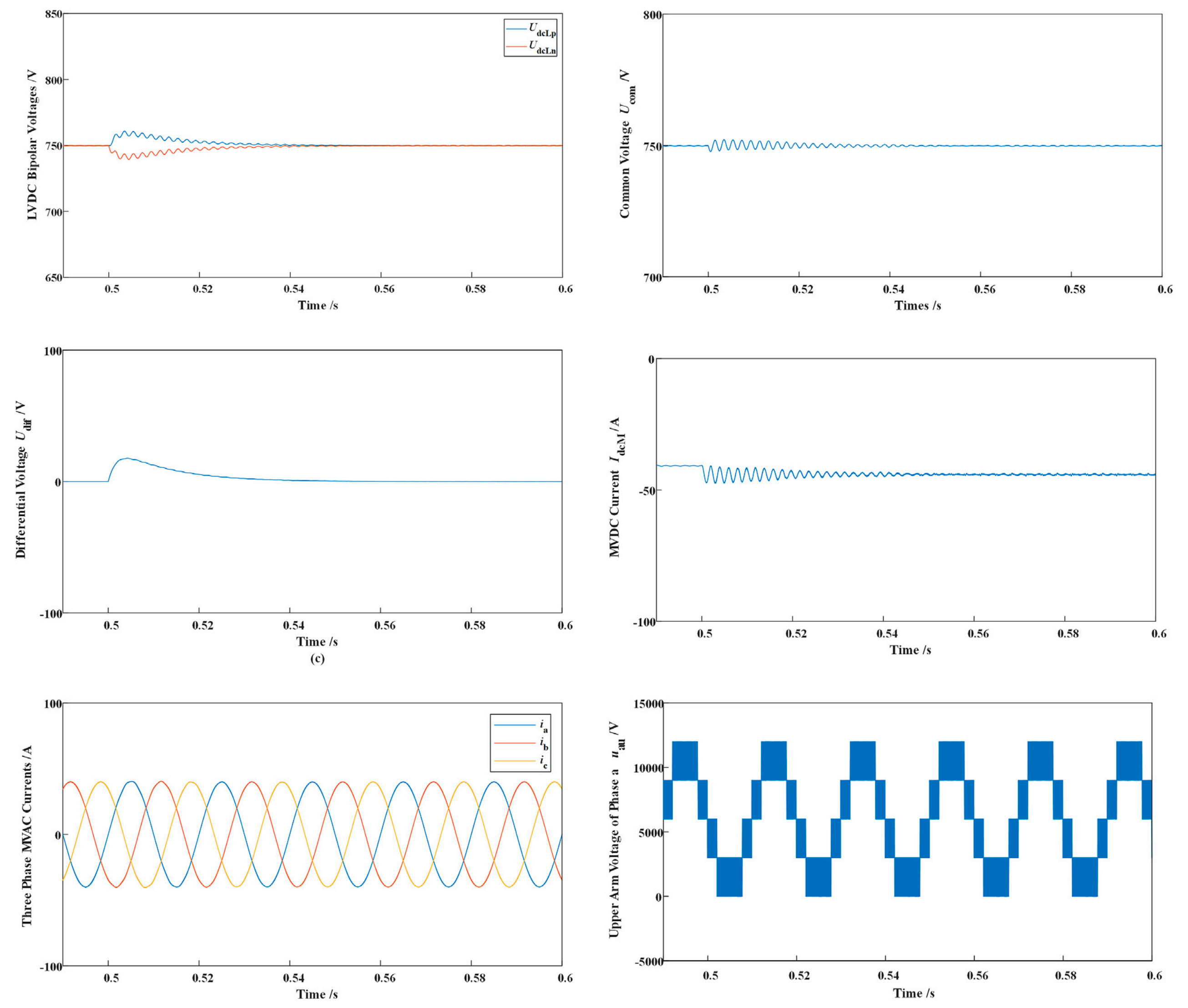

FIGURE 10 | Simulation results of a power imbalance event (LVDC bipolar voltages; LVDC common voltage U_{com}; LVDC differential voltage U_{dif}; MVDC current I_{dcM}; Three-phase MVAC currents i_a, i_b, and i_c; and upper arm voltage of phase a).

the common buses in a ±6kV MVDC distribution system. The MVAC port is linked to a 10-kV MVAC distribution system using a three-phase 50-Hz transformer with 3:5 ratio.

A bipolar power imbalance event starts at 0.5 s. Before 0.5 s, each LVDC pole carries 100 kW load. The MVAC active power is controlled at 240 kW. At 0.5 s, the LVDC negative load immediately increases 40% up to 140 kW. Naturally, the negative voltage U_{dcLn} falls and U_{dcLp} rises. Then the bipolar balance controller starts to eliminate the bipolar voltage difference by regulating the DC and AC modulations, as shown in **Figure 10**.

It can be seen from **Figure 10** that the voltage difference between U_{dcLn} and U_{dcLp} is controlled to zero nearly 0.06 s after the power imbalance within three MVAC cycles. Since the common voltage is not affected from the power imbalance, the fluctuation of U_{com} is only caused by 40 kW rises on the LVDC total load. At nearly 0.504 s, U_{dif} reaches its maximum value 18 V, which is 2.4% of the rated LVDC voltage.

The steady operation of the MVDC and MVAC systems is not disturbed by the power imbalance event. The three-phase MVAC currents are not influenced during the balance control, and the variation of the MVDC current I_{dcM} is controlled by the LVDC common voltage controller.

The modulation regulation during the event is illustrated in **Figure 11** the DC modulations are regulated away from the original value 0.5. Since the MVDC system is delivering power to the I-M^{2}C and the negative pole consumes more power, the DC modulation of the submodules connected to the negative pole D_{n} is higher than D_{p}. Similarly, the AC modulation of the submodules linked to the negative pole is lower than the positive pole since the MVAC system is receiving power from the I-M^{2}C.

5.1 Analysis on the Modulation Regulation

As discussed in **Section 4.3**, the controllable range of LVDC bipolar imbalance is determined by the proportion of MVAC/MVDC power to the LVDC total power. Modulation variations of different cases are listed in **Figure 12**. The simulation results of power balance control with 0 MVAC power is shown in Fig. 19. It can be seen that the DC modulations vary with different load deviations.

The DC differential modulation D_{dif} becomes smaller when the MVAC power becomes higher. The d-axis AC differential modulation d_{difd} becomes smaller when the MVAC power increases from 240 kW to 960 kW, which is caused by the increase in $P_{\mathrm{acM}}/P_{\mathrm{dcL}}$.

The effect of MVAC reactive power on the differential modulation regulation is also demonstrated. The simulation results indicate that the reactive power on the MV side can also be utilized to compensate the active power imbalance on the LV side.

5.2 Influence of LVDC Load Condition

According to **(4)** and **(11)**, the differential power required to achieve voltage balance becomes larger when the LVDC power consumption becomes larger. However, according to **(12)**, the variation of differential is mostly dependent on the ratio of MVAC power and the LVAC power. The simulation of different load conditions is illustrated in **Figure 13**. It can be seen that the response speed for

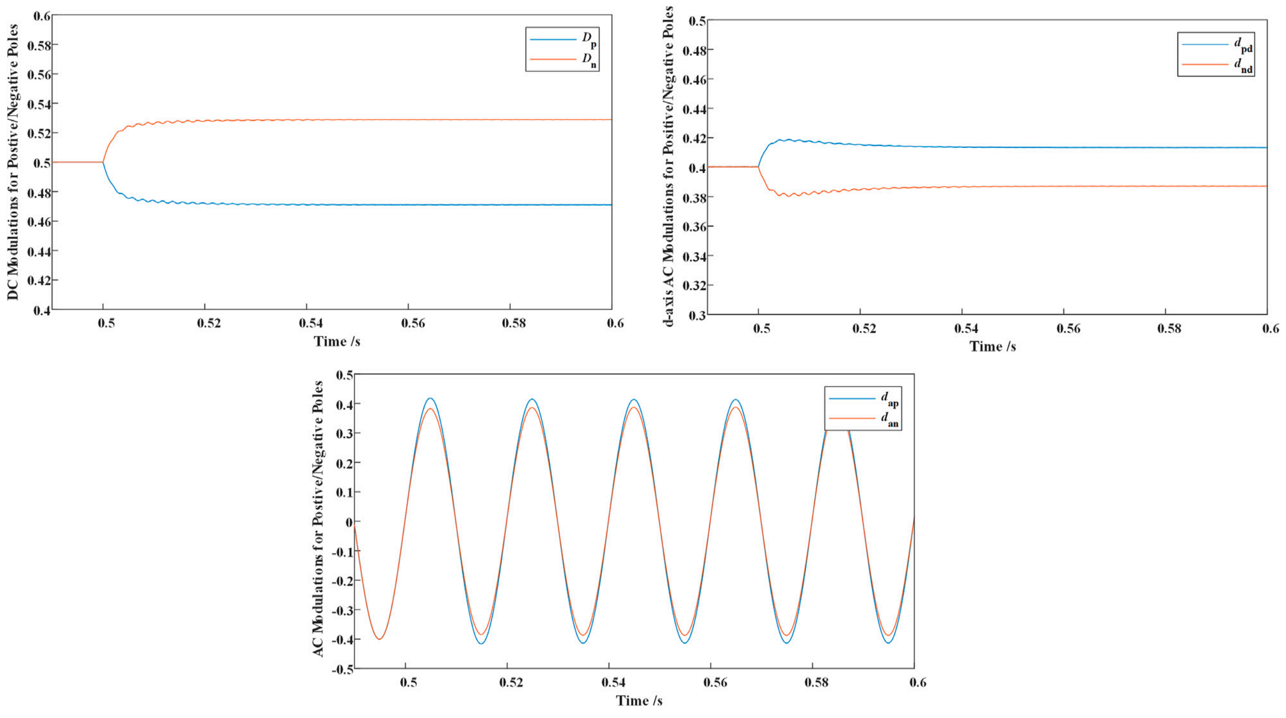

FIGURE 11 | Modulation variation during the event (DC modulations D_{p} and D_{n}; d-axis AC modulations d_{pd} and d_{nd}; and AC modulations for phase A d_{ap} and d_{an}).

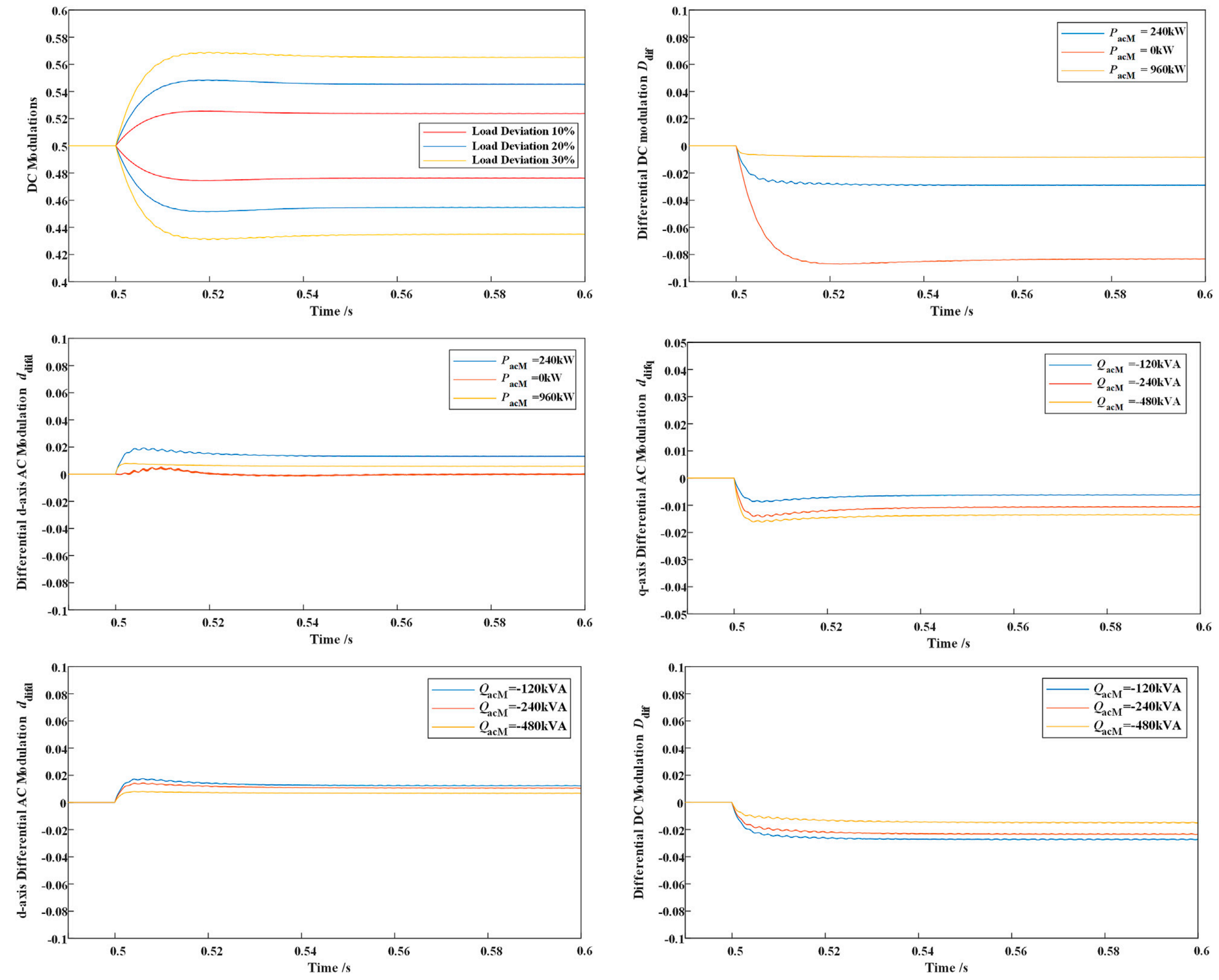

FIGURE 12 | Comparison on the modulation in different cases (DC modulations with different load deviation; differential DC modulation D_{dif} varies with MVAC active power; differential d-axis AC modulation d_{difd} varies with MVAC active power; differential q-axis AC modulation d_{difq} varies with MVAC reactive power; differential d-axis AC modulation d_{difd} varies with MVAC reactive power; and differential DC modulation D_{dif} varies with MVAC reactive power).

TABLE 2 | Comparison results with existing LVDC bipolar schemes.

LVDC bipolar balance scheme	Response time/ms	Peak voltage difference/V	Steady voltage ripple/mV
Buck/boost type in Rivera et al. (2021)	500	76	300
Dual-buck type in Rivera et al. (2021)	200	35	20
Grounding transformer in Li et al. (2018)	280	132	200
Enhanced CLLC in Li Y et al. (2021)	200	17	12
Proposed method	150	17	40

heavier load is faster, but the maximum voltage difference for lighter load is smaller. It can be shown from **Figure 13** that the DC differential modulation varies slightly with different load conditions but with same P_{acM}/P_{dcL}. The result can be compared with the cases where the MVAC power remains the same. It can be referred that any imbalance in the LVDC system can be controlled if the MVAC or MVDC power is much larger than the LVDC power.

5.3 Comparison With Existing LVDC Balance Schemes

Four existing LVDC balance topologies, introduced in Li et al. (2018); Rivera et al. (2021) and Li Y et al. (2021), are modeled in MATLAB/Simulink in order to compare with the proposed I-M^{2}C balance method. As shown in **Figure 14**, the control performances of the buck/boost, dual-buck, and grounding

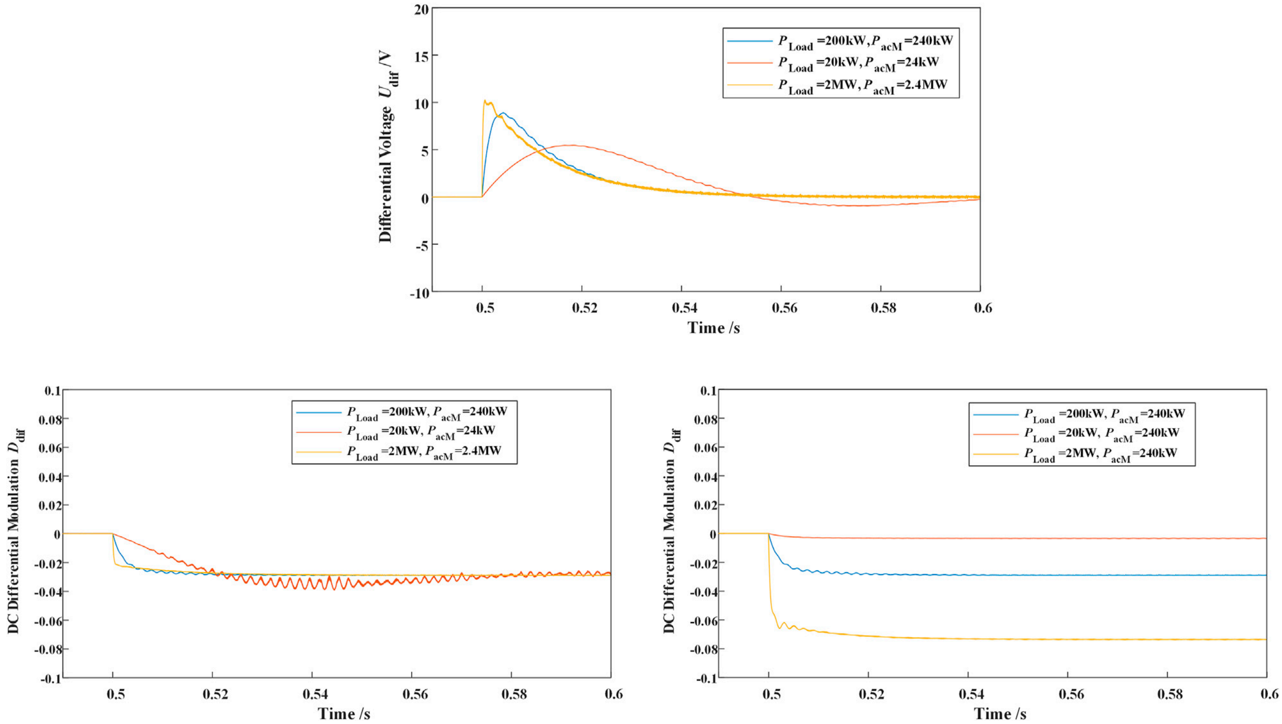

FIGURE 13 | Simulation results of bipolar balance with different load conditions.

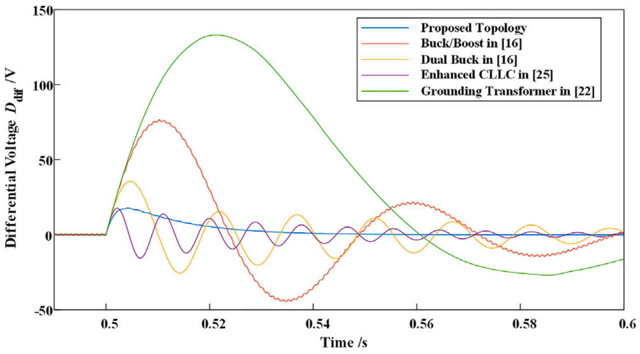

FIGURE 14 | Differential Voltage U_{dif} with different LVDC balance topologies.

transformer type are relatively worse than those of the proposed method due to the extra usage of capacitors and inductors. The control speed and differential voltage suppression of the enhanced DAB topology in Li Y et al. (2021) is similar to those of the proposed method, which is resulted from the smaller neutral inductors and smaller oscillation capacitors. The detailed control performance comparison is listed in **Table 2**.

6 CONCLUSION

For the high-efficiency and eco-friendly nature, the LVDC and MVDC distribution systems have become a suitable selection for urban power grid enhancement with the high penetration of renewable energy and DC loads represented by electric vehicles. For achieving reliable interconnecting between the LVDC, MVDC, and MVAC systems, the MMC-based three-port solid-state transformers (SSTs) have become an essential device. Compared to other types of the MMC-based three-port SSTs, the I-M^{2}C is attractive for its reliable operating characteristic and cost-effective performance. However, the I-M^{2}C is not applicable for bipolar LVDC with the existing topology and control methods. In order to maintain the voltage stability and eliminate the bipolar voltage deviation, a novel bipolar balance method for the I-M^{2}C is proposed in this article. Based on the symmetrical decomposition of AC and DC modulation freedoms, the proposed method can generate the differential power between the two poles without changing the power flow on the MV side. The simulation on MATLAB/Simulink verifies the validity and control performance of the proposed balance method. The simulation results indicate that the proposed method can balance the LVDC port from large imbalance disturbance within 200 ms and is adaptive to different working conditions.

DATA AVAILABILITY STATEMENT

The original contributions presented in the study are included in the article/Supplementary Material; further inquiries can be directed to the corresponding author.

AUTHOR CONTRIBUTIONS

Conceptualization: LL, K-JL, and ZL; writing—original draft preparation: LL, K-JL, and KS; writing—review and editing: KS and WW; visualization: WW and LL; supervision: K-JL; and funding acquisition: K-JL. All authors have read and agreed to the published version of the manuscript.

FUNDING

This work was supported by the National Natural Science Foundation of China (U2166202).

REFERENCES

Agrawal, A., Nalamati, C. S., and Gupta, R. (2019). Hybrid DC-AC Zonal Microgrid Enabled by Solid-State Transformer and Centralized ESD Integration. *IEEE Trans. Ind. Electron.* 66 (11), 9097–9107. doi:10.1109/TIE.2019.2899559

Chew, B. S. H., Xu, Y., and Wu, Q. (2019). Voltage Balancing for Bipolar DC Distribution Grids: A Power Flow Based Binary Integer Multi-Objective Optimization Approach. *IEEE Trans. Power Syst.* 34 (1), 28–39. doi:10.1109/TPWRS.2018.2866817

Cui, S., Lee, J.-H., Hu, J., De Doncker, R. W., and Sul, S.-K. (2019). A Modular Multilevel Converter with a Zigzag Transformer for Bipolar MVDC Distribution Systems. *IEEE Trans. Power Electron.* 34 (2), 1038–1043. doi:10.1109/TPEL.2018.2855082

Gu, Y., Li, W., and He, X. (2016). Analysis and Control of Bipolar LVDC Grid with DC Symmetrical Component Method. *IEEE Trans. Power Syst.* 31 (1), 685–694. doi:10.1109/TPWRS.2015.2403310

Hakala, T., Lähdeaho, T., and Järventausta, P. (2015). Low-Voltage DC Distribution-Utilization Potential in a Large Distribution Network Company. *IEEE Trans. Power Deliv.* 30 (4), 1694–1701. doi:10.1109/TPWRD.2015.2398199

Lee, J.-O., Kim, Y.-S., and Moon, S.-I. (2021). Current Injection Power Flow Analysis and Optimal Generation Dispatch for Bipolar DC Microgrids. *IEEE Trans. Smart Grid* 12 (3), 1918–1928. doi:10.1109/TSG.2020.3046733

Li, Y., Junyent-Ferré, A., and Rodriguez-Bernuz, J.-M. (2018). A Three-Phase Active Rectifier Topology for Bipolar DC Distribution. *IEEE Trans. Power Electron.* 33 (2), 1063–1074. doi:10.1109/TPEL.2017.2681740

Li, Y., Gao, W., Yan, W., Huang, S., Wang, R., Gevorgian, V., et al. (2021). Data-driven Optimal Control Strategy for Virtual Synchronous Generator via Deep Reinforcement Learning Approach. *J. Mod. Power Syst. Clean Energ.* 9 (4), 919–929. doi:10.35833/MPCE.2020.000267

Li, B., Fu, Q., Mao, S., Zhao, X., Xu, D., Gong, X., et al. (2021). DC/DC Converter for Bipolar LVdc System with Integrated Voltage Balance Capability. *IEEE Trans. Power Electron.* 36 (5), 5415–5424. doi:10.1109/TPEL.2020.3032417

Liao, J., Zhou, N., Wang, Q., and Chi, Y. (2021). Load-Switching Strategy for Voltage Balancing of Bipolar DC Distribution Networks Based on Optimal Automatic Commutation Algorithm. *IEEE Trans. Smart Grid* 12 (4), 2966–2979. doi:10.1109/TSG.2021.3057852

Liao, J., Zhou, N., Huang, Y., and Wang, Q. (2021). Decoupling Control for DC Electric Spring-Based Unbalanced Voltage Suppression in a Bipolar DC Distribution System. *IEEE Trans. Ind. Electron.* 68 (4), 3239–3250. doi:10.1109/TIE.2020.2978714

Liu, C., Liu, C., Cai, G., Ying, H., Zhang, Z., Shan, R., et al. (2020). An Isolated Modular Multilevel Converter (I-M2c) Topology Based on High-Frequency Link (HFL) Concept. *IEEE Trans. Power Electron.* 35 (2), 1576–1588. doi:10.1109/TPEL.2019.2923355

Ma, D., Chen, W., Shu, L., Qu, X., Zhan, X., and Liu, Z. (2020). A Multiport Power Electronic Transformer Based on Modular Multilevel Converter and Mixed-Frequency Modulation. *IEEE Trans. Circuits Syst.* 67 (7), 1284–1288. doi:10.1109/TCSII.2019.2931529

Ma, D., Chen, W., Shu, L., Qu, X., and Hou, K. (2021). A MMC-Based Multiport Power Electronic Transformer with Shared Medium-Frequency TransformerIEEE Transactions on Circuits and Systems II: Express Briefs. *IEEE Trans. Circuits Syst.* 68 (2), 727–731. doi:10.1109/TCSII.2020.3012293

Rivera, S., Lizana, R. F., Kouro, S., Dragicevic, T., and Wu, B. (2021). Bipolar DC Power Conversion: State-Of-The-Art and Emerging Technologies. *IEEE J. Emerg. Sel. Top. Power Electron.* 9 (2), 1192–1204. doi:10.1109/JESTPE.2020.2980994

Sun, K., Xiao, H., Pan, J., and Liu, Y. (2021). Cross-Seam Hybrid MTDC System for Integration and Delivery of Large-Scale Renewable Energy. *J. Mod. Power Syst. Clean Energ.* 9, 1352–1362. doi:10.35833/MPCE.2021.000008

Sun, K., Xiao, H., Pan, J., and Liu, Y. (2021). VSC-HVDC Interties for Urban Power Grid Enhancement. *IEEE Trans. Power Syst.* 36 (5), 4745–4753. doi:10.1109/tpwrs.2021.3067199

Sun, K., Qiu, W., Yao, W., You, S., Yin, H., and Liu, Y. (2021). Frequency Injection Based HVDC Attack-Defense Control via Squeeze-Excitation Double CNN. *IEEE Trans. Power Syst.* 36 (6), 5305–5316. doi:10.1109/TPWRS.2021.3078770

Xiao, H., Sun, K., Pan, J., Li, Y., and Liu, Y. (2021). Review of Hybrid HVDC Systems Combining Line Communicated Converter and Voltage Source Converter. *Int. J. Electr. Power Ener.* 129, 106713. doi:10.1016/j.ijepes.2020.106713

Zhang, N., Sun, Q., Wang, J., and Yang, L. (2021). Distributed Adaptive Dual Control via Consensus Algorithm in the Energy Internet. *IEEE Trans. Ind. Inf.* 17 (7), 4848–4860. doi:10.1109/TII.2020.3031437

Zhao, B., Song, Q., Li, J., Liu, W., Liu, G., and Zhao, Y. (2016). High-Frequency-Link DC Transformer Based on Switched Capacitor for Medium-Voltage DC Power Distribution Application. *IEEE Trans. Power Electron.* 31 (7), 4766–4777. doi:10.1109/TPEL.2015.2483543

Zheng, L., Kandula, R. P., and Divan, D. (2021). Soft-Switching Solid-State Transformer with Reduced Conduction Loss. *IEEE Trans. Power Electron.* 36 (5), 5236–5249. doi:10.1109/TPEL.2020.3030795

Zhou, J., Zhang, J., Wang, J., Zang, J., Shi, G., Feng, X., et al. (2021). Design and Control of Power Fluctuation Delivery for Cell Capacitance Optimization in Multiport Modular Solid-State Transformers. *IEEE Trans. Power Electron.* 36 (2), 1412–1427. doi:10.1109/TPEL.2020.3006956

Conflict of Interest: The authors declare that the research was conducted in the absence of any commercial or financial relationships that could be construed as a potential conflict of interest.

frontiers
in Energy Research

ORIGINAL RESEARCH
published: 28 February 2022
doi: 10.3389/fenrg.2022.842318

Synchronous Generator Imitation Control and Dynamic Power Sharing for Distributed Power Generation Systems

Huangqing Xiao**, Bicheng Liu, Xiaowei Huang and Zexiang Cai

School of Electric Power Engineering, South China University of Technology, Guangzhou, China

In this paper, a control method called synchronous generator imitation control (SGIC) as well as a dynamic power sharing for distributed power generation systems (DPGSs) are presented. In order to imitate the behavior of a synchronous generator (SG), the SGIC method for the voltage source converter (VSC) station is proposed. The SGIC includes three loops, namely active power and frequency loop (*Pf* loop), reactive power and voltage loop (*QU* loop) as well as inner current loop. The *Pf* loop is used to emulate the swing equation of the SG. The exciter of the SG is mimicked by the *QU* loop. The inner current loop is developed for fast current and voltage regulations as well as current limiting. The system stability performances are analyzed through small-signal model, and the effectiveness of the proposed control is validated by PSCAD/EMTDC simulations. The results show that the *Pf* loop of the VSC emulates the motion equation of the SG rotor very well, which makes the VSC station to have inertia just as a SG; the VSC station can maintain a stable output voltage and regulate the reactive power at the same time; through the dynamic power sharing, precise power control, frequency offset elimination and system stability improvement are achieved; the system has the merits of fault ride-through capability as well as good dynamic performance.

Keywords: distributed power generation system, inertia, small-signal model, dynamic power sharing, synchronous generator imitation control

Edited by:
Chee Wei Tan,
University of Technology Malaysia,
Malaysia

Reviewed by:
Razman Ayop,
University of Technology Malaysia,
Malaysia
Jitendra Kumar,
National Institute of Technology,
Jamshedpur, India

****Correspondence:***
Huangqing Xiao
xiaohq@scut.edu.cn

Specialty section:
This article was submitted to
Smart Grids,
a section of the journal
Frontiers in Energy Research

Received: *23 December 2021*
Accepted: *09 February 2022*
Published: *28 February 2022*

Citation:
Xiao H, Liu B, Huang X and Cai Z
(2022) Synchronous Generator
Imitation Control and Dynamic Power
Sharing for Distributed Power
Generation Systems.
Front. Energy Res. 10:842318.
doi: 10.3389/fenrg.2022.842318

INTRODUCTION

Recently, distributed power generation system (DPGS) with renewable energy sources, such as wind turbines and photovoltaic, has been attracting more and more attentions for solving energy crisis and environmental issues. However, when the penetration level of renewable energy is high, the grid equivalent rotational inertia becomes low (Blaabjerg et al., 2017). DPGS with low inertia, which is also known as weak grid, may result in poor voltage and frequency response during large disturbances (Xiao et al., 2021a).

In general, there are two ways to solve this problem. One is to install large number of storage batteries in the DPGS, which is not practical considering the high construction cost. The other solution is to develop new control method that can increase the grid inertia or make the interfacing voltage source converter (VSC) participate in voltage and frequency regulation of the grid (Ashabani and Mohamed, 2014a). This paper will look for a solution from the latter.

In conventional VSC control system, the dq-axis decoupling method is used. That is, the active power is controlled by regulating the d-axis current component, while the reactive power is controlled by regulating the q-axis current component. In this way, the active power and reactive power can be controlled independently. The exiting studies found that the widely used current vector controller for VSC based high voltage direct current (HVDC) systems is not applicable when the AC system is very weak (Zhang et al., 2011a; Zhou and Gole, 2012; Hu et al., 2019). When the AC system is weak (the short circuit ratio is small), the d-axis and q-axis of the current is no longer decoupled. The active power and reactive power cannot be regulated independently. Therefore, in weak AC system, the dq-axis decoupling characteristic of the current vector controller is destroyed, which may lead to the instability of the system (Zhang et al., 2011b).

In order to overcome the above limitation, the conventional droop control (CDC) method is usually adopted for the VSC station (Chandorkar et al., 1993; Coelho et al., 1999; Xiao et al., 2022). With the CDC method, the frequency and the amplitude of the output voltage are directly proportional to the real-time transmission active and reactive power. But there are some serious drawbacks for this method. Important among them are permanent offset of frequency due to the change of power, inaccurate power sharing and no contribution for the system inertia (Mohamed and El-Saadany, 2008), (Ashabani et al., 2015).

Another control method for the VSC connected to weak grid or islanded system is the virtual synchronous generator (VSG) control, which operates the VSC in the similar way as the synchronous generator (SG) (Beck and Hesse, 20072007). So far there have been many VSG models (Zhang et al., 2010; Zhong and Weiss, 2011; Zhong et al., 2014; Ashabani and Mohamed, 2014b; Guan et al., 2015). One of them is presented in (Zhong and Weiss, 2011), with which the characteristics of SG are well mimicked. But the additional control loop makes the control scheme complicated, and also this model is lack of current limiting capability. Another VSG model which is well known as power-synchronization control is proposed in (Zhang et al., 2010). This model is successfully used in powering a weak grid and achieves good performance. But the secondary frequency regulation is not realized by this model, which will cause the frequency offset. A simple and practical VSG model is realized in (Guan et al., 2015). The secondary frequency regulation is also achieved. But the exciter of the SG is not emulated, which means the reactive power cannot be controlled precisely.

In order to precisely control the power and optimize power sharing among distributed generators (DGs), higher level controllers (secondary or tertiary controllers) are usually activated. In general, the controller can be divided into two categories: centralized and decentralized (Xin et al., 2015; Olivares et al., 2014; Xiao et al., 2021b). In a decentralized system each DG is controlled by its local controller and the new DGs can be easily plugged into the grid (Xin et al., 2013). However, it is difficult for the decentralized controller to handle the operation of DPGS requiring high levels of coordination (Olivares et al., 2014). Therefore, centralized controllers containing communication system are needed in a DPGS with strong coupling between DGs. A power sharing method with communication is presented in (Liang et al., 2013) to precisely control the reactive power. But the frequency offset is not eliminated and also the system stability is very sensitive to the communication delays (Kahrobaeian and Ibrahim Mohamed, 2015).

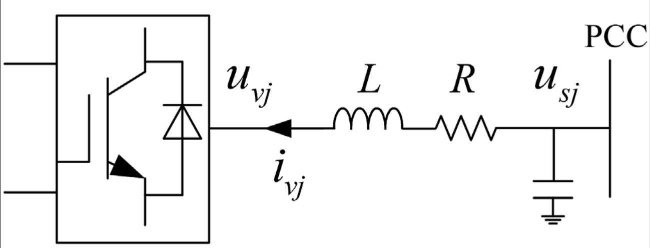

FIGURE 1 | Single-phase equivalent circuit of VSC connected to AC system.

Motivated by the aforementioned reasons, an enhanced control and a novel power sharing for DPGS are proposed in this paper. In this control scheme, each DG adopts a novel control method called synchronous generator imitation control (SGIC). The novel SGIC consists of three loops, including active power and frequency loop (*Pf* loop), reactive power and voltage loop (*QU* loop) as well as inner current loop. The novelty and contribution of this paper is summarized as follows:

1) An enhanced control method called synchronous generator imitation control is proposed in this paper. With the proposed control, the VSC could imitate the behavior of a synchronous generator so that the multiple VSCs could operate stably in the weak AC grid or islanded system as well as provide frequency and voltage support for the power systems.
2) A dynamic power sharing control for the DPGS is also proposed. With this power sharing, the reference values of the active and reactive power are adjusted dynamically instead of being constant. As a result, the power can be allocated precisely; the frequency offset can be eliminated; and the system stability can be improved.

This paper is organized as follows. *Synchronous Generator Imitation Control of VSC* Section presents the principle of SGIC method. The dynamic power sharing for DGPS is introduced in *Dynamic Power Sharing for DPGS* Section. The small-signal model of a DGPS with multiple DGs is built and the stability performance is analysis in *Small-Signal Analysis for a DPGS With the Proposed Control Scheme* Section. *Case Study* Section shows the simulation results of the system in different operation conditions. Finally, *Conclusion* Section concludes the paper.

SYNCHRONOUS GENERATOR IMITATION CONTROL OF VSC

Due to the high penetration level of renewable energy in the power system, the equivalent rotational inertia of the grid is dramatically reduced. It will be of great benefit if the VSC

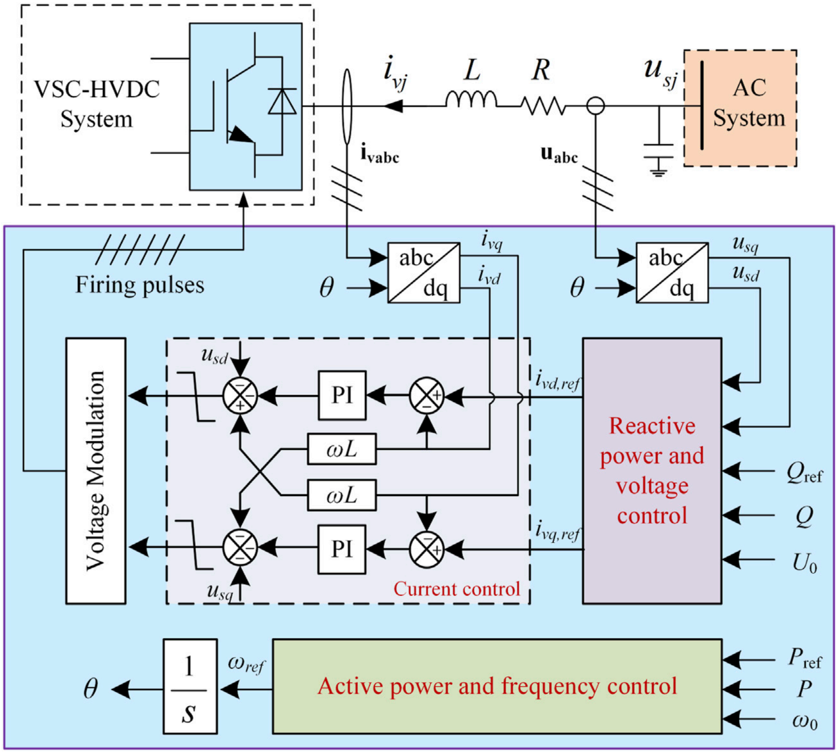

FIGURE 2 | Overall control diagram of the proposed SGIC method.

stations can increase the inertia of the grid just like a SG. In such a manner, the VSC stations can also provide frequency and voltage support for the local grid. In this section, the SGIC method, including inner current loop, Pf loop and QU loop, is presented.

Inner Current Loop

The equivalent circuit of VSC connected to an AC system is shown in **Figure 1** According to the VSC mathematical model in (Xu et al., 2005; Honglin Zhou et al., 2011; Xiao et al., 2015), the equations describing the dynamic characteristics of the VSC can be rewritten as

$$\left.\begin{aligned} L\frac{di_{va}}{dt} + Ri_{va} &= u_{va} - u_{sa} \\ L\frac{di_{vb}}{dt} + Ri_{vb} &= u_{vb} - u_{sb} \\ L\frac{di_{vc}}{dt} + Ri_{vc} &= u_{vc} - u_{sc} \end{aligned}\right\} \tag{1}$$

where, u_{sj} (j = a,b,c) denotes the grid voltage of phase j. u_{vj} and i_{vj} represent the output voltage and current of the VSC respectively. R and L are the resistance and inductance of the interfacing reactor (Xiao et al., 2015). From **Eq. 1** it can be seen that the output current of the VSC i_{vj} can be controlled by adjusting the output voltage u_{vj}. In the dq-axis synchronous frame, the dynamic equations of the VSC can be expressed as (Xiao et al., 2015)

$$\left.\begin{aligned} L\frac{di_{vd}}{dt} + Ri_{vd} &= u_{vd} - u_{sd} + \omega Li_{vq} \\ L\frac{di_{vq}}{dt} + Ri_{vq} &= u_{vq} - u_{sq} - \omega Li_{vd} \end{aligned}\right\} \tag{2}$$

where, ω is the angular frequency of the power grid. According to **Eq. 2** the inner current loop is built in **Figure 2**. It should be noted that the inner current loop can provide current regulation and limit the current amplitude during fault and transient process.

Active Power and Frequency Loop

The inertia effect of the SG is mainly reflected in the motion of the rotor. When there is an unbalance between mechanical and electromagnetic power or torque, the net power or torque will change the angular velocity of the rotor. The inertia of the SG directly affects the angular acceleration. The motion equation representing this process is widely known as the swing equation (Kundru, 1993)

$$J\frac{d(\omega^* - \omega_0)}{dt} = P_0 - P - D(\omega^* - \omega_0) \tag{3}$$

where, P_0 is the mechanical power for the SG or the reference active power for the VSC in this paper. P is the electromagnetic power for the SG or the output transmission power for the VSC. J is the inertia coefficient and D is the damping factor. ω_0 is the nominal angular frequency of the power grid.

Applying the Laplace transform to **Eq. 3**, the expression in **Eq. 4** can be obtained. Then the reference of angular frequency is given by **Equation 5**. **Equation 5** is the control equation of the *Pf* loop for the SGIC.

$$Js(\omega^* - \omega_0) = P_0 - P - D(\omega^* - \omega_0) \tag{4}$$

$$\omega^* = \omega_0 - \frac{P - P_0}{Js + D} \tag{5}$$

If the inertia coefficient $J = 0$, **Equation 5** can be transformed to the conventional active power droop control equation

$$\omega^* = \omega_0 - \frac{P - P_0}{D} \tag{6}$$

From **Eqs 5**, **6** it can be seen that the *Pf* loop can be realized by adding a first-order inertia element to the CDC method. This not only increases the inertia of the local grid, but also greatly simplifies the design process of the controller. Furthermore, the virtual inertia coefficient J is a parameter of the controller. Its value can be adjusted to an expected one according to the operation conditions of the grid. In this way, the VSC can achieve the performances that the SG cannot realize because the inertia coefficient of a SG is fixed.

Reactive Power and Voltage Loop (QU loop)

The *QU* loop is used to emulate the exciter of the SG. The main function of the exciter comprises the control of voltage and reactive power flow, as well as the enhancement of system stability (Kundru, 1993).

The *QU* loop contains two parts, including the reactive power regulation component and the output voltage regulation component. Therefore, the reference voltage U^* also consists of two parts. One part is the no-load voltage U_0, the other is the fluctuation component ΔU which is used to regulate the reactive power. Thus, the control equation of *QU* loop can be expressed as

$$U^* = U_0 + \left(k_G + \frac{k_T}{s}\right)(Q_0 - Q) \tag{7}$$

where, Q_0 is the reference reactive power, and Q is the output reactive power of the VSC.

When the integral constant $k_T = 0$, **Eq. 7** is transformed to the conventional reactive power droop control equation

$$U^* = U_0 + k_G(Q_0 - Q) \tag{8}$$

After the reference of voltage is obtained, the output current reference i_{vd}^* and i_{vq}^* of the inner current loop can be get through PI controllers

$$i_{vd}^* = \left(k_{pd} + \frac{k_{id}}{s}\right)(u_{sd}^* - u_{sd}) \tag{9}$$

$$i_{vq}^* = \left(k_{pq} + \frac{k_{iq}}{s}\right)(u_{sq}^* - u_{sq}) \tag{10}$$

where the references of *dq*-axis voltage components are given by

$$u_{sd}^* = U^* \tag{11}$$

$$u_{sq}^* = 0 \tag{12}$$

So far, the complete model of the SGIC for a VSC station is obtained. The overall control diagram can be seen in **Figure 2**.

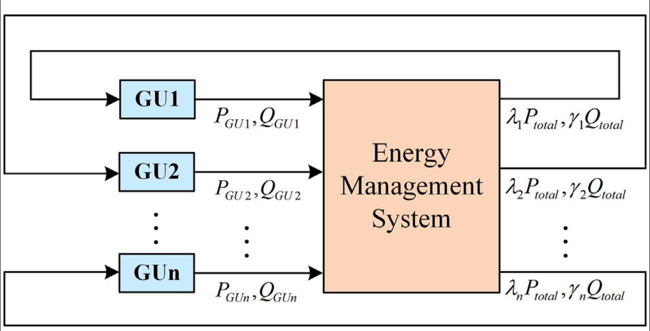

FIGURE 3 | Schematic diagram of the dynamic power sharing.

DYNAMIC POWER SHARING FOR DPGS

When the CDC method or the proposed SGIC method is used in a DPGS, there exist three problems for the whole system. 1) The output power of the VSC stations will deviate from its original set value due to the change of the load demand, which in turn causes the frequency offsets. 2) The reactive power cannot be shared accurately among VSC stations. 3) System stability is highly sensitive to the droop coefficients and the communication delays, which results in low stability margin.

In this section, a novel method named dynamic power sharing is proposed to solve the above three problems.

When the SGIC method is used, each VSC station can be regarded as a SG. In this paper, the real SG and the VSC stations with SGIC method are collectively called generation units (GUs).

In order to eliminate the frequency offset, the power references are adjusted dynamically. The references of active power and reactive power are given by

$$P_{GUi} = \lambda_i P_{total} \tag{13}$$

$$Q_{GUi} = \gamma_i Q_{total} \tag{14}$$

where, $P\ GUi$ is the active power reference of GU_i and $Q\ GUi$ is the reactive power reference. $P_{total} = \sum P\ GUi$ and $Q_{total} = \sum Q\ GUi$ are the total active and reactive powers of the local grid. λ_i is the active power allocation factor of GU_i. γ_i is the reactive power allocation factor of GU_i. The active and reactive power allocation factors satisfy the following equations

$$\sum_{i=1}^{n} \lambda_i = 1 \tag{15}$$

$$\sum_{i=1}^{n} \gamma_i = 1 \tag{16}$$

Figure 3 is the schematic diagram of the dynamic power sharing. The active and reactive powers generated by each GU are transmitted to the energy management system (EMS) so that the total power demand can be calculated. Then the desired active and reactive powers $\lambda_i P_{total}$, $\gamma_i Q_{total}$ are sent back to the GUs as their references.

Because the power references are dynamically adjusted according to the real-time power demand, the frequency offset can be eliminated.

Inserting **Eqs 13**, **14** to **Eqs 5**, **7**, the following equations can be obtained

$$\omega_i^* = \omega_0 + \frac{1}{J_i s + D_i}\left(\lambda_i P_{total} - P_i\right) \tag{17}$$

$$U_i^* = U_0 + \left(k_{Gi} + \frac{k_{Ti}}{s}\right)\left(\gamma_i Q_{total} - Q_i\right) \tag{18}$$

One of the issues that need to be considered in a centralized based EMS is the handling for a failure of the communication system. When the communication system fails, the power reference for each GU becomes zero (that is $\lambda_i = \gamma_i = 0$). In order to stabilize the voltage, the integral term of the QU loop should be set to zero (that is $k_{Ti} = 0$). In this way, the control equations can be rewritten as in **Eqs 19**, **20**

$$\omega_i^* = \omega_0 - \frac{1}{J_i s + D_i} P_i \tag{19}$$

$$U_i^* = U_0 - k_{Gi} Q_i \tag{20}$$

SMALL-SIGNAL ANALYSIS FOR A DPGS WITH THE PROPOSED CONTROL SCHEME

In order to analyze the dynamic performance of the system and optimize the controller parameters, it is necessary to carry out small-signal modeling and analysis on the system with the proposed control scheme. This section will perform a small-signal analysis of a DPGS containing n distributed power supplies.

The load angle derivative is given by

$$\Delta\dot{\delta}_i = \Delta\omega_i \tag{21}$$

Linearization of **Eq. 17** yields

$$\Delta\dot{\omega}_i = -\frac{D_i}{J_i}\Delta\omega_i - \frac{1}{J_i}\Delta P_i + \frac{\lambda_i}{J_i}\sum_{j=1}^{n}\Delta P_i \tag{22}$$

The average active and reactive powers are obtained through low-pass filter as following equations

$$P_i = \frac{\omega_c}{s + \omega_c} p_i \tag{23}$$

$$Q_i = \frac{\omega_c}{s + \omega_c} q_i \tag{24}$$

where ω_c is the bandwidth of the low-pass filter. p_i and q_i are the instantaneous active and reactive power. The small-signal equations of **Eqs 23**, **24** are given by

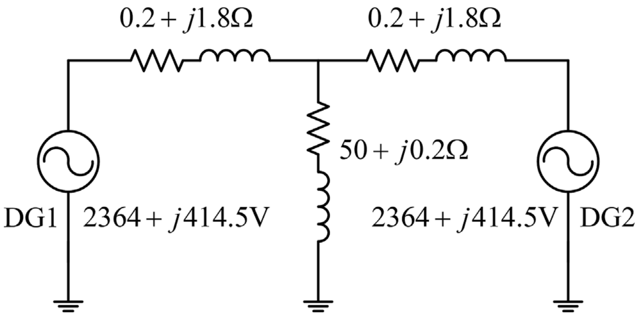

FIGURE 4 | A DPGS for small-signal analysis.

$$\Delta\dot{P}_i = -\omega_c \Delta P_i + \omega_c p_i \tag{25}$$

$$\Delta\dot{Q}_i = -\omega_c \Delta Q_i + \omega_c q_i \tag{26}$$

The linearized form of **Eq. 18** can be expressed as

$$\Delta\dot{U}_i = \left(k_{Ti} - \omega_c k_{Gi}\right)\gamma_i \sum_{j=1}^{n}\Delta Q_j - \left(k_{Ti} - \omega_c k_{Gi}\right)\Delta Q_i + \omega_c k_{Gi}\gamma_i \sum_{j=1}^{n}\Delta Q_j - \omega_c \Delta Q_i \tag{27}$$

For a DPGS with n power-generating nodes and m load nodes, the network equations can be written as

$$\begin{bmatrix} I_n \\ \cdots \\ 0 \end{bmatrix} = \begin{bmatrix} Y_{nn} & \vdots & Y_{nm} \\ \cdots & \cdots & \cdots \\ Y_{mn} & \vdots & Y_{mm} \end{bmatrix} \begin{bmatrix} U_n \\ \cdots \\ U_m \end{bmatrix} \tag{28}$$

In order to simplify the analysis, Kron reduction (Anderson and Foad, 2003)- (Dorfler and Bullo, 2013) is used on **Eq. 28**. Then we can get the system equation containing only n power-generating nodes as

$$\left.\begin{aligned} I_n &= Y_{eq} U_n \\ Y_{eq} &= Y_{nn} - Y_{nm} Y_{mm}^{-1} Y_{mn} \end{aligned}\right\} \tag{29}$$

The active and reactive power injected by each generation unit can be expressed as

$$\begin{aligned} p_i = {} & U_i \cos\delta_i \sum_{j=1}^{n} U_j \left(G_{ij}\cos\delta_j - B_{ij}\sin\delta_j\right) \\ & + U_i \sin\delta_i \sum_{j=1}^{n} U_j \left(G_{ij}\sin\delta_j + B_{ij}\cos\delta_j\right) \end{aligned} \tag{30}$$

$$\begin{aligned} q_i = {} & U_i \sin\delta_i \sum_{j=1}^{n} U_j \left(G_{ij}\cos\delta_j - B_{ij}\sin\delta_j\right) \\ & - U_i \cos\delta_i \sum_{j=1}^{n} U_j \left(G_{ij}\sin\delta_j + B_{ij}\cos\delta_j\right) \end{aligned} \tag{31}$$

where G_{ij} and B_{ij} are the real and imaginary parts of the element Y_{ij} in the equivalent admittance matrix Y_{eq} (ie, $Y_{ij} = G_{ij} + jB_{ij}$).

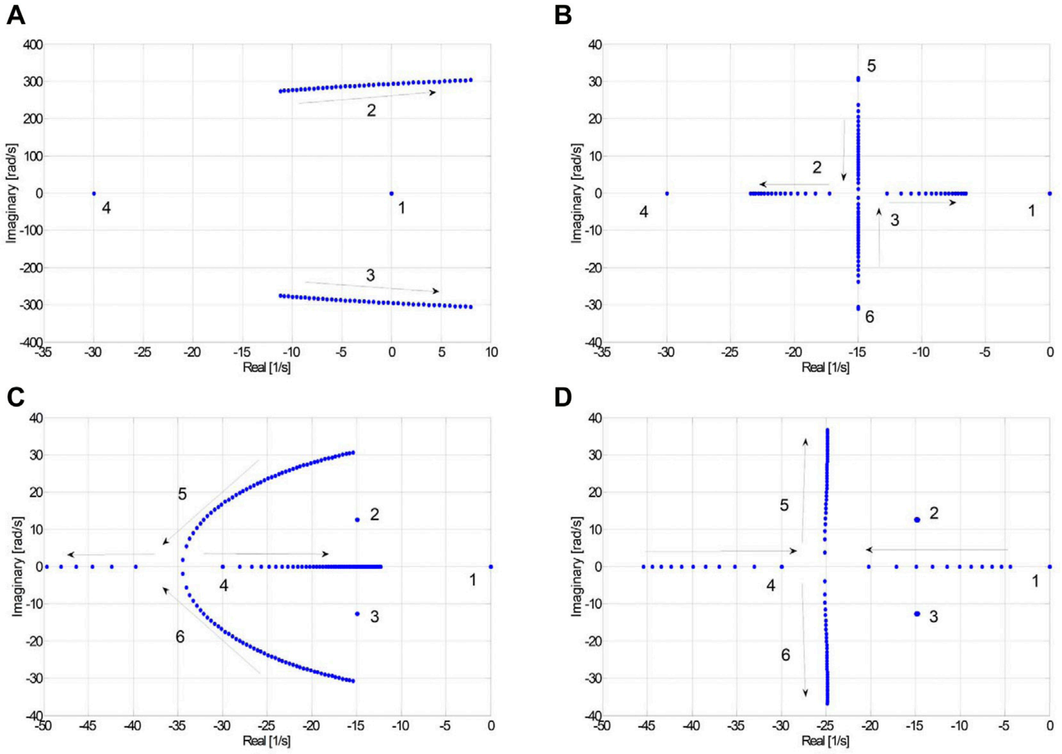

FIGURE 5 | System eigenvalue spectrum when **(A)** $k_G = 0$, $k_T = 0$, $D = 1{,}000$ and J changes from 0.1 to 0.5; **(B)** $k_G = 0$, $k_T = 0.03$, $J = 0.1$, D from 1e5 to 5e5; **(C)** $k_T = 0.03$, $D = 2e5$, $J = 0.1$ and k_G changes from 2e-5 to 2e-3; **(D)** $k_G = 5e\text{-}4$, $D = 2e5$, $J = 0.1$ and k_T changes from 0.005 to 0.05.

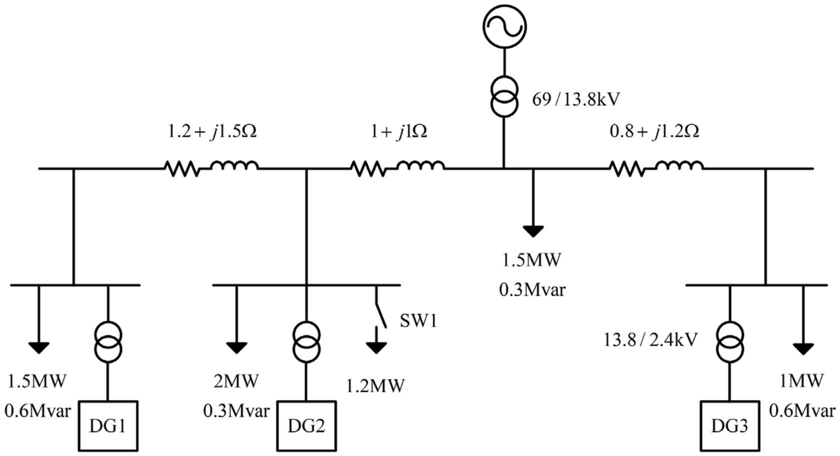

FIGURE 6 | A DPGS with three distributed generators.

The linearized form of **Eqs 30**, **31** can be presented as

$$\Delta p_i = \sum_{j=1}^{n} \frac{\partial p_i}{\partial \delta_j} \Delta \delta_j + \sum_{j=1}^{n} \frac{\partial p_i}{\partial U_j} \Delta U_j \tag{32}$$

$$\Delta q_i = \sum_{j=1}^{n} \frac{\partial q_i}{\partial \delta_j} \Delta \delta_j + \sum_{j=1}^{n} \frac{\partial q_i}{\partial U_j} \Delta U_j \tag{33}$$

The small-signal model of a DPGS with n distributed power supplies is described in **Eqs 21**, **22**; **Eqs 25–27**;

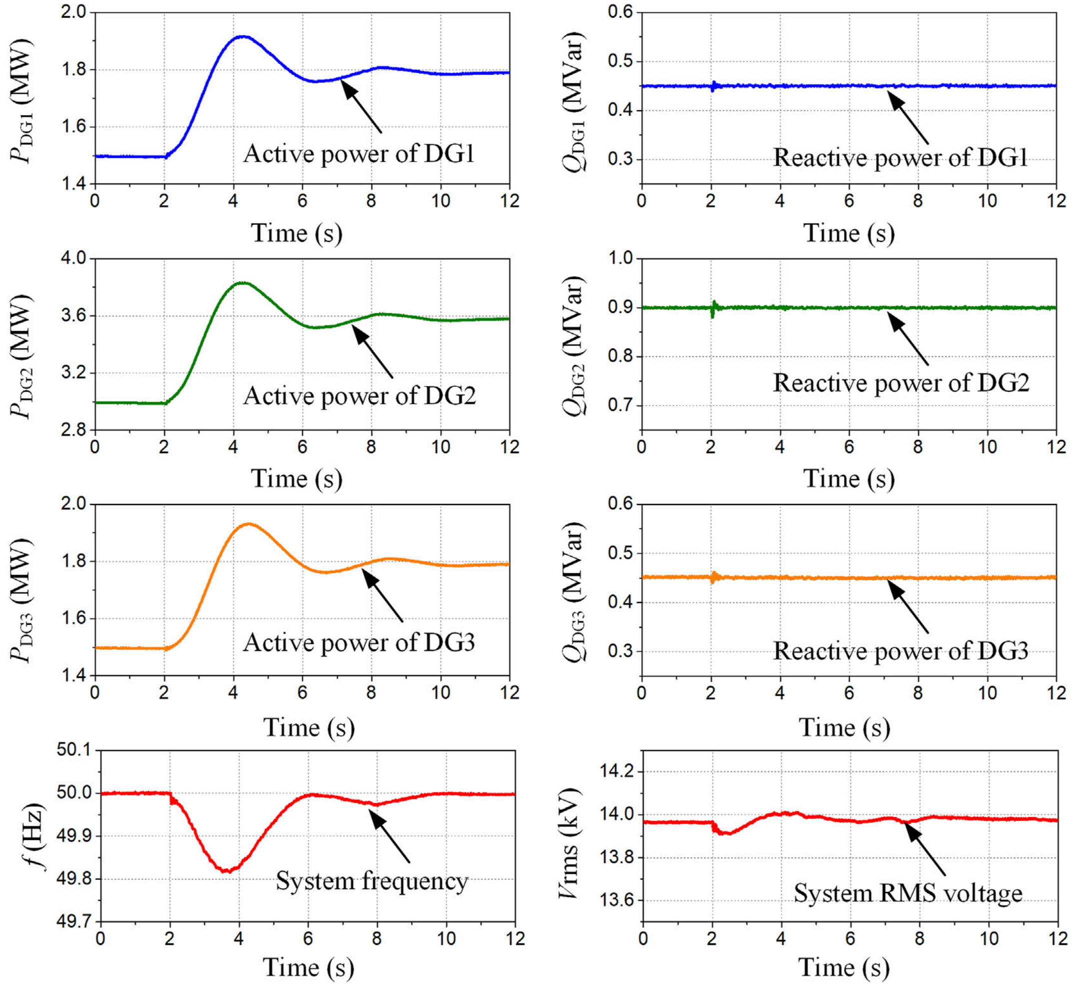

FIGURE 7 | Simulation results under load change.

Eqs 30–33. The overall system small-signal state-space model can be derived as

$$\Delta\dot{x} = A\Delta x \tag{34}$$

$$A = \begin{bmatrix} 0_{n\times n} & I_{n\times n} & 0_{n\times n} & 0_{n\times n} & 0_{n\times n} \\ 0_{n\times n} & \begin{pmatrix} -\frac{D_1}{J_1} & \cdots & 0 \\ \vdots & \ddots & \vdots \\ 0 & \cdots & -\frac{D_n}{J_n} \end{pmatrix} & T_3 & 0_{n\times n} & 0_{n\times n} \\ \omega_c\left(\frac{\partial p}{\partial \delta}\right)_{n\times n} & 0_{n\times n} & -\omega_c I_{n\times n} & 0_{n\times n} & \omega_c\left(\frac{\partial p}{\partial U}\right)_{n\times n} \\ \omega_c\left(\frac{\partial q}{\partial \delta}\right)_{n\times n} & 0_{n\times n} & 0_{n\times n} & -\omega_c I_{n\times n} & \omega_c\left(\frac{\partial q}{\partial U}\right)_{n\times n} \\ T_2\times\left(\frac{\partial q}{\partial \delta}\right)_{n\times n} & 0_{n\times n} & 0_{n\times n} & T_1 & T_2\times\left(\frac{\partial q}{\partial U}\right)_{n\times n} \end{bmatrix} \tag{35}$$

where state variable set is $\Delta x = [\,\Delta\delta_i \quad \Delta\omega_i \quad \Delta P_i \quad \Delta Q_i \quad \Delta U_i\,]^T$ (for $i = 1,2\ldots n$). T_1, T_2 and T_3 are given by

$$T_1 = \begin{bmatrix} (k_{T1}-\omega_c k_{G1})(\gamma_1 - 1) & (k_{T1}-\omega_c k_{G1})\gamma_1 & \cdots & (k_{T1}-\omega_c k_{G1})\gamma_1 \\ (k_{T2}-\omega_c k_{G2})\gamma_2 & (k_{T2}-\omega_c k_{G2})(\gamma_2 - 1) & \cdots & (k_{T2}-\omega_c k_{G2})\gamma_2 \\ \vdots & \vdots & \ddots & \vdots \\ (k_{Tn}-\omega_c k_{Gn})\gamma_n & (k_{Tn}-\omega_c k_{Gn})\gamma_n & \cdots & (k_{Tn}-\omega_c k_{Gn})(\gamma_n - 1) \end{bmatrix}$$

$$T_2 = \begin{bmatrix} \omega_c k_{G1}(\gamma_1 - 1) & \omega_c k_{G1}\gamma_1 & \cdots & \omega_c k_{G1}\gamma_1 \\ \omega_c k_{G2}\gamma_2 & \omega_c k_{G2}(\gamma_2 - 1) & \cdots & \omega_c k_{G2}\gamma_2 \\ \vdots & \vdots & \ddots & \vdots \\ \omega_c k_{Gn}\gamma_n & \omega_c k_{Gn}\gamma_n & \cdots & \omega_c k_{Gn}(\gamma_n - 1) \end{bmatrix}$$

$$T_3 = \begin{bmatrix} (\lambda_1 - 1)/J_1 & \lambda_1/J_1 & \cdots & \lambda_1/J_1 \\ \lambda_2/J_2 & (\lambda_2 - 1)/J_2 & \cdots & \lambda_2/J_2 \\ \vdots & \vdots & \ddots & \vdots \\ \lambda_n/J_n & \lambda_n/J_n & \cdots & (\lambda_n - 1)/J_n \end{bmatrix}$$

The proposed model is applied to a DPGS shown in **Figure 4**. In this system, two VSC stations supply power to a common load through respective connected lines. In order to simplify the analysis, it is assumed that the parameters of the two VSC

TABLE 1 | Control parameters of three VSC stations.

Parameter	DG1	DG2	DG32
Rated output voltage	2.4 kV	2.4 kV	2.4 kV
J	0.15	0.15	0.15
D	70,000	140,000	70,000
k_G	0.0004	0.0004	0.0004
k_T	0.05	0.05	0.05
Λ	0.25	0.5	0.25
Γ	0.25	0.5	0.25
ω_c	30 rad/s	30 rad/s	30 rad/s

stations are the same. The active power allocation factor and reactive power allocation factor for the two VSC are 0.5.

Figure 5 shows the system eigenvalue spectrum with different control parameters.

Figure 5A shows the system root locus when $k_G = 0$, $k_T = 0$, $D = 1{,}000$ and J changes from 0.1 to 0.5. It can be seen from the figure that with the increase of J, eigen2 and eigen3 move from the left half plane to the imaginary axis. In particular, when $J >$ 0.35, the two conjugate complex roots go into the right half plane, indicating that the system is unstable.

Figure 5B shows the location of eigenvalue with $k_G = 0$, $k_T = 0.03$, $J = 0.1$, D from 1e5 to 5e5. As can be seen from the figure, eigen2 and eigen3 are very sensitive to parameter D while eigen5 and eigen6 are almost constant. As D increases, eigen2 and eigen3 change from a pair of conjugate complex roots to two real roots. The absolute value of a real root becomes smaller gradually, which indicates that the stability margin of the system decreases.

Figure 5C shows the system eigenvalue spectrum when $k_T = 0.03$, $D = 2e5$, $J = 0.1$ and k_G changes from 2e-5 to 2e-3. It can be seen that eigen5 and eigen6 are greatly influenced by k_G. When k_G is less than 1e-3, with the increase of k_G, the speed of the system response to the disturbance is accelerated.

Figure 5D shows the system root locus when $k_G = 5e{-}4$, $D = 2e5$, $J = 0.1$ and k_T changes from 0.005 to 0.05. When $k_T < 0.015$, eigen5 and eigen6 are negative real roots; when $k_T > 0.015$, a pair of conjugate complex roots is generated and the

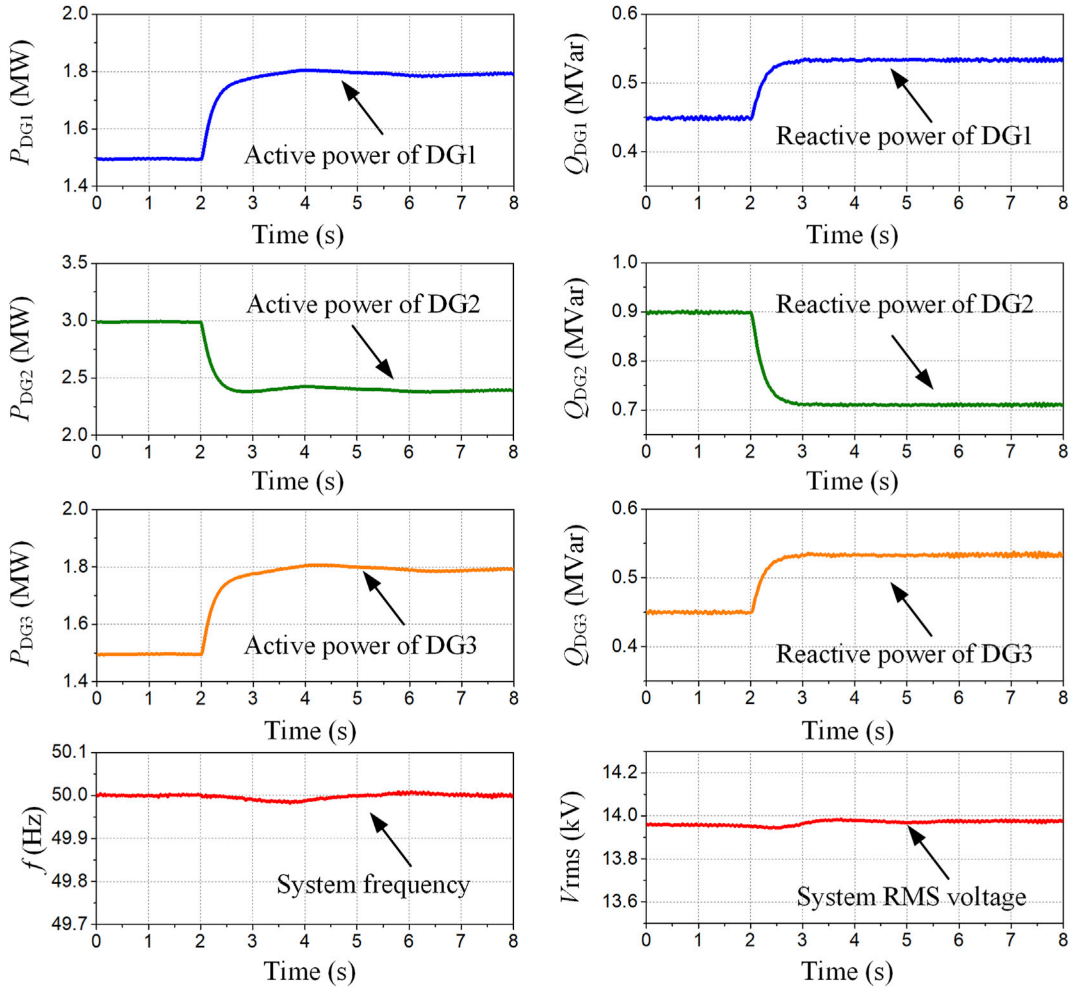

FIGURE 8 | Simulation results with power allocation factors adjustment.

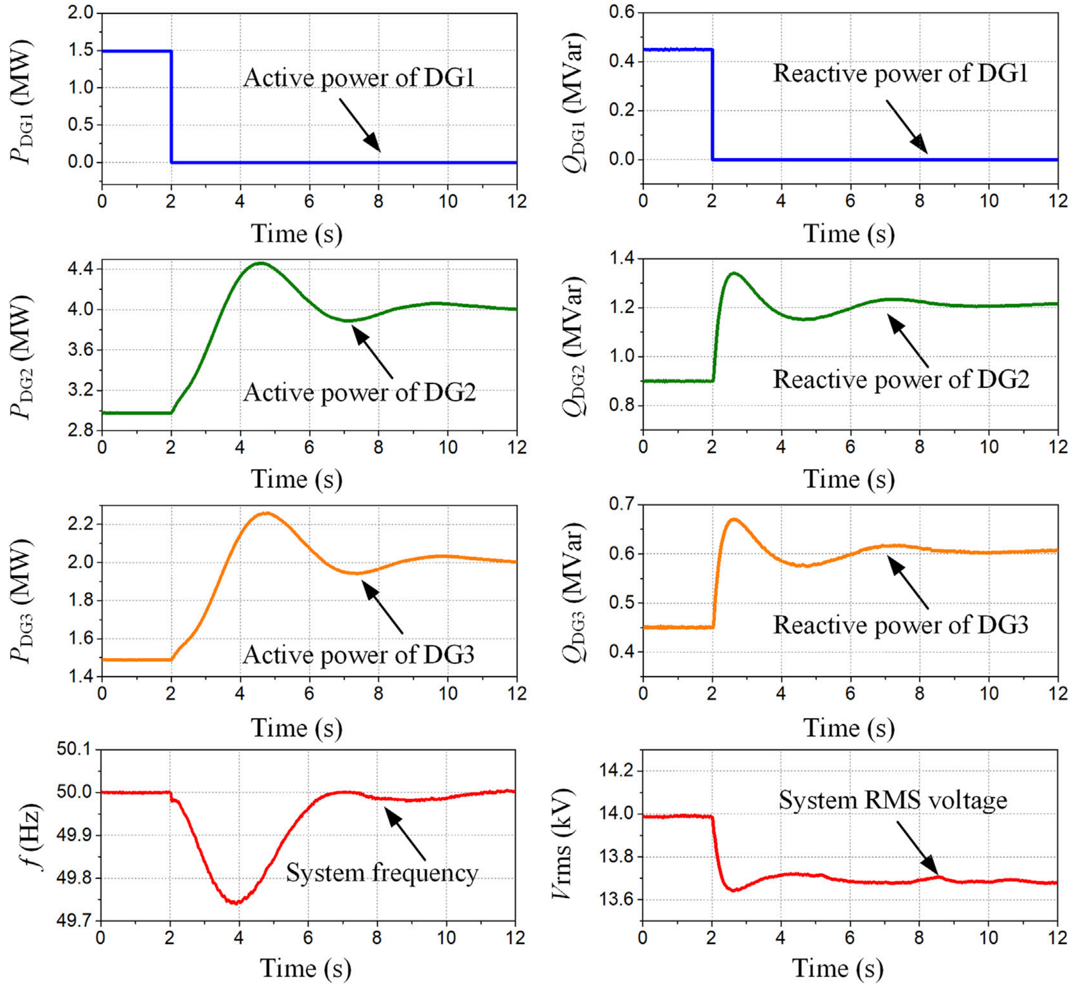

FIGURE 9 | Simulation results under station fault condition.

oscillation frequency of the system increases. But other dominant roots are almost constant, which means satisfactory performance and fast response can be achieved without the loss of stability.

CASE STUDY

In order to verify the accuracy and validity of the proposed control strategy, a DPGS with three distributed generators shown in **Figure 6** is built in PSCAD/EMTDC simulation software. The control parameters of the VSC stations can be seen in **Table 1**.

Case 1: Load Change

Assuming that the system operates at steady state before $t = 0$. At $t = 2$s, an additional load of 1.2 MW is added to the system by closing switch SW1. The corresponding responses of the system are shown in **Figure 7**. When the additional load is added, the system frequency drops due to the power unbalance. After that the SGIC takes effect and the three DGs inject more power to the system. Thus, the system frequency increases gradually. Finally, the system restored to a new steady state. During the transient process, the active power of DG2 is increased from 3.0 to 3.6 MW with increment of 0.6 MW. For DG1 and DG3, both active powers are increased from 1.5 to 1.8 MW with increment of 0.3 MW. The ratio of the power increments for the three DGs is 1:2:1, which is equal to the ratio of their allocation factors (0.25:0.5:0.25). It also can be seen that the system frequency restores its nominal value. That means the change of the active power does not lead to frequency offset, which is one of the advantages of the proposed control scheme.

Case 2: Adjustment of Power Allocation Factors

Another advantage of the proposed control scheme is that the system can flexibly select the optimal power output according to different operating conditions. The system adjusts the active and reactive power outputs of DGs at t = 2s so that DG1 provides 40%

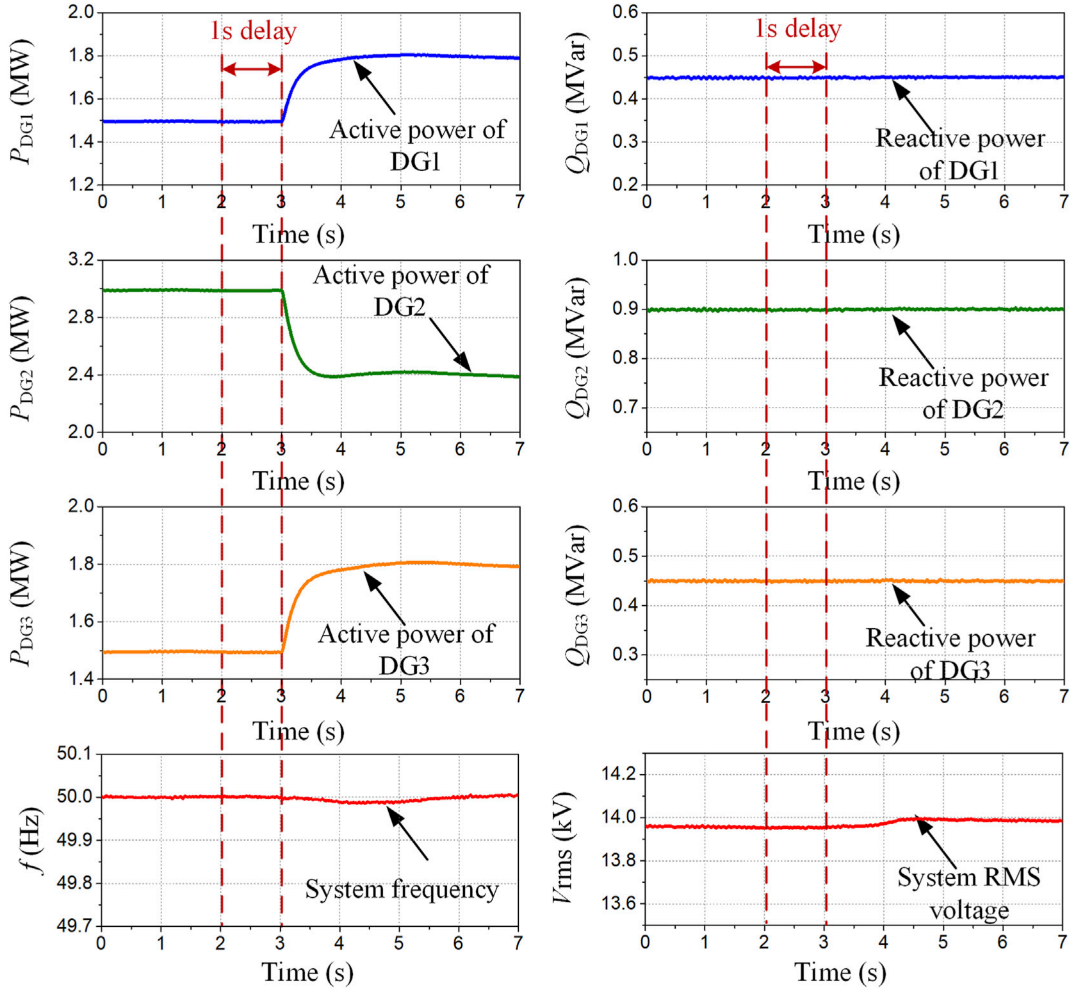

FIGURE 10 | Simulation results with communication delay.

of the total demands, while both DG2 and DG3 provide 30%. The system performances are illustrated in **Figure 8**. This process can be achieved only by adjusting the power allocation factors of each DG to $\lambda_1 = \gamma_1 = 0.4$, $\lambda_2 = \gamma_2 = 0.3$ and $\lambda_3 = \gamma_3 = 0.3$. However, for the CDC method, it is necessary to change the controllers' droop coefficients of each DG to realize this function. As can be seen from the figure, after less than 1s the system transition to a new steady state point. During the transient, the system voltage and frequency fluctuations are very small, which indicates that the disturbance to the system is small.

Case 3: Station Fault

A fault is applied in DG1, which makes it disconnected from the local grid at $t = 2$s. After fault, DG1 no longer participates in dynamic power sharing. The loss of the power is compensated by DG2 and DG3. **Figure 9** shows the corresponding responses of the system. From the figure it can be seen that the active and reactive power of DG2 is changed from 3.0 MW, 0.9 Mvar to 4.0 MW, 1.2 Mvar; and DG3 from 1.5 MW, 0.45 Mvar to 2.0 MW, 0.6 Mvar. The system frequency decreases at the initial state due to the loss of DG1, but restores to its nominal value when DG2 and DG3 compensate the loss. The voltage is mainly affected by reactive power. So, when the reactive power is changed, the voltage will also change. Even though the total amount of reactive power restores to the pre-defined value, the voltage cannot restore to the original value because the voltage is a locally quantity and the its allocation will also change the voltage. This simulation case also shows that the outage of one VSC station will not cause the blackout of the local grid, which means that the system with the proposed control scheme has high reliability and stability.

Case 4: Performances with Communication Delays

Time delay is an unavoidable problem for communication systems. The time delay of a communication system with quantities measured on a remote bus can be more than 100 ms (Milano and Anghel, 2012). But it loses stability when the communication delay reaches 24 ms for some fully centralized EMSs (Kahrobaeian and Ibrahim Mohamed, 2015).

This indicates that the communication delay is a key factor affecting the stability of the fully centralized communication system. As a contrast, the control scheme proposed in this paper only needs to transmit the power reference values without transmitting voltage amplitude and angle reference and other quantities. Therefore, the time delay does not affect the stability of the system. **Figure 10** shows the system performance when the active power allocation factors change at $t = 2$s with 1s of communication delay. It can be seen that the new active power references take effect after 1s delay. The system has good steady state and dynamic performance.

CONCLUSION

This paper presents a control and power sharing method for the distributed power generation system. In this scheme, each of the VSC stations adopts the proposed SGIC method. In order to eliminate the frequency offset, control the power precisely and improve the system stability when there are communication delays, a novel control called dynamic power sharing is proposed. Small-signal model of the whole system has been built and analyzed. A DPGS with three DGs is built in PSCAD/EMTDC software. Various operation conditions including load changes, power allocation factors adjustment, station fault and communication delay are simulated. According to this paper, the important advantages for the proposed scheme can be concluded as follows:

1) The *Pf* loop is designed through simply adding a first-order inertia element to the CDC method, by which the VSC has the similar inertia as the SG. The *QU* loop is used to imitate the exciter of the SG. With this loop the VSC station is able to keep the output voltage stable and control the reactive power at the same time.
2) The inner current loop merits fast current response and current limiting ability, which can avoid overcurrent problems during converter blocking or fault.
3) Through the dynamic power sharing, precise power control, frequency offset elimination and system stability improvement are achieved.
4) With the proposed scheme, the system has the merits of fault ride-through capability as well as good dynamic performance.

DATA AVAILABILITY STATEMENT

The raw data supporting the conclusions of this article will be made available by the authors, without undue reservation.

AUTHOR CONTRIBUTIONS

HX: Conceptualization, Methodology, Writing—original draft. BL and XH: Software, Data curation. ZC: Writing—review and editing.

FUNDING

This work was supported by the Science and Technology Project of China Southern Power Grid Corporation under Grant GDKJXM20198236.

REFERENCES

Anderson, P., and Foad, A. (2003). *Power System Control and Stability*. Hoboken, NJ: Wiley-IEEE Press.

Ashabani, M., and Mohamed, Y. A.-R. I. (2014a). Integrating VSCs to Weak Grids by Nonlinear Power Damping Controller with Self-Synchronization Capability. *IEEE Trans. Power Syst.* 29 (2), 805–814. doi:10.1109/tpwrs.2013.2280659

Ashabani, M., Mohamed, Y. A.-R. I., Mirsalim, M., and Aghashabani, M. (2015). Multivariable Droop Control of Synchronous Current Converters in Weak Grids/Microgrids with Decoupled Dq-Axes Currents. *IEEE Trans. Smart Grid* 6 (4), 1610–1620. doi:10.1109/tsg.2015.2392373

Ashabani, M., and Mohamed, Y. A.-R. I. (2014b). Novel Comprehensive Control Framework for Incorporating VSCs to Smart Power Grids Using Bidirectional Synchronous-VSC. *IEEE Trans. Power Syst.* 29 (2), 943–957. doi:10.1109/tpwrs.2013.2287291

Beck, H. P., and Hesse, R. (20072007). Virtual Synchronous Machine. in 9th International Conference on Electrical Power Quality and Utilisation. Barcelona, 1–6. doi:10.1109/epqu.2007.4424220

Blaabjerg, F., Yang, Y., Yang, D., and Wang, X. (2017). Distributed Power-Generation Systems and Protection. *Proc. IEEE* 105 (7), 1311–1331. doi:10.1109/jproc.2017.2696878

Chandorkar, M. C., Divan, D. M., and Adapa, R. (1993). Control of Parallel Connected Inverters in Standalone AC Supply Systems. *IEEE Trans. Ind. Applicat.* 29 (1), 136–143. doi:10.1109/28.195899

Coelho, E. A. A., Cortizo, P. C., and Garcia, P. F. D. (1999). Small Signal Stability for Single Phase Inverter Connected to Stiff AC systemIndustry Applications Conference. *Thirty-fourth IAS Annu. Meet. Conf. Rec. 1999 IEEE, Phoenix, AZ* 4, 2180–2187. doi:10.1109/ias.1999.798756

Dorfler, F., and Bullo, F. (2013). Kron Reduction of Graphs with Applications to Electrical Networks. *IEEE Trans. Circuits Syst.* 60 (1), 150–163. doi:10.1109/tcsi.2012.2215780

Guan, M., Pan, W., Zhang, J., Hao, Q., Cheng, J., and Zheng, X. (2015). Synchronous Generator Emulation Control Strategy for Voltage Source Converter (VSC) Stations. *IEEE Trans. Power Syst.* 30 (6), 3093–3101. doi:10.1109/tpwrs.2014.2384498

Honglin Zhou, Z., Geng Yang, Y., and Jun Wang, W. (2011). Modeling, Analysis, and Control for the Rectifier of Hybrid HVdc Systems for DFIG-Based Wind Farms. *IEEE Trans. Energ. Convers.* 26 (1), 340–353. doi:10.1109/tec.2010.2096819

Hu, Q., Fu, L., Ma, F., and Ji, F. (2019). Large Signal Synchronizing Instability of PLL-Based VSC Connected to Weak AC Grid. *IEEE Trans. Power Syst.* 34 (4), 3220–3229. doi:10.1109/tpwrs.2019.2892224

Kahrobaeian, A., and Ibrahim Mohamed, Y. A.-R. (2015). Networked-Based Hybrid Distributed Power Sharing and Control for Islanded Microgrid Systems. *IEEE Trans. Power Electron.* 30 (2), 603–617. doi:10.1109/tpel.2014.2312425

Kundru, P. (1993). *Power System Stability and Control*. New York, NY, USA: McGraw-Hill.

Liang, H., Choi, B. J., Zhuang, W., and Shen, X. (2013). Stability Enhancement of Decentralized Inverter Control through Wireless Communications in Microgrids. *IEEE Trans. Smart Grid* 4 (1), 321–331. doi:10.1109/tsg.2012.2226064

Milano, F., and Anghel, M. (2012). Impact of Time Delays on Power System Stability. *IEEE Trans. Circuits Syst.* 59 (4), 889–900. doi:10.1109/tcsi.2011.2169744

Mohamed, Y., and El-Saadany, E. F. (2008). Adaptive Decentralized Droop Controller to Preserve Power Sharing Stability of Paralleled Inverters in Distributed Generation Microgrids. *IEEE Trans. Power Electron.* 23 (6), 2806–2816. doi:10.1109/tpel.2008.2005100

Olivares, D. E., Mehrizi-Sani, A., Etemadi, A. H., Canizares, C. A., Iravani, R., Kazerani, M., et al. (2014). Trends in Microgrid Control. *IEEE Trans. Smart Grid* 5 (4), 1905–1919. doi:10.1109/tsg.2013.2295514

Xiao, H., Huang, X., Xu, F., Dai, L., Zhang, Y., and Cai, Z. (2022). Improved Multiline HVDC Circuit Breakers with Asymmetric Conducting Branches. *Int. J. Electr. Power Energ. Syst.* 137, 107882. doi:10.1016/j.ijepes.2021.107882

Xiao, H., Sun, K., Pan, J., Li, Y., and Liu, Y. (2021b). Review of Hybrid HVDC Systems Combining Line Communicated Converter and Voltage Source Converter. *Int. J. Electr. Power Energ. Syst.* 129, 106713. doi:10.1016/j.ijepes.2020.106713

Xiao, H., Sun, K., Pan, J., Xiao, L., Gan, C., and Liu, Y. (2021a). Coordinated Frequency Regulation Among Asynchronous AC Grids with an MTDC System. *Int. J. Electr. Power Energ. Syst.* 126 (3), 1–11. doi:10.1016/j.ijepes.2020.106604

Xiao, H., Xu, Z., Xue, G. Y., and Tang, G. (2015). Complete Mathematical Model Derivation for Modular Multilevel Converter Based on Successive Approximation Approach. *IET Power Elect.* 8 (12), 2396–2410. doi:10.1049/iet-pel.2014.0892

Xin, H., Zhang, L., Wang, Z., Gan, D., and Wong, K. P. (2015). Control of Island AC Microgrids Using a Fully Distributed Approach. *IEEE Trans. Smart Grid* 6 (2), 943–945. doi:10.1109/tsg.2014.2378694

Xin, H., Zhang, M., Seuss, J., Wang, Z., and Gan, D. (2013). A Real-Time Power Allocation Algorithm and its Communication Optimization for Geographically Dispersed Energy Storage Systems. *IEEE Trans. Power Syst.* 28 (4), 4732–4741. doi:10.1109/tpwrs.2013.2277592

Xu, L., Andersen, B. R., and Cartwright, P. (2005). VSC Transmission Operating under Unbalanced AC Conditions-Analysis and Control Design. *IEEE Trans. Power Deliv.* 20, 427–434. doi:10.1109/tpwrd.2004.835032

Zhang, L., Harnefors, L., and Nee, H.-P. (2011a). Interconnection of Two Very Weak AC Systems by VSC-HVDC Links Using Power-Synchronization Control. *IEEE Trans. Power Syst.* 26 (1), 344–355. doi:10.1109/tpwrs.2010.2047875

Zhang, L., Harnefors, L., and Nee, H.-P. (2011b). Modeling and Control of VSC-HVDC Links Connected to Island Systems. *IEEE Trans. Power Syst.* 26 (2), 783–793. doi:10.1109/tpwrs.2010.2070085

Zhang, L., Harnefors, L., and Nee, H.-P. (2010). Power-Synchronization Control of Grid-Connected Voltage-Source Converters. *IEEE Trans. Power Syst.* 25 (2), 809–820. doi:10.1109/tpwrs.2009.2032231

Zhong, Q. C., Phi-Long Nguyen, P. L., Wanxing Sheng, Z., and Sheng, W. (2014). Self-Synchronized Synchronverters: Inverters without a Dedicated Synchronization Unit. *IEEE Trans. Power Electron.* 29 (2), 617–630. doi:10.1109/tpel.2013.2258684

Zhong, Q.-C., and Weiss, G. (2011). Synchronverters: Inverters that Mimic Synchronous Generators. *IEEE Trans. Ind. Electron.* 58 (4), 1259–1267. doi:10.1109/tie.2010.2048839

Zhou, J., and Gole, A. (2012). VSC Transmission Limitations Imposed by AC System Strength and AC Impedance Characteristics. in AC and DC Power Transmission (ACDC 2012). Birmingham: 10th IET International Conference on, 1–6. doi:10.1049/cp.2012.1986

Conflict of Interest: The authors declare that the research was conducted in the absence of any commercial or financial relationships that could be construed as a potential conflict of interest.

ORIGINAL RESEARCH
published: 13 April 2022
doi: 10.3389/fenrg.2022.844713

A Unified Modeling Scheme of Modular Multilevel Converter for Hybrid AC/DC Power Grids

Xingfeng Xie[1,2], **Zaijun Wu**[1]*, **Qinran Hu**[1], **Xiangjun Quan**[1], **Xiaobo Dou**[1] **and Xiaoyong Cao**[1]

[1]*School of Electrical Engineering, Southeast University, Nanjing, China,* [2]*College of Electrical Engineering and Information Engineering, Lanzhou University of Technology, Lanzhou, China*

Modular multilevel converters (MMCs), as one of the core components of hybrid AC/DC power grids, become the preferred converter topology and show good developments. Urgently, a general MMC modeling scheme with good model accuracy needs to be developed to realize small-signal analyses and designs for the large-scale AC/DC power grids easily. This paper proposes a unified modeling scheme (UMS) for MMC systems in a synchronous rotating (*dq*) reference frame. Based on the dynamic phasor theory and with the proposed modular decouple modeling (MDM), the nonlinear state-space model of the overall MMC system can be obtained by configuring and connecting the input and output of the state-space model of each subsystem. Besides, the unified controller, modeling different control modes, normalizes the MMC systems modeling. Simultaneously, with the proposal of UMS, linearization and splicing could be uesd to develop a small-signal model of the overall MMC system directly. Therefore, the proposed model is suitable for simulating the large-scale hybrid AC/DC power grids and analyzing the stability of small-signal. Finally, the simulation results verify the accuracy and effectiveness of the proposed modeling method.

Keywords: MMC, virtual resistor, module decouple connection method, small signal, MMC modeling, AC/DC power grids

Edited by:
Kaiqi Sun,
Shandong University, China

Reviewed by:
Yizhen Wang,
Tianjin University, China
Ruiyang Yu,
University of Texas at Austin,
United States

***Correspondence:**
Zaijun Wu
zjwu@seu.edu.cn

Specialty section:
This article was submitted to
Smart Grids,
a section of the journal
Frontiers in Energy Research

Received: *28 December 2021*
Accepted: *21 January 2022*
Published: *13 April 2022*

Citation:
Xie X, Wu Z, Hu Q, Quan X, Dou X and Cao X (2022) A Unified Modeling Scheme of Modular Multilevel Converter for Hybrid AC/DC Power Grids.
Front. Energy Res. 10:844713.
doi: 10.3389/fenrg.2022.844713

1 INTRODUCTION

A large number of distributed energy resources (DERs), from transmission systems to distribution networks, have been integrated into power grids to realize low-carbon energy systems. Flexible hybrid AC/DC power grids can effectively serve the grid connection and consumption of large-scale renewable energy. In particular, high-voltage direct current (HVDC) transmission technology has good application prospects in the field of renewable consumption and long-distance transmission (Liu et al., 2014; Zhu et al., 2021; Zhao and Tao, 2021); In addition, with the development of urbanization and the rapid growth of DC load, DC distribution network has attracted extensive attentions from scholars and the industry because of its flexible control (Sun et al., 2021; Xianyong et al., 2021). Modular multilevel converters (MMCs) become the preferred topology of high power converters for flexible AC/DC power grids, showing good development prospects (Trinh et al., 2016; Wang et al., 2021). Therefore, a model reflecting the general operating rules of MMC systems can provide essential guidance in studying the operation characteristics of hybrid AC/DC power grids, selecting the operational parameters of circuits, designing the controllers, and analyzing the stability of AC/DC power grids.

The internal dynamic of MMC is very complex (Harnefors et al., 2013) due to circulating currents and internal capacitor voltages, which results in the harmonic components in the arms (Ilves et al., 2012). Therefore, compared to traditional two-level VSC systems, MMC is more challenging to model and control.

As to the MMC modeling in large-scale hybrid AC/DC power grids, the computational burden introduced by the detailed electromagnetic transient (EMT) highlights the need to develop simplified models that provide similar behaviors and dynamic responses. Because the average arm model (AAM) significantly reduces complexity while maintaining a satisfactory representation of internal dynamics (Antonopoulos et al., 2009), the average model represented by AAM is suitable for simplified simulations and analyses, and has been widely used in the design of control systems (Harnefors et al., 2013; Saad et al., 2015).

Based on the AAM approach in three-phase stationary (*ABC*) reference frame, Gnanarathna et al. (2011) proposed a time-varying model of MMC and Peralta et al. (2012) put forward a detailed and averaged MMC model to improve simulation speed. Although these models can improve simulation speed in large-scale system simulation. However, they are not suitable for eigenvalue analyses due to the time-variance.

Motivated by the need for studies in eigenvalue-based small-signal stability of MMC-based power grids, the modeling in the *dq* reference frame has been widely used for modeling MMC systems. In addition, the design of MMC's control system is usually implemented in the *dq* frame, making the development of the overall MMC model and its interfacing much easier. Munch et al. (2009) presented a state-space description in the *dq* frame for the optimal design of the controller. Vatani et al. (2015) put forward other simplified fundamental frequency models of MMC. In order to facilitate the analysis of large-scale AC/DC power systems. Trinh et al. (2016) and Li et al. (2018) developed the simplified and reduced-order MMC models. But these models are only fit for the fundamental frequency, ignoring the high harmonic parts of the internal dynamics of the converter, such as harmonic circulating currents.

The dynamic-phasor-based modeling, which is based on the generalized average method (Sanders et al., 1990), can replace traditional modeling with time-domain (differential) equations, because the dynamic-phasor modeling is inherent time-invariance and greatly reduces the simulation time without losing accuracy. Deore et al. (2012) first applied the dynamic phasor modeling method in the MMC-HVDC system, where a state-space model with 98 states was developed. However, the model is highly complex, including many complex dynamic equations. Jamshidifar and Jovcic (2016) proposed a dynamic state-space model of MMC for analyzing small-signal dynamics and designing controllers, but control system modeling is not covered in the model. Jovcic and Jamshidifar (2015) built an average-model-based dynamic phasor model of MMC, whose electrical system and control system are coupled together, leading to the inconvenience of connecting the MMC model with both external control and DC electrical parts.

As seen from the previous analyses, the models in the *ABC* frame are applicable to the trial-and-error study of time-domain simulation, but these models are not suitable for the study of the eigenvalue-based small-signal stability in MMC-based power grids. Although many efforts have been made on MMC modeling in the *dq* frame, a general MMC modeling scheme with high model accuracy urgently needs to develop to realize small-signal analyses and designs for the large-scale AC/DC power grids easily.

This paper proposes a unified modeling scheme (UMS) for MMC systems in a synchronous (*dq*) reference frame for the analyses of both MMC-based system operation and small-signal stability. The modular decouple modeling (MDM) and the unified controller modeling make MMC systems modeling more flexible and expansible to adapt to different hybrid AC/DC power grids. Besides, based on the proposed model, the small-signal model of the overall MMC system could be developed directly by linearizing and then splicing our model, which can avoid the direct derivation of the overall system matrix element. Therefore, our model is suitable for simulating the large-scale hybrid AC/DC power grids as well as studying small-signal stability. The accuracy and effectiveness of the proposed modeling method are verified by a simulation test system in MATLAB/Simulink.

2 MODELING MODULAR MULTILEVEL CONVERTER SYSTEMS WITH UNIFIED MODELING SCHEME

A three-phase model of MMC is shown in **Figure 1**. The MMC is assumed to be connected to an infinite power supply through a transformer. Each phase unit of the MMC comprises two bridge arms, positive (P) and negative (N). In **Figure 1**, when submodules (SMs) are half-bridge circuits composed of insulated gate bipolar translator (IGBT), the model of MMC is a detailed EMT (D-EMT) model; when arms in **Figure 1** are equivalent to the circuits of a controlled voltage source, the model of MMC is an average EMT (AVE-EMT) model. The parameters represented by each variable in the **Figure 1** are shown in **Table 1**.

Since the proposed UMS for MMC systems is achieved in *dq* frame, the model proposed in this paper can be derived by transforming the dynamic average model built in *ABC* frame based on *Park* transformation and dynamic phasor theory. First, with MDM, the overall MMC system is partitioned into five parts (specifically, they are MMC internal electrical system, DC interface system, AC system, signal sampling filter, and controller) and modeled separately. Then, by configuring and connecting the input and the output of the state-space model of each system, we can obtain the nonlinear state-space model of the overall MMC system.

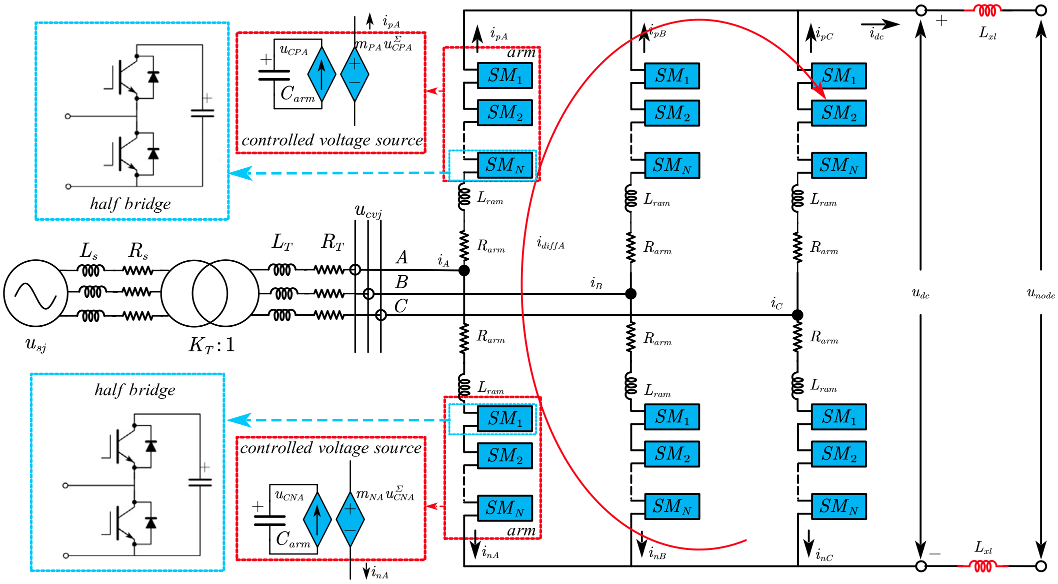

FIGURE 1 | Structure of an MMC.

TABLE 1 | Parameters of the MMC systems.

Parameter name	Symbol	Parameter name	Symbol
Line voltage of AC system	u_s	Equivalent arm currents	i_{pj}, i_{nj}
Voltage frequency of AC system	f	Circulating current of bridge arm	$i_{\mathrm{diff}j}$
Equivalent inductance of AC system	L_{sj}	Modulation ratio of bridge arm	m_{Pj}, m_{Nj}
Equivalent resistance of AC system	R_{sj}	Equivalent capacitor of bridge arm	C_{arm}
Equivalent inductance of transformer	L_{Tj}	Equivalent Inductance of bridge arm	L_{arm}
Equivalent resistance of transformer	R_{Tj}	Equivalent resistance of bridge arm	R_{arm}
Ratio of transformer	K_T	Number of bridge arm sub-modules	N
Total voltage of submodule capacitor of bridge arm	$u^{\Sigma}_{\mathrm{CP}j}$, $u^{\Sigma}_{\mathrm{CN}j}$	DC side current of MMC	i_{dc}
Equivalent arm voltages	$u_{\mathrm{CP}j}$, $u_{\mathrm{CN}j}$	DC side voltage of MMC	u_{dc}
Voltage of MMC connection point	u_{cvj}	Current-limiting inductance	L_{xl}

2.1 Modeling Modular Multilevel Converter Internal Electrical System

2.1.1 Modeling in ABC Reference Frame

Since the MMC model established in this paper focuses on system operation and stability analysis without any consideration of AC or DC faults, the following assumptions are made for modeling MMC systems:

1) All three-phase components are symmetric; 2) The operations of the positive and negative arms of each phase are symmetric; 3) The modeling of a phase-locking loop (PLL) is not taken into account, because the voltage deviation of the point of common coupling (PCC) bus is diminutive during normal operation due to a relatively high ratio of short circuit of the AC system connected to MMC.

Remark 1. In order to reduce the complexity of the formula, the following formula derivation takes one phase as an example (j = A, B, C) and omits the subscript j representing three phases.

According to **Figure 1**, the circulating current can be expressed as:

$$i_{\mathrm{diff}} = \frac{i_p - i_n}{2} \tag{1}$$

and

$$C_{arm} = \frac{C_e}{N} \tag{2}$$

where C_e is the capacitance value of the submodule.

The dynamic model of u^{Σ}_{CP} and u^{Σ}_{CN} are expressed as **Eq. 3**.

$$\begin{aligned} \frac{du^{\Sigma}_{\mathrm{CP}}}{dt} &= -\frac{m_P i_p}{C_{arm}} = -\frac{m_P}{2C_{arm}} i - \frac{m_P}{C_{arm}} i_{\mathrm{diff}} \\ \frac{du^{\Sigma}_{\mathrm{CN}}}{dt} &= \frac{m_N i_n}{C_{arm}} = \frac{m_N}{2C_{arm}} i - \frac{m_N}{C_{arm}} i_{\mathrm{diff}} \end{aligned} \tag{3}$$

where i=i_p−i_n

For positive and negative bridge arms, the following equations can be obtained by KVL:

$$\frac{u_{dc}}{2} + R_{arm} i_p + L_{arm}\frac{di_p}{dt} - m_P u_{\mathrm{CP}}^{\Sigma} = u_{cv} \tag{4}$$

$$-\frac{u_{dc}}{2} + R_{arm} i_n + L_{arm}\frac{di_n}{dt} + m_N u_{\mathrm{CN}}^{\Sigma} = u_{cv} \tag{5}$$

By **Eq. 4** minus **Eq. 5**, the dynamic equation of the circulating current can be expressed as **Eq. 6**.

$$\frac{di_{\mathrm{diff}}}{dt} = -\frac{R_{arm} i_{\mathrm{diff}}}{L_{arm}} + \frac{m_P u_{\mathrm{CP}}^{\Sigma}}{2L_{arm}} + \frac{m_N u_{\mathrm{CN}}^{\Sigma}}{2L_{arm}} - \frac{u_{dc}}{2L_{arm}} \tag{6}$$

Add **Eq. 4** to **Eq. 5**, the dynamic equation of the AC current can be expressed as **Eq. 7**.

$$\frac{\mathrm{d}i}{\mathrm{d}t} = \frac{2u_{cv}}{L_{\mathrm{arm}}} - \frac{m_N u_{\mathrm{CN}}^{\Sigma} - m_P u_{\mathrm{CP}}^{\Sigma}}{L_{\mathrm{arm}}} - \frac{R_{\mathrm{arm}}}{L_{\mathrm{arm}}} i = \frac{2u_{cv}}{L_{\mathrm{arm}}} - \frac{2e_{MMC}}{L_{\mathrm{arm}}} - \frac{R_{\mathrm{arm}}}{L_{\mathrm{arm}}} i \tag{7}$$

Here, in **Eq. 7**, e_{MMC} is as follows.

$$e_{MMC} = \frac{m_N u_{\mathrm{CN}}^{\Sigma} - m_P u_{\mathrm{CP}}^{\Sigma}}{2} \tag{8}$$

When the three-phase voltage of AC system is symmetrical, the components of voltage, current and modulation signal are relatively simple (Jamshidifar and Jovcic, 2016), u_s, u_{cv}, u_{CP}^{Σ}, u_{CN}^{Σ}, i, i_{diff}, m_P and m_N can be expressed in terms of its sub-components as follows.

$$\begin{cases} u_s = U_s \cos(\theta + \theta_{s1}) \\ u_{cv} = U_{cv} \cos(\theta + \theta_{cv1}) \\ m_P = \dfrac{1}{2}\left(1 - M_1 \cos(\theta - \theta_{m1}) + M_2 \cos(2\theta - \theta_{m2})\right) \\ m_N = \dfrac{1}{2}\left(1 + M_1 \cos(\theta - \theta_{m1}) + M_2 \cos(2\theta - \theta_{m2})\right) \end{cases} \tag{9}$$

$$\begin{cases} i = I\cos(\theta + \theta_{i1}) \\ i_{\mathrm{diff}} = I_{\mathrm{diff0}} + I_{\mathrm{diff2}} \cos(2\theta + \theta_{\mathrm{diff2}}) \\ u_{\mathrm{CP}}^{\Sigma} = U_{CP0} + U_{CP1} \cos(\theta + \theta_{CP1}) + U_{CP2} \cos(2\theta + \theta_{CP2}) \\ u_{\mathrm{CN}}^{\Sigma} = U_{CN0} + U_{CN1} \cos(\theta + \theta_{CN1}) + U_{CN2} \cos(2\theta + \theta_{CN2}) \end{cases} \tag{10}$$

where the subscripts 0, 1, and 2 in the amplitudes (U_s, U_{cv}, M_1, M_2, I_{diff0}, I, I_{diff2}, U_{CP0}, U_{CP1}, U_{CP2}, U_{CN0}, U_{CN1}, and U_{CN2}) and the initial phase angles (θ_{s1}, θ_{cv1}, θ_{m1}, θ_{m2}, θ_{i1}, θ_{diff2}, θ_{CP1}, θ_{CP2}, θ_{CN1}, and θ_{CN2}) represent the zero sequence, the fundamental-frequency, and the second-order harmonic components, respecitvely; $\theta = \omega t$ (ω is the grid fundamental frequency) is a synchronized phasor angle with the grid voltage.

2.1.2 Modeling in *dq* Reference Frame

To obtain the steady-state time invariants model of MMC, we need to transform variables u_s, u_{cv}, u_{CP}^{Σ}, u_{CN}^{Σ}, i, i_{diff}, m_P and m_N in *ABC* reference frame into *dq* reference frame by means of a park transformation P_{Park} at ω. P_{Park} and its inverse matrix P_{Park}^{-1} are as follows.

$$P_{park} = \frac{2}{3}\begin{bmatrix} \cos\theta & \cos\left(\theta - \frac{2}{3}\pi\right) & \cos\left(\theta + \frac{2}{3}\pi\right) \\ -\sin\theta & -\sin\left(\theta - \frac{2}{3}\pi\right) & -\sin\left(\theta + \frac{2}{3}\pi\right) \\ \frac{1}{2} & \frac{1}{2} & \frac{1}{2} \end{bmatrix} \tag{11}$$

$$P_{park}^{-1} = \begin{bmatrix} \cos\theta & -\sin\theta & 1 \\ \cos\left(\theta - \frac{2}{3}\pi\right) & -\sin\left(\theta - \frac{2}{3}\pi\right) & 1 \\ \cos\left(\theta + \frac{2}{3}\pi\right) & -\sin\left(\theta + \frac{2}{3}\pi\right) & 1 \end{bmatrix} \tag{12}$$

Thus, u_s, u_{cv}, u_{CP}^{Σ}, u_{CN}^{Σ}, i, i_{diff}, m_P and m_N in *dq* reference frame are expressed as follows by **Eq. 12**.

$$\begin{cases} u_s = u_{sd} \cos\theta - u_{sq} \sin\theta \\ u_{cv} = u_{cvd} \cos\theta - u_{cvq} \sin\theta \\ m_P = \dfrac{1}{2}\left(1 - M_d \cos\theta + M_q \sin\theta - M_{d2} \cos 2\theta - M_{q2} \sin 2\theta\right) \\ m_N = \dfrac{1}{2}\left(1 + M_q \cos\theta - M_q \sin\theta - M_{d2} \cos 2\theta - M_{q2} \sin 2\theta\right) \end{cases} \tag{13}$$

$$\begin{cases} i = i_d \cos\theta - i_q \sin\theta \\ i_{\mathrm{diff}} = i_{\mathrm{diff0}} + i_{\mathrm{diff}d2} \cos 2\theta - i_{\mathrm{diff}q2} \sin 2\theta \\ u_{\mathrm{CP}}^{\Sigma} = u_{\mathrm{CP0}}^{\Sigma} + u_{\mathrm{CP}d}^{\Sigma} \cos\theta - u_{\mathrm{CP}q}^{\Sigma} \sin\theta + u_{\mathrm{CP}d2}^{\Sigma} \cos 2\theta - u_{\mathrm{CP}q2}^{\Sigma} \sin 2\theta \\ u_{\mathrm{CN}}^{\Sigma} = u_{\mathrm{CN0}}^{\Sigma} + u_{\mathrm{CNd}}^{\Sigma} \cos\theta - u_{\mathrm{CP}q}^{\Sigma} \sin\theta + u_{\mathrm{CNd2}}^{\Sigma} \cos 2\theta - u_{\mathrm{CP}q2}^{\Sigma} \sin 2\theta \end{cases} \tag{14}$$

where the variables with subscripts *d* and *q* represent the fundamental frequency components of the corresponding variables in *dq* reference frame; the variables with subscripts d_2 and q_2 represent second-order harmonic components of the corresponding variables in *dq* reference frame; the variables with subscript 0 represent the DC components of the corresponding variables in *dq* reference frame.

To obtain the sub-components' dynamic equations of the variables u_{CP}^{Σ}, u_{CN}^{Σ}, i, and i_{diff} in *dq* reference frame, we substitute **Eq. 13** and **Eq. 14** into **Eq. 3**, **Eq. 6**, **Eq. 7** to derive the expression (Exp1) of $\frac{du_{\mathrm{CP}}^{\Sigma}}{dt}$, $\frac{du_{\mathrm{CN}}^{\Sigma}}{dt}$, $\frac{di_{\mathrm{diff}}}{dt}$, and $\frac{di}{dt}$.

Remark 2. Due to space constraints, detailed substitution processes are omitted. The substitution process contains the product term like $m_P u_{\mathrm{CP}}^{\Sigma}$ and $m_N u_{\mathrm{CN}}^{\Sigma}$, which can be calculated by **Eq. 15**. The third-order harmonic component generated by the product term lets to more high-frequency components, but this paper does not focus on these, and the third-order harmonic component is out of consideration.

$$XY = a + a_d \cos\theta - a_q \sin\theta + a_{d2} \cos 2\theta + a_{q2} \sin 2\theta \tag{15}$$

where variables X and Y have the expressions in **Eq. 16**.

$$\begin{cases} X = X_0 + X_d \cos\theta - X_q \sin\theta + X_{d2} \cos 2\theta + X_{q2} \sin 2\theta \\ Y = Y_0 + Y_d \cos\theta - Y_q \sin\theta + Y_{d2} \cos 2\theta + Y_{q2} \sin 2\theta \end{cases} \tag{16}$$

And in **Eq. 15**, the coefficients a, a_0, a_d, a_q, a_{d2}, and a_{q2} are as follows.

$$\begin{cases} a_0 = X_0 Y_0 + \dfrac{X_d Y_d}{2} + \dfrac{X_{d2} Y_{d2}}{2} + \dfrac{X_q Y_q}{2} + \dfrac{X_{q2} Y_{q2}}{2} \\ a_d = X_0 Y_d + X_d Y_0 + \dfrac{X_d Y_{d2}}{2} + \dfrac{X_{d2} Y_d}{2} + \dfrac{X_q Y_{q2}}{2} + \dfrac{X_{q2} Y_q}{2} \\ a_q = X_0 Y_q + X_q Y_0 + \dfrac{X_d Y_{q2}}{2} - \dfrac{X_{d2} Y_q}{2} - \dfrac{X_q Y_{d2}}{2} + \dfrac{X_{q2} Y_d}{2} \\ a_{d2} = X_0 Y_{d2} + X_{d2} Y_0 + \dfrac{X_d Y_d}{2} - \dfrac{X_q Y_q}{2} \\ a_{q2} = X_0 Y_{q2} + X_{q2} Y_0 + \dfrac{X_d Y_q}{2} + \dfrac{X_q Y_d}{2} \end{cases} \tag{17}$$

Additionally, another expression (Exp2) of $\frac{du_{CP}^{\Sigma}}{dt}$, $\frac{du_{CN}^{\Sigma}}{dt}$, $\frac{di_{diff}}{dt}$, and $\frac{di}{dt}$ in dq reference frame can be obtained by taking the derivative of **Eq. 14**. Here, the derivation can be carried out according to **Eq. 18**, and the detailed processes of the derivation are omitted.

$$\begin{cases} \left(\dfrac{dX}{dt}\right)_0 = \dfrac{dX_0}{dt} \\ \left(\dfrac{dX}{dt}\right)_{dn} = \dfrac{dX_{dn}}{dt} - n\omega X_{qn}, n = 1, 2 \ldots \\ \left(\dfrac{dX}{dt}\right)_{qn} = \dfrac{dX_{qn}}{dt} + n\omega X_{dn}, n = 1, 2 \ldots \end{cases} \tag{18}$$

Finally, Exp1 and Exp2 are employed to build equations in which we let the corresponding terms equal to each other. And then we can get 10*th* order dynamic equations **Eq. 19** of the MMC electrical system in dq reference frame as follows.

$$\begin{cases} \dfrac{\mathrm{d}i_{\mathrm{diff}d2}}{\mathrm{d}t} = \dfrac{u_{\mathrm{CP}d2}^{\Sigma}}{2L_{\mathrm{arm}}} - \dfrac{M_d u_{\mathrm{CP}d}^{\Sigma}}{4L_{\mathrm{arm}}} + \dfrac{M_q u_{\mathrm{CP}q}^{\Sigma}}{4L_{\mathrm{arm}}} - \dfrac{M_{d2} u_{\mathrm{CP}0}^{\Sigma}}{2L_{\mathrm{arm}}} + 2\omega i_{\mathrm{diff}q2} - \dfrac{R_{\mathrm{arm}} i_{\mathrm{diff}d2}}{L_{\mathrm{arm}}} \\ \dfrac{\mathrm{d}i_{\mathrm{diff}q2}}{\mathrm{d}t} = \dfrac{u_{\mathrm{CP}q2}^{\Sigma}}{2L_{\mathrm{arm}}} - \dfrac{M_q u_{\mathrm{CP}d}^{\Sigma}}{4L_{\mathrm{arm}}} - \dfrac{M_d u_{\mathrm{CP}q}^{\Sigma}}{4L_{\mathrm{arm}}} - \dfrac{M_{q2} u_{\mathrm{CP}0}^{\Sigma}}{2L_{\mathrm{arm}}} - 2\omega i_{\mathrm{diff}d2} - \dfrac{R_{\mathrm{arm}} i_{\mathrm{diff}q2}}{L_{\mathrm{arm}}} \\ \dfrac{\mathrm{d}i_d}{\mathrm{d}t} = -\dfrac{M_d u_{\mathrm{CP}d2}^{\Sigma}}{2L_{\mathrm{arm}}} - \dfrac{M_q u_{\mathrm{CP}q2}^{\Sigma}}{2L_{\mathrm{arm}}} + \dfrac{2 - M_{d2}}{2L_{\mathrm{arm}}} u_{\mathrm{CP}d}^{\Sigma} - \dfrac{M_{q2} u_{\mathrm{CP}q}^{\Sigma}}{2L_{\mathrm{arm}}} - \dfrac{M_d u_{\mathrm{CP}0}^{\Sigma}}{L_{\mathrm{arm}}} - \dfrac{R_{\mathrm{arm}} i_d}{L_{\mathrm{arm}}} + \omega i_q + \dfrac{2u_{cvd}}{L_{\mathrm{arm}}} \\ \dfrac{\mathrm{d}i_q}{\mathrm{d}t} = \dfrac{M_q u_{\mathrm{CP}d2}^{\Sigma}}{2L_{\mathrm{arm}}} - \dfrac{M_d u_{\mathrm{CP}q2}^{\Sigma}}{2L_{\mathrm{arm}}} - \dfrac{M_{q2} u_{\mathrm{CP}d}^{\Sigma}}{2L_{\mathrm{arm}}} + \dfrac{M_{d2} + 2}{2L_{\mathrm{arm}}} u_{\mathrm{CP}q}^{\Sigma} - \dfrac{M_q u_{\mathrm{CP}0}^{\Sigma}}{L_{\mathrm{arm}}} - \dfrac{R_{\mathrm{arm}} i_q}{L_{\mathrm{arm}}} - \omega i_d + \dfrac{2u_{cvq}}{L_{\mathrm{arm}}} \\ \dfrac{\mathrm{d}i_{\mathrm{diff}0}}{\mathrm{d}t} = -\dfrac{M_{d2} u_{\mathrm{CP}d2}^{\Sigma}}{4L_{\mathrm{arm}}} - \dfrac{M_{q2} u_{\mathrm{CP}q2}^{\Sigma}}{4L_{\mathrm{arm}}} - \dfrac{M_d u_{\mathrm{CP}d}^{\Sigma}}{4L_{\mathrm{arm}}} - \dfrac{M_q u_{\mathrm{CP}q}^{\Sigma}}{4L_{\mathrm{arm}}} + \dfrac{u_{\mathrm{CP}0}^{\Sigma}}{2L_{\mathrm{arm}}} - \dfrac{R_{\mathrm{arm}} i_{\mathrm{diff}0}}{L_{\mathrm{arm}}} - \dfrac{1}{2L_{\mathrm{arm}}} u_{\mathrm{dc}} \\ \dfrac{\mathrm{d}u_{\mathrm{CP}d2}^{\Sigma}}{\mathrm{d}t} = 2\omega u_{\mathrm{CP}q2}^{\Sigma} - \dfrac{1}{2C_{\mathrm{arm}}} i_{\mathrm{diff}d2} + \dfrac{M_{d2}}{2C_{\mathrm{arm}}} i_{\mathrm{diff}0} + \dfrac{M_d}{8C_{\mathrm{arm}}} i_d - \dfrac{M_q}{8C_{\mathrm{arm}}} i_q \\ \dfrac{\mathrm{d}u_{\mathrm{CP}q2}^{\Sigma}}{\mathrm{d}t} = -2\omega u_{\mathrm{CP}d2}^{\Sigma} - \dfrac{1}{2C_{\mathrm{arm}}} i_{\mathrm{diff}q2} + \dfrac{M_{q2}}{2C_{\mathrm{arm}}} i_{\mathrm{diff}0} + \dfrac{M_q}{8C_{\mathrm{arm}}} i_d + \dfrac{M_d}{8C_{\mathrm{arm}}} i_q \\ \dfrac{\mathrm{d}u_{\mathrm{CP}d}^{\Sigma}}{\mathrm{d}t} = \omega u_{\mathrm{CP}q}^{\Sigma} + \dfrac{M_d}{4C_{\mathrm{arm}}} i_{\mathrm{diff}d2} + \dfrac{M_q}{4C_{\mathrm{arm}}} i_{\mathrm{diff}q2} + \dfrac{M_d}{2C_{\mathrm{arm}}} i_{\mathrm{diff}0} + \dfrac{M_{d2} - 2}{8C_{\mathrm{arm}}} i_d + \dfrac{M_{q2}}{8C_{\mathrm{arm}}} i_q \\ \dfrac{\mathrm{d}u_{\mathrm{CP}q}^{\Sigma}}{\mathrm{d}t} = -\omega u_{\mathrm{CP}d}^{\Sigma} - \dfrac{M_q}{4C_{\mathrm{arm}}} i_{\mathrm{diff}d2} + \dfrac{M_d}{4C_{\mathrm{arm}}} i_{\mathrm{diff}q2} + \dfrac{M_q}{2C_{\mathrm{arm}}} i_{\mathrm{diff}0} + \dfrac{M_{q2}}{8C_{\mathrm{arm}}} i_d - \dfrac{M_{d2} + 2}{8C_{\mathrm{arm}}} i_q \\ \dfrac{\mathrm{d}u_{\mathrm{CP}0}^{\Sigma}}{\mathrm{d}t} = \dfrac{M_{d2}}{4C_{\mathrm{arm}}} i_{\mathrm{diff}d2} + \dfrac{M_{q2}}{4C_{\mathrm{arm}}} i_{\mathrm{diff}q2} - \dfrac{1}{2C_{\mathrm{arm}}} i_{\mathrm{diff}0} + \dfrac{M_d}{8C_{\mathrm{arm}}} i_d + \dfrac{M_q}{8C_{\mathrm{arm}}} i_q \end{cases} \tag{19}$$

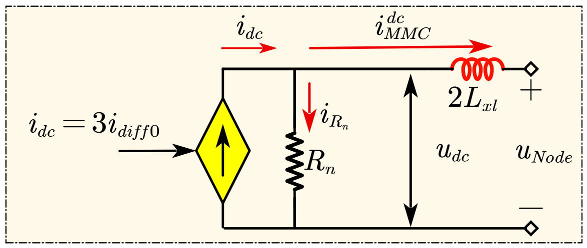

FIGURE 2 | DC interface of MMC.

The model of MMC electrical system is sorted out into the state equation and the output equation as follows.

$$\begin{cases} \dot{x}_{MMC}^{ele} = f\left(x_{MMC}^{ele}, u_{MMC}^{ele}\right) = f\left(x_{MMC}^{ele}, u_{MMC}^{ele1}, u_{MMC}^{ele2}\right) \\ y_{MMC}^{ele} = f'\left(x_{MMC}^{ele}, u_{MMC}^{ele}\right) = f'\left(x_{MMC}^{ele}, u_{MMC}^{ele1}, u_{MMC}^{ele2}\right) \end{cases}$$
$$= \left[i_{\mathrm{diff}0}, i_{\mathrm{diff}d2}, i_{\mathrm{diff}q2}, i_d, i_q\right]^T \tag{20}$$

where state variables $x_{MMC}^{ele} = [u_{\mathrm{CP}d2}^{\Sigma}, u_{\mathrm{CP}q2}^{\Sigma}, u_{\mathrm{CP}d}^{\Sigma}, u_{\mathrm{CP}q}^{\Sigma}, u_{\mathrm{CP}0}^{\Sigma}, i_{\mathrm{diff}0}, i_{\mathrm{diff}d2}, i_{\mathrm{diff}q2}, i_d, i_q]^T$; input variables $u_{MMC}^{ele} = [u_{MMC}^{ele1}, u_{MMC}^{ele2}]^T$ (here, $u_{MMC}^{ele1} = [M_d, M_q, M_{d2}, M_{q2}]^T$, $u_{MMC}^{ele2} = [u_{cvd}, u_{cvq}]^T$); output variables $y_{MMC}^{ele} = [y_{MMC}^{ele1}, y_{MMC}^{ele2}, y_{MMC}^{ele3}]^T$ (here, $y_{MMC}^{ele1} = i_{\mathrm{diff}0}$, $y_{MMC}^{ele2} = [i_{\mathrm{diff}d2}, i_{\mathrm{diff}q2}]^T$, and $y_{MMC}^{ele3} = [i_d, i_q]^T$) .

Remark 3. In this paper, the state variables, the system's inputs, and the system's outputs in the state equations and output equations are represented by x, u, and y, respectively. And different subsystems are represented by the different subscripts and superscripts. The subscripts AC and MMC represent the AC system connected to the MMC and the MMC system except for the AC system, respectively; the superscripts *ele*, int, *fil*, and *ctrl* indicate the MMC internal electrical system, DC interface, signal filter, and controller, respectively. Besides, the input u and the output y are divided into several subvectors with the superscript notation to facilitate the modular splicing of each subsystem, respectively.

2.2 Modeling the State Space Model for DC Interface

The DC interface of MMC is modeled to connect the MMC electrical system with the DC network conveniently. The DC interface of MMC is modeled as a controlled current source, whose output is i_{dc} ($i_{dc} = 3i_{\mathrm{diff}0}$). The MMC's DC side input is the DC voltage connected to the DC network nodes. For decoupling, a virtual resistor R_n is introduced. As long as R_n is selected large enough, the DC network and the MMC electrical system can be decoupled without affecting the modeling accuracy of the system (Pogaku et al., 2007). Besides, when a failure occurs to the DC side, the DC interface of MMC is usually connected with the current limiting reactance in series to prevent a large fault current impact. Finally, the equivalent circuit of the DC interface is shown in **Figure 2**.

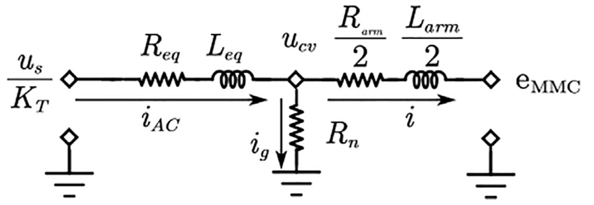

FIGURE 3 | Equivalent circuit of AC system.

According to the equivalent circuit in **Figure 2**, its dynamic equation is expressed as **Eq. 21**.

$$\begin{cases} \dfrac{di_{MMC}^{dc}}{dt} = \dfrac{u_{dc}}{2L_{xl}} - \dfrac{u_{node}}{2L_{xl}} = \dfrac{-R_n i_{MMC}^{dc}}{2L_{xl}} + \dfrac{3R_n i_{\text{diff0}}}{2L_{xl}} - \dfrac{u_{node}}{2L_{xl}} \\ u_{dc} = R_n\left(i_{dc} - i_{MMC}^{dc}\right) = -R_n i_{MMC}^{dc} + 3R_n i_{\text{diff0}} \end{cases} \tag{21}$$

where i_{MMC}^{dc} is the current of L_{xl}; u_{node} is the voltage of the DC node connected to the MMC.

The model of the DC interface is sorted out into the dynamic equation and the output equation, which are expressed as follows:

$$\begin{cases} \dot{x}_{MMC}^{int} = f\,(x_{MMC}^{int}, u_{MMC}^{int}) = f\,(x_{MMC}^{int}, u_{MMC}^{int1}, u_{MMC}^{int2}) \\ y_{MMC}^{int} = f'\,(x_{MMC}^{int}, u_{MMC}^{int1}) = \left[i_{MMC}^{dc}, u_{dc}\right]^T \end{cases} \tag{22}$$

where state variables $x_{MMC}^{int} = i_{MMC}^{dc}$; input variables $u_{MMC}^{int} = [u_{MMC}^{int1}, u_{MMC}^{int2}]^T = [i_{\text{diff0}}, u_{node}]^T$; onput variables $y_{MMC}^{int} = [y_{MMC}^{int1}, y_{MMC}^{int2}]^T$.

2.3 Modeling the AC System

As to the modeling of AC system, a virtual resistor is also used to decouple the AC system from the MMC electrical system. The AC system in **Figure 1** is reduced to the one shown in **Figure 3**. In **Figure 3**, $L_{eq} = \frac{L_s+L_{T1}}{K_T^2} + L_{T2}$ and $R_{eq} = \frac{R_s+R_{T1}}{K_T^2} + R_{T2}$ (here, R_{T1} and R_{T2} are the equivalent resistances of the primary and secondary windings of the transformer, respectively; L_{T1} and L_{T2} are the equivalent inductances of the primary and secondary windings of the transformer, respectively; L_{eq} is equivalent inductance of AC system and R_{eq} is equivalent resistance of AC system). According to the equivalent circuit in **Figure 3**, the state equation and the output equation of the AC system in *dq* reference frame are expressed as **Eq. 23**.

$$\begin{cases} L_{eq}\dfrac{di_{dAC}}{dt} = -\left(R_{eq} + R_n\right)i_{dAC} + L_{eq}wi_{qAC} + R_n i_d + \dfrac{u_{sd}}{K_T} \\ L_{eq}\dfrac{di_{qAC}}{dt} = -\left(R_{eq} + R_n\right)i_{qAC} - L_{eq}wi_{dAC} + R_n i_q + \dfrac{u_{sq}}{K_T} \\ u_{cvd} = R_n * (i_{dAC} - i_d) \\ u_{cvq} = R_n * \left(i_{qAC} - i_q\right) \end{cases} \tag{23}$$

where i_{dAC} and i_{qAC} are d-axis current and q-axis current of AC system in *dq* reference frame, respectively; u_{sd} is equal to the phase voltage amplitude of the AC grid and $u_{sq} = 0$ if the grid voltage directional control is adopted.

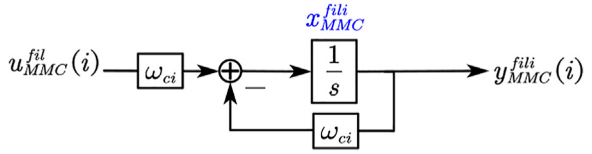

FIGURE 4 | Principle diagram of filter.

The model of AC system is sorted out as **Eq. 24**.

$$\begin{cases} \dot{x}_{AC} = f\,(x_{AC}, u_{AC}^1, u_{AC}^2) \\ y_{AC} = f'\,(x_{AC}, u_{AC}^1) = \left[u_{cvd}, u_{cvq}\right]^T \end{cases} \tag{24}$$

where state variables $x_{AC} = [i_{dAC}, i_{qAC}]^T$ and input variables $u_{AC} = [u_{AC}^1, u_{AC}^2]^T$ (here, $u_{AC}^1 = [i_d, i_q]^T$, $u_{AC}^2 = [u_{sd}, u_{sq}]^T$).

2.4 Modeling of The Signal Filter

The input signals of the MMC controller are the measurement signals of MMC's parameters. There is noise and interference in the actual measurement, and signals need to be filtered and then sent to the controller. Therefore, the modeling and analysis of the signal filter are required. In this paper, the first-order low-pass filter as shown in **Figure 4** is used, and the dynamic equations of the filters are expressed as **Eq. 25**.

$$\begin{cases} \dfrac{\mathrm{d}x_{MMC}^{fil}}{\mathrm{d}t} = -\omega_c x_{MMC}^{fil} + \omega_c u_{MMC}^{fil} \\ y_{MMC}^{fil} = x_{MMC}^{fil} \end{cases} \tag{25}$$

where cut-off frequency $\omega_c = \text{diag}[w_{c1}, \omega_{c2}, \omega_{c3}, \omega_{c4}, \omega_{c5}, \omega_{c6}, \omega_{c7}]$.

The model of filters is sorted out as **Eq. 26**.

$$\begin{cases} \dot{x}_{MMC}^{fil} = f\left(x_{MMC}^{fil}, u_{MMC}^{fil}\right) = f\left(x_{MMC}^{fil}, u_{MMC}^{fil1}, u_{MMC}^{fil2}, u_{MMC}^{fil3}\right) \\ y_{MMC}^{fil} = f'\left(x_{MMC}^{fil}\right) = \left[u_{dc}^{fil}, i_{\text{diff}d2}^{fil}, i_{\text{diff}q2}^{fil}, i_d^{fil}, i_q^{fil}, u_{cd}^{fil}, u_{cq}^{fil}\right]^T \end{cases} \tag{26}$$

where state variables $x_{MMC}^{fil} = [x_{u_{dc}}, x_{\text{diff}d2}, x_{\text{diff}q2}, x_d, x_q, x_{cd}, x_{cq}]^T$; input variables $u_{MMC}^{fil} = [u_{MMC}^{fil1}\ u_{MMC}^{fil2}\ u_{MMC}^{fil3}\ ]^T$ (here, $u_{MMC}^{fil1} = u_{dc}$, $u_{MMC}^{fil2} = [i_{\text{diff}d2}, i_{\text{diff}q2}, i_d, i_q]^T$, and $u_{MMC}^{fil3} = [u_{cvd}, u_{cvq}]^T$); $u_{dc}^{fil}, i_{\text{diff}d2}^{fil}, i_{\text{diff}q2}^{fil}, i_d^{fil}, i_q^{fil}, u_{cd}^{fil}$, and u_{cq}^{fil} are the output signals after filtering the input signals.

2.5 Modeling of the Controller

The controller plays a decisive role in the dynamic behavior of MMC. The double closed-loop vector control strategy based on *dq* reference frame, which is a standardized control mode of MMC, can realize the decoupling of active and reactive power. Therefore, in this paper, the controller is modeled in the *dq* reference frame. Since MMC usually contains multiple control modes which need to be switched with the changes of the operation state of AC/DC

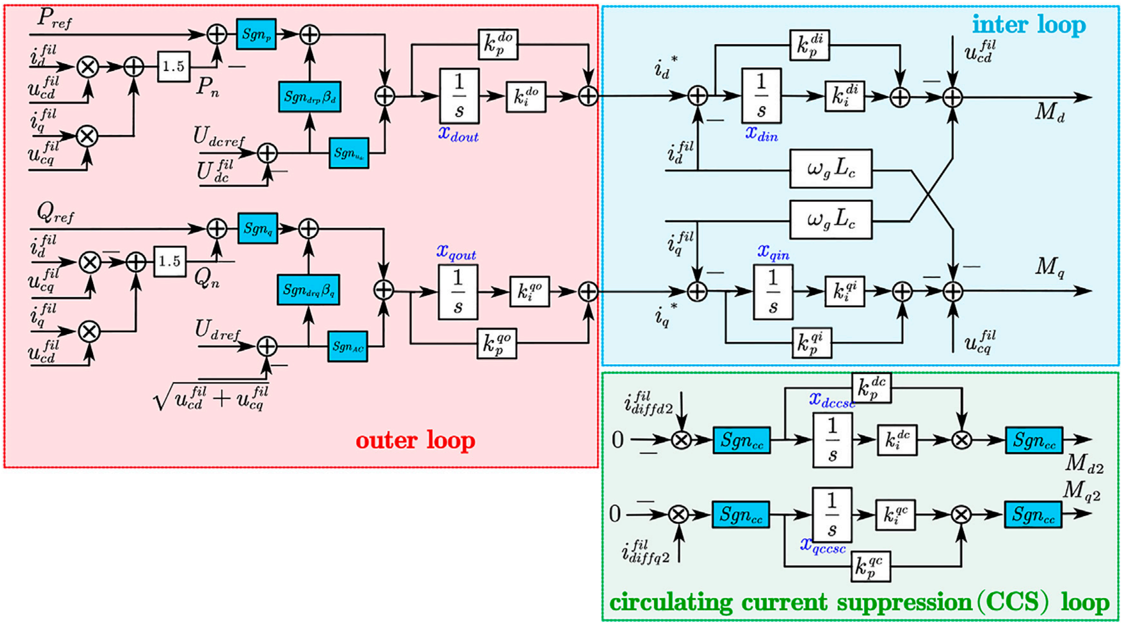

FIGURE 5 | Diagram of controller.

TABLE 2 | Configuration of control modes.

Control mode	d axis control mode			q axis control mode			with CCS	no CCS
	Sgn_p	Sgn_{drp}	$Sgn_{u_{dc}}$	Sgn_q	Sgn_{drq}	Sgn_{ac}	Sgn_{cc}	Sgn_{cc}
Constant DC and constant AC voltage	0	0	1	0	0	1	0	1
Constant DC voltage and constant reactive power	0	0	1	1	0	0		
Constant DC voltage and reactive droop	0	0	1	0	1	0		
Constant active power and constant AC voltage	1	0	0	0	0	1		
Constant active power and constant reactive	1	0	0	1	0	0		
Constant active and reactive power droop	1	0	0	0	1	0		
Active droop and constant AC voltage	0	1	0	0	0	1		
Active droop and constant reactive power	0	1	0	1	0	0		
Active droop and reactive droop	0	1	0	0	1	0		

power grids, this paper uses the unified modeling method for MMC's controller to simplify the modeling and realize the normalization of the controller model. Thus, remodeling the MMC systems is avoided when the MMC's control modes need to be changed, increasing the flexibility of modeling the AC/DC power grids. Different control modes can be selected in the unified model by configuring control mode variables, avoiding the inconvenience of modeling the MMC separately for different control modes. **Figure 5** is the diagram of the controller using unified modeling, and **Table 2** shows the configuration of the control mode variables for different MMC control modes.

In **Figure 5**, U_{dcref}, U_{dref}, P_{ref}, and Q_{ref} are the references of DC voltage, AC voltage, active power, and reactive power, respectively. x_{din}, x_{dout}, x_{qin}, x_{qout}, x_{dcsc}, and x_{qcsc} are the states of the integrators. k_p^{do} (k_p^{qo}), k_p^{di} (k_p^{qi}), and k_p^{dc} (k_p^{qc}) represent the proportional coefficient of the outer loop, the inner loop and the circulating current suppression (CCS) loop in d-axis (q-axis), respectively; k_i^{do} (k_i^{qo}), k_i^{di} (k_i^{qi}), and k_i^{dc} (k_i^{qc}) represent the integral coefficient of the outer loop, the inner loop and the CCS loop in d-axis (q-axis), respectively. Sgn_p, Sgn_{drp} ,$Sgn_{u_{dc}}$, Sgn_q, Sgn_{drq}, Sgn_{ac}, and Sgn_{cc} are the boolean variables used to select the control modes of MMC.

According to the diagram of the unified controller, its state equation and output equation are expressed as **Eq. 27**.

$$
\begin{cases}
\frac{\mathrm{d}x_{din}}{\mathrm{d}t} = i_d^* - i_d^{fil} = i_{d^*} = k_i^{do} x_{dout} + k_p^{do} \frac{dx_{dout}}{dt} - i_d^{fil} \\
\quad = k_i^{do} x_{dout} + k_p^{do} \begin{pmatrix} Sgn_{U_{dc}}\left(U_{\mathrm{dc}ref} - u_{dc}^{fil}\right) \\ +Sgn_{drp}\beta_d\left(U_{\mathrm{dc}ref} - u_{dc}^{fil}\right) \\ +Sgn_P\left(P_{ref} - 1.5\left(u_{cd}^{fil} i_d^{fil} + u_{cq}^{fil} i_q^{fil}\right)\right) \end{pmatrix} - i_d^{fil} \\
\frac{\mathrm{d}x_{qin}}{\mathrm{d}t} = i_q^* - i_q^{fil} = k_i^{qo} x_{qout} + k_p^{qo} \frac{dx_{qout}}{dt} - i_q^{fil} \\
\quad = k_i^{qo} x_{qout} + k_p^{qo} \begin{pmatrix} Sgn_{U_{AC}}\left(U_{\mathrm{d}ref} - u_d^{fil}\right) \\ +Sgn_{drq}\beta_q\left(U_{\mathrm{d}ref} - u_d^{fil}\right) \\ +Sgn_q\left(Q_{ref} - 1.5\left(u_{cd}^{fil} i_q^{fil} - u_{cq}^{fil} i_d^{fil}\right)\right) \end{pmatrix} - i_q^{fil} \\
\frac{\mathrm{d}x_{dout}}{\mathrm{d}t} = Sgn_{u_{dc}}\left(U_{\mathrm{dc}ref} - \sqrt{u_{cd}^{fil} + u_{cq}^{fil}}\right) \\
\quad +Sgn_{drp}\beta_d\left(U_{\mathrm{dc}ref} - \sqrt{u_{cd}^{fil} + u_{cq}^{fil}}\right) \\
\quad +Sgn_P\left(P_{ref} - 1.5\left(u_{cd}^{fil} i_d^{fil} + u_{cq}^{fil} i_q^{fil}\right)\right) \\
\frac{\mathrm{d}x_{qout}}{\mathrm{d}t} = Sgn_{u_{AC}}\left(U_{\mathrm{d}ref} - \sqrt{u_{cd}^{fil} + u_{cq}^{fil}}\right) \\
\quad +Sgn_{drq}\beta_q\left(U_{\mathrm{d}ref} - \sqrt{u_{cd}^{fil} + u_{cq}^{fil}}\right) \\
\quad +Sgn_Q\left(Q_{ref} - 1.5\left(u_{cd}^{fil} i_q^{fil} - u_{cq}^{fil} i_d^{fil}\right)\right) \\
\frac{dx_{dccsc}}{dt} = Sgn_{cc}\left(0 - i_{\mathrm{diff}d2}^{fil}\right) \\
\frac{\mathrm{d}x_{qccsc}}{\mathrm{d}t} = Sgn_{cc}\left(0 - i_{\mathrm{diff}q2}^{fil}\right) \\
M_d = -\left(k_i^{di} x_{din} + k_p^{di} \frac{dx_{din}}{dt}\right) + \omega L_{arm} i_q^{fil} + u_{cd}^{fil} \\
M_q = -\left(k_i^{qi} x_{qin} + k_p^{qi} \frac{dx_{qin}}{dt}\right) - \omega L_{arm} i_d^{fil} + u_{cq}^{fil} \\
M_{d2} = Sgn_{cc}\left(k_i^{dc} x_{dccsc} + k_p^{dc} \frac{dx_{dccsc}}{dt}\right) \\
M_{q2} = Sgn_{cc}\left(k_i^{qc} x_{qccsc} + k_p^{qc} \frac{dx_{dccsc}}{dt}\right)
\end{cases}
\tag{27}
$$

The model of the unified controller is sorted out as **Eq. 28**.

$$
\begin{cases}
\dot{x}_{MMC}^{ctrl} = f\left(x_{MMC}^{ctrl}, u_{MMC}^{ctrl}\right) = f\left(x_{MMC}^{ctrl}, u_{MMC}^{ctrl1}, u_{MMC}^{ctrl2}\right) \\
y_{MMC}^{ctrl} = f'\left(x_{MMC}^{ctrl}, u_{MMC}^{ctrl}\right) = f'\left(x_{MMC}^{ctrl}, u_{MMC}^{ctrl1}, u_{MMC}^{ctrl2}\right) = \left[M_d, M_q, M_{d2}, M_{q2}\right]^T
\end{cases}
\tag{28}
$$

where $x_{MMC}^{ctrl} = [x_{din}, x_{dout}, x_{qin}, x_{qout}, x_{d\,\mathrm{csc}}, x_{q\,\mathrm{csc}}]^T$ and $u_{MMC}^{ctrl} = [u_{MMC}^{ctrl1}, u_{MMC}^{ctrl2}]^T$ (here, $u_{MMC}^{ctrl1} = [u_{dc}^{fil}, i_{\mathrm{diff}d2}^{fil}, i_{\mathrm{diff}q2}^{fil}, i_d^{fil}, i_q^{fil}, u_{cd}^{fil}, u_{cq}^{fil}]^T$, $u_{MMC}^{ctrl2} = [U_{dcref}, U_{dref}, P_{ref}, Q_{ref}]^T$).

3 MODELING THE OVERALL MODULAR MULTILEVEL CONVERTER SYSTEM

According to **Eq. 20**, **Eq. 22**, **Eq. 24**, **Eq. 26**, **Eq. 28**, we can establish the relationships of the input and output among subsystems as follows: $u_{MMC}^{ele1} = y_{MMC}^{ctrl}$, $u_{MMC}^{ele2} = y_{AC}$; $u_{MMC}^{int1} = y_{MMC}^{ele1}$, $u_{MMC}^{int2} = u_{node}$; $u_{MMC}^{fil1} = y_{MMC}^{int1}$, $u_{MMC}^{fil2} = [y_{MMC}^{ele2}, y_{MMC}^{ele2}]^T$, $u_{MMC}^{fil3} = y^{AC}$; $u_{AC}^1 = y_{MMC}^{ele3}$, $u_{AC}^2 = [u_{sd}, u_{sq}]^T$; $u_{MMC}^{ctrl1} = y_{MMC}^{fil}$, $u_{MMC}^{ctrl2} = [U_{dcref}, U_{dref}, P_{ref}, Q_{ref}]^T$; $y_{MMC}^{int2} = i_{MMC}^{dc}$. Therefore, the dynamic model of the overall system is derived by connecting each subsystem according to the connection relationship of input and output. The dynamic model of the overall MMC system with the MDM is shown in **Figure 6**.

The MDM makes modeling MMC systems more expansible to adapt to different hybrid AC/DC power grids. For example, if one of the subsystems of the MMC systems needs to be changed, we only need to remodel the subsystem rather than the entire MMC system. Besides, due to decoupling and modularizing the MMC systems, the small-signal model of the overall MMC system could be developed directly through linearizing and splicing proposed model, which enables our model to analyze the small-signal stability of large-scale hybrid AC/DC power grids.

4 SIMULATION RESULTS

For purposes of validation, a simulation system is shown in **Figure 7**. The system consists of an AC system, an MMC, and a resistive load. To verify the accuracy and superiority of the established model, we compared the proposed model with D-EMT and AVE-EMT models by the simulation test system. **Table 3** and **Table 4** list the system parameters and control parameters, respectively.

Here, we set the control modes of MMC as constant DC voltage and constant reactive power, and the dynamic response under load mutation and control instruction step are compared under closed-loop control. The working condition is set as follows: at 2 s, a load with a resistance of 100 Ω is suddenly put into; at 3 s, the resistance increases from 100 Ω to 200 Ω; at 4 s, the DC voltage steps from 1 pu to 1.05 pu; at 5 s, the DC voltage steps from 1.05 pu to 1 pu.

The per-unit (pu) wapveforms of u_{dc}, i_{dc}, i_d, i_q, u_{cvd}, and u_{cvq} are shown in **Figures 8–13**. By testing the above working conditions, it can be seen from these figures that the accomplished state-space model of overall MMC system is highly consistent with the detailed electromagnetic transient model and the average electromagnetic transient model. The accuracy and validity of the proposed modeling method are verified.

In addition, **Table 5** shows the comparison results of the actual simulation time of the three models. It is at least 59.8 times more efficient than the D-EMT and 4.6 times more efficient than the AVE-EMT for the same simulation conditions. Therefore, the proposed model greatly accelerates the simulation speed while obtaining high precision.

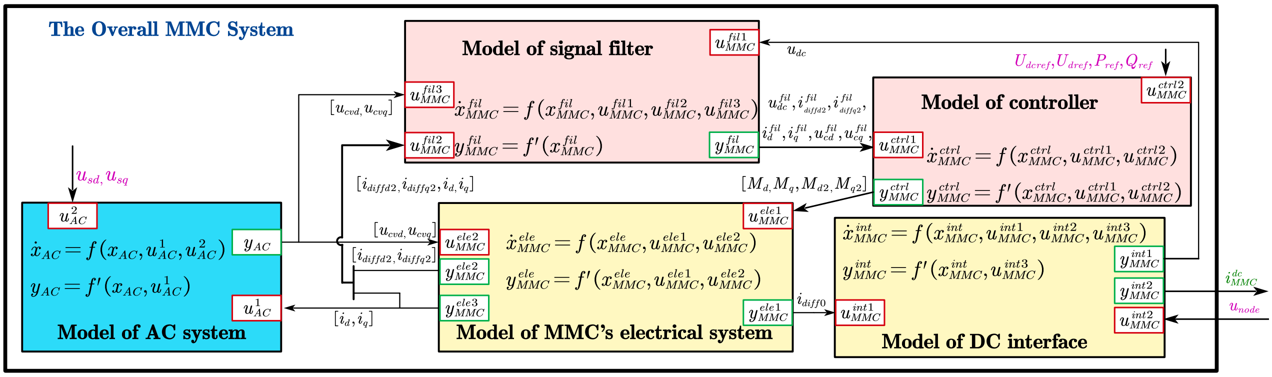

FIGURE 6 | Model of the overall MMC system with the MDM.

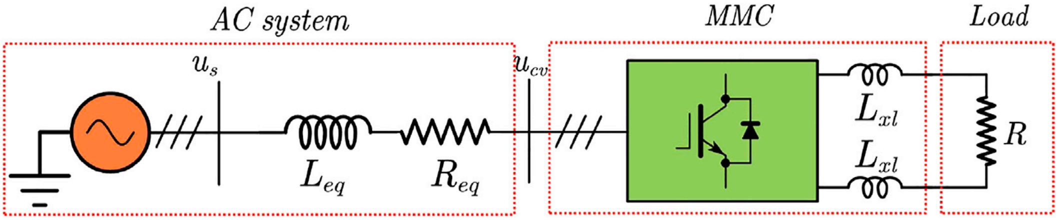

FIGURE 7 | Simulation test system of the overall MMC system.

TABLE 3 | Parameters of the MMC systems.

Symbol	u_s (kV)	K_T	f (Hz)	L_{eq} (mH)	$R_{eq}\Omega$	C_{arm} (mH)	L_{arm} (mH)	R_{arm} (Ω)	N	L_{xl} (mH)
Value	35	3.5	50	5.2	0.021 6	0.52	10	0.03	20	5

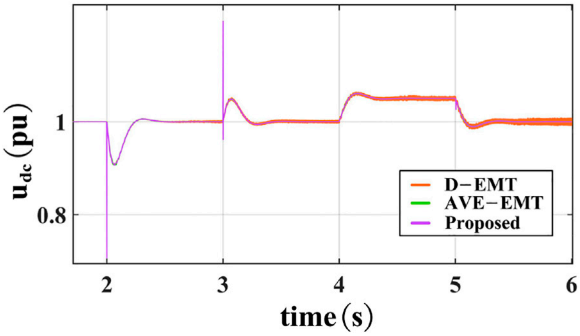

FIGURE 8 | Per-unit waveform of u_{dc}.

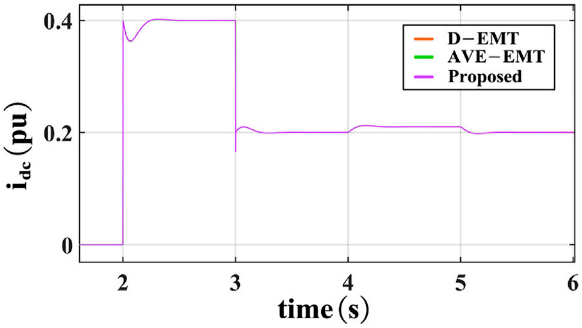

FIGURE 9 | Per-unit waveform of i_{dc}.

TABLE 4 | The control parameters.

Symbol	Value	Symbol	Value
k_p^{do}, k_p^{qo}	1.95	k_i^{do}, k_i^{qo}	119
k_p^{di}, k_p^{qi}	10	k_i^{di}, k_i^{qi}	1000
k_p^{dc}, k_p^{qc}	3.9	k_i^{dc}, k_i^{qc}	23.8

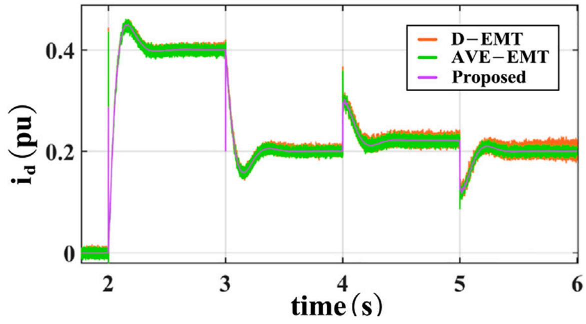

FIGURE 10 | Per-unit waveform of i_d.

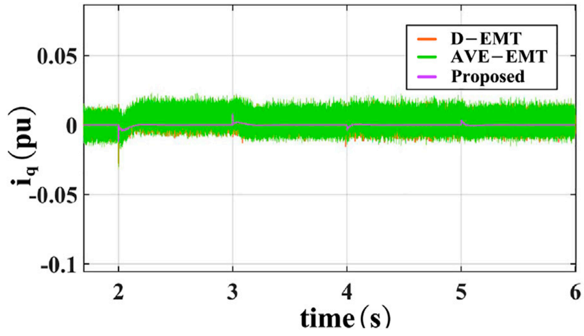

FIGURE 11 | Per-unit waveform of i_q.

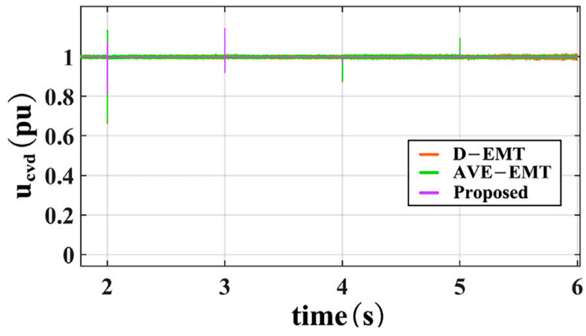

FIGURE 12 | Per-unit waveform of u_{cvd}.

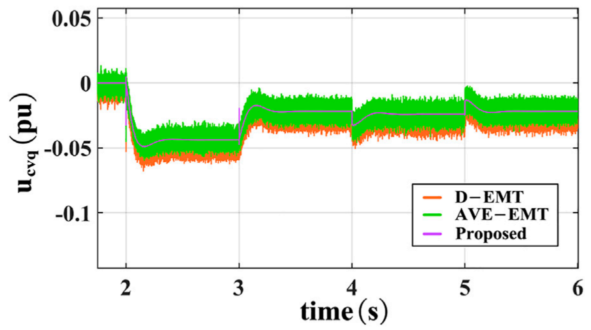

FIGURE 13 | Per-unit waveform of u_{cvq}.

TABLE 5 | Comparison results of the actual simulation time.

Model	Simulation interval/s	Actual time/s
D-EMT	[0 6]	1025.44
AVE-EMT	[0 6]	78.86
Proposed	[0 6]	17.14

5 CONCLUSION

A unified modeling scheme (UMS) for MMC systems in a synchronous (*dq*) reference frame is proposed in this paper. A simulation test system verifies our model in MATLAB/Simulink.

(1) The modular decouple modeling (MDM) and the unified controller modeling make modeling MMC systems more flexible and expansible to adapt to different hybrid AC/DC power grids.
(2) The proposed model shows an accurate replication to the dynamic performance of the EMTs (D-EMT and AVE-EMT) model.
(3) The proposed model greatly reduces the simulation time. For the same simulation conditions, it is at least 59.8 times more efficient than the D-EMT and 4.6 times more efficient than the AVE-EMT. Therefore, our model is suitable for simulating the large-scale hybrid AC/DC power grids.
(4) The small-signal model of the overall MMC system could be developed directly by linearizing and then splicing proposed model. Therefore, the proposed model is suitable for studying the stability of small-signal.

DATA AVAILABILITY STATEMENT

The original contributions presented in the study are included in the article/Supplementary Material, further inquiries can be directed to the corresponding author.

AUTHOR CONTRIBUTIONS

XX: Writing—original draft and Writing—review. ZW and QH: Conceptualization. XQ, XD, and XC: Formal analysis and revision.

REFERENCES

Antonopoulos, A., Angquist, L., and Nee, H.-P. (2009). "On Dynamics and Voltage Control of the Modular Multilevel Converter," in 2009 13th European Conference on Power Electronics and Applications, Barcelona, Spain, September 08-10, 2009, 1–10.

Deore, S. R., Darji, P. B., and Kulkarni, A. M. (2012). "Dynamic Phasor Modeling of Modular Multi-Level Converters," in 2012 IEEE 7th International Conference on Industrial and Information Systems (ICIIS), Chennai, India, August 06-09, 2012, 1–6. doi:10.1109/ICIInfS.2012.6304792

Gnanarathna, U. N., Gole, A. M., and Jayasinghe, R. P. (2011). Efficient Modeling of Modular Multilevel Hvdc Converters (Mmc) on Electromagnetic Transient Simulation Programs. *IEEE Trans. Power Deliv.* 26, 316–324. doi:10.1109/tpwrd.2010.2060737

Harnefors, L., Antonopoulos, A., Norrga, S., Angquist, L., and Nee, H.-P. (2013). Dynamic Analysis of Modular Multilevel Converters. *IEEE Trans. Ind. Electron.* 60, 2526–2537. doi:10.1109/TIE.2012.2194974

Ilves, K., Antonopoulos, A., Norrga, S., and Nee, H.-P. (2012). Steady-state Analysis of Interaction between Harmonic Components of Arm and Line Quantities of Modular Multilevel Converters. *IEEE Trans. Power Electron.* 27, Structure of an MMC. 57–68. doi:10.1109/TPEL.2011.2159809

Jamshidifar, A., and Jovcic, D. (2016). Small-Signal Dynamic DQ Model of Modular Multilevel Converter for System Studies. *IEEE Trans. Power Deliv.* 31, 191–199. doi:10.1109/TPWRD.2015.2478489

Jovcic, D., and Jamshidifar, A. (2015). "Phasor Model of Modular Multilevel Converter with Circulating Current Suppression Control," in 2015 IEEE Power Energy Society General Meeting, Denver, CO, USA, July 26-30, 2015, 1. doi:10.1109/PESGM.2015.7286104

Li, Y., Tang, G., Ge, J., He, Z., Pang, H., Yang, J., et al. (2018). Modeling and Damping Control of Modular Multilevel Converter Based Dc Grid. *IEEE Trans. Power Syst.* 33, 723–735. doi:10.1109/TPWRS.2017.2691737

Liu, S., Xu, Z., Hua, W., Tang, G., and Xue, Y. (2014). Electromechanical transient modeling of modular multilevel converter based multi-terminal hvdc systems. *IEEE Trans. Power Syst.* 29, 72–83. doi:10.1109/TPWRS.2013.2278402

Munch, P., Liu, S., and Dommaschk, M. (2009). "Modeling and Current Control of Modular Multilevel Converters Considering Actuator and Sensor Delays," in 2009 35th Annual Conference of IEEE Industrial Electronics, Porto, Portugal, November 03-05, 2009, 1633–1638. doi:10.1109/IECON.2009.5414756

Peralta, J., Saad, H., Dennetiere, S., Mahseredjian, J., and Nguefeu, S. (2012). Detailed and Averaged Models for a 401-level Mmc-Hvdc System. *IEEE Trans. Power Deliv.* 27, 1501–1508. doi:10.1109/TPWRD.2012.2188911

Pogaku, N., Prodanovic, M., and Green, T. C. (2007). Modeling, Analysis and Testing of Autonomous Operation of an Inverter-Based Microgrid. *IEEE Trans. Power Electron.* 22, 613–625. doi:10.1109/TPEL.2006.890003

Saad, H., Guillaud, X., Mahseredjian, J., Dennetiere, S., and Nguefeu, S. (2015). Mmc Capacitor Voltage Decoupling and Balancing Controls. *IEEE Trans. Power Deliv.* 30, 704–712. doi:10.1109/TPWRD.2014.2338861

Sanders, S. R., Noworolski, J. M., Liu, X. Z., and Verghese, G. C. (1990). Generalized Averaging Method for Power Conversion Circuits. 21st Annual IEEE Conference on Power Electronics Specialists, San Antonio, TX, USA, June 11-14, 1990, 333–340. doi:10.1109/PESC.1990.131207

Sun, P., Jiao, Z., and Gu, H. (2021). Calculation of short-circuit current in dc distribution system based on mmc linearization. *Front. Energy Res.* 9, 26. doi:10.3389/fenrg.2021.634232

Trinh, N.-T., Zeller, M., Wuerflinger, K., and Erlich, I. (2016). Generic Model of Mmc-Vsc-Hvdc for Interaction Study with Ac Power System. *IEEE Trans. Power Syst.* 31, 27–34. doi:10.1109/TPWRS.2015.2390416

Vatani, M., Hovd, M., and Saeedifard, M. (2015). Control of the Modular Multilevel Converter Based on a Discrete-Time Bilinear Model Using the Sum of Squares Decomposition Method. *IEEE Trans. Power Deliv.* 30, 2179–2188. doi:10.1109/TPWRD.2015.2412151

Wang, W., Wang, L., Zhu, B., Li, G., Xin, Y., and Jiang, S. (2021). Power decoupling control of mmc and small-signal stability analysis of ac/dc distribution network with renewable energy. *Front. Energy Res.* 9, 170. doi:10.3389/fenrg.2021.660236

Xianyong, Z., Zijuan, G., Yaohong, H., Li, L., Weikuan, P., and Jian, C. (2021). Power decoupling control of mmc and small-signal stability analysis of ac/dc distribution network with renewable energy. *Front. Energy Res.* 9, 465. doi:10.3389/fenrg.2021.734797

Zhao, J., and Tao, Y. (2021). Control characteristic analysis and coordinated strategy design for hybrid hvdc with multi-infeed mmc inverters. *Front. Energy Res.* 9, 558. doi:10.3389/fenrg.2021.737294

Zhu, B., Li, H., Xu, P., Jiao, S., Zhang, L., and Xin, Y. (2021). Coordinated control strategy of dc fault ride-through for the wf connected to the grid through the mmc-hvdc. *Front. Energy Res.* 9, 579. doi:10.3389/fenrg.2021.743465

FUNDING

This work is supported in part by National Natural Science Foundation of China under Grant 51867016, in part by National Key R&D program of China under Grant 2018YFB0904700.

Conflict of Interest: The authors declare that the research was conducted in the absence of any commercial or financial relationships that could be construed as a potential conflict of interest.

frontiers | Frontiers in Energy Research

ORIGINAL RESEARCH
published: 27 April 2022
doi: 10.3389/fenrg.2022.895163

Time Delay of Wide Area Damping Control in Urban Power Grid: Model-Based Analysis and Data-Driven Compensation

Buxin She, Yuqing Dong and Yilu Liu*

Department of Electrical Engineering and Computer Science, The University of Tennessee, Knoxville, TN, United States

Due to the rapid development of economies, large urban cities consume an increasing amount of energy and have a higher requirement for power quality. Voltage source converter based high voltage direct current (VSC-HVDC) is a promising device to transmit clean power from remote regions to urban power systems, while also providing wide area damping control (WADC) for frequency stabilization. However, the time-delay naturally existing in the VSC-HVDC system may degrade the performance of WADC and even result in instability. To address this issue, this paper develops a time-delay correction control strategy for VSC-HVDC damping control in urban power grids. First, a small signal model of WADC is built to analyze the negative impacts of time delay. Then, a data-driven approach is proposed to compensate for the inherent time delay in VSC-HVDC damping control. The extensive training data will be generated under various disturbances. After offline training, the long short-term memory network (LSTM) can be implemented online to predict the actual frequency deviation based on real-time measurements. Finally, the proposed method is validated through MATLAB-Simulink in a two-area four-machine system. The results indicate that the data-driven compensation has a strong generalization ability for random delay time constants and can improve the performance of WADC significantly.

Keywords: wide area damping control, HVDC, small signal modeling, time delay compensation, long short-term memory

Edited by:
Kaiqi Sun,
Shandong University, China

Reviewed by:
Yuqing Qu,
Tianjin University, China
Weiying Dai,
Southeast University, China

****Correspondence:***
Yuqing Dong
ydong22@utk.edu

Specialty section:
This article was submitted to Smart Grids, a section of the journal Frontiers in Energy Research

Received: *13 March 2022*
Accepted: *08 April 2022*
Published: *27 April 2022*

Citation:
She B, Dong Y and Liu Y (2022) Time Delay of Wide Area Damping Control in Urban Power Grid: Model-Based Analysis and Data-Driven Compensation.
Front. Energy Res. 10:895163.
doi: 10.3389/fenrg.2022.895163

INTRODUCTION

Urbanization has witnessed the development of modern civilization (Jiang et al., 2019). Urban power grids are accommodating more people and consuming more energy than ever before (Xiao et al., 2022). With distributed energies and loads from distant areas (Pan et al., 2021; Sun et al., 2022; Yang et al., 2022), VSC-HVDC has been widely used to transmit clean energy from remote regions to urban power (Fu et al., 2021; Sun et al., 2021b; Xiao et al., 2021). On the other hand, the increasing uncertainty of distributed energy resources (Li S. et al., 2021; Zhang J. et al., 2022), extreme weather, and flexible loads like electrical vehicles pose great challenges to the frequency regulation of urban power grids (Xiong et al., 2021). With the interconnection of different regions of power grids, the inter-area low-frequency oscillations have also become a serious issue that threatens the system's stability (Baltas et al., 2021).

Wide area damping control (WADC) provides a promising approach to mitigate the oscillations of frequency and thus improve the stability of urban power grids (Li and Chen, 2018). However, in

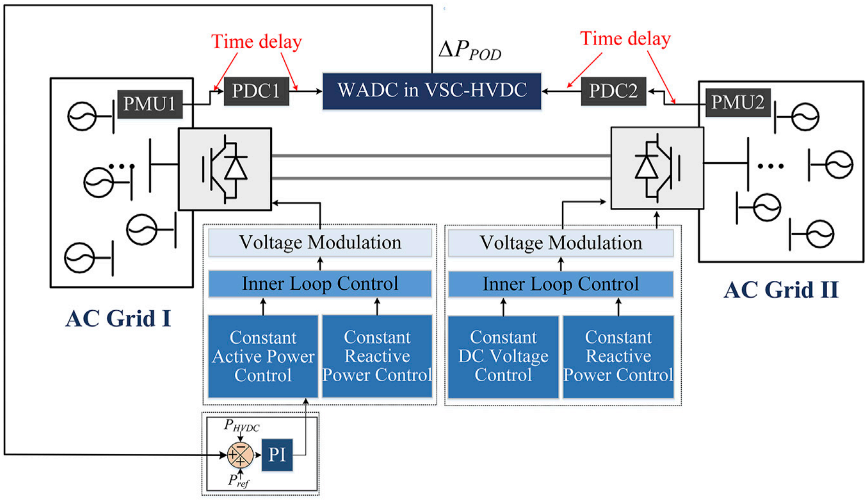

FIGURE 1 | System diagram of VSC-HVDC.

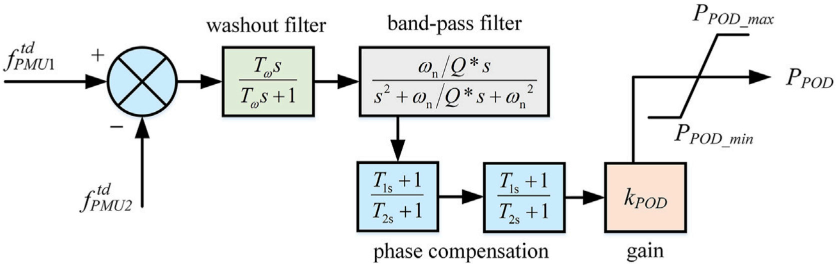

FIGURE 2 | Control diagram of WADC.

WADC, the control signals measured by phasor measurement unit (PMU) are transmitted from a distant region through communication channels, which may bring an unavoidable time delay (Musleh et al., 2018). Such kind of delay can vary from tens to hundreds of milliseconds (He et al., 2009), depending on different communication distances, protocols, and measuring devices. Some research have reported that the existing time delay, even with a small value, will result in the loss of WADC control and power system instability (Xu et al., 2020). Considering the fast power controllability of VSC-HVDC (Sun et al., 2021a; Dong et al., 2021), the time delay in the control signal may bring a more destabilizing influence than other devices.

Some control strategies have been proposed to deal with the time delay in WADC. One of the conventional methods focuses on the offline parameter optimization of WADC, based on linear matrix inequality theory (LMI) (Chang et al., 2006; Li et al., 2010), Smith Predictor (Chaudhuri et al., 2004) and robust control strategies (Wang et al., 2010), which usually relies on known models and uses fixed parameters. To adapt to the varying conditions of the system operation, some adaptive control strategies are put forward to compensate the time delay more realistically (Cheng et al., 2014) (Zhu et al., 2016). The main idea of the adaptive control is to schedule the control gains and the phase compensation parameters according to the online identification of the system model and oscillation modes. Nevertheless, the model estimation requires characteristic extraction from continuous ambient data injection, which may be influenced by system background noise and is not necessarily accurate and instantaneous.

Recently, the rapid development of artificial intelligence has created the potential for time delay compensation with neural networks. Among the various neural networks, the long short-term memory network (LSTM) is a kind of modern recurrent neural network that is designed for handling time series data (Xu et al., 2021). It has been successfully employed in power systems for islanding detection (Abdelsalam et al., 2020), load and generation forecast (Liu et al., 2020)-(Alavi et al., 2021), fast event identification (Li Z. et al., 2021), and measurements prediction (Wang et al., 2021). One common feature of these studies is that they made the best use of the time-series properties of power system data. Actually, the delayed PMU measurements are awesome time series data that can help predict the real time frequency deviation for WADC. Apart from LSTM, multilayer perception (MLP) and convolutional network (CNN) may also be used to predict delayed signals. However, MLP suffers from the computational burden when dealing with time-series data, and CNN cannot preserve the long-term information and skip the

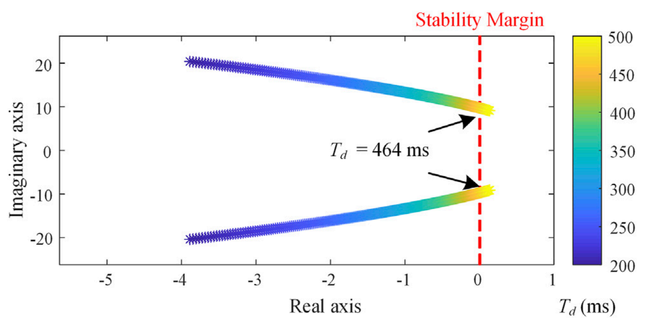

FIGURE 3 | Dominant eigenvalue of *A*.

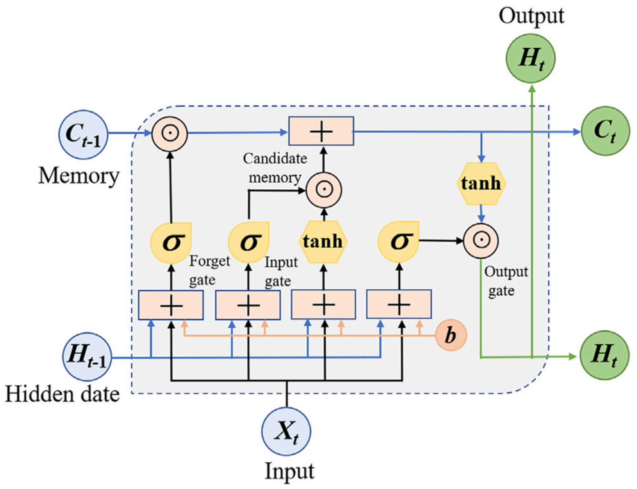

FIGURE 4 | Basic cell of LSTM.

short-term input at the same time. Hence, this paper tries to integrate LSTM into the time delay compensation of urban VSC-HVDC systems. Compared with the existing literature, this paper has the following contributions.

- Formulated a small signal model of WADC with time delay and mathematically proved that the uncorrected PUM signals can result in the instability of the urban power grids.
- Proposed a data-driven delay compensation approach for WADC, leveraging the modern recurrent neural network LSTM. A well-trained LSTM was implemented online for time delay compensation after thorough offline training under various disturbances.
- Verified the proposed method through numerical simulation. Results showed that the LSTM-based compensation method has strong generalization ability. It can adapt to random delay time in real system even though the delay time constants were not included in the training dataset.

The rest of this paper is organized as follows. *Model-Based Analysis on Time Delay of Wide Area Damping Control Section* builds up the small signal model of WADC with time delay and analyzes the negative impacts based on eigenvalue analysis. In *Data-Driven Delay Compensation With LSTM Section*, a data-driven delay compensation approach is developed using LSTM. *Case Study Section* validates the proposed method in a two-area four machine system with a comprehensive test. Finally, conclusions are drawn in *Conclusion Section*.

MODEL-BASED ANALYSIS ON TIME DELAY OF WIDE AREA DAMPING CONTROL

Wide Area Damping Control With Time Delay

With the large-scale application of PMU measurement and power electronics technology, VSC-HVDC has been widely used in the field of WADC. The typical framework is shown in **Figure 1**. According to the frequency data collected by the PMUs in different regions, the WADC adjusts the DC power reference value to suppress the inter-area low-frequency oscillations.

In **Figure 1**, f_{PMU1}, f_{PMU2} are the real-time frequencies collected by PMU1 and PMU2, respectively. f^{td}_{PMU1} and f^{td}_{PMU2} are the delayed frequencies after passing through the communication channels. The workflow of WADC in VSC-HVDC consists of the following five steps:

- The PMU configured in the AC grid measures the three-phase bus voltage and calculates the bus frequency.
- After data packaging, the frequency data from different PMUs is transmitted to the phase data concentrators (PDCs). During the transmission process, a special communication protocol, such as IEEE C37.118, is used to ensure the transmission security and accuracy.
- The PDC then unpacks the frequency data and sends it to the WADC of the VSC-HVDC.
- **Figure 2** illustrates the block diagram of the WADC. It consists of a washout block, a band-pass filter, two phase compensation blocks, and a gain block. The input of the controller is the difference between the frequencies collected by the two PMUs; while the output of the controller is the active power reference value P_{POD}. The time constant T_ω of the washout filter is chosen as 10s. In the band-pass filter, ω_n is the system oscillation frequency, and Q is the quality factor, which is usually set as 1. For active power modulation, the time constant in the compensation block can be considered as the same value, i.e., $T_{1s} = T_{2s}$; k_{POD} is the controller gain. P_{POD_max} and P_{POD_min} are the output limits of the WADC.
- P_{POD} will then be added as an auxiliary signal to the P_{ref} of the VSC-HVDC outer loop control to modulate the DC active power.

In the practical system operation, the time delay exists from PMU to PDC, and then to the WADC.

Small Signal Modeling

In order to quantitatively analyze the influence of the time delay in VSC-HVDC system, a small signal model of VSC-HVDC with WADC considering the time delay has been established. In the test system, two generators are modeled to represent the two distant areas. A VSC station is connected to the two areas through transmission lines. The control strategy of the VSC-HVDC includes the WADC, outer loop control, inner loop control, and phase-locked loop (PLL).

For the generators in two areas, the rotor motion equations are shown in (**Eq. 1**).

$$\begin{cases} \dfrac{d\delta_{1,2}}{dt} = \omega_{g1,2} - \omega_0 \\ T_{J1,2}\dfrac{d\omega_{g1,2}}{dt} = T_{m1,2} - T_{e1,2} - D_{1,2}\omega_{g1,2} \end{cases} \tag{1}$$

where $\delta_{1,2}$ and $\omega_{g1,2}$ are the rotor phase and rotor angular velocity of the two generators. $T_{J1,2}$ is the inertia time constant; $D_{1,2}$ is the damping coefficient; $T_{m1,2}$ is the mechanical torque; while $T_{e1,2}$ is the electrical torque.

In the test system, the PMUs collect the frequencies at the ports of the two generators, so it can be considered that f_{PMU1}, f_{PMU2} are consistent with the corresponding generator frequencies, as shown in (**Eq. 2**).

$$\omega_{g1,2} = 2\pi f_{PMU1,2} \tag{2}$$

After the time delay, the difference between f_{PMU1}^{td} and f_{PMU2}^{td} is taken as the input to the WADC. The total time delay of the frequency difference can be assumed as T_d. Since the transfer function e^{-sT_d} is nonlinear, a fourth-order Pade approximation can be utilized to represent the characteristics of the time delay (Xu et al., 2020).

$$\frac{f_{error}^{td}}{f_{error}} = e^{-sT_d} \approx \frac{(T_d s)^4 - 20(T_d s)^3 + 180(T_d s)^2 - 840(T_d s) + 1680}{(T_d s)^4 + 20(T_d s)^3 + 180(T_d s)^2 + 840(T_d s) + 1680} \tag{3}$$

where $f_{error} = f_{PMU1}$- f_{PMU2}.

The state space equation of the Pade approximation can be transformed from (**Eq. 3**).

$$\begin{cases} \dfrac{d}{dt}z_p = A_p z_p + B_p u_p \\ y_p = C_p z_p + D_p u_p \end{cases} \tag{4}$$

Eq. 4 introduces four state variables $z_p = [z_1\ z_2\ z_3\ z_4]^{\mathrm{T}}$; the input variable $u_p = f_{error}$; the output variable is $y_p = f_{error}^{td}$.

The delayed frequency signal can then be expressed as (5):

$$\begin{aligned} f_{error}^{td} &= -\frac{40}{T_d}z_1 - \frac{1680}{T_d^3}z_3 + f_{error} \\ &= -\frac{40}{T_d}z_1 - \frac{1680}{T_d^3}z_3 + \frac{1}{2\pi}\left(\omega_{g1} - \omega_{g2}\right) \end{aligned} \tag{5}$$

where f_{error}^{td} is the actual input of the WADC. The output P_{POD} will be superimposed on the active power reference value of VSC outer loop control. The transfer function of WADC can be described in (**Eq. 6**):

$$P_{POD} = k_{POD}\cdot\frac{T_\omega s}{T_\omega s + 1}\,\frac{\omega_n/Q\cdot s}{s^2 + \omega_n/Q\cdot s + \omega_n^2}f_{error}^{td} \tag{6}$$

Transforming it into the state space form:

$$\frac{d}{dt}\begin{bmatrix} x_{POD1} \\ x_{POD2} \\ x_{POD3} \end{bmatrix} = \begin{bmatrix} -\dfrac{\omega_n T_\omega/Q + 1}{T_\omega} & -\dfrac{\omega_n/Q + \omega_n^2 T_\omega}{T_\omega} & -\dfrac{\omega_n^2}{T_\omega} \\ 1 & 0 & 0 \\ 0 & 1 & 0 \end{bmatrix}\begin{bmatrix} x_{POD1} \\ x_{POD2} \\ x_{POD3} \end{bmatrix} + \begin{bmatrix} 1 \\ 0 \\ 0 \end{bmatrix} f_{error}^{td} \tag{7}$$

$$P_{POD} = \begin{bmatrix} \omega_n/Q & 0 & 0 \end{bmatrix}\begin{bmatrix} x_{POD1} \\ x_{POD2} \\ x_{POD3} \end{bmatrix} \tag{8}$$

Combining with the outer loop control, inner loop control, and PLL function of the VSC, the small signal model of the complete test system can be obtained after linearization, as shown in (**Eq. 9**).

$$\frac{\mathrm{d}\Delta x}{\mathrm{d}t} = A\Delta x + B\Delta u \tag{9}$$

where $\boldsymbol{A}$ is a 21 × 21 state matrix; $\boldsymbol{B}$ is a 21 × 2 input matrix.

$$\boldsymbol{A}_{SG} = \begin{bmatrix} -\dfrac{E_{1d0}'}{\omega_0 T_{J1}} & -\dfrac{E_{1q0}'}{\omega_0 T_{J1}} & 0 & 0 \\ 0 & 0 & -\dfrac{E_{2d0}'}{\omega_0 T_{J2}} & -\dfrac{E_{2q0}'}{\omega_0 T_{J2}} \end{bmatrix}\boldsymbol{A}_{delay}$$

$$= \begin{bmatrix} -\dfrac{20}{T_d} & -\dfrac{180}{T_d^2} & -\dfrac{840}{T_d^3} & -\dfrac{1680}{T_d^4} \\ 1 & 0 & 0 & 0 \\ 0 & 1 & 0 & 0 \\ 0 & 0 & 1 & 0 \end{bmatrix}$$

$$\boldsymbol{A}_{x\omega} = \begin{bmatrix} 1/2\pi & -1/2\pi \\ 0 & 0 \\ 0 & 0 \end{bmatrix},$$

$$\boldsymbol{A}_{xz} = \begin{bmatrix} -40/T_d & 0 & -1680/T_d^3 & 0 \\ 0 & 0 & 0 & 0 \\ 0 & 0 & 0 & 0 \end{bmatrix},$$

$$\boldsymbol{A}_{\omega} = \begin{bmatrix} -D_1/T_{J1} & 0 \\ 0 & -D_2/T_{J2} \end{bmatrix}, \boldsymbol{A}_{ii} = \begin{bmatrix} 0 & \omega_0 \\ -\omega_0 & 0 \end{bmatrix}$$

$$\boldsymbol{a} = \begin{bmatrix} 0 & -1/X_f \\ 1/X_f & 0 \end{bmatrix}, \boldsymbol{b} = \frac{3}{2}\cdot\begin{bmatrix} i_{sd0} & i_{sq0} \\ i_{sq0} & -i_{sd0} \end{bmatrix},$$

$$\boldsymbol{c} = \frac{3}{2}\cdot\begin{bmatrix} u_{sd0} & u_{sq0} \\ -u_{sq0} & u_{sd0} \end{bmatrix}, \boldsymbol{d} = \begin{bmatrix} -1/L_1 & 0 \\ 0 & -1/L_1 \end{bmatrix},$$

$$\boldsymbol{e} = \begin{bmatrix} -1/L_2 & 0 \\ 0 & -1/L_2 \end{bmatrix}$$

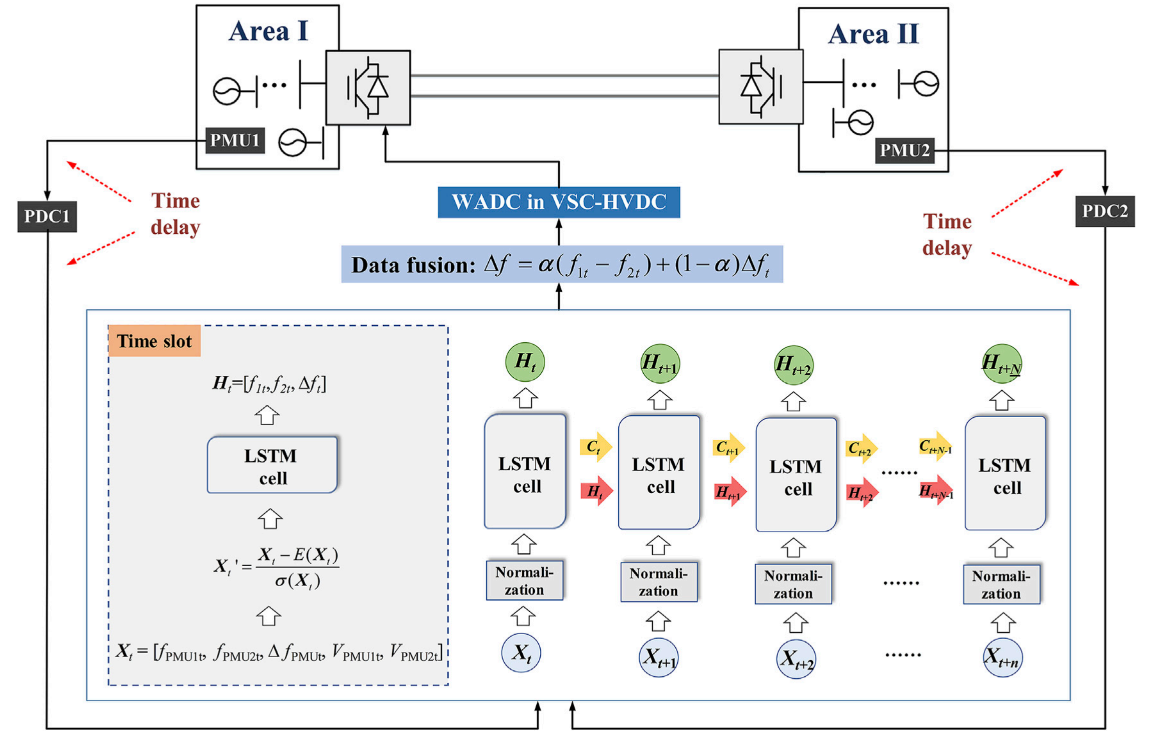

FIGURE 5 | Diagram of employing LSTM for time-delay compensation.

$$\boldsymbol{K}_1=\begin{bmatrix}-\dfrac{\omega_n T_\omega/Q+1}{T_\omega} & -\dfrac{\omega_n/Q+\omega_n^2 T_\omega}{T_\omega} & -\dfrac{\omega_n^2}{T_\omega}\\ 1 & 0 & 0\\ 0 & 1 & 0\end{bmatrix},$$

$$\boldsymbol{K}_{21}=\begin{bmatrix}k_{pp} & 0\\ 0 & k_{pq}\end{bmatrix},\boldsymbol{K}_{22}=\begin{bmatrix}k_{ip} & 0\\ 0 & k_{iq}\end{bmatrix},\boldsymbol{K}_{31}=\begin{bmatrix}k_{pid} & 0\\ 0 & k_{piq}\end{bmatrix},$$

$$\boldsymbol{K}_{32}=\begin{bmatrix}k_{iid} & 0\\ 0 & k_{iiq}\end{bmatrix},\boldsymbol{K}_4=\begin{bmatrix}0 & k_{iPLL}\\ 0 & k_{pPLL}\end{bmatrix}$$

$$\boldsymbol{M}_1=\begin{bmatrix}\dfrac{3u_{cqo}-3i_{sd0}X_f}{2X_f} & \dfrac{2u_{s0}-3u_{cdo}-3i_{sq0}X_f}{2X_f}\\ \dfrac{-2u_{s0}+3u_{cdo}-3i_{sq0}X_f}{2X_f} & \dfrac{3u_{cqo}+3i_{sd0}X_f}{2X_f}\end{bmatrix},$$

$$\boldsymbol{M}_2=\begin{bmatrix}\dfrac{3u_{cqo}}{2X_f} & \dfrac{2u_{c0}-3u_{cdo}}{2X_f}\\ \dfrac{2u_{c0}+3u_{cdo}-4u_{s0}}{2X_f} & \dfrac{3u_{cqo}}{2X_f}\end{bmatrix}$$

$$\boldsymbol{M}_3=\boldsymbol{I}-\boldsymbol{M}_1^{-1}\boldsymbol{M}_2,$$

$$\boldsymbol{M}=(\boldsymbol{I}+\boldsymbol{a}^2-\boldsymbol{K}_{31}\boldsymbol{K}_{21}\boldsymbol{K}_1\boldsymbol{ca}+\boldsymbol{K}_{31}\boldsymbol{a})\boldsymbol{M}_3-\boldsymbol{K}_{31}\boldsymbol{K}_{21}\boldsymbol{K}_1\boldsymbol{b}$$

$$\boldsymbol{A}_{PQ}=\begin{bmatrix}-\boldsymbol{K}_{22}\boldsymbol{K}_1(\boldsymbol{b}+\boldsymbol{caM}_3)\boldsymbol{M}^{-1}\boldsymbol{K}_{31}\\ -\boldsymbol{K}_{22}\boldsymbol{K}_1(\boldsymbol{b}+\boldsymbol{caM}_3)\boldsymbol{M}^{-1}\\ \boldsymbol{K}_{22}\boldsymbol{K}_1(\boldsymbol{b}+\boldsymbol{caM}_3)\boldsymbol{M}^{-1}\boldsymbol{K}_{31}\boldsymbol{K}_{21}\boldsymbol{K}_1\end{bmatrix}^T$$

$$\boldsymbol{A}_{is}=\begin{bmatrix}\boldsymbol{K}_{22}-\boldsymbol{K}_{22}\boldsymbol{K}_{21}\boldsymbol{K}_1(\boldsymbol{b}+\boldsymbol{caM}_3)\boldsymbol{M}^{-1}\boldsymbol{K}_{31}-\boldsymbol{K}_{32}\boldsymbol{aM}_3\boldsymbol{M}^{-1}\boldsymbol{K}_{31}\\ -\boldsymbol{K}_{22}\boldsymbol{K}_{21}\boldsymbol{K}_1(\boldsymbol{b}+\boldsymbol{caM}_3)\boldsymbol{M}^{-1}-\boldsymbol{K}_{32}\boldsymbol{aM}_3\boldsymbol{M}^{-1}\\ \boldsymbol{K}_{22}\boldsymbol{K}_{21}-\boldsymbol{K}_{22}\boldsymbol{K}_{21}\boldsymbol{K}_1(\boldsymbol{b}+\boldsymbol{caM}_3)\boldsymbol{M}^{-1}\boldsymbol{K}_{31}\boldsymbol{K}_{21}-\boldsymbol{K}_{32}\boldsymbol{aM}_3\boldsymbol{M}^{-1}\boldsymbol{K}_{31}\boldsymbol{K}_{21}\end{bmatrix}^T$$

$$\boldsymbol{A}_{ig}=\begin{bmatrix}\boldsymbol{dM}^{-1}\boldsymbol{K}_{31} & \boldsymbol{eM}^{-1}\boldsymbol{K}_{31}\\ \boldsymbol{dM}^{-1} & eM^{-1}\\ -\boldsymbol{dM}^{-1}\boldsymbol{K}_{31}\boldsymbol{K}_{21}\boldsymbol{K}_1 & -\boldsymbol{eM}^{-1}\boldsymbol{K}_{31}\boldsymbol{K}_{21}\boldsymbol{K}_1\end{bmatrix}^T,$$

$$\boldsymbol{A}_{PLL}=\begin{bmatrix}\boldsymbol{K}_4\boldsymbol{M}^{-1}\boldsymbol{K}_{31}\\ \boldsymbol{K}_4\boldsymbol{M}^{-1}\\ \boldsymbol{K}_4\boldsymbol{M}^{-1}\boldsymbol{K}_{31}\boldsymbol{K}_{21}\boldsymbol{K}_1\end{bmatrix}^T$$

Time Delay Analysis

With the established small signal state space model, eigenvalue analysis can be conducted to investigate the stability of the system. As shown in **Figure 3**, the dominant eigenvalue of $\boldsymbol{A}$ is presented with time delay T_d varying from 200 to 500 ms. The other parameters of the test system remain constant.

In **Figure 3**, with the increase of T_d, the dominant eigenvalue gradually moves towards the positive direction of the real-axis. When T_d is greater than 464 ms, the eigenvalue will pass through the imaginary-axis and reach the right half plane of the coordinate axis, indicating that the system becomes unstable.

It can be concluded that: the stability margin of the system is reduced with the increase of the time delay, and even instability

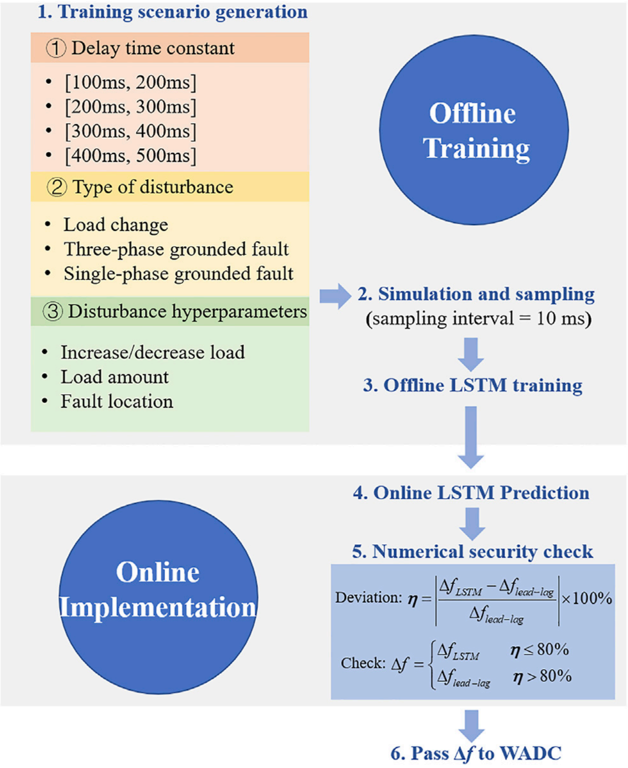

FIGURE 6 | Diagram of offline training and online implementation.

may occur. Therefore, in a VSC-HVDC system with WADC strategy, the time delay issue needs to be carefully resolved to guarantee the system stability.

DATA-DRIVEN DELAY COMPENSATION WITH LSTM

This section firstly gives an overview of LSTM and then employs it on time-delay compensation for WADC.

Preliminaries on LSTM

To improve the numerical instability of RNNs, several tricks such as new structure design are developed and implemented in the sophisticated sequence models. LSTM is one of the promising models that solves the problem of preserving the long-term information and skipping short-term input. **Figure 4** shows the basic cell of LSTM. Apart from the typical input and output, the cell also includes a few gates recurrent units (GRUs), memory, candidate memory, and hidden state. They are illustrated as follows (Zhang A. et al., 2022).

Gate Recurrent Units

There are three gate recurrent units utilized in LSTM: 1). input gate $\boldsymbol{I}_t$ is to decide whether to read data into the cell; 2). output gate $\boldsymbol{O}_t$ is responsible for reading out the entries from the cell; and 3). forget gate $\boldsymbol{F}_t$ is designed for resetting the content of the cell. The hidden states and the input data are fed to the three units and processed by fully-connected layers with sigmoid activation functions. The output of the three GRUs is calculated as follows.

$$\begin{cases} \boldsymbol{I}_{t+1} = \boldsymbol{\sigma}\left(\boldsymbol{X}_{t+1}\boldsymbol{W}_{xi} + \boldsymbol{H}_t\boldsymbol{W}_{ni} + \mathbf{b}_i\right) \\ \boldsymbol{F}_{t+1} = \boldsymbol{\sigma}\left(\boldsymbol{X}_{t+1}\boldsymbol{W}_{xf} + \boldsymbol{H}_t\boldsymbol{W}_{nf} + \mathbf{b}_f\right) \\ \boldsymbol{O}_{t+1} = \boldsymbol{\sigma}\left(\boldsymbol{X}_{t+1}\boldsymbol{W}_{xo} + \boldsymbol{H}_t\boldsymbol{W}_{no} + \mathbf{b}_o\right) \end{cases} \tag{10}$$

where $\boldsymbol{W}_{xi}$, $\boldsymbol{W}_{xf}$, $\boldsymbol{W}_{xo}$, $\boldsymbol{W}_{ni}$, $\boldsymbol{W}_{nf}$ and $\boldsymbol{W}_{no}$ are weight parameters, and $\mathbf{b}_i$, $\mathbf{b}_f$, and $\mathbf{b}_i$ are bias parameters.

Memory and Candidate Memory

LSTM can choose to remember or forget the information from the last time slot, leveraging the input gate and forget gate. First, candidate memory is generated using a tanh function as activation function.

$$\tilde{\boldsymbol{C}}_{t+1} = \tanh\left(\boldsymbol{X}_{t+1}\boldsymbol{W}_{xc} + \boldsymbol{H}_t\boldsymbol{W}_{nc} + \mathbf{b}_c\right) \tag{11}$$

where $\tilde{\boldsymbol{C}}_{t+1}$ is the output of candidate memory. Then, the current cell memory is generated through fusing the past cell memory and candidate memory as follows.

$$\boldsymbol{C}_{t+1} = \mathbf{F}_{t+1} \odot \boldsymbol{C}_t + \boldsymbol{I}_{t+1} \odot \tilde{\boldsymbol{C}}_{t+1} \tag{12}$$

where ⊙ is the Hadamard (elementwise) robust operator. The combination of past cell memory and candidate memory enables the pass of cell memory and thus alleviates the vanishing gradient problem.

Hidden State

As shown in (**Eq. 13**), hidden state $\boldsymbol{H}_t$ is calculated by integrating the current memory into the last hidden state. $\boldsymbol{H}_t$ belongs to [-1, 1] because it is processed by tanh before passed to the next cell.

$$\boldsymbol{H}_t = \boldsymbol{O}_t \odot \tanh\left(\boldsymbol{C}_t\right) \tag{13}$$

With the special designs above, LSTM can finally capture the dependencies from historical data and predict the future value accurately.

Delay Compensation With LSTM

This subsection dives into the implementation of LSTM for delay compensation of WADC.

Fundamental Idea

Figure 5 shows the fundamental idea of the time delay compensation. PMU1 and PMU2 are implemented locally in two urban power grids to measure voltage and frequency. The delay usually happens on the signal transmission from PMU to damping control center. Typically, the delay is within the range of [10 ms, 500 ms], and the delay time constant varies depending on the distance of PUM to damping control center and the types of disturbances. An LSTM is employed locally in the damping control center to correct the sampled data before passing the delayed signals to controllers. In this way, the damping controller can function effectively without worrying about the negative impacts of communication time delay.

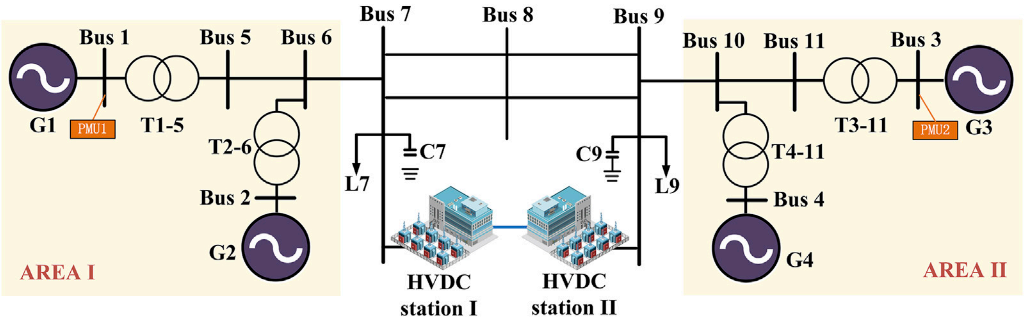

FIGURE 7 | Diagram of the two-area four-machine system. Scenario I: Partial Dataset Training.

TABLE 1 | Training hyperparameter of LSTM.

Name	Value
Optimizer	Adam
Initial learning rate	0.005
Learning rate decaying factor	0.2
Learning rate decaying period	125
Maximum episode	250

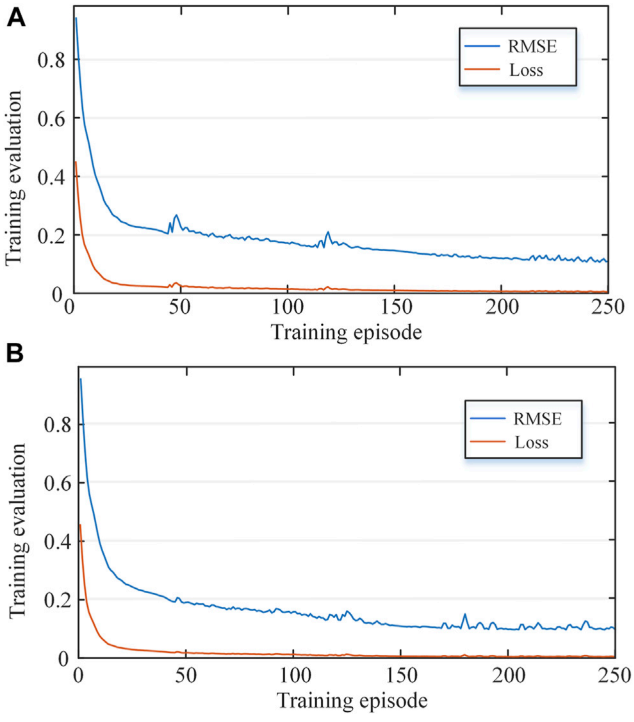

FIGURE 8 | Offline training error. **(A)** Scenario I. **(B)** Scenario II.

Input-Output Design

LSTM predicts the real time frequency of Area I and Area II based on the delayed data from PMU1 and PMU2. For each time slot, the input data $\boldsymbol{X}_t = [f_{\mathrm{PMU1}t}, f_{\mathrm{PMU2}t}, \Delta f_{\mathrm{PMU}t}, V_{\mathrm{PMU1}t}, V_{\mathrm{PMU2}t}]$. The number of hidden units is denoted by N, representing how far LSTM looks back when correcting the time delay. Then, the input data are normalized before being fed into the LSTM cell. Finally, LSTM outputs the real time f_{1t}, f_{2t}, and Δf_t.

Before feeding the predicted frequency error to damping controller, data fusion is utilized to increase the robustness of the time delay compensation. The final frequency error is calculated by integrating the predicted frequency into the predicted error as follows.

$$\Delta f = \boldsymbol{\alpha}\left(f_{1t} - f_{2t}\right) + (1 - \boldsymbol{\alpha})\Delta f_t \tag{14}$$

where α is a hyperparameter that controls the fusion rate. The data fusion can smooth the prediction error and increase the stability of the data-driven approach.

Offline Training and Online Implementation

The strategy of offline training and online implementation is used in this paper. As shown in **Figure 6**, the offline training is three-fold: training scenario generation, simulation and data sampling, and LSTM training, while online implementation includes LSTM prediction, numerical security check, and data passing. They are illustrated in detail in the following subsections.

Offline Training

The training data is generated under various disturbances. With the random combination of the three key elements that determine a disturbance, i.e., delay time constant, type of disturbance, and disturbance hyperparameters, the training data set can cover common disturbances in urban power systems. For each generated disturbance, perform numerical simulation in MATLAB-Simulink and sample the input data with time delay and the output data without time delay. The time interval of sampling is set as 10 ms, which is identical to the PMU sampling rate in reality. Then, all the training data are packaged for LSTM training.

Online Implementation

After extensive training, the well-trained LSTM is ready for online implantation. As shown in **Figure 5**, LSTM network

TABLE 2 | Validation condition.

Scenario	No.	Type of Disturbance	Delay Time Constant (ms)	Disturbance Hyper Parameters	Settings that Are Different from the Training Dataset
Scenario I	1	Load increase	250	Area I, Δp = 300 MW	②③
	2	Load decrease	250	Area II, Δp = -300 MW	②③
	3	Three-phase grounded fault	250	Area I, t = 0.1s (clearing time)	①②③
	4	Single-phase grounded fault	250	Area II, t = 0.1s	①②③
Scenario II	1	Load increase	250	Area I, Δp = 300 MW	②
	2	Load decrease	250	Area II, Δp = -300 MW	②
	3	Three-phase grounded fault	250	Area I, t = 0.1s	②
	4	Single-phase grounded fault	250	Area II, t = 0.1s	②

Note: ① is type of disturbance; ② is delay time constant; ③ is disturbance hyperparameter.

predicts the real time frequency error between the two urban power systems based on the delayed PMU data. To guarantee the security of implementing unexplainable neural network, a numerical security check is performed before passing the predictions to damping controller. The online prediction of LSTM is compared with that of the model-based lead-lag time delay compensator. If the prediction of LSTM deviates less than 80% from the lead-lag controller, the prediction is passed to damping controller. Otherwise, the conventional predictor will be used. The security check is designed to prevent the numerical instability of neural network prediction. Due to the non-interpretability of LSTM, we cannot guarantee that LSTM always predicts the error within an acceptable range. Hence, the model-based lead-lag module is used to generate the interpretable correction signals that are certainly secure. **Eqs 15**, **16** show the security check process, which enhances the stability and reliability of the data-driven compensation.

$$\boldsymbol{\eta} = \left| \frac{\Delta f_{LSTM} - \Delta f_{lead-lag}}{\Delta f_{lead-lag}} \right| \times 100\% \tag{15}$$

$$\Delta f = \begin{cases} \Delta f_{LSTM} & \boldsymbol{\eta} \leq 80\% \\ \Delta f_{lead-lag} & \boldsymbol{\eta} > 80\% \end{cases} \tag{16}$$

CASE STUDY

This section validates the proposed time-delay compensation approach in a two-area four-machine system.

Case Overview

As shown in **Figure 7**, both Area I and Area II have two synchronous generators supplying local loads, and they are connected through AC transmission lines and VSC-HVDC. The AC transition is responsible for the transmission of active power, while the VSC-HVDC performs wide area damping control based on PMU measurements. PMU1 and PMU2 are equipped at the terminal of G1 and G3, respectively.

To better validate the generalization of the data-driven method, the offline training data is divided into several groups based on delay time constant, type of disturbance, and disturbance hyperparameters. In Scenario I, LSTM is trained on a dataset of partial disturbances, while in Scenario II, LSTM is trained on a dataset of all kinds of disturbances.

In Scenario I, the training dataset is generated on the disturbance of load change with delay time constant belonging to (100 ms, 200 ms) and (300 ms, 400 ms). Then, conduct LSTM training using the hyperparameters listed in **Table 1**, and the training results are presented in **Figure 8**. After 250 episodes, the LSTM's prediction root mean square error (RMSE) and training loss are both near zero, indicating that the LSTM has a high forecast accuracy on the training dataset.

Assume the fusion rate α = 0.5, the well-trained LSTM is implemented online and tested under the conditions in **Table 2**. The validation results are plotted in **Figure 9A**, based on which we have the following observations.

- Time delay degrades the performance of the WADC. The oscillation becomes severe when directly utilizing the delayed signal from PMU.
- In No.1 and No. 2 validation conditions, although the delay time constant 250 ms doesn't belong to the training dataset, LSTM can still correct the delayed frequency accurately.
- There is a minor oscillation around 4 Hz in No.1 validation condition. The oscillation is outside WADC's target suppression mode, so it is not suppressed considerably.
- In No. 3 and No. 4 validation conditions, LSTM doesn't compensate for the delayed signals well because neither of the three key elements that determine a disturbance belongs to the training dataset. However, the performance of WADC is somewhat improved with the compensation of LSTM.

Scenario II: Complete Dataset Training

To validate the overall performance of LSTM, the dataset of three kinds of disturbance is used for offline training in Scenario II. The delay time constant and the disturbance hyperparameters are identical to those in Scenario II. Using the training hyperparameters in **Table 1**, the LSTM's prediction RMSE and training loss converge to 0 after training for 250 episodes. **Figure 9B** shows the training error, which suggests that LSTM can predict the un-delayed signals accurately.

Assume the fusion rate α = 0.5, the well-trained LSTM is implemented online and tested under the conditions in **Table 2**.

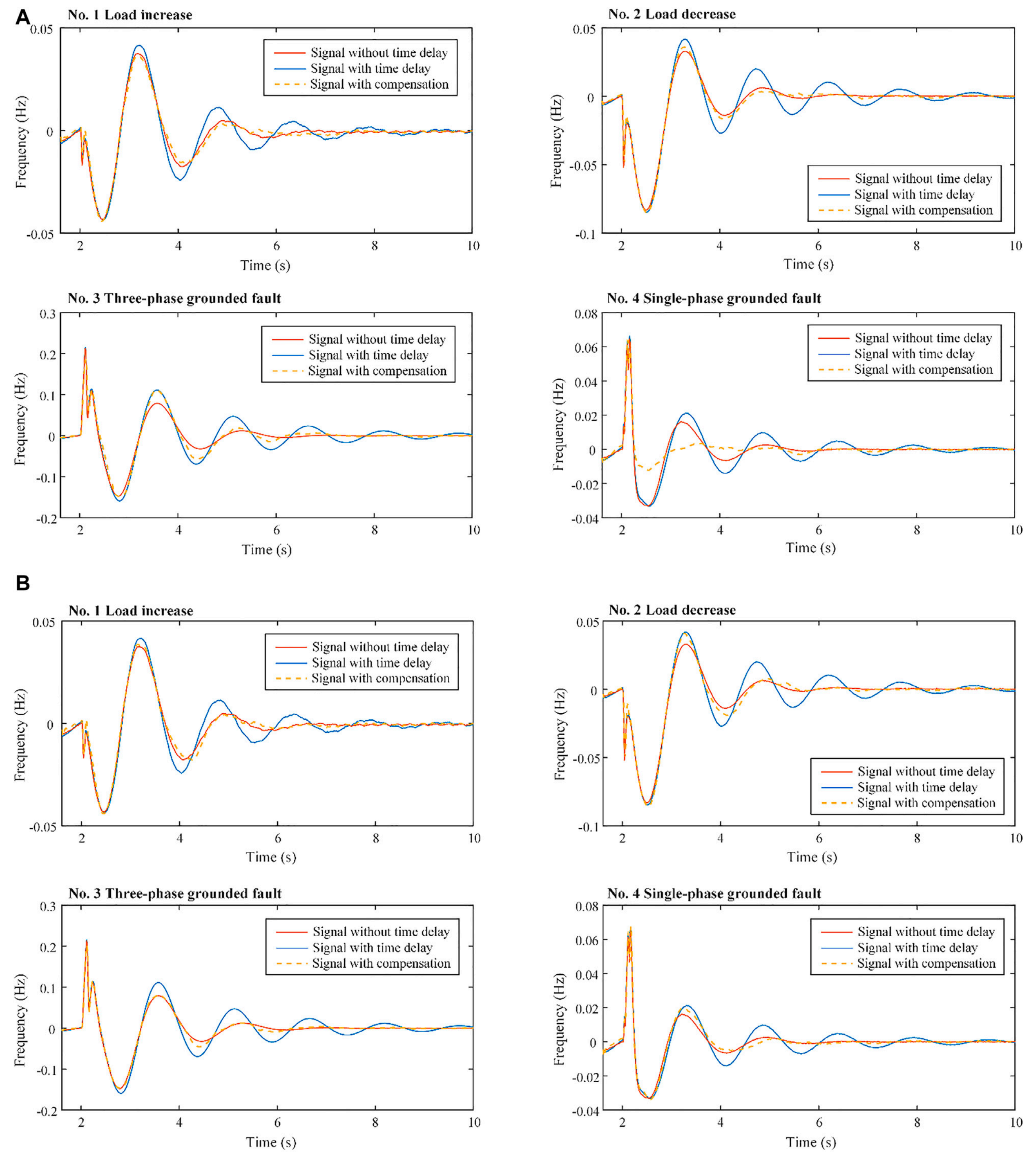

FIGURE 9 | Online validation results. **(A)** Scenario I. **(B)** Scenario II.

Figure 9 shows the dynamic frequency with and without the compensation. We can see that in the four validation conditions, although the test delay time constant 250 ms doesn't belong to the training dataset, LSTM can predict the error of delay accurately. The performance of WADC's has improved significantly. **Figure 10** further plots the normalized online prediction error, which can be expressed in (**Eq. 17**).

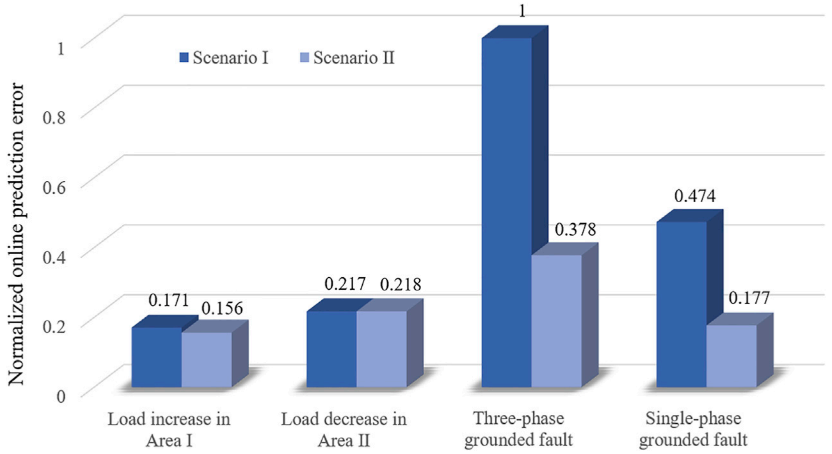

FIGURE 10 | Normalized online prediction error of LSTM in Scenario I and Scenario II.

$$\mathbf{NOPE}_i = \sum_{time} \Delta f_{LSTMi} \Big/ \max\left(\sum_{time} \Delta f_{LSTMi} \right) \qquad (17)$$

where NOPE is the "normalized online prediction error"; i represents the respective case in each scenario.

The NOPE of three-phase grounded fault and single-phase grounded fault in Scenario I is much less than that in Scenario II, indicating that LSTM has insufficient generalization ability for the type of disturbance. Hence, the training dataset should cover all types of disturbance as much as possible in practical application.

In general, a well-trained LSTM can provide accurate correction signals for WADC. It has strong generalization ability for delay time constant, which is beneficial to its employment in real systems. With the delay compensator, WADC can address the random time delay and improve its damping performance significantly.

CONCLUSION

The time delay in WADC can degrade the performance of damping controllers and even results in instability. The root cause is revealed through small signal modeling and eigenvalue analysis in this paper. To address this issue, this paper further proposed a data-driven approach to compensate for the delayed PMU signals, which leverages the modern recurrent neural network LSTM. The compensation procedure includes offline training and online implantation. Through partial dataset training and complete dataset training in a two-area four-machine system, it is verified that LSTM corrects the delayed frequency accurately. LSTM has strong generalization ability for delay time constant and can deal with the random time delay caused by commination and disturbances in urban power grids. After employing the delay correction approach, the damping performance of WADC is improved significantly.

One potential weakness of our work is that LSTM needs as many training data that cover all kinds of disturbances as possible. Our future work may include developing a more efficient training method with less training data, improving the generalization ability of LSTM to handle new disturbances, integrating the topology change into data generation, and validating the data-driven approach in a hardware-in-the-loop system.

DATA AVAILABILITY STATEMENT

The original contributions presented in the study are included in the article/Supplementary Material, further inquiries can be directed to the corresponding author.

AUTHOR CONTRIBUTIONS

BS contributed to conception and design of the study. YD generated the database and implemented simulation. YL provided guidance to the study. BS and YD wrote the draft of the manuscript. All authors contributed to manuscript revision, read, and approved the submitted version.

REFERENCES

Abdelsalam, A. A., Salem, A. A., Oda, E. S., and Eldesouky, A. A. (2020). Islanding Detection of Microgrid Incorporating Inverter Based DGs Using Long Short-Term Memory Network. *IEEE Access* 8, 106471–106486. doi:10.1109/ACCESS.2020.3000872

Alavi, S. A., Mehran, K., Vahidinasab, V., and Catalao, J. P. S. (2021). Forecast-Based Consensus Control for DC Microgrids Using Distributed Long Short-Term Memory Deep Learning Models. *IEEE Trans. Smart Grid* 12, 3718–3730. doi:10.1109/TSG.2021.3070959

Baltas, G. N., Lai, N. B., Tarraso, A., Marin, L., Blaabjerg, F., and Rodriguez, P. (2021). AI-based Damping of Electromechanical Oscillations by Using Grid-Connected Converter. *Front. Energ. Res.* 9, 598436. doi:10.3389/fenrg.2021.598436

Chang, Y., Chen, H., Cheng, G. H., and Xie, J. (2006). "Design of HVDC Supplementary Controller Accommodating Time Delay of the WAMS Signal in Multi-Machine System," in *IEEE Power Engineering Society General Meeting*. Montreal, QC, Canada: IEEE, 7. doi:10.1109/PES.2006.1709071

Chaudhuri, B., Majumder, R., and Pal, B. C. (2004). Wide-area Measurement-Based Stabilizing Control of Power System Considering Signal Transmission Delay. *IEEE Trans. Power Syst.* 19, 1971–1979. doi:10.1109/TPWRS.2004.835669

Cheng, L., Chen, G., Gao, W., Zhang, F., and Li, G. (2014). Adaptive Time Delay Compensator (ATDC) Design for Wide-Area Power System Stabilizer. *IEEE Trans. Smart Grid* 5, 2957–2966. doi:10.1109/TSG.2014.2347401

Dong, Y., Ma, J., Wang, S., Liu, T., Chen, X., and Huang, H. (2021). An Accurate Small Signal Dynamic Model for LCC-HVDC. *IEEE Trans. Appl. Supercond.* 31, 1–6. doi:10.1109/TASC.2021.3107804

Fu, Y., Hu, C.-H., and Yang, D.-X. (2021). Conservative or Aggressive? the Dynamic Adjustment of the Feed-In Tariff Policy for Photovoltaic Power Generation in China. *Front. Energ. Res.* 9, 672920. doi:10.3389/fenrg.2021.672920

He, J., Wu, X., Li, P., Lu, C., and Wu, J. (2009). Design and experiment of Wide Area HVDC Supplementary Damping Controller Considering Time Delay in China Southern Power Grid. *IET Generation, Transm. Distribution* 3, 17–25. doi:10.1049/iet-gtd:20080129

Jiang, X., Xiao, J., She, B., and Zu, G. (2019). Locating and Sizing of Partition Flexible Interconnection Converter Station in Large Urban Power Grids. *IET Generation, Transm. & Distribution* 13, 4830–4841. doi:10.1049/iet-gtd.2018.6871

Li, M., and Chen, Y. (2018). A Wide-Area Dynamic Damping Controller Based on Robust H∞ Control for Wide-Area Power Systems with Random Delay and Packet Dropout. *IEEE Trans. Power Syst.* 33, 4026–4037. doi:10.1109/TPWRS.2017.2782792

Li, S., Hou, J., Yang, A., and Li, J. (2021). DNN-based Distributed Voltage Stability Online Monitoring Method for Large-Scale Power Grids. *Front. Energ. Res.* 9. doi:10.3389/fenrg.2021.625914

Li, Y., Rehtanz, C., Yang, D. C., Gorner, K., Ruberg, S., and Luo, L. F. (2010). "Wide-area Time-Delay Damping Control to Prevent Power Oscillations in HVDC/AC Interconnected Power Systems," in 2010 International Conference on Power System Technology. Zhejiang, China: IEEE, 1–6. doi:10.1109/POWERCON.2010.5666549

Li, Z., Liu, H., Zhao, J., Bi, T., and Yang, Q. (2021). Fast Power System Event Identification Using Enhanced LSTM Network with Renewable Energy Integration. *IEEE Trans. Power Syst.* 36, 4492–4502. doi:10.1109/TPWRS.2021.3064250

Liu, B., Chen, J., Wang, H., and Wang, Q. (2020). Renewable Energy and Material Supply Risks: a Predictive Analysis Based on an LSTM Model. *Front. Energ. Res.* 8, 163. doi:10.3389/fenrg.2020.00163

Musleh, A. S., Muyeen, S. M., Al-Durra, A., Kamwa, I., Masoum, M. A. S., and Islam, S. (2018). Time-Delay Analysis of Wide-Area Voltage Control Considering Smart Grid Contingences in a Real-Time Environment. *IEEE Trans. Ind. Inf.* 14, 1242–1252. doi:10.1109/TII.2018.2799594

Pan, G., Hu, Q., Gu, W., Ding, S., Qiu, H., and Lu, Y. (2021). Assessment of Plum Rain's Impact on Power System Emissions in Yangtze-Huaihe River basin of China. *Nat. Commun.* 12, 6156. doi:10.1038/s41467-021-26358-w

Sun, K., Li, K.-J., Zhang, Z., Liang, Y., Liu, Z., and Lee, W.-J. (2022). An Integration Scheme of Renewable Energies, Hydrogen Plant, and Logistics Center in the Suburban Power Grid. *IEEE Trans. Ind. Applicat.* 58, 2771–2779. doi:10.1109/TIA.2021.3111842

Sun, K., Qiu, W., Yao, W., You, S., Yin, H., and Liu, Y. (2021a). Frequency Injection Based HVDC Attack-Defense Control via Squeeze-Excitation Double CNN. *IEEE Trans. Power Syst.* 36, 5305–5316. doi:10.1109/TPWRS.2021.3078770

Sun, K., Xiao, H., Pan, J., and Liu, Y. (2021b). VSC-HVDC Interties for Urban Power Grid Enhancement. *IEEE Trans. Power Syst.* 36, 4745–4753. doi:10.1109/TPWRS.2021.3067199

Wang, M., Liu, J., and Liu, J. (2010). "Delay-dependent Robust H∞ Control of Nonlinear Uncertain Time-Delay Systems," in *IEEE ICCA*. Xiamen, China: IEEE, 1249–1254. doi:10.1109/ICCA.2010.5524229

Wang, Q., Bu, S., He, Z., and Dong, Z. Y. (2021). Toward the Prediction Level of Situation Awareness for Electric Power Systems Using CNN-LSTM Network. *IEEE Trans. Ind. Inf.* 17, 6951–6961. doi:10.1109/TII.2020.3047607

Xiao, H., Sun, K., Pan, J., Li, Y., and Liu, Y. (2021). Review of Hybrid HVDC Systems Combining Line Communicated Converter and Voltage Source Converter. *Int. J. Electr. Power Energ. Syst.* 129, 106713. doi:10.1016/j.ijepes.2020.106713

Xiao, J., Cai, Z., Liang, Z., and She, B. (2022). Mathematical Model and Mechanism of TSC Curve for Distribution Networks. *Int. J. Electr. Power Energ. Syst.* 137, 107812. doi:10.1016/j.ijepes.2021.107812

Xiong, M., Xu, X., Sun, K., and Wang, B. (2021). "Approximation of the Frequency-Amplitude Curve Using the Homotopy Analysis Method," in *2021 IEEE Power Energy Society General Meeting (PESGM)*. Washington, DC, United States: IEEE, 1–5. doi:10.1109/PESGM46819.2021.9638009

Xu, L., Guo, C., Peng, Y., Yang, S., and Zhao, C. (2020). "Small Signal Model of VSC-HVDC Considering the Impact of Time Delay," in 2020 10th International Conference on Power and Energy Systems (ICPES), 286–291. doi:10.1109/ICPES51309.2020.9349709

Xu, Y., Gao, W., Qian, F., and Li, Y. (2021). Potential Analysis of the Attention-Based LSTM Model in Ultra-short-term Forecasting of Building HVAC Energy Consumption. *Front. Energ. Res.* 9. doi:10.3389/fenrg.2021.730640

Yang, D., Jin, Z., Zheng, T., and Jin, E. (2022). An Adaptive Droop Control Strategy with Smooth Rotor Speed Recovery Capability for Type III Wind Turbine Generators. *Int. J. Electr. Power Energ. Syst.* 135, 107532. doi:10.1016/j.ijepes.2021.107532

Zhang, A., Lipton, Z. C., Li, M., and Smola, A. J. (2022). *Dive into Deep Learning*, 1027.

Zhang, J., She, B., Peng, J. C.-H., and Li, F. (2022). A Distributed Consensus-Based Optimal Energy Management Approach in DC Microgrids. *Int. J. Electr. Power Energ. Syst.* 140, 108015. doi:10.1016/j.ijepes.2022.108015

Zhu, L., Liu, H., Pan, Z., Liu, Y., Farantatos, E., Patel, M., et al. (2016). "Adaptive Wide-Area Damping Control Using Measurement-Driven Model Considering Random Time Delay and Data Packet Loss," in *2016 IEEE Power and Energy Society General Meeting (PESGM)*. Boston, MA, United States: IEEE, 1–5. doi:10.1109/PESGM.2016.7741971

Conflict of Interest: The authors declare that the research was conducted in the absence of any commercial or financial relationships that could be construed as a potential conflict of interest.

frontiers | Frontiers in Energy Research

ORIGINAL RESEARCH
published: 05 May 2022
doi: 10.3389/fenrg.2022.907770

Virtual Inertial Control Strategy Based on Fuzzy Logic Algorithm for PMSG Wind Turbines to Enhance Frequency Stability

Qun Li[1], *Bixing Ren*[1,2], *Qiang Li*[1], *Dajiang Wang*[1], *Weijia Tang*[1], *Jianhui Meng*[3]* and *Xiaolong Wu*[3]

[1]State Grid Jiangsu Electric Power Company Ltd. Research Institute, Nanjing, China, [2]State Grid Jiangsu Electric Power Company Ltd., Nanjing, China, [3]State Key Laboratory of Alternate Electrical Power System with Renewable Energy Sources, North China Electric Power University, Baoding, China

With the increase of the penetration rate of wind power in the power grid, the high proportion of renewable energy and the high proportion of power electronic equipment in the power system will continuously reduce the inertia of the grid, and the frequency stability of the system will be seriously affected. The inertia of the system is an important parameter for system frequency regulation and stability calculation. For this reason, a virtual inertial control technology based on fuzzy logic control is proposed in this paper, which is used for wind turbines to participate in grid frequency regulation. In this method, based on power tracking, a fuzzy logic controller is designed to adjust the frequency adjustment coefficient adaptively, and fuzzy logic rules are used to optimize the power tracking curve online. Finally, by building a hardware-in-the-loop real-time simulation platform, the effectiveness of this method in providing system frequency support and improving the frequency response of the power grid is verified.

Keywords: PMSG, wind turbines, virtual inertial control, fuzzy logic, frequency support

Edited by:
Kaiqi Sun,
Shandong University, China

Reviewed by:
Hengshan Xu,
China Three Gorges University, China
Jun Yin,
North China University of Water Resources and Electric Power, China

Correspondence:
Jianhui Meng
mengjianhui2008@163.com

Specialty section:
This article was submitted to Smart Grids, a section of the journal Frontiers in Energy Research

Received: *30 March 2022*
Accepted: *19 April 2022*
Published: *05 May 2022*

Citation:
Li Q, Ren B, Li Q, Wang D, Tang W, Meng J and Wu X (2022) Virtual Inertial Control Strategy Based on Fuzzy Logic Algorithm for PMSG Wind Turbines to Enhance Frequency Stability. Front. Energy Res. 10:907770. doi: 10.3389/fenrg.2022.907770

1 INTRODUCTION

In recent years, with the result of increased new energy, the power grid has been moving toward a new power system with new energy sources as the mainstay. The traditional synchronous generators in power grids have better inertia and damping properties. As the high percentage of new energy and power electronic equipment gradually replace the traditional synchronous generators, the lack of inertia in the power system to support the grid is becoming apparent, and the frequency regulation capability available in the system is significantly reduced (Fang et al., 2018; Nguyen et al., 2019; Kheshti et al., 2020). Therefore, it is significant to study the importance of improving the inertia of the power system to support the frequency stability of the system while the power system is gradually moving toward low inertia.

China has abundant wind resources, and the installed wind capacity has grown exponentially. The replacement of conventional generating units with wind power reduces the effective inertia of the system, and the magnitude of inertia reflects the ability to prevent sudden changes in system frequency. Virtual inertia control techniques for improving the frequency stability of new energy systems are rapidly developing. The method of virtual inertia control technology used to improve the frequency stability of new energy systems is developing rapidly. In order to realize the inertial support of wind turbines to the system, Holdsworth et al. proposed the virtual inertia control of the variable speed wind turbines in 2004 (Holdsworth et al., 2004). It regulates the electromagnetic power in response to the frequency change of the grid and provides inertial support by varying the converter control strategy. The paper (Lalor et al., 2005) further proposed an additional frequency control scheme for wind turbines. The differential link is used to convert the rotational speed signal into an additional torque signal. After the system frequency drops, the rotational kinetic energy of the wind turbine is released to achieve the inertial response of the wind turbine. The paper (Chau et al., 2018) also introduced an inertial response to grid frequency by instantaneously releasing rotor kinetic energy, but did not fully analyze the control effect of the additional controllers. In (Wang et al., 2015), an artificial inertial control strategy is proposed. The kinetic energy is extracted by dynamically modifying the optimal power curve of the wind turbine. The kinetic energy is extracted by dynamically modifying the optimal power curve of the wind turbine. Yan et al. (2020) and Terazono et al. (2021) designed a synchronizer with multiple virtual rotating masses to improve the active power tracking performance and facilitate the inertial control of the synchronizer. But the problem of impaired power tracking has not been resolved. The paper (Liu et al., 2021) adopts a nonlinear virtual inertial control method based on a wind power integrated power system to provide the primary frequency support of the power grid. In (Wang and Tomsovic, 2018), a novel active power control framework was proposed to make the doubly-fed induction generator modify the reserve input under different operating modes. However, only inertia and primary frequency support are provided, and there are also deficiencies in the frequency response. Bao et al. (2021) and Ren et al. (2021) designs a hierarchical inertial control scheme that coordinates the active power output in the inertial control process between the wind turbine and the battery energy storage system to improve the frequency response of the system. There will also be excessive rotor speed deceleration and high-cost question.

With the rapid development of fuzzy logic and fuzzy theory in recent decades, its application research has achieved fruitful results. Using expert control experience, fuzzy logic control has better control characteristics for nonlinear and complex research objects, and has been widely and effectively applied in industrial process control, robotics, transportation, etc. (Tan et al., 2020; Oshnoei et al., 2021; Yap et al., 2021). The application of fuzzy logic control is also quite extensive in the control of new energy power generation. For example, literature (Miao et al., 2015) adopts fuzzy logic control for rotor speed recovery controller to achieve inertial control of rotor kinetic energy, but this method cannot adaptively control the control parameters for complex changing power grids. Athari and Ardehali (2016) and Karimi et al. (2020) developed a fuzzy logic controller to control the state of charge of the energy storage battery, which is still difficult to resist the disturbance of unknown parameters. The literature (Kerdphol et al., 2019) proposes a fuzzy logic inertial control method for grid frequency stability under high penetration conditions, which automatically adjusts virtual inertial constants according to active power and system frequency deviation to achieve a fast inertial response. In the literature (Long et al., 2021), a new control method combining fuzzy logic control and model predictive controller is proposed to effectively reduce the frequency deviation when dealing with large load changes. Therefore, in this paper, aiming at the low inertia system of new energy power electronic equipment, taking the wind turbine network system as the research object, this paper proposes a fuzzy logic controller to adaptively optimize the power tracking and enhance the frequency support and response capability of the system.

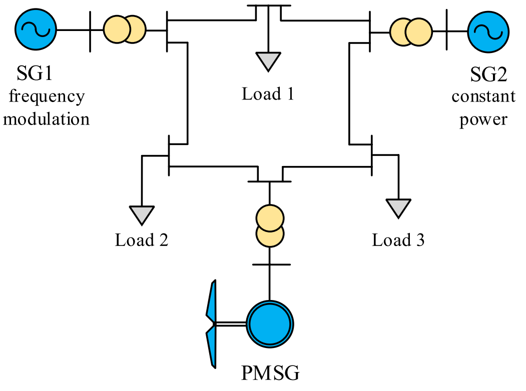

FIGURE 1 | 3-machine 9-node networking system topology.

In order to solve the problem of the lack of inertia of the power system and the reduction of the system frequency support capacity caused by a high percentage of new energy sources on the grid, this paper proposes a virtual inertia control strategy for permanent magnet synchronous wind turbine based on the fuzzy logic method. This strategy has promising research significance, and its main contributions to the paper can be summarized as follows:

1) In this paper, according to the grid frequency deviation and frequency change rate, the fuzzy logic controller is designed with fuzzy logic, and the virtual inertial control strategy based on power tracking is optimized.
2) By combining the fuzzy controller with the optimized PMSG virtual inertia control, the self-adaptive adjustment of the system inertia is achieved to support the system frequency.
3) A hardware-in-the-loop real-time experimental platform based on RT-LAB is built to verify the effectiveness of the proposed method.

This paper takes the three-machine, nine-node system for grid-connected wind power generation as the test object, and is organized as follows. Firstly, **Section 2** introduces the three-machine, nine-node system for grid-connected PMSG, and mathematically models the PMSG. Secondly, **Section 3** analyzes two typical virtual inertia control techniques by analyzing the influence between wind turbines and system frequency stability. In **Section 4**, based on the previous analysis of virtual inertial control technology, the virtual inertial control strategy based on power tracking is optimized, and a virtual inertial control based on fuzzy logic control is proposed. The fuzzy logic rules are used to optimize the power tracking online, and the system inertia can be improved to enhance the frequency support

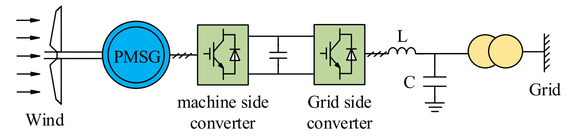

FIGURE 2 | Permanent magnet direct drive wind turbine.

capability of the system. Finally, in **Section 5**, a hardware-in-the-loop test platform is built based on a three-machine nine-node test system to verify the effectiveness of the proposed method.

2 3-MACHINE 9-NODE SYSTEM AND MODELING

The inertia in the traditional power grid mainly comes from the synchronous generator. With the integration of large-scale new energy into the power grid, the frequency regulation capability of the power grid in low inertia operation is reduced, and the system stability performance is poor. In order to better study the stability of the new energy grid system, build the test system as shown in **Figure 1**.

It shows the topology of the constructed 3-machine 9-node networking system. The system includes three constant impedance loads and transformers, frequency modulation unit SG1, constant power unit SG2 and PMSG wind turbine.

Wind turbine based on permanent magnet synchronous generator adopts three-blade wind turbine and multi-pole low-speed permanent magnet synchronous generator with the same speed as the wind turbine. The PMSG stator is connected to the power grid through the full power converter, and the grid-side converter realizes the grid-connected operation of the wind turbine and ensures the quality of the power delivered by the turbine. The output characteristics of the wind turbine depend entirely on the control system design of the inverter and the wind speed variation.

Figure 2 shows the structure of the permanent magnet direct drive wind turbine. The PMSG wind turbine has few control loops and has high operational reliability and efficiency. Define the PMSG stator voltage as U_s, I_s is the stator current, Ψ_f is the excitation flux linkage, and the potential E. Then E can be expressed as:

$$E = j\omega_r\psi_f \tag{1}$$

where ω_r is the PMSG rotor angular velocity.

The flux linkage and the electromagnetic torque of the PMSG in the two-phase synchronously rotating dq coordinate system are

$$\Psi_s = \left(L_d I_{sd} + jL_q I_{sq}\right) + \psi_f \tag{2}$$

$$T_e = \frac{3}{2}p_n Im\left[\Psi_s \hat{I}_s\right] \tag{3}$$

where L_d and L_q are the equivalent inductance of stator windings on the d-axis and q-axis, respectively, p_n is the number of PMSG pole pairs, T_e is the mechanical torque.

The stator voltage of PMSG in the dq coordinate system can be expressed as

$$U_s = R_s I_s + \frac{d\Psi_s}{dt} + j\omega_r\Psi_s \tag{4}$$

Through the above formula, the output power and electromagnetic torque of the stator side of PMSG in the dq coordinate system can be expressed as

$$P_s = -\frac{3}{2}\left(u_{sd}i_{sd} + u_{sq}i_{sq}\right) \tag{5}$$

$$Q_s = -\frac{3}{2}\left(u_{sq}i_{sd} - u_{sd}i_{sq}\right) \tag{6}$$

$$T_e = \frac{3}{2}p_n\left(\psi_{sq}i_{sd} - \psi_{sd}i_{sq}\right) = -\frac{3}{2}p_n\left[\psi_f i_{sq} + \left(L_d - L_q\right)i_{sd}i_{sq}\right] \tag{7}$$

where P_s and Q_s are the output active power and reactive power of the stator side, respectively. u_{sd}, u_{sq}, i_{sd}, and i_{sq} are the voltage and current of the stator at dq axis respectively. ψ_{sd} and ψ_{sq} are the flux linkage component of the dq axis.

The PMSG rotor structure is usually symmetrical, and $L_d = L_q$ can be set. Then **Eq. 7** can be simplified as

$$T_e = -\frac{3}{2}p_n\psi_f i_{sq} \tag{8}$$

3 VIRTUAL INERTIA CONTROL AND FREQUENCY STABILITY

3.1 Inertia to Frequency Stability

As wind power is integrated into the grid, the lack of effective support for the system poses a threat to grid frequency stability. The inertia of the system is an important characteristic of the grid frequency stability. In a conventional grid, when the output power of the system is not equal to the load consumption, a power deviation is generated, which is compensated by the rotational kinetic energy stored in the rotor of a conventional synchronous generator, resulting in a lower SG speed and a deviation of the system frequency from the rated value.

For traditional synchronous generator sets, when the output power of the system is not equal to the load consumption, the deviation is compensated by the rotational kinetic energy E_k stored in the SG, and the deviation ΔE_k can be expressed as

$$\Delta E_k = \int \Delta P dt = \frac{1}{2}J\Delta\omega_m^2 = \frac{1}{2p^2}J\Delta\omega_g^2 \tag{9}$$

where ΔP is the power deviation between the output power and the load consumption; ω_m and ω_g are the mechanical angular frequency and electrical angular frequency of SG, respectively; J is the rotational inertia; p is the polar logarithm, and when p is 1, **Eq. 9** can be expressed as

$$\Delta P = J\Delta\omega_g\frac{d\Delta\omega_g}{dt} \tag{10}$$

When there are n SGs in the system, **Eq. 10** can be expressed as

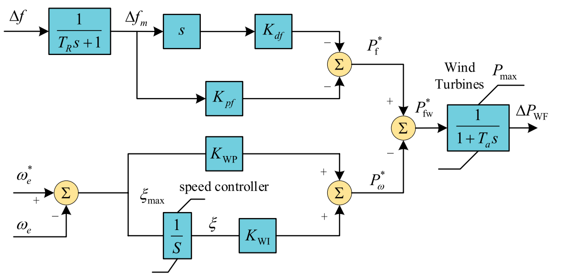

FIGURE 3 | Inertial control structure.

$$\Delta P = \sum_{i=1}^{n} \Delta P_i = \left(\sum_{i=1}^{n} J_i \right) \Delta\omega_g \frac{\mathrm{d}\Delta\omega_g}{\mathrm{d}t} = J_t \Delta\omega_g \frac{\mathrm{d}\Delta\omega_g}{\mathrm{d}t} \tag{11}$$

where J_t is the total rotational inertia of the system.

In order to make the wind turbine inverter simulate the rotational inertia of the conventional synchronous generator, a function can be established by the relationship between the active power output through the inverter and the system frequency and can be expressed as

$$\begin{aligned} \Delta P = \Delta P_{SG} + \Delta P_{Wind} &= \sum_{i=1}^{n} \Delta P_{SG,i} + \sum_{j=1}^{m} \Delta P_{Wind,j} \\ &= \left(\sum_{i=1}^{n} J_{SG,i} + \sum_{j=1}^{m} J_{Wind,j} \right) \Delta\omega_g \frac{\mathrm{d}\Delta\omega_g}{\mathrm{d}t} \end{aligned} \tag{12}$$

where J_{SG} and J_{Wind} denote the total inertia of SG and the virtual inertia simulated by the fan inverter, respectively. n and m are respectively the number of SG and wind turbines.

At this time, the total inertia of the system can be expressed as

$$J_t = \sum_{i=1}^{n} J_{SG,i} + \sum_{j=1}^{m} J_{Wind,j} \tag{13}$$

It can be seen from **Eq. 13** that the total inertia of the system is determined by the two. The rotational inertia of the SG relatively decreases when the proportion of new energy in the power system is higher. If the wind turbine connected to the grid does not have inertia, the total inertia of the system will reduce, thus affecting the decrease of the frequency stability of the system. If the control strategy is used to enable the wind turbine connected to the grid system have virtual inertia, the total inertia momentum of the system will be increased and the frequency stability of the system will be improved.

3.2 Two Classical Inertial Control Strategies

The magnitude of the inertia in the power grid is closely related to the ability to prevent frequency abrupt changes. In conventional maximum power tracking control, the wind turbine only adjusts its active output according to the change of the turbine speed, and when active disturbances occur in the grid, the wind turbine is unable to provide inertia support by adjusting its output power.

3.2.1 Virtual Inertia Control Based on Differential Link

The inertial response is realized by using the differential link, and its controller structure as shown in **Figure 3**. The controller consists of two parts, the upper part is the frequency controller, which enables the wind turbine to change the grid frequency accordingly by attaching a frequency signal to the power reference value. The mathematical model of additional control is

$$P_f^* = -K_{df} \frac{\mathrm{d}\Delta f}{\mathrm{d}t} - K_{pf} \Delta f \tag{14}$$

where K_{df} is the coefficient of the frequency change rate, K_{pf} is the frequency deviation scale factor.

The lower part of the controller is the speed controller, its mathematical model type is

$$P_\omega^* = K_{WP} \left(\omega_e^* - \omega_e \right) + K_{WI} \int \left(\omega_e^* - \omega_e \right) \mathrm{d}t \tag{15}$$

where K_{WP} and K_{WI} are the control coefficients of the PI controller.

It can be seen from **Figure 3** that the total active power output of the system fan under this control is

$$P_{f\omega}^* = P_f^* - P_\omega^* \tag{16}$$

The additional controller based on differential links, as described above, can simulate the inertial response of wind turbines according to the system frequency change rate. When the grid frequency changes, it compensates the power shortage of the system and provides inertial support. However, the additional inertia control interacts with the speed controller in dynamic adjustment, making it difficult to achieve the desired control objectives.

3.2.2 Virtual Inertia Control Based on Power Tracking

The virtual inertia control strategy based on power tracking is optimized based on traditional maximum power tracking control, and alleviates the sudden change of grid frequency through the change of its own rotational speed and kinetic energy, so that the variable speed wind turbine has the ability to support the inertia of the system. The principle block diagram of this control strategy is shown in **Figure 4**. The active power and speed regulation are achieved by changing the scale factor k_{opt} of the maximum power tracking curve.

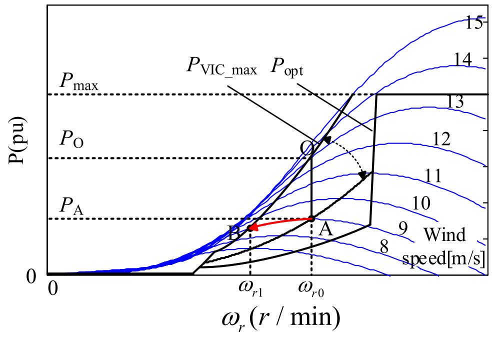

FIGURE 4 | Schematic diagram of power tracking curve switching of virtual inertia.

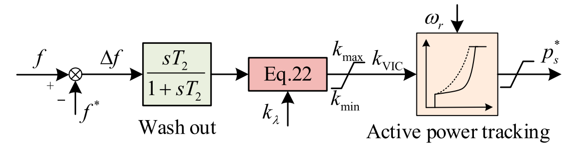

FIGURE 5 | Virtual inertial control structure diagram.

This strategy finds the steady state by power tracking when the wind speed varies, it can improve the stability of the system in the process of speed regulation. When there is a sudden increase in power resulting in a sudden drop in frequency, the fan speed is reduced and released kinetic energy, and the operating state is switched from point A to point B in **Figure 4**, in this transient process, the power at points A and B is approximately equal, that is

$$k'_{\mathrm{opt}}\omega_{\mathrm{r1}}^{3} = k_{\mathrm{opt}}\omega_{\mathrm{r0}}^{3} \tag{17}$$

$$\omega_{\mathrm{r1}} = \omega_{\mathrm{r0}} + \Delta\omega_{\mathrm{r}} = \omega_{\mathrm{r0}} + \lambda\Delta\omega_{\max} = \omega_{\mathrm{r0}} + 2\pi\lambda\Delta f_{\max} \tag{18}$$

where ω_{r0} and ω_{r1} are the rotational speeds corresponding to two points AB respectively.

Therefore, the scale factor of the new power tracking curve can be calculated by the following equation

$$k_{opt}^{*} = \frac{\omega_{ro}^{3}}{\left(\omega_{r0} + 2\pi\Delta f_{\max}\right)^{3}} k_{opt} \tag{19}$$

$$k_{\mathrm{opt\_min}} \le k'_{\mathrm{opt}} \le k_{\mathrm{opt\_max}} \tag{20}$$

According to **Eq. 19**, after introducing the frequency deviation signal, a new maximum power tracking scale factor can be obtained to adjust the speed variation. The amplitude range is limited by the scaling factor k_{opt}, and **Eq. 20** ensures a stable operating point in a wide range of wind speeds. The control takes full advantage of the rapid regulation capability of wind turbines and provides dynamic frequency support for the grid.

4 VIRTUAL INERTIAL CONTROL BASED ON FUZZY LOGIC CONTROL

4.1 Virtual Inertial Control Optimization

The traditional maximum power point tracking of wind turbines depends on the proportional coefficient of the power tracking curve k_{opt}. Wang et al. (2015) provides a detailed analysis of the virtual inertia control based on power tracking, and this paper optimizes the power tracking curve in the virtual inertia control on this basis. The active reference is as follows

$$P_{VIC}^{*} = \begin{cases} k_{VIC}\omega_r^{3} & \omega_0 < \omega_r < \omega_1 \\ \dfrac{\left(P_{\max} - k_{VIC}\omega_1^{3}\right)}{\omega_{\max} - \omega_1}\left(\omega_r - \omega_{\max}\right) + P_{\max} & \omega_1 < \omega_r < \omega_{\max} \\ P_{\max} & \omega_r > \omega_{\max} \end{cases} \tag{21}$$

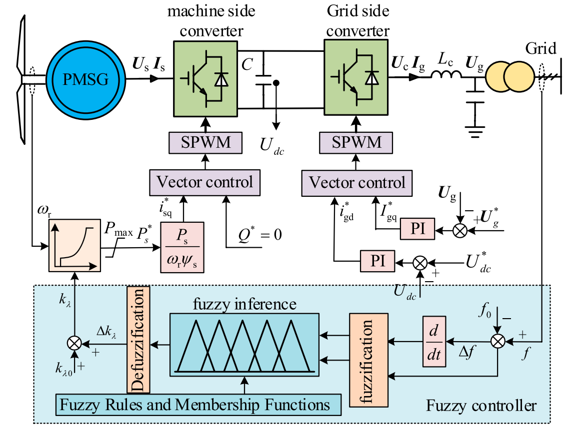

FIGURE 6 | Block diagram of virtual inertial control based on fuzzy control.

$$k_{VIC} = \frac{\omega_{ro}^{3}}{\left(\omega_{r0} + k_{\lambda}\Delta f_{\max}\right)^{3}} k_{opt} \tag{22}$$

where k_{VIC} is the proportional coefficient of the power tracking curve under virtual inertia control and the period value can be adjusted by the system frequency deviation value. k_{λ} can be defined as the frequency adjustment coefficient.

The structure of the virtual inertial controller based on power tracking optimization is shown in **Figure 5**, where the power tracking curve can be recovered with frequency after the inertial response is completed. It can be seen from **Eq. 21** that, the power tracking curve changes with the proportional coefficient k_{VIC}. At the same time, by adjusting its value, the optimal power tracking curve can be found. **Eq. 22** shows that the virtue inertia of the wind turbine, in addition to its own inherent inertia, depends on the angular velocity ω_{r0} of the wind turbine before the frequency change of the system and its frequency regulation factor k_{λ}.

4.2 Basic Vagueness Logic Illusionary Restraint

In view of the above analysis, this paper proposes fuzzy logic control rules for online optimization of the frequency regulation coefficient to improve the inertia support capability of the system. The fuzzy logic controller consists of three parts: fuzzification, fuzzy inference, and defuzzification. The requirement is lower and the control is based on expert experience. As shown in **Figure 6**, the block diagram of virtual inertial control based on fuzzy logic control is constructed.

The input and output of the fuzzy logic controller are exact quantities, and the fuzzy values are obtained after fuzzification. Then the fuzzy values are input to fuzzy inference for processing. Finally, the output quantities can be obtained by defuzzification. When using MATLAB toolbox to build a fuzzy logic controller, it is necessary to design the basic domain of input and output quantities and their corresponding fuzzy subsets, affiliation functions, and to specify the fuzzy rule table. In order to be able to adjust the frequency regulation coefficient more accurately

TABLE 1 | Fuzzy rule table of Δk_λ.

Δk_λ		Δf				
		NB	**NS**	**ZE**	**PS**	**PB**
$\Delta f/t$	NB	NB	NB	NS	NS	ZE
	NS	NB	NS	NS	ZE	PS
	ZE	NS	NS	ZE	PS	PS
	PS	NS	ZE	PS	PS	PB
	PB	ZE	PS	PS	PB	PB

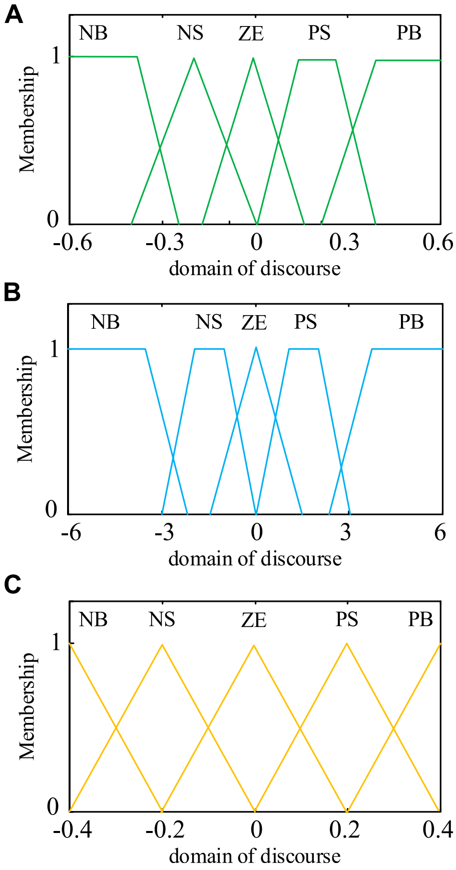

FIGURE 7 | Membership function of each variable. **(A)** The affiliation function of the frequency deviation quantity Δf. **(B)** The affiliation function of the rate of change of frequency $d\Delta f/dt$. **(C)** The affiliation function of the output Δk_λ.

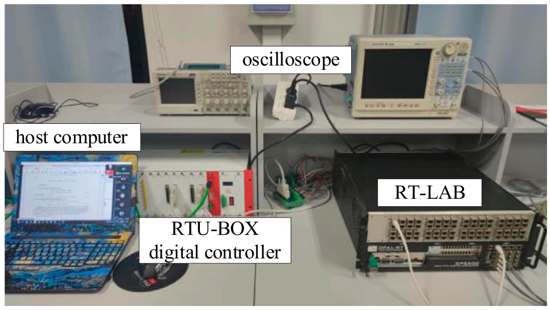

FIGURE 8 | Hardware-in-the-loop real-time simulation experimental platform.

and maximize the optimization effect, this paper takes the frequency deviation amount $\Delta f = f - f_0$ and the frequency change rate $d\Delta f/dt$ as fuzzy input variables and the output variable of the fuzzy controller is Δk_λ. The fuzzy rules are used to adjust the frequency regulation coefficient k_λ online. The fuzzy rule table of Δk_λ is shown in **Table.1**. The table shows that when the system frequency is lower than the rated frequency of 50 Hz, the system frequency change rate is measured. If the change rate is negative, the frequency continues to decrease at this time, and the frequency regulation coefficient k_λ needs to be reduced, and the proportional coefficient k_{VIC} of the power tracking curve is increased by **Eq. 22**, thus increasing the active power from wind turbine and supporting the system frequency, and so on.

The fuzzy linguistic variable intervals are uniformly classified as (NB, NS, ZE, PS, PB) and have five interval subsets of NB (negative big), NS (negative small), ZE (zero), PS (positive small), and PB (positive big). The theoretical domain of the frequency deviation quantity Δf is (−0.6, −0.3, 0, 0.3, 0.6). The theoretical domain of the frequency change rate dΔf/dt is (−6, −3, 0, 3, 6), and the theoretical domain of Δkλ is (−0.4, −0.2, 0, 0.2, 0.4). The affiliation function is to map the input value in the fuzzy domain to an affiliation degree between 0 and 1. The function should be selected according to its selection principle. When the degree of intersection between the functions is large, the fuzzy controller has good robustness and low sensitivity, and when the degree of intersection is small, the sensitivity is high. Therefore, the intersection degree can be adjusted reasonably according to the variation law of input and output variables. In this paper, a combination of triangular and trapezoidal affiliation function is used for the fuzzy input variables, and a simple triangular affiliation function is used for the fuzzy output variables, and then the input and output affiliation functions are derived, as shown in **Figure 7.**

5 EXPERIMENTAL VERIFICATION

5.1 Hardware-in-the-loop Real-Time Simulation Experiment Platform

In order to verify the effectiveness of the virtual inertial control method based on the fuzzy logic method proposed in this paper, a hardware-in-the-loop real-time simulation experiment is built based on the three-machine nine-node test system composed of wind turbines connected to the grid and two synchronous generators. The platform is shown in **Figure 8**. The experimental platform mainly consists of RT-LAB real-time simulator, RTU-BOX real-time digital controller and host computer, etc. Among them, the main topology of the three-machine nine-node test system model is mainly deployed in the RT-LAB real-time simulator, and the control strategies of other wind turbine controls including the grid-side converter and machine-side converter run in the RTU-BOX digital

TABLE 2 | System and control parameters.

Parameter name	Value
Wind turbine rated power P_{PMSG}	1000 MW
Synchronous generators P_{SG1}	1000 MW
Synchronous generators P_{SG2}	400 MW
Wind turbine rated voltage Vnom	690 V
Synchronous generator rated voltage V_{SG}	22 kV
Load P_1	800 MW
Load P_2	500 MW
Load P_3	500 MW
V_{dc_nom}	1200 V
C_1	0.8 mF
L_1	5 mH
$\Delta k_{\lambda 0}$	−0.6

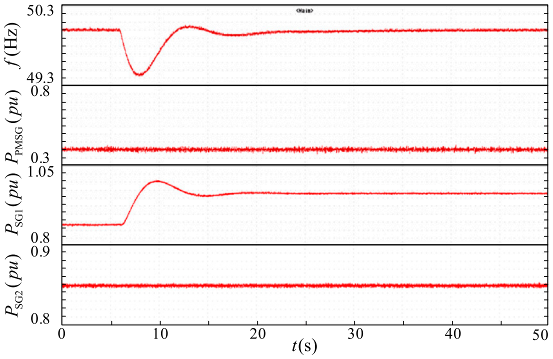

FIGURE 9 | System frequency and output power under MPPT.

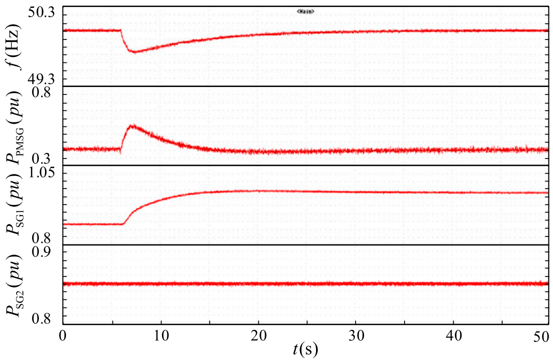

FIGURE 10 | System frequency and output power under the fixed inertia coefficient control.

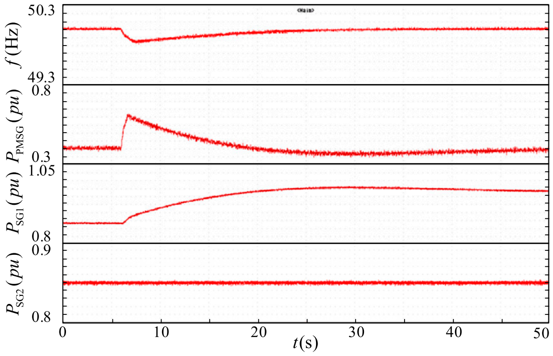

FIGURE 11 | System frequency and output power under the adaptive inertial control based on fuzzy control.

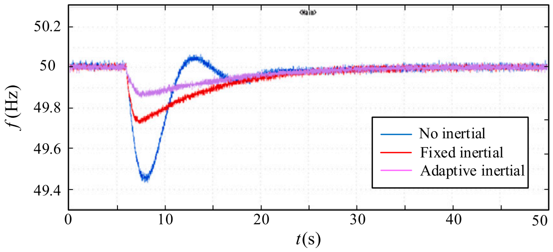

FIGURE 12 | System frequency under different controls.

controller. The controller and the emulator are directly connected to the level conversion board through AD and DA interfaces. The experimental waveforms are recorded by a wave recorder.

In the normal operation of the system, it is known that the total load of the system is 1800 MW, which is shared by the frequency modulation unit SG1, the constant power unit SG2, and the wind turbine. Among them, the frequency modulation unit SG1 is mainly used to provide support for the inertia and frequency of the system; the constant power unit SG2 emits a fixed active power of 400 MW, which is used to simulate the lack of inertia of the system and does not has the ability of frequency regulation. The wind turbine grid-connected system is used to verify the control strategy proposed in this paper. The rated frequency of the system is 50 Hz, and the system and control parameters can be seen in **Table.2**.

5.2 Experimental Verification

In order to verify the virtual inertial control method based on fuzzy logic control proposed in this paper, in the 6th second of the normal operation of the system, a sudden increase of 500 MW load was carried out to test the dynamic response characteristics of this control strategy, and the experimental waveform was observed through a wave recorder.

Figure 9 shows the system frequency and output power waveforms under virtual-free inertia control and MPPT control. As can be seen from the figure, when the load is suddenly increased, the system frequency drops significantly, and the frequency drops to about 49.43 Hz, with a large fluctuation range and small oscillation amplitude. The power is mainly supported by the additional active power generated by the frequency-modulating unit, and the constant power unit SG2 issues constant active power.

Figure 10 shows the system frequency and output power waveforms under the fixed inertia coefficient control. At this time, we can observe the frequency waveform, the system frequency also exists in the case of falling, but compared to the no virtual inertia control, the frequency drop range is significantly lower, only 49.72 Hz. The wind turbine will return to a constant output after the active power rises, which provides a certain support effect for the system frequency.

Figure 11 shows the system frequency and output power waveforms under the adaptive inertial control based on fuzzy logic control. It can be seen from the figure that when the load is suddenly increased, the lowest value of the system frequency is 49.85 Hz, with the smallest range of decline, and the wind turbine sends out a higher active rise and then resumes a constant output.

Comparing the system frequency and output power waveforms under the three control methods, the system frequency decreases under the three different control methods when the system suddenly increases the load, and the corresponding lowest values of frequency are 49.43 Hz, 49.72 Hz, and 49.85 Hz, respectively. Compared with the virtual inertia-free control, the inertia control strategy with a fixed frequency adjustment coefficient can effectively reduce the deviation, and the frequency reduction amplitude is reduced by about 49%. However, compared with the adaptive inertial control based on fuzzy control proposed in this paper, the amplitude of frequency reduction is smaller, and the frequency deviation value is reduced by about 53% compared with the inertial control with a fixed frequency adjustment coefficient. It is obtained from the output power waveform that the adaptive inertia control wind turbine based on fuzzy logic control emits more active power to support the system after a sudden load increase. It can be seen that the method proposed in this paper can significantly improve the system frequency support capability and enhance the system stability. **Figure 12** shows the frequency response waveforms of the system under different controls. It can be seen from the figure that in the case of sudden load increase, the frequency of adaptive adjustment of inertia coefficient based on fuzzy logic control proposed in this paper falls the least and reaches stability as soon as possible, which further verifies the effectiveness of the modified control.

6 CONCLUSION

Due to the increased penetration of wind power in the AC grid, the inertia of the power system is missing, and the frequency problem of the system is affected. Aiming at this problem, this paper proposes a virtual inertial control based on fuzzy logic control. It is used for wind turbine participation in grid frequency support. Based on power tracking, the method uses fuzzy rules to optimize power tracking online, so as to improve system inertia and enhance system frequency support capability. Finally, a hardware-in-the-loop test platform is built based on the 3-machine 9-node test system to verify the effectiveness of the proposed method.

DATA AVAILABILITY STATEMENT

The raw data supporting the conclusions of this article will be made available by the authors, without undue reservation.

AUTHOR CONTRIBUTIONS

QUL, BR, QIL, DW, WT, and XW were responsible for the main writing of the paper. JM conceived the idea for this survey paper. All authors contributed to the article and approved the submitted version.

FUNDING

This work was supported by the Science and Technology Project of State Grid Jiangsu Electric Power Company Limited (J2021177) (Research on the influence mechanism of high aggregation access of offshore wind farms on the inertia of Jiangsu Power grid and key technologies to improve the accommodation capacity).

REFERENCES

Athari, M. H., and Ardehali, M. M. (2016). Operational Performance of Energy Storage as Function of Electricity Prices for On-Grid Hybrid Renewable Energy System by Optimized Fuzzy Logic Controller. *Renew. Energy* 85, 890–902. doi:10.1016/j.renene.2015.07.055

Bao, W., Wu, Q., Ding, L., Huang, S., and Terzija, V. (2021). A Hierarchical Inertial Control Scheme for Multiple Wind Farms with BESSs Based on ADMM. *IEEE Trans. Sustain. Energy* 12 (2), 751–760. doi:10.1109/TSTE.2020.2995101

Chau, T. K., Yu, S. S., Fernando, T. L., Iu, H. H., and Small, M. (2018). A Novel Control Strategy of DFIG Wind Turbines in Complex Power Systems for Enhancement of Primary Frequency Response and LFOD. *IEEE Trans. Power Syst.* 32 (5), 1811–1823. doi:10.1109/tpwrs.2017.2726160

Fang, J., Li, H., Tang, Y., and Blaabjerg, F. (2018). Distributed Power System Virtual Inertia Implemented by Grid-Connected Power Converters. *IEEE Trans. Power Electron.* 33 (10), 8488–8499. doi:10.1109/tpel.2017.2785218

Holdsworth, L., Ekanayake, J. B., and Jenkins, N. (2004). Power System Frequency Response from Fixed Speed and Doubly Fed Induction Generator-Based Wind Turbines. *Wind Energy* 7, 21–35. doi:10.1002/we.105

Karimi, A., Khayat, Y., Naderi, M., Dragicevic, T., Mirzaei, R., Blaabjerg, F., et al. (2020). Inertia Response Improvement in AC Microgrids: A Fuzzy-Based Virtual Synchronous Generator Control. *IEEE Trans. Power Electron.* 35 (4), 4321–4331. doi:10.1109/TPEL.2019.2937397

Kerdphol, T., Watanabe, M., Hongesombut, K., and Mitani, Y. (2019). Self-Adaptive Virtual Inertia Control-Based Fuzzy Logic to Improve Frequency Stability of Microgrid with High Renewable Penetration. *IEEE Access* 7, 76071–76083. doi:10.1109/access.2019.2920886

Kheshti, M., Ding, L., Bao, W., Yin, M., Wu, Q., and Terzija, V. (2020). Toward Intelligent Inertial Frequency Participation of Wind Farms for the Grid Frequency Control. *IEEE Trans. Ind. Inf.* 16 (11), 6772–6786. doi:10.1109/TII.2019.2924662

Lalor, G., Mullane, A., and O'Malley, M. (2005). Frequency Control and Wind Turbine Technologies. *IEEE Trans. Power Syst.* 20 (4), 1905–1913. doi:10.1109/TPWRS.2005.857393

Liu, B., Zhao, J., Huang, Q., Milano, F., Zhang, Y., and Hu, W. (2021). Nonlinear Virtual Inertia Control of WTGs for Enhancing Primary Frequency Response and Suppressing Drivetrain Torsional Oscillations. *IEEE Trans. Power Syst.* 36 (5), 4102–4113. doi:10.1109/TPWRS.2021.3055262

Long, B., Liao, Y., Chong, K. T., Rodriguez, J., and Guerrero, J. M. (2021). Enhancement of Frequency Regulation in AC Microgrid: A Fuzzy-MPC Controlled Virtual Synchronous Generator. *IEEE Trans. Smart Grid* 12 (4), 3138–3149. doi:10.1109/TSG.2021.3060780

Miao, L., Wen, J., Xie, H., Yue, C., and Lee, W.-J. (2015). Coordinated Control Strategy of Wind Turbine Generator and Energy Storage Equipment for Frequency Support. *IEEE Trans. Ind. Appl.* 51 (4), 2732–2742. doi:10.1109/TIA.2015.2394435

Nguyen, H. T., Yang, G., Nielsen, A. H., and Jensen, P. H. (2019). Combination of Synchronous Condenser and Synthetic Inertia for Frequency Stability Enhancement in Low-Inertia Systems. *IEEE Trans. Sustain. Energy* 10 (3), 997–1005. doi:10.1109/tste.2018.2856938

Oshnoei, A., Kheradmandi, M., Muyeen, S. M., and Hatziargyriou, N. D. (2021). Disturbance Observer and Tube-Based Model Predictive Controlled Electric Vehicles for Frequency Regulation of an Isolated Power Grid. *IEEE Trans. Smart Grid* 12 (5), 4351–4362. doi:10.1109/TSG.2021.3077519

Ren, M., Li, T., Shi, K., Xu, P., and Sun, Y. (2021). Coordinated Control Strategy of Virtual Synchronous Generator Based on Adaptive Moment of Inertia and Virtual Impedance. *IEEE J. Emerg. Sel. Top. Circuits Syst.* 11 (1), 99–110. doi:10.1109/JETCAS.2021.3051320

Tan, C., Li, Y., Lan, Q., Xiao, X., Ding, Q., Zhang, X., et al. (2020). Multi-Area Automatic Generation Control Scheme Considering Frequency Quality in Southwest China Grid: Challenges and Solutions. *IEEE Access* 8, 199813–199828. doi:10.1109/ACCESS.2020.3035067

Terazono, D., Liu, J., Miura, Y., Sakabe, S., Bevrani, H., and Ise, T. (2021). Grid Frequency Regulation Support from Back-To-Back Motor Drive System with Virtual-Synchronous-Generator-Based Coordinated Control. *IEEE Trans. Power Electron.* 36 (3), 2901–2913. doi:10.1109/TPEL.2020.3015806

Wang, S., and Tomsovic, K. (2018). A Novel Active Power Control Framework for Wind Turbine Generators to Improve Frequency Response. *IEEE Trans. Power Syst.* 33 (6), 6579–6589. doi:10.1109/TPWRS.2018.2829748

Wang, Y., Meng, J., Zhang, X., and Xu, L. (2015). Control of PMSG-Based Wind Turbines for System Inertial Response and Power Oscillation Damping. *IEEE Trans. Sustain. Energy* 6 (2), 565–574. doi:10.1109/tste.2015.2394363

Yan, W., Cheng, L., Yan, S., Gao, W., and Gao, D. W. (2020). Enabling and Evaluation of Inertial Control for PMSG-WTG Using Synchronverter with Multiple Virtual Rotating Masses in Microgrid. *IEEE Trans. Sustain. Energy* 11 (2), 1078–1088. doi:10.1109/TSTE.2019.2918744

Yap, K. Y., Beh, C. M., and Sarimuthu, C. R. (2021). Fuzzy Logic Controller-Based Synchronverter in Grid-Connected Solar Power System with Adaptive Damping Factor. *Chin. J. Electr. Eng.* 7 (2), 37–49. doi:10.23919/CJEE.2021.000014

Conflict of Interest: Authors QUL, BR, QIL, DW, and WT were employed by the company State Grid Jiangsu Electric Power Company Ltd. Research Institute. Author BR was employed by the company State Grid Jiangsu Electric Power Company Ltd.

The remaining authors declare that the research was conducted in the absence of any commercial or financial relationships that could be construed as a potential conflict of interest.

frontiers | Frontiers in Energy Research

ORIGINAL RESEARCH
published: 11 May 2022
doi: 10.3389/fenrg.2022.908293

A Generic User-Defined Modeling Method in PSS/E and Its Application in an MMC-HVDC System

Lin Zhu[1], Zhigang Wu[1]*, Da Chen[2], Yuchuan Chen[3], Chao Xing[4] and Qing Li[5]*

[1]School of Electric Power Engineering, South China University of Technology, Guangzhou, China, [2]State Grid Jiangsu Electric Power CO., Ltd Extra High Voltage Company, Nanjing, China, [3]Department of Electrical and Computer Engineering, University of Saskatchewan, Saskatoon, SK, Canada, [4]Electric Power Research Institute of Yunnan Power Grid Co., Ltd, Kunming, China, [5]Maintenance & Test Center, CSG EHV Power Transmission Company, Guangzhou, China

This paper studies the user-defined modeling (UDM) method in PSS/E and applies it to a modular multilevel converter high-voltage direct current (MMC-HVDC) system. First, the mechanism of PSS/E UDM is discussed, including the requirements of the model call, storage space allocation, and flows of dynamic simulation. Then, a generic UDM method applicable to various objects is proposed in PSS/E, considering both the internal structures of models and their interfaces with the PSS/E main program. Next, the design of multiple time scales of UDM is presented for hybrid step size simulation. Accordingly, a user-defined MMC-HVDC system model is built in PSS/E considering the converter, DC-line, control system, and system interface. Finally, the model is compared with a PSCAD electromagnetic transient MMC-HVDC model in a modified two-area-four-generator system. The simulation results demonstrate the proposed UDM method.

Keywords: user-defined modeling method, PSS/E, modular multilevel converter highvoltage direct current , electromechanical transient, interface

Edited by:
Kaiqi Sun,
Shandong University, China

Reviewed by:
Changcheng Li,
Guangxi University, China
Zhou Li,
Southeast University, China

****Correspondence:***
Lin Zhu
zhul@scut.edu.cn
Zhigang Wu
epzgwu@scut.edu.cn

Specialty section:
This article was submitted to
Smart Grids,
a section of the journal
Frontiers in Energy Research

Received: *30 March 2022*
Accepted: *26 April 2022*
Published: *11 May 2022*

Citation:
Zhu L, Wu Z, Chen D, Chen Y, Xing C and Li Q (2022) A Generic User-Defined Modeling Method in PSS/E and Its Application in an MMC-HVDC System.
Front. Energy Res. 10:908293.
doi: 10.3389/fenrg.2022.908293

INTRODUCTION

Power system simulation is crucial for system planning, design, and operations; accurate modeling plays a key role in identifying potential system deficiencies. Recently, various power electronics-based devices such as voltage source converter high voltage direct current (VSC-HVDC) and wind power plants have been integrated into grids, presenting a challenge of system simulation and analysis (Liu et al., 2014; Vennelaganti and Chaudhuri, 2018; Li et al., 2019; Wang et al., 2019).

Although simulation toolsets provide various system component models, challenges exist, especially in extending, modifying, and improving the models. UDM is an effective solution that enables users to build, customize and refine models based on users' requirements (Ahn et al., 2013). To cope well with various study cases, users would specify intellectual models that are perhaps not generic or supported by manufacturers.

The benefits of UDM have been studied in previous research (Saeedifard and Iravani, 2010; Peralta et al., 2012a; Peralta et al., 2012b; Xu et al., 2014; Kwon et al., 2017; Tang et al., 2018). Studies in (Xu et al., 2014) show that power system numerical simulations can be extended to MATLAB through UDM. UDM can also facilitate the development of models and control strategies. For instance, (Saeedifard and Iravani, 2010) develops a comprehensive mathematical model based on the negative and positive sequence decomposition technique. (Kwon et al., 2017) shows an improved droop control strategy for stability enhancement of VSC-MTDC systems in PSCAD/EMTDC. A novel topology of modular multilevel converter (MMC)-

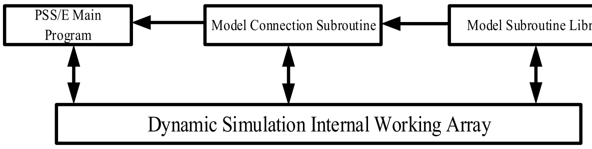

FIGURE 1 | Relationships among different modules associated with UDM.

based distributed power flow controller is proposed in (Tang et al., 2018), providing an alternate method for power flow control. Furthermore, UDM allows considerable features and knowledge based on years of experience or design standardization to be integrated into PSS/E. A new UDM method is proposed in (Peralta et al., 2012a) and further developed in (Peralta et al., 2012b) based on the authors' experience to enable accurate d-q frame VSC modeling in the blocked state.

As widely used in the power system simulation and analysis, PSS/E has been equipped with comprehensive UDM capabilities, which are prevalent in power system studies and result in economical and flexible solutions (Chen et al., 2014; Kwon et al., 2015; Zhang et al., 2015). In (Chen et al., 2014), SVC is modeled as a current source in PSS/E, injecting current into the connected bus to generate a transient response. Further studies in (Zhang et al., 2015) show that the modeling method proposed in (Chen et al., 2014) could apply to HVDC. The correctness of the user-defined CIGRE benchmark HVDC system is demonstrated through comparison with the example file in PSCAD. Moreover, a new controller for HVDC systems is integrated into PSS/E to improve transient variations in the DC voltage and current (Kwon et al., 2015).

The above reviews of UDM in PSS/E only focus on modeling a specific system or improving the response characteristics through PSS/E UDM. To the best of the authors' knowledge, the fundamental nature of UDM in PSS/E, including mechanisms and modeling methods, is still poorly explored. Feature optimization and improvement of model accuracy of UDM in PSS/E also receive little attention.

Therefore, this paper explores the fundamentals of UDM in PSS/E. It studies the UDM mechanism in PSS/E in detail based on high fidelity modeling, including call processing, the storage and sharing of model data. It then proposes a generic UDM method applicable to various model objects. Subsequently, modeling with multiple time scales is achieved to improve accuracy. Finally, a user-defined MMC-HVDC system in PSS/E is modeled and compared with an accurate electromagnetic transient model in PSCAD, and time-domain simulations validate the proposed method.

The rest of this paper is organized as follows. **Section 2** presents the mechanism of UDM in PSS/E. **Section 3** describes the UDM method of PSS/E in depth. **Section 4** implements the detailed modeling of an MMC-HVDC transmission system with the proposed method. In **Section 5**, case studies are presented to verify the proposed method, followed by conclusions.

MECHANISM OF USER-DEFINED MODELING IN PSS/E

The Framework of User-Defined Modeling in PSS/E

By achieving "industry standard" status, PSS/E has developed a natural evolution of organizational structures in response to a very definite power system simulation need. Due to space limitations, this study focuses on UDM, explaining how UDM works and interacts with PSS/E main program. **Figure 1** is the framework describing relationships among different modules associated with UDM.

Users can design a wide range of constitutive models in PSS/E, when a standard library model cannot meet their requirements. User-defined models are recommended to be programmed in Fortran, compiled as a dynamic link library (DLL), added to the PSS/E working directory, and loaded by the main program.

The object subroutine library is the core of UDM and is also a sequence of models, carrying specific properties of the objects of interest. Usually, we use differential algebraic equations (DAEs) to describe equipment dynamics and build custom control blocks. However, these cannot be called directly by the PSS/E main program, as shown in **Figure 1**. Instead, this library needs to cooperate with other subroutines during the transient simulation process.

CONEC and CONET are a set of connection subroutines that link equipment models and their data with network elements. The model connection subroutines are specifications that prescribe a set of routines for performing common operations, such as calling a user-defined model from the model library and solving DAEs to update variables. In other words, the model connection subroutines bridge the gap between the PSS/E main program and the user model. These models require user designs for input and output flow. They are also a sequence of Fortran CALL statements connecting models from the PSS/E model library to network components.

The internal working arrays are responsible for storing and sharing data involved in UDM and participate in every single stage, including definition, connection, and calculation. The types of data involved in dynamic simulation calculations can be divided into four categories: constants, state variables, algebraic variables, and input variables. Obviously, one specific kind of internal working array corresponds to one specific type of data. Some general-purpose storage arrays bear the responsibility of storing model parameters in the model subroutine, while the interface arrays are designed for the network solutions in the main program. Furthermore, PSS/E specifies the location of one specific model through the storage locations reserved for that model reference during the model connection stage.

Requirements of Model Call and Storage Space Allocation

Figure 1 shows that internal working arrays associate with all of the other modules in UDM. During a simulation, the implementation of model functions often requires the call of

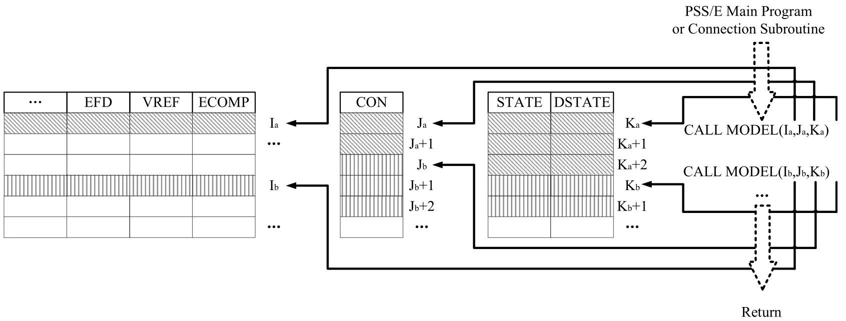

FIGURE 2 | Mechanisms for storage space allocation of internal arrays in PSS/E. The flow of dynamic simulation for UDM

TABLE 1 | Functions of MODE in PSS/E.

Flag	Value	Stage
MODE	1	The initialization of arrays and variables
	2	The integral calculation, the results of which are placed into the DSTATE array
	3	Each model must compute the present value of its output and place it in the specialized arrays
	4	Setting maximum number of integrators
	5	Writing the report of model data
	6	Writing the record of model data
	7	Checking the model parameters
	8	Explanations of parameters applied to user-defined model

relevant data and the return of calculation results. These data or results are stored in a group of named arrays, related to buses, machines, and loads. These quantities, such as VOLT, BSFREQ, MBASE, etc., are frequently needed as inputs and outputs in setting up and displaying the results of dynamic simulations (Siemens, 2013). User-defined models can access these quantities through the bus, machine, and load numbering sequences. There are also four general-purpose storage arrays: CON stores the model parameters that do not vary during the simulation, VAR stores the algebraic variables, STATE stores the state variables determined by differential equations, and DSTATE stores the state variable derivatives versus time.

Generally, the modeling of a complete system comprises numerous models in the PSS/E model library and user-defined model. The respective functions of these models are completed through the data call and the return of results. This process requires assigning individual spaces to each model and calling these data according to the types. Taking the storage space allocation of two user-defined models as an example, as shown in **Figure 2**, from the perspective of a single user-defined model A, different types of data are allocated in the corresponding locations of arrays using array indexes Ia, Ja, and Ka. For example, the EFD, VREF, and ECOMP arrays use index Ia, the CON array uses index Ja, while the STATE and DSTATE arrays use index Ka. As for the storage space allocation of two user-defined models, we only discuss the CON array; the other arrays are similar. Supposing that the location of the CON array in user-defined model A starts at Ja and ends at Ja+1, then the location of the CON array in user-defined model B starts at Jb, and the next locations are Jb+1, Jb+2, and so on.

Understanding the requirements of models in PSS/E is necessary whenever a new user-defined model is required. Each model completes different types of computations at different stages in the dynamic simulation process. As a result, a set of flags are used to communicate among PSS/E dynamic simulation activities. The simulation flag MODE varies from 1 to 8 and suits individual needs, as shown in **Table 1**.

Stages represented by MODE 1 to MODE 8 are not all cyclically executed in each step during the simulation. When a user-defined model participates in simulation, MODE 1, 4, and 8 are executed only once during its initialization. On the contrary, MODE 2 and MODE 3 are dominant and are executed circularly in the user-defined model. MODE 7 checks the model parameters just after the dynamic data file is loaded. MODE 5 and MODE 6 are executed optionally, if necessary. Here, we only discuss the stages represented by MODE 1, 2, 3, 4, and 8. The primary flow of dynamic simulation based on MODE is shown in **Figure 3**.

USER-DEFINED MODELING METHOD IN PSS/E

In this section, we propose a generic UDM method after identifying the mechanism of UDM in PSS/E in **Section 2**. The proposed method is well designed and easily coordinated with various objects. This method is composed of two main parts: the reasonable description of the internal structure and arranging the interface between the model output and PSS/E main program.

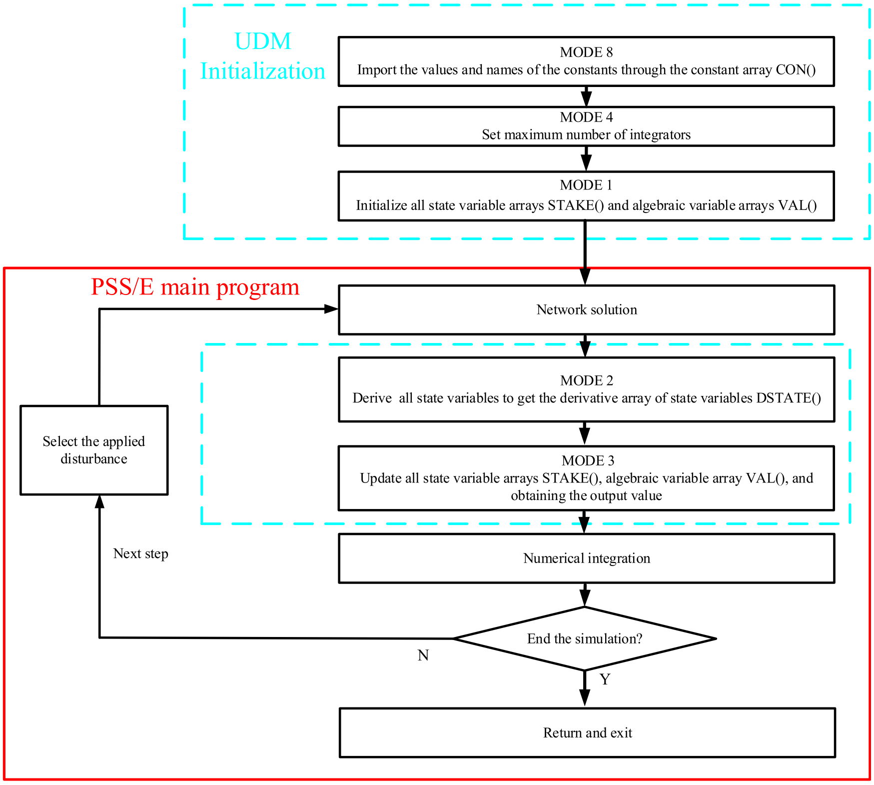

FIGURE 3 | Flow of dynamic simulation based on MODE.

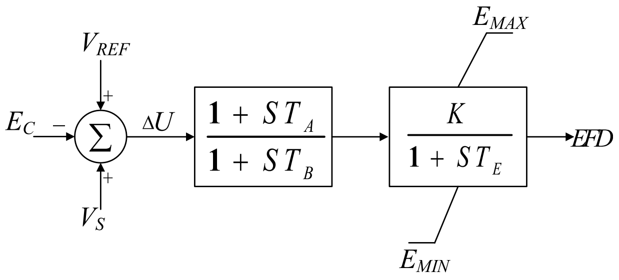

FIGURE 4 | The control block of SEXS.

Realization of the Internal Structure

The core of this part is making clear the DAEs of an object and writing the responding subroutine to meet the requirements of UDM. Users need to analyze the DAEs first and confirm how many constant parameters, algebraic variables, and state variables relevant to the model are used, and distribute space in the CON, VAR, and STATE arrays by rules. Here, we consider the excitation system model 'SEXS' in the standard model library as an example.

As can be seen from the control block in **Figure 4**, the model is mainly composed of a lead-lag block and an inertia block. Suppose that the state variable in relation to the lead-lag block is E_1, and the state variable in relation to the inertia block is E_2. The allocation of storage space for constant parameters, state variables, and algebraic variables is shown in **Table 2**.

The definition of arrays from CON(J) to CON(J+5) is carried out in MODE 8, and the number of state variables is subsequently updated in MODE 4. In the meantime, the initial values of the input, output, and state variables are confirmed through the power flow results in MODE 1. That is to say, we can obtain initial values of ECOMP(I), VREF(I), VOTHSG(I), and EFD (I) from the main program. Then the initial values of STATE(K) and STATE (K+1) can be determined through the logical relations among state variables, inputs, and outputs. The characteristic equations and DAEs representing the control system are written in the frequency domain in MODE 2. The decomposition of the first lead-lag block is shown in **Figure 5**.where E_1 is set as STATE(K) and its derivative is stored in DSTATE(K), which can be expressed as:

$$\boldsymbol{STATE}(\boldsymbol{K}) = \Delta \boldsymbol{U}\left(\frac{1-\frac{\boldsymbol{T_a}}{\boldsymbol{T_b}}}{1+\boldsymbol{T_b}}\right) \tag{1}$$

$$\boldsymbol{DSTATE}(\boldsymbol{K}) = \frac{\Delta \boldsymbol{U}\left(1-\frac{\boldsymbol{T_A}}{\boldsymbol{T_B}}\right)-\boldsymbol{E}_1}{\boldsymbol{T_B}} \tag{2}$$

The output of the second lag block E_2 is set as STATE (K+1), and DSTATE (K+1) is handled similar to DSTATE(K). Finally, the values of the above state variables and algebraic variables are updated in MODE 3.

TABLE 2 | Storage allocation of array for SEXS.

Constant Parameter	Stored Value	State Variable, Input, and Output	Stored Value
CON(J)	T_A	STATE(K)	E_1
CON(J+1)	T_B	STATE (K+1)	E_2
CON(J+2)	K	ECOMP(I)	E_C
CON(J+3)	T_E	VREF(I)	V_{REF}
CON(J+4)	E_{MAX}	VOTHSG(I)	V_S
CON(J+5)	E_{MIN}	EFD(I)	EFD

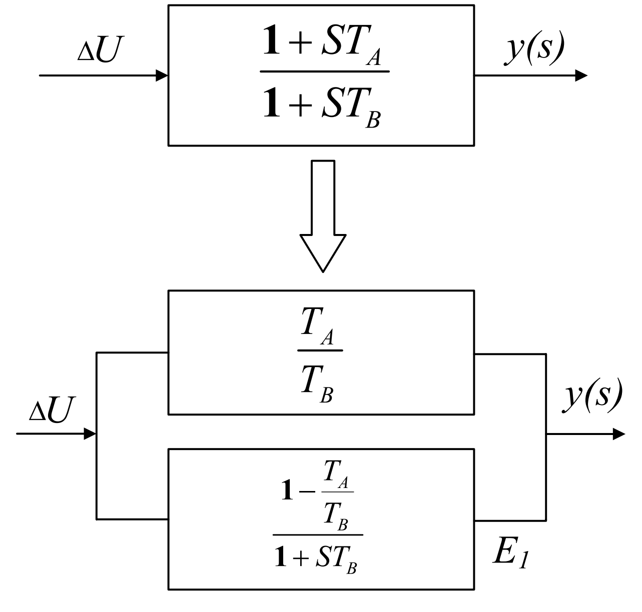

FIGURE 5 | Decomposition of lead-lag control block.

The Interface Between the User-Defined odel and PSS/E Main Program

An interface can connect the user-defined model and PSS/E main program. This interface is a shared boundary during simulation across which the user-defined model and PSS/E main program exchange information. The interface is not necessarily the same for all dynamic models because some models' outputs must match with specific internal working arrays in the data library of PSS/E. In other words, these specific internal working arrays act as protocols to receive and send data. The excitation system of the generator, prime mover, and governor are typical representations. Again, taking the exciter as an example, the output variable excitation voltage is stored in the EFD array, which can be recognized and called by the main program directly. These internal working arrays serve as the interface and make interacting with the user-defined model and PSS/E main program easier.

On the other hand, no internal working arrays correspond to the physical variables represented by the models' outputs for a flexible alternating current transmission system (FACTS), HVDC, or other complex electrical devices. Under these circumstances, the outputs cannot be directly recognized or called by the main program. Usually, an electrical device or component impacts the system at the connected bus by injecting power while the system provides a voltage that affects the dynamics of the component. Converting the injecting power into the equivalent current is advised not to lose impact at the connected bus. Consequently, the output as the injected current can be stored in the internal working array CURNT. This interface is established as shown in **Figure 6**.

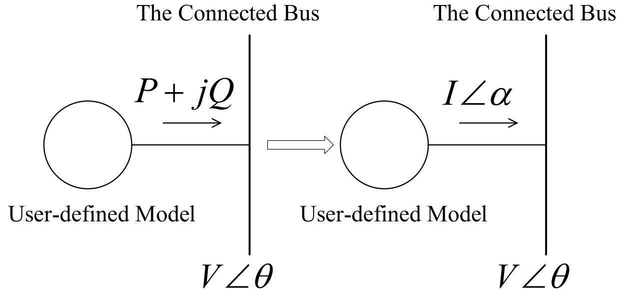

FIGURE 6 | Interface of user-defined model.

Realization of Modeling With Multiple Time Scales

A power system is a large-scale nonlinear system with high complexity, consisting of a large number of variables with different time constants. Some of the variables change rapidly, whereas others change relatively slowly. In this scenario, multiple time scales can characterize the power system. PSS/E mainly concentrates on electromechanical transients of power systems with a large step size, such as a half-circle; this is widely accepted, especially in AC systems. With full use of power electronic devices such as HVDC and FACTS, these models need a smaller step size than AC devices for precision. The contradiction arises when there is a large fixed step size and requirements for precision without additional computational burden. This section will discuss multiple time scales in UDM for higher accuracy.

The PSS/E main program performs data interactions with the user-defined model during each iteration of each step. When the user-defined model performs the internal calculation, the main program waits until the calculation ends. During this period, the value of the user-defined model imported by the main program

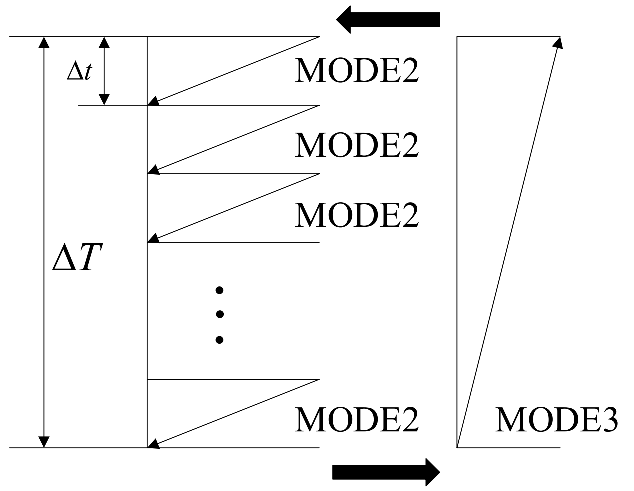

FIGURE 7 | Realization mechanism of modeling with multiple time scales.

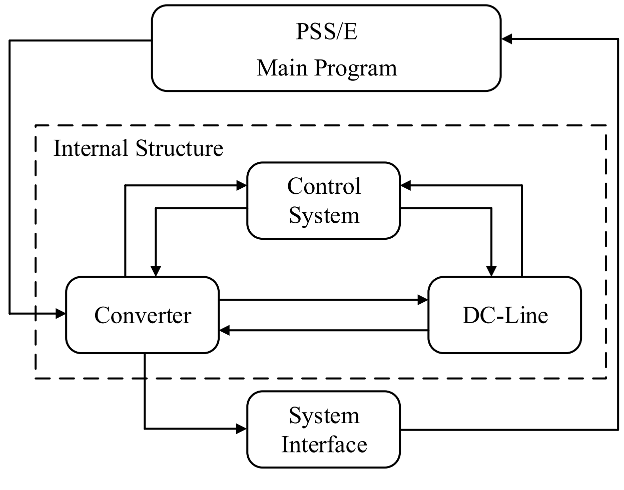

FIGURE 8 | Diagram of the modeling of an MMC-HVDC system.

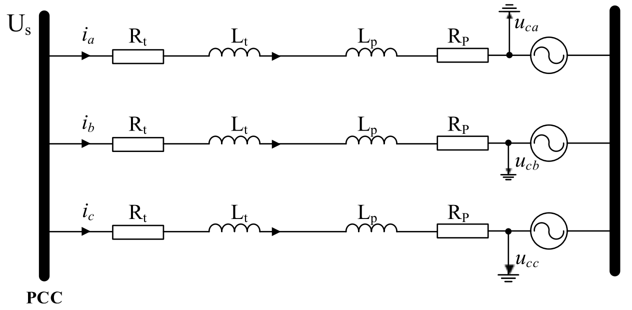

FIGURE 9 | The equivalent structure of a single MMC on the AC side.

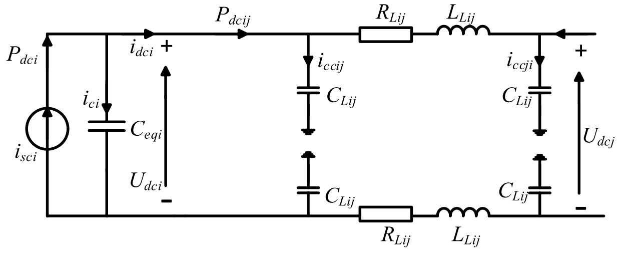

FIGURE 10 | Equivalent circuit of the DC-line.

maintains the current value. Once the calculation of the user-defined model is finished, the main program continues, and the user-defined model passes the results to the main program as a fixed value in the subsequent cycle of calculation.

According to the characteristics of the user-defined model, the entire calculation process is independent of the main program. The interface between the main program and the user-defined model is only for data transmission and does not affect the respective simulation processes. Therefore, a simulation with a hybrid step size can be realized by modifying the internal calculation process of the user-defined model. One needs to preset a large time step ΔT for the main program of PSS/E and a small time step Δt for the user-defined model (e.g., HVDC system). During the time step ΔT, MODE 2 is executed in loops solving the differential equations according to the ratio of ΔT to Δt, while MODE 3 is executed only once to update the model's output and return it to the main program. The realization mechanism of modeling with multiple time scales is shown in **Figure 7**.

USER-DEFINED MODELING OF AN MODULAR MULTILEVEL CONVERTER -HIGH VOLTAGE DIRECT CURRENT SYSTEM IN PSS/E

This section performs UDM of an MMC-HVDC system with the generic method proposed in this paper. **Figure 8** is a diagram of the modeling of the MMC-HVDC system, which includes four modules: 1) converter; 2) DC-line; 3) control system; and 4) system interface. Modules 1), 2), and 3) are a realization of the internal structure, and module 4) is the interface between the user-defined model and PSS/E main program.

Internal Structure

Converter

The equivalent circuit of a single MMC on the AC side is shown in **Figure 9**, where point of common coupling (PCC) is the converter bus on the network side, R_t and L_t respectively represent the resistance and reactance of the converter transformer, and R_p and L_p respectively represent the resistance and reactance of the bridge arm.

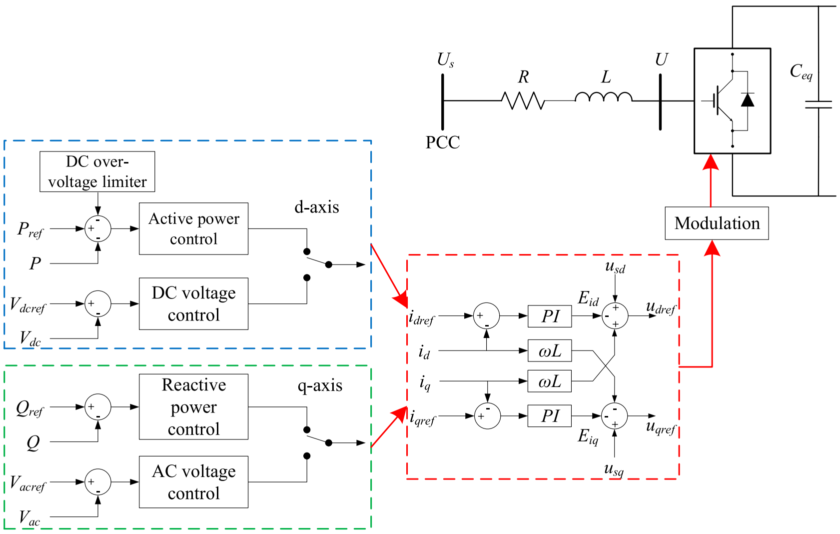

FIGURE 11 | Control architecture of a single MMC.

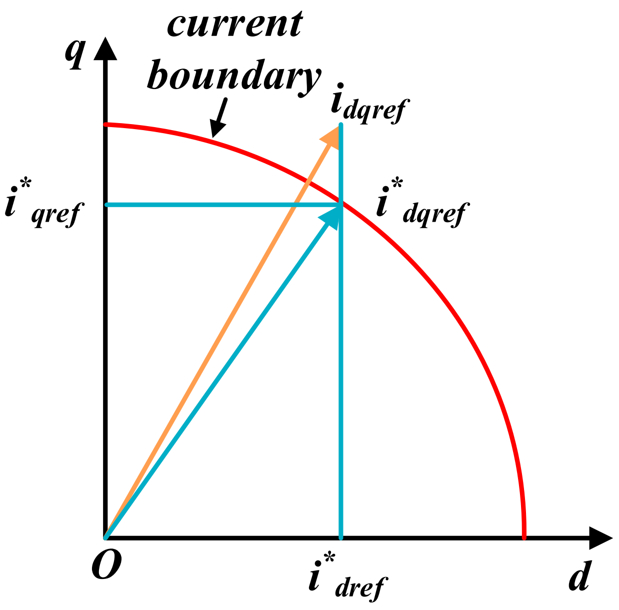

FIGURE 12 | The principle of d-axis priority current limiting.

To facilitate the analysis and independent control of each physical quantity, the three-phase time varying quantities of the MMC-HVDC system are transformed into physical quantities under the d-q rotating coordinate system perpendicular to each other. Assuming that the positive sequence fundamental component of the converter bus voltage is in the same direction as the d-axis, the mathematical model of the voltage source converter at this coordinate is as follows:

$$\begin{cases} \frac{di_d}{dt} = \frac{1}{L}\left(u_{sd} - u_d + \omega L \cdot i_q - R \cdot i_d\right) \\ \frac{di_q}{dt} = \frac{1}{L}\left(u_{sq} - u_q + \omega L \cdot i_d - R \cdot i_q\right) \end{cases} \tag{3}$$

where $L = L_t + L_p$, $R = R_t + R_p$, ω is the fundamental angular frequency of the system, u_{sd} and u_{sq} are respectively the d and q components of the voltage at converter bus, u_d and u_q are respectively the d and q components of the fundamental voltage at the midpoint of the converter bridge arm, and i_d and i_q are respectively the d and q components of the current injected into the converter bus.

DC-Line

This paper uses a π-type circuit to simulate the DC transmission line. The equivalent circuit diagram is shown in **Figure 10**.

In **Figure 10**, the subscript i represents the variable of the MMC$_i$ and Ceq$_i$ is the equivalent sub-module capacitance for six bridge arms of MMC, which can be expressed as:

$$C_{eqi} = \frac{6}{N_{sm}} C_{sm} \tag{4}$$

where C_{sm} and N_{sm} respectively represent the capacitance and number of sub-modules.

For MMC$_i$ on the DC side, the equations are as follows:

$$C_{eqi} \frac{du_{dci}}{dt} = i_{sci} - i_{dci} = i_{ci} \tag{5}$$

where i_{sci} is the total current injected into the DC side of MMC$_i$, and is composed of the current i_{ci} injected into the equivalent capacitor and the current i_{dci} from DC node i to DC node j.

For the DC-line from i to j, the equations are as follows:

TABLE 3 | Storage allocation of CON array for MMC-HVDC.

Constant Parameter	Stored Value
CON(J)~CON(J+3)	Proportional gains of d/q axis PI controller in outer loop
CON(J+4)~CON(J+7)	Integral time constants of d/q axis PI controller in outer loop
CON(J+8)~CON(J+15)	Upper and lower limits of d/q axis PI controller in outer loop
CON(J+16)~CON(J+17)	Upper and lower limits of DC over-voltage limiter
CON(J+18)~CON(J+21)	Proportional gains of d/q axis PI controller in inner loop
CON(J+22)~CON(J+25)	Integral time constants of d/q axis PI controller in inner loop
CON(J+26)~CON(J+33)	Upper and lower limits of d/q axis PI controller in inner loop
CON(J+34)~CON(J+37)	Time constants of d/q axis modulation controller
CON(J+38)~CON(J+39)	Current boundaries of current limiter
CON(J+40)~CON(J+41)	Capacitances of sub-modules
CON(J+42)~CON(J+44)	Resistance, inductance, and capacitance of DC-line
CON(J+45)~CON(J+46)	Equivalent resistance and inductance of an MMC on AC side

TABLE 4 | Storage allocation of STATE array for MMC-HVDC.

State Variable	Stored Value	State Variable	Stored Value
STATE(K)~STATE (K+1)	i_{dref}	STATE (K+10)~STATE (K+11)	E_{iq}
STATE (K+2)~STATE (K+3)	i_{qref}	STATE (K+12)~STATE (K+13)	i_d
STATE (K+4)~STATE (K+5)	u_d	STATE (K+14)~STATE (K+15)	i_q
STATE (K+6)~STATE (K+7)	u_q	STATE (K+16)~STATE (K+17)	u_{dc}
STATE (K+8)~STATE (K+9)	E_{id}	STATE (K+18)~STATE (K+19)	i_{dc}

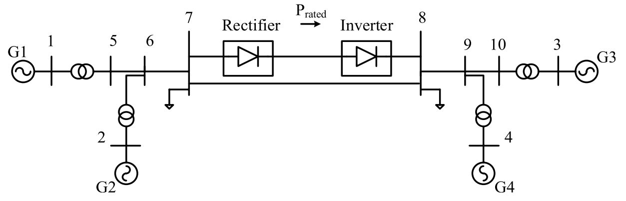

FIGURE 13 | Test system.

$$C_{Lij}\frac{d\left(u_{dci}/2\right)}{dt} = i_{ccij} \tag{6}$$

$$L_{Lij}\frac{d\left(i_{dci} - i_{ccij}\right)}{dt} = \frac{u_{dci} - u_{dcj}}{2} - R_{Lij}\left(i_{dci} - i_{ccij}\right) \tag{7}$$

where C_{Lij}, L_{Lij}, and R_{Lij} are respectively the capacitance, inductance, and resistance of the DC-line and i_{ccij} is the current injected into the capacitor of the DC-line.

Control System

The basic controller of a single MMC in the HVDC system is shown in **Figure 11**, and consists of inner and outer control loops accompanied by a modulation controller. Consider the presence of certain time lags when u_d and u_q track u_{dref} and u_{qref}:

$$u_d = \frac{u_{qref}}{1 + sT_v} \tag{8}$$

$$u_d = \frac{u_{qref}}{1 + sT_v} \tag{9}$$

Considering that the outer loop controller may generate excessive reference current even beyond the physical tolerance of the valve when the system is undergoing disturbances, a current limiting link should be added between the outer loop controller and the inner loop controller. This paper adopts the d-axis priority current limiting mode, as shown in **Figure 12** (Giroux and Sybille, 2006).

System Interface

According to the above details, the system interface of an MMC-HVDC system should be achieved through CURNT, which is an internal array loading the injection current data and feeding it back to the network for calculation. The model output needs to be converted into the current injection in accordance with the format of CURNT, which is composed of real and imaginary components. The converter equation shows that the outputs are i_{sd} and i_{sq} in the *d*-*q* rotating coordinate system. Therefore, it is necessary to perform a coordinate transformation to obtain the current in the *x*-*y* stationary reference frame. The *d*, *q* components of the current mentioned above are converted into P, Q, and then we can get the *x*, *y* component of the current as shown in **(Eq. 10)**:

$$\begin{cases} i_x = Re\left(|u_s| \cdot i_d - j|u_s| \cdot i_q\right)^* \Big/ u_s^* \\ i_y = Im\left(|u_s| \cdot i_d - j|u_s| \cdot i_q\right)^* \Big/ u_s^* \end{cases} \tag{10}$$

where i_d and i_q are the same as those in **(Eq. 1)**; i_x and i_y are the x and y components of the current injected into converter bus, respectively; u_s is the voltage vector at the converter bus; *j* is the imaginary unit; and Re and Im respectively represent the real and imaginary parts of the vector.

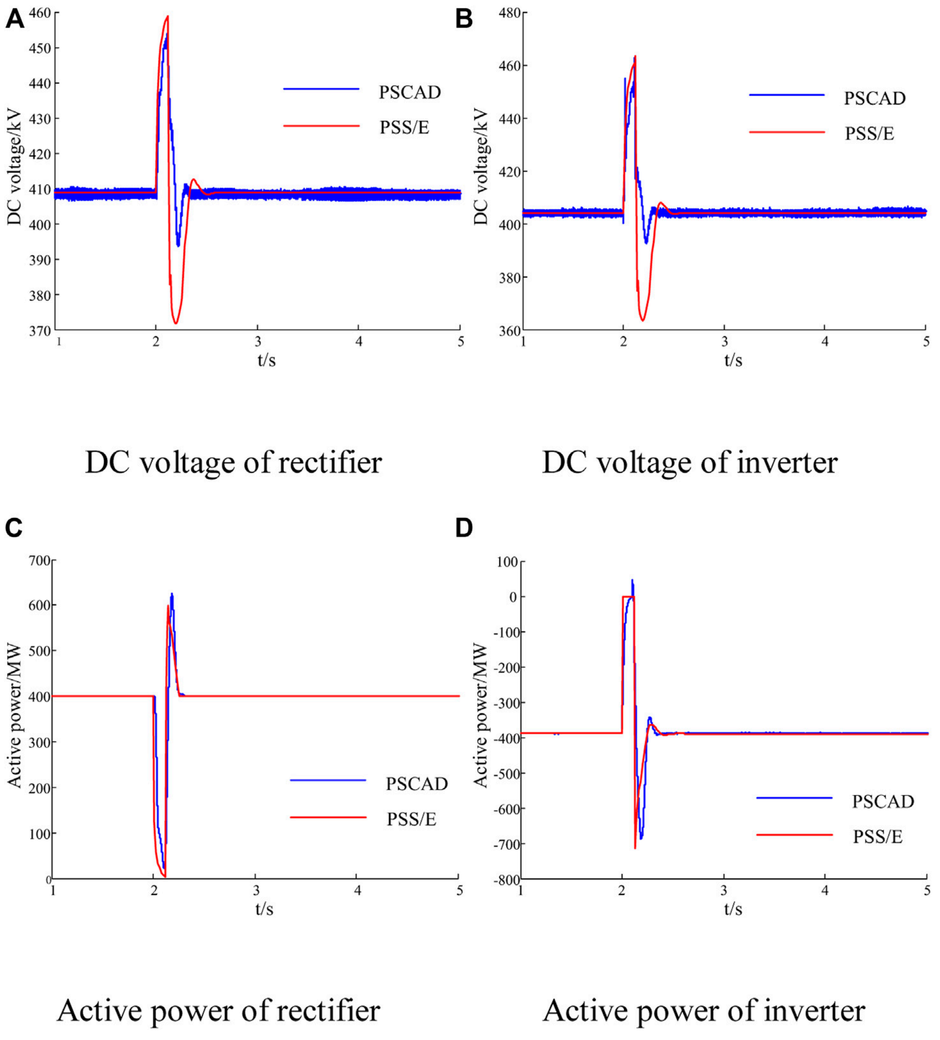

FIGURE 14 | Dynamic response of the MMC-HVDC system in PSCAD and PSS/E. **(A)** DC voltage of rectifier **(B)** DC voltage of inverter. **(C)** Active power of rectifier **(D)** Active power of inverter.

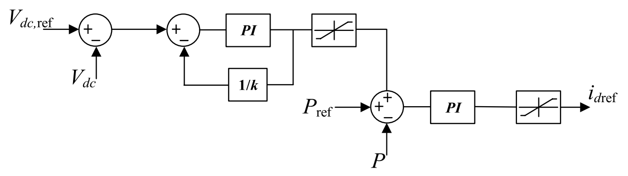

FIGURE 15 | Control architecture of user-defined auxiliary controller.

When a fault is applied to the system, the MMC-HVDC system will change the output current value so as to control the active power, DC voltage, and bus voltage. The implementation of the process is shown as follows:

$$\boldsymbol{CURNT}(\boldsymbol{I})_{n+1} = \boldsymbol{CURNT}(\boldsymbol{I})_{n} + \left(\boldsymbol{i}_x + \boldsymbol{j}\cdot \boldsymbol{i}_y\right) \tag{11}$$

where $CURNT(I)_{\mathrm{n}}$ and $CURNT(I)_{\mathrm{n+1}}$ are current injection value in the N-th time step and the next time step, respectively; I is the number of the converter bus; and i_{x} and i_{y} are the x and y components of the current injected into the converter bus, respectively.

Detailed Modeling Procedure

In summary, in MODE 8 the CON array allocates storage for constants such as gains and time constants of control blocks, resistances and capacitances of the DC-line, etc. The detailed allocation of storage space for constant parameters is shown in **Table 3**. Subsequently, the maximum number of integrators is set to 20 according to the number of state variables in MODE 4. The state variables involved in the MMC-HVDC system are mainly the outputs of PI controllers, DC voltages, DC currents, and valve currents. The allocation of storage space for state variables is shown in **Table 4**. All of the above variables are initialized using the steady-state solutions of the AC and DC networks in MODE 1.

After initialization, we can handle the DAEs of converters, DC-line, outer loop, inner loop, and modulation controller. In

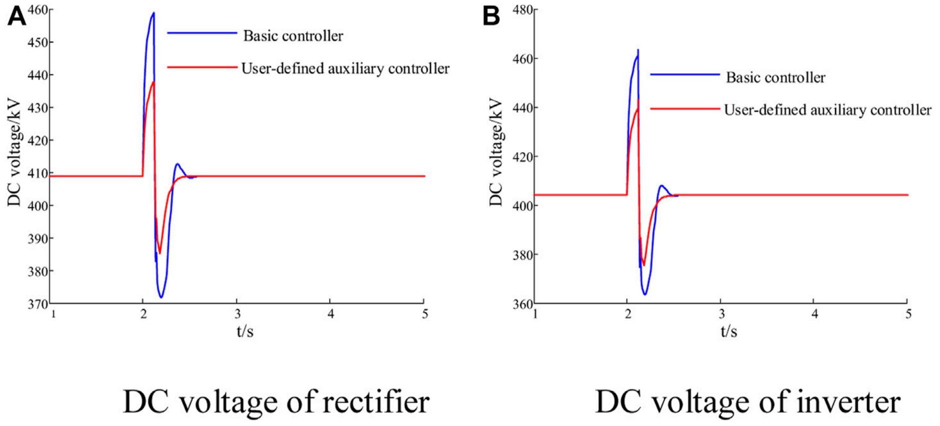

FIGURE 16 | Dynamic response of the MMC-HVDC system with two different controllers in PSS/E. **(A)** DC voltage of rectifier **(B)** DC voltage of inverter.

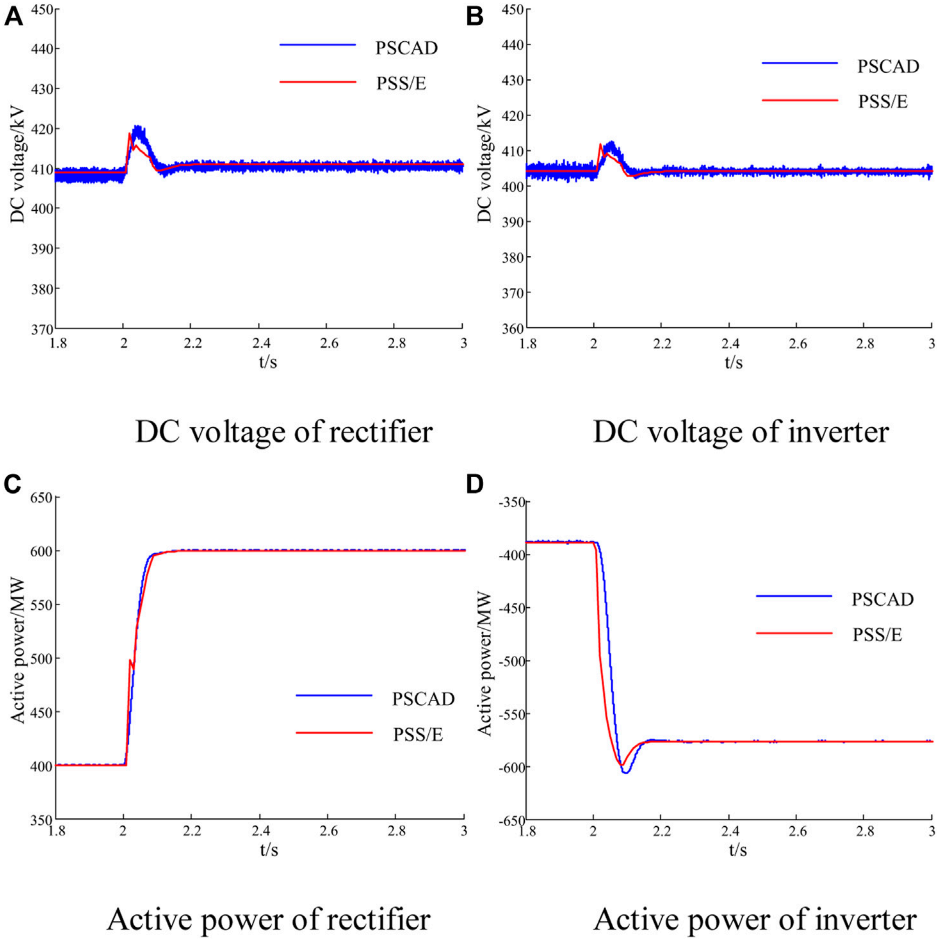

FIGURE 17 | Dynamic response of MMC-HVDC in Case 3. **(A)** DC voltage of rectifier **(B)** DC voltage of inverter. **(C)** Active power of rectifier **(D)** Active power of inverter.

MODE 3, the output quantities such as active power, reactive power, and DC voltage, etc., are updated. These quantities are then delivered to MODE 2 as inputs of the DAEs. In MODE 2, derivatives of the state variables in the DAEs are confirmed and stored in DSTATE arrays. Through integral calculation, the valve currents and DC voltages are finally delivered to MODE

3 again to update the output quantities. Considering that the transient simulation of the MMC-HVDC system is in need of hybrid time steps, during a single time step MODE 2 is executed in loops to solve the DAEs as presented in **Section 3** while MODE 3 is executed only once to update the output of the model. MODE 2 and MODE 3 are executed in turns until the simulation ends. As for the system interface, the update of CURNT is implemented through writing the codes in the form of auxiliary functions in MODE 3. In this way, the internal structure and dynamics of the MMC-HVDC system are successfully presented.

STUDY CASES

Test System and Simulation Conditions

A modified two area-four generator system is used to validate the proposed method and MMC-HVDC user-defined model, as shown in **Figure 13**. The rated active power of the MMC-HVDC system is 400 MW, and the AC transmission line transfers 200 MW of active power from bus 7 to bus 8. The rated DC voltage of the MMC-HVDC system is 400 kV; other detailed parameters of the test system are from (Kundur et al., 1994).

This section builds the user-defined electromechanical model of MMC-HVDC in PSS/E and compares performance with the accurate electromagnetic transient model in PSCAD. The simulation step sizes are 200us in PSCAD and 10 ms in PSS/E.

Transient Simulation and Comparison

Case 1: MMC-HVDC systems with controls are modeled separately in PSCAD and PSS/E. The model in PSCAD is accurate and acts as the reference. The rectifier controls the active power and the AC voltage, while the inverter controls the DC voltage to the set point and the AC voltage. At 2.0 s, an instant three-phase fault is applied to bus 8 then cleared 0.1 s later. **Figure 14** shows responses of the DC voltage and active power.

As shown in **Figure 14**, the DC voltage and active power are almost the same in PSCAD and PSS/E in the steady states. Even during the transient process, the largest mismatch is less than 0.1 p.u. This demonstrates that the dynamic responses of the models in PSS/E and PSCAD coincide well. Although the results in PSCAD contain some high-frequency oscillations, the effect of the oscillation on the transient stability is clearly restricted. The main differences between the two models lie in the fact that the electromechanical transient model only considers the fundamental wave. However, the electromagnetic transient model takes the high-frequency component into consideration.

Case 2: According to the above results, the stability of the DC voltage during transient simulation can be further improved. The extensibility of UDM is illustrated with a user-defined auxiliary controller added to the above MMC-HVDC model in PSS/E. The controller, the structure of which is shown in **Figure 15**, is proposed in (Stamatiou and Bongiorno, 2017) and has been proven effective. The rectifier and inverter both select the user-defined auxiliary controller, and they still control the AC voltage simultaneously. The same fault is applied again, with the results of models with the basic controller and user-defined controller in PSS/E shown in **Figure 16**.

During the transient process, the DC voltage of the model with the user-defined controller fluctuates in a smaller range and recovers faster compared with the basic controller. The flexibility of UDM is highlighted.

Case 3: A severe permanent trip-line fault is executed in both PSCAD and PSS/E further to test the performance of the user-defined MMC-HVDC system. A three-phase permanent fault is applied to bus 8 at 2.0 s, and the AC transmission line from bus 7 to bus 8 is permanently tripped 0.1 s later. Regarding the flexibility of the MMC-HVDC system, the set point of the active power at the rectifier is increased from 400 to 600 MW to make up the power shortage. **Figure 17** shows the active power and DC voltage responses in Case 3.

Figure 17 shows that the results in both PSS/E and PSCAD still match with negligible error in terms of magnitude and phase. The rectifier rapidly follows the change of power set point and reaches the new stable condition of 600 MW at about 2.1 s. At the same time, the inverter still controls the DC voltage at the initial set point after the fluctuation of power due to constant DC voltage control. As a result, the whole system is stable again with the adjustment of the MMC-HVDC system. The controllability and validity of the user-defined MMC-HVDC system model are thus again verified. This approach can be applied to extend various complex models.

The efficiencies of PSS/E built-in models, the user-defined model with a basic controller, and the user-defined model with an auxiliary controller are also compared. The simulation is carried out on a platform featuring an Intel i5 CPU with 8 GB of RAM and employing PSS/E version 33.04. In conclusion, the user-defined models in PSS/E are all highly efficient and applicable to large-scale power systems.

CONCLUSION

In this paper, the mechanism of UDM in PSS/E is thoroughly investigated, including requirements of model call, storage space allocation, and flows of dynamic simulation for UDM The proposed method can effectively deal with the internal dynamic of a user-defined model and the interface between a user-defined model and PSS/E main program. The design of multiple time scales is proposed to meet the requirement of hybrid simulation steps. The significant contribution of this paper is the UDM method, which is suited to various objects in PSS/E. Following this method, a user-defined MMC-HVDC system model is presented in PSS/E and compared with the accurate electromagnetic transient MMC-HVDC model in PSCAD on a modified two area-four generator system. Detailed case studies show the validity of the proposed method and the user-defined MMC-HVDC model. Notably, a user-defined auxiliary controller based on users' insight demonstrates the benefits of UDM, which shows the flexibility and extension for individual requirements. All results indicate that the proposed generic UDM method in PSS/E is efficient and fulfills requirements for model expansion, modification, and improvement.

DATA AVAILABILITY STATEMENT

The original contributions presented in the study are included in the article/Supplementary Material, further inquiries can be directed to the corresponding authors.

AUTHOR CONTRIBUTIONS

LZ and DC conceived of the presented idea. ZW contributed significantly to analysis and manuscript preparation. CX and QL carried out the experiments. DC and YC verified the analytical methods. LZ and ZW took the lead in writing the manuscript. All authors discussed the results and contributed to the final manuscript.

FUNDING

This study received funding from China Southern Power Grid Company Limited (No. GDKJXM20198236). The funder was not involved in the study design, collection, analysis, interpretation of data, the writing of this article or the decision to submit it for publication. All authors declare no other competing interests.

REFERENCES

Ahn, S., Choi, J., Go, S., Jung, W., Il-Keun, S., and Dong-Jun, W. (2013). "Development of Simulation Platform of Distribution Systems with DGs and SVR for Voltage Control Studies," in 2013 IEEE Power & Energy Society General Meeting (PESGM), Vancouver, BC, Canada, 1–5.

Chen, Y., Zhu, L., Yang, H., Cai, Z., and Li, S. (2014). "User-defined Modeling of Static Var Compensation for Electromechanical Transient Simulation in PSS/E," in 2014 IEEE PES Asia-Pacific Power and Energy Engineering Conference (APPEEC), Hong Kong, China, 1–6. doi:10.1109/appeec.2014.7066095

Giroux, P., and Sybille, G. (2006). *Static Synchronous Compensator (STATCOM) Used for Midpoint Voltage Regulation on a 500kV Transmission Line*. Natick, MA: The MathWorks, Inc.

Kundur, P., Balu, N. J., and Lauby, M. G. (1994). *Power System Stability and Control*. New York: McGraw-Hill.

Kwon, D., Kim, Y., Moon, S., and Kim, C. (2017). Modeling of HVDC System to Improve Estimation of Transient DC Current and Voltages for AC Line-To-Ground Fault-An Actual Case Study in Korea. *Energies* 10, 1543. doi:10.3390/en10101543

Kwon, D., Moon, H., Kim, R., Kim, C., and Moon, S. (2015). "Modeling of CIGRE Benchmark HVDC System Using PSS/E Compared with PSCAD," in 2015 5th International Youth Conference on Energy (IYCE), Pisa, Italy, 1–8. doi:10.1109/iyce.2015.7180781

Li, B., Liu, Y., Li, B., Hong, C., Zhang, Y., and Yang, J. (2019). Computationally Efficient Modeling Method of MMC Based on Arm Equivalent Time-Variant Capacitance. *Int. Trans. Electr. Energ Syst.* 29, e2732. doi:10.1002/etep.2732

Liu, S., Xu, Z., Hua, W., Tang, G., and Xue, Y. (2014). Electromechanical Transient Modeling of Modular Multilevel Converter Based Multi-Terminal HVDC Systems. *IEEE Trans. Power Syst.* 29, 72–83. doi:10.1109/tpwrs.2013.2278402

Peralta, J., Saad, H., Dennetière, S., and Mahseredjian, J. (2012). "Dynamic Performance of Average-Value Models for Multi-Terminal VSC-HVDC Systems," in 2012 IEEE Power and Energy Society General Meeting (PESGM), San Diego, CA, USA, 1–8.

Peralta, J., Saad, H., Dennetiere, S., Mahseredjian, J., and Nguefeu, S. (2012). Detailed and Averaged Models for a 401-Level MMC-HVDC System. *IEEE Trans. Power Deliv.* 27, 1501–1508. doi:10.1109/tpwrd.2012.2188911

Saeedifard, M., and Iravani, R. (2010). Dynamic Performance of a Modular Multilevel Back-To-Back HVDC System. *IEEE Trans. Power Deliv.* 25, 2903–2912. doi:10.1109/tpwrd.2010.2050787

Siemens, P. T. I. (2013). *Program Operation Manual of PSS/E-33.4*. Schenectady, NY, USA: Siemens PTI, 21–23.

Stamatiou, G., and Bongiorno, M. (2017). Power-dependent Droop-based Control Strategy for Multi-terminal HVDC Transmission Grids. *IET Gener. Transm. & Distrib.* 11, 383–391. doi:10.1049/iet-gtd.2016.0764

Tang, A., Shao, Y., Huang, Y., and Xu, Q. (2018). A New Topology of the Distributed Power Flow Controller and its Electromagnetic Transient Characteristics. *Electr. Power Syst. Res.* 163, 280–287. doi:10.1016/j.epsr.2018.07.002

Vennelaganti, S. G., and Chaudhuri, N. R. (2018). Ratio-Based Selective Inertial and Primary Frequency Support through MTDC Grids with Offshore Wind Farms. *IEEE Trans. Power Syst.* 33, 7277–7287. doi:10.1109/tpwrs.2018.2850145

Wang, Y. Z., Wen, W. J., Wang, C. S., Liu, H. T., Zhan, X., and Xiao, X. L. (2019). Adaptive Voltage Droop Method of Multiterminal VSC-HVDC Systems for DC Voltage Deviation and Power Sharing. *IEEE Trans. Power Del.* 34, 169–176.

Xiao, H., Sun, K., Pan, J., Li, Y., and Liu, Y. (2021). Review of Hybrid HVDC Systems Combining Line Communicated Converter and Voltage Source Converter. *Int. J. Electr. Power & Energy Syst.* 129, 1–9. doi:10.1016/j.ijepes.2020.106713

Xu, X., Zhang, H., and Xu, Q. (2014). "An Approach to User-Defined Modeling Implemented with MATLAB," in 2014 IEEE PES Asia-Pacific Power and Energy Engineering Conference (APPEEC), 1–4. doi:10.1109/appeec.2014.7066083

Zhang, D., Jin, X., Zhou, B., Su, H., Chen, Y., and Zhu, L. (2015). "A Study on HVDC User-Defined Modeling in PSS/E," in 2015 5th International Conference on Electric Utility Deregulation and Restructuring and Power Technologies (DRPT), Changsha, China, 386–391. doi:10.1109/drpt.2015.7432263

Conflict of Interest: LZ and ZW are employed by South China University of Technology. DC is employed by State Grid Jiangsu Electric Power CO., Ltd. Extra High Voltage Company. YC is employed by University of Saskatchewan. CX is employed by Electric Power Research Institute of Yunnan Power Grid Co., Ltd. QL is employed by Maintenance & Test Center, CSG EHV Power Transmission Company.All authors declare no other competing interests

frontiers | Frontiers in Energy Research

ORIGINAL RESEARCH
published: 19 May 2022
doi: 10.3389/fenrg.2022.888585

Dual Set-Membership State Estimation for Power Distribution Networks Under Event-Triggered Mechanism

Xingzhen Bai[1], **Guhui Li**[1], **Mingyu Ding**[1], **Xingquan Ji**[1], **Jing Li**[2]* and **Xinlei Zheng**[1]

[1]College of Electrical Engineering and Automation, Shandong University of Science and Technology, Qingdao, China,
[2]College of Electronic and Information Engineering, Shandong University of Science and Technology, Qingdao, China

This article is concerned with the set-membership state estimation problem for power distribution networks (PDNs) over a resource-constrained communication network under the influence of unknown but bounded (UBB) noises. Firstly, in order to alleviate the pressure of information communication network (ICN) while meeting the state estimation requirements, the event-triggered mechanism is adopted to send data containing more valid information to estimation center, reasonably reducing the signal transmission frequency. Secondly, an event-triggered dual set-membership filter (ET-DSMF) is designed to improve the performance of state estimation. The proposed filter performs a discrete approximation for a semi-infinite programming problem by the random sampling technique, and a compact linearization error bounding ellipsoid is obtained by solving the dual problem of the nonlinear programming. Subsequently, a sufficient condition for the existence of the estimated ellipsoid is derived depending on the mathematical induction method. The key time-varying filter gain matrix and optimal estimated ellipsoid are determined recursively by solving a convex optimization problem, according to the minimum trace criterion. Finally, the effectiveness of the proposed filtering algorithm is demonstrated by performing simulation experiments on the IEEE 13 distribution test system.

Keywords: power distribution network, state estimation, set-membership filter, event-triggered mechanism, convex optimization

Edited by:
Ke-Jun Li,
Shandong University, China

Reviewed by:
Wei Qiu,
The University of Tennessee, United States
Weiyu Bao,
Shandong University, China

***Correspondence:**
Jing Li
peilianglj@163.com

Specialty section:
This article was submitted to Smart Grids,
a section of the journal Frontiers in Energy Research

Received: 03 March 2022
Accepted: 24 March 2022
Published: 19 May 2022

Citation:
Bai X, Li G, Ding M, Ji X, Li J and Zheng X (2022) Dual Set-Membership State Estimation for Power Distribution Networks Under Event-Triggered Mechanism.
Front. Energy Res. 10:888585.
doi: 10.3389/fenrg.2022.888585

1 INTRODUCTION

In recent years, the operation and control of power distribution networks (PDNs) are facing severe challenges with the large access of flexible loads and renewable energy (Dehghanpour et al., 2018; Fang et al., 2020; Zhang and Wang, 2020). In order to improve the power quality, the distribution management system (DMS) is required to achieve a higher level of control and management for the PDNs. As the basis of the smart grid situation perception, the state estimation module is the core part of the DMS. By using real-time measurement data, the operation state of the system can be estimated, and its accuracy directly determines the dispatching and control ability of the DMS to PDNs.

The traditional static state estimation completely depends on the measurement set at a certain time to obtain the operation state of the system at that time, ignoring the change process of the system state in continuous time (Jin et al., 2020). By contrast, dynamic state estimation is to track the changes of system states by recursive update estimation, and another advantage is that it can predict the state of the next time. Therefore, it is more conducive to improve the management level of DMS and has attracted the extensive attention of researchers (Wang et al., 2020; Ji et al., 2021). So far, the estimation methods based on the Kalman filtering framework have been widely applied in the dynamic state estimation of PDNs, such as extended Kalman filter (EKF), unscented Kalman filter (UKF), and robust recursive Kalman filter (RKF). Specifically, aiming at the state estimation problem of nonlinear systems, the EKF linearizes the nonlinear equation by the Taylor series and truncates it to the first order. Nevertheless, large errors will be produced for some strongly nonlinear systems due to the ignoring of higher-order remainder terms (Zhao et al., 2016; Ćetenović et al., 2021). Differently, the UKF directly obtains the approximate probability distribution of nonlinear function with the help of unscented transform technique (Zhao and Mili, 2017; Bai et al., 2021b), which avoids the linearization process and fully considers the influence of the higher-order terms. The RKF can deduce the filter gain by solving the upper bound of the error covariance matrix, and the higher-order remainder is expressed by a combination of uncertain linear matrices. It has been proved that the estimation accuracy is significantly improved by considering the influence of linearization error (Bai et al., 2018; Tan et al., 2021).

It is worth noting that the abovementioned filtering algorithms are all designed based on the assumption that the system noises obey Gaussian distribution. Actually, in the engineering practice, the statistical characteristics of the PDNs noises are unknown, which will inevitably bring errors to the estimation results (Wang et al., 2017). Fortunately, although the statistical characteristics of the PDNs noises are unknown, their boundaries are usually easy to obtain. For example, the dynamic modeling error of the state space model can be restricted by a known interval, and the measurement errors of phasor measurement units (PMUs) are described as less than one percent of the total vector errors according to the IEEE standards (Martin et al., 2008; Qing et al., 2013). To deal with such unknown but bounded (UBB) noises, the set-membership filtering algorithm has been proposed by Schweppe (1968), and its main idea is to provide a set of state estimation that always contains the real states of the system (Cerone et al., 2014). In order to facilitate the description, the state estimation set is usually outsourced using regular geometry, such as ellipsoid (Calafiore, 2005; Ding et al., 2019), zonotope (Kühn, 1998; Alamo et al., 2005), and box (Ping et al., 2020). And the ellipsoid set becomes the geometric representation tool selected in this article due to its simple representation and smooth derivable boundary. After years of development, the results of the set-membership filtering algorithm in linear systems have been widely published (Becis-Aubry et al., 2008; Gubarev and Melnichuk, 2015; Liu et al., 2016). To realize the application of the set-membership theory in nonlinear systems, the nonlinear set-membership filtering algorithm has been developed (Scholte and Campbell, 2003; Calafiore, 2005) and widely applied in various fields, such as target tracking (Yu et al., 2016; Bai et al., 2021a), generator state estimation (Cheng et al., 2018), and power system state estimation (Qing et al., 2013; Zhang et al., 2020). In addition, what should be concerning is how to obtain the compact bound of the linearization error for strongly nonlinear systems. In this regard, the extended set-membership filter (ESMF) has been developed in Scholte and Campbell (2003), in which the interval analysis method is used to determine the uncertain boundary of linearization error. However, this method will increase the conservatism of boundary estimation. Here, we try to solve the tighter linearized error boundary by the semi-infinite programming approach (Vandenberghe and Boyd, 1996). Specifically, firstly, the dual form of semi-infinite programming is derived by the known lemma. Then, the continuous measure is discretized and approximated by random sampling technology (Wang et al., 2018) (e.g., the Monte Carlo sampling method), such that the discrete expressions of the compact linearized error boundary ellipsoid center and shape matrix can be obtained recursively.

From another perspective, the measurement and communication technologies have been developed rapidly in recent years. In comparison with the conventional distribution remote terminal units (DRTUs), the PMUs can accurately measure the phasor of voltage and current, and high-frequency sampling provides a lot of real-time system information for dynamic state estimation, which is more conducive to the implementation of dynamic state estimation (Zhang et al., 2020; Mohammadrezaee et al., 2021; Qu et al., 2021). However, due to the limited bandwidth of the information communication network (ICN), the transmission of large amounts of data inevitably leads to certain network-induced phenomena such as channel congestion and communication delay (Wei et al., 2015; Hu et al., 2020). In order to alleviate the transmission pressure of the ICN, the researchers have proposed many effective solutions (Ge et al., 2017; Peng and Li, 2018; Liu et al., 2019; Zou et al., 2021). Among them, the event-triggered mechanism has recently attracted increasing research interest in the field of power systems (Liu et al., 2017; Bai et al., 2021b; Cheng and Bai, 2021).

Different from the traditional time-based periodic transmission mechanism, event-triggered transmission mechanism refers to using the constructed trigger function to judge whether the measurement at the current time meets the trigger requirements, and only the data that meet the specific conditions are transmitted to the estimator for processing. It can effectively reduce the communication frequency and improve the communication efficiency while ensuring the PDNs state estimation performance. Nonetheless, so far, the problem of dynamic state estimation for the PDNs based on the event-triggered mechanism has not been fully studied considering nonlinear and unknown but bounded noises, which is the main motivation of our research.

In view of the above discussion, we aim to design a dual set-membership filtering algorithm for the PDNs state estimation under the event-triggered mechanism to achieve a balance of network resource utilization and system filtering performance. The main technical contributions for this article can be summarized as follows:

1) An event-triggered mechanism suitable for PDNs data transmission is proposed, which can reasonably reduce the data transmission frequency on the premise of ensuring the accuracy of state estimation, so as to provide a feasible method to alleviate the communication pressure and save network resources;
2) With the help of random sampling technique, the compact linearized error ellipsoid is obtained by solving the dual problem of nonlinear programming to reduce the conservatism of the set-membership filtering algorithm;
3) Based on recurrent linear matrix inequality (RLMI) and convex optimization theories, sufficient conditions for the existence of the estimated ellipsoid are derived, and the time-varying gain matrix is solved. Then, an event-triggered dual set-membership filter (ET-DSMF) is developed to realize the online state monitoring of the system and further improve the perception ability of the PDNs.

The contents of the article are organized as follows: **Section 2** establishes the dynamic state model of the PDNs. **Section 3** proposes the event-triggered mechanism. **Section 4** mainly introduces the calculation method of the compact boundary of the linearization errors, and a dual set-membership filter based on the event-triggered mechanism is designed. In **Section 5**, The IEEE 13 PDN test system serves as an example to verify the effectiveness of the filtering algorithm proposed in this article. Finally, we summarize this article in **Section 6**.

2 SYSTEM MODEL OF POWER DISTRIBUTION NETWORKS

In the dynamic state estimation of the PDNs, the system model is utilized to estimate the operation states at the current and predict the state changes at the next. In abstract, the system model of the PDNs includes the state model and measurement model, and its general model can be expressed by **Eq. 1**:

$$\begin{cases} x_{k+1} = f\left(x_k\right) + \omega_k \\ y_k = \mathrm{g}\left(x_k\right) + v_k \end{cases} \tag{1}$$

where $x_k \in \mathbb{R}^n$ and $y_k \in \mathbb{R}^m$ are the system state vector and the measurement vector, respectively. $x_k = [U_1, \ldots, U_i, \ldots, U_N]^T$ and the element is specifically expressed as $U_i = [U_i^{re,a}, U_i^{im,a}, U_i^{re,b}, U_i^{im,b}, U_i^{re,c}, U_i^{im,c}]$. N denotes the number of system buses. $U_i^{re,p}$ and $U_i^{im,p}$ $(p \in \{a, b, c\})$ represent, respectively, the p-phase real and imaginary voltage at the ith bus. $f(\cdot)$ and $h(\cdot)$ are the state transfer equation and the measurement equation, respectively. In addition, the system noises and initial state values satisfy the following assumptions:

Assumption 1: The noise sequence ω_k and v_k satisfy the following ellipsoid constraints:

$$\begin{cases} W_k \triangleq \left\{\omega_k \in \mathbb{R}^n : \omega_k^T Q_k^{-1} \omega_k \leqslant 1\right\} \\ V_k \triangleq \left\{v_k \in \mathbb{R}^m : v_k^T R_k^{-1} v_k \leqslant 1\right\} \end{cases} \tag{2}$$

where $Q_k \in \mathbb{R}^{n\times n}$ and $R_k \in \mathbb{R}^{m\times m}$ are known symmetric positive definite matrices.

Assumption 2: The initial state x_0 belongs to the initial state ellipsoid ϕ_0 and defined as

$$\phi_0 \triangleq \left\{x \in \mathbb{R}^{n\times n} : \left(x - \hat{x}_0\right)^T P_0^{-1} \left(x - \hat{x}_0\right) \leqslant 1\right\} \tag{3}$$

where $\hat{x}_0$ is the center for the estimation set and $P_0 \in \mathbb{R}^{n\times n}$ is the symmetric positive definite matrix describing the shape and orientations for the initial state ellipsoid.

2.1 State Model

In this article, the system is assumed in a quasi-steady state operation, and a widely used dynamic model is adopted to represent the equation of state:

$$x_{k+1} = A_k x_k + B_k + \omega_k \tag{4}$$

where A_k is the state transfer matrix, which represents the speed of the state transfer; B_k is the input matrix, reflecting the changing trend in the state trajectory. The Holt-Winters two-parameter exponential smoothing method is employed to compute A_k and B_k online.

$$\begin{cases} A_k = \alpha\left(1 + \beta\right) I_n \\ B_k = \left(1 + \beta\right)\left(1 - \alpha\right) \hat{x}_{k|k-1} - \beta c_{k-1} + \left(1 - \beta\right) b_{k-1} \end{cases} \tag{5}$$

subject to

$$\begin{cases} c_k = \alpha \hat{x}_k + \left(1 - \alpha\right) \hat{x}_{k|k-1} \\ b_k = \beta\left(c_k - c_{k-1}\right) + \left(1 - \beta\right) b_{k-1} \end{cases} \tag{6}$$

in which, α and β indicate smoothing parameters, taking the values between 0 and 1; $\hat{x}_{k|k-1}$ is the state prediction value at $k - 1$; and $\hat{x}_k$ is the state estimate value at k.

2.2 Measurement Model

At present, hybrid measurements with DRTUs and PMUs are adopted in the PDNs to coordinate the economy of power network construction and the accuracy of state estimation. The use of various measurement devices increases the measurement redundancy and then provides reasonable measurement data for the PDNs state estimation. The DRTU measurements are expressed as

$$U_i^p = \sqrt{\left(U_i^{re,p}\right)^2 + \left(U_i^{im,p}\right)^2}, \tag{7}$$

$$\begin{cases} P_{i-j}^p = \sum\limits_{q\in\{a,b,c\}} G_{i-j}^{pq}\left[U_i^{re,p} \overrightarrow{U}_{i-j}^{re,q} + U_i^{im,p} \overrightarrow{U}_{i-j}^{im,q}\right] + B_{i-j}^{pq}\left[U_i^{im,p} \overrightarrow{U}_{i-j}^{re,q} - U_i^{re,p} \overrightarrow{U}_{i-j}^{im,q}\right] \\ Q_{i-j}^p = -\dfrac{b_{i-j}^p}{2}\left[\left(U_i^{re,p}\right)^2 + \left(U_i^{im,p}\right)^2\right] \\ \qquad + \sum\limits_{q\in\{a,b,c\}} G_{i-j}^{pq}\left[U_i^{im,p} \overrightarrow{U}_{i-j}^{re,q} - U_i^{re,p} \overrightarrow{U}_{i-j}^{im,q}\right] - B_{i-j}^{pq}\left[U_i^{im,p} \overrightarrow{U}_{i-j}^{im,q} + U_i^{re,p} \overrightarrow{U}_{i-j}^{re,q}\right] \end{cases}, \tag{8}$$

$$\begin{cases} P_i^p = \sum\limits_{j=1, j\neq i}^{j=N} \gamma_{j-i} P_{j-i}^p \\ Q_i^p = \sum\limits_{j=1, j\neq i}^{j=N} \gamma_{j-i} Q_{j-i}^p \end{cases} \tag{9}$$

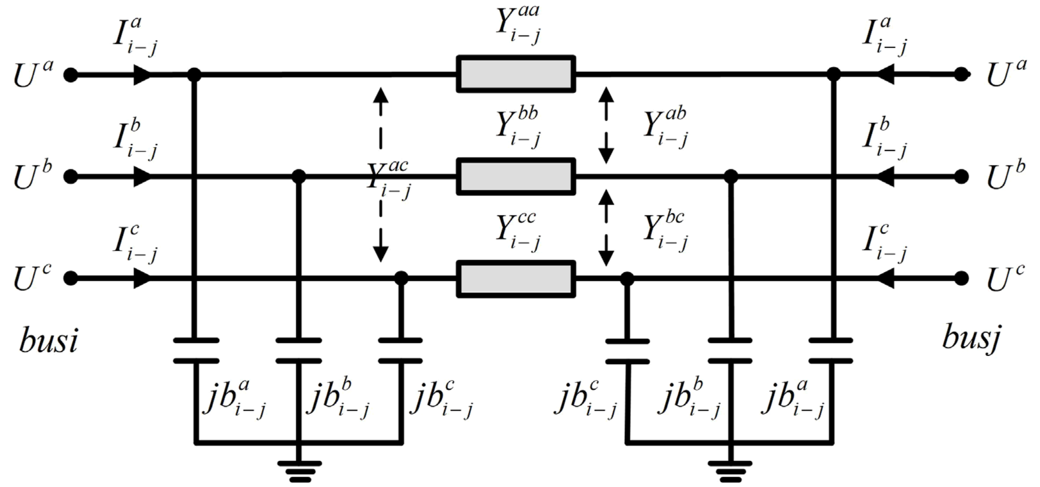

FIGURE 1 | Three-phase unbalanced line model of the PDNs.

where $\vec{U}^{re,q}_{i-j} = U^{re,q}_i - U^{re,q}_j, \vec{U}^{im,q}_{i-j} = U^{im,q}_i - U^{im,q}_j$, P^p_{i-j} and Q^p_{i-j} are the p-phase active and reactive power flow measurements at the $i-j$ branch, respectively. P^p_i and Q^p_i are the p-phase active and reactive power injection measurements at the ith bus, respectively. b^p_{i-j} represents p-phase ground guide at the $i-j$ branch. γ_{j-i} is a scalar describing the mutual coupling between the network nodes. If Θ represents the set of neighbor nodes of node i, then

$$\gamma_{j-i} = \begin{cases} 1, & j \in \Theta \\ 0, & j \notin \Theta \end{cases} \tag{10}$$

Besides, the PMU measurements are expressed as

$$\begin{cases} U^{re,p}_i = U^{re,p}_i \\ U^{im,p}_i = U^{im,p}_i, \end{cases} \tag{11}$$

$$\begin{cases} I^{re,p}_{i-j} = -\dfrac{b^p_{i-j}}{2} U^{im,p}_i + \sum\limits_{q\in\{a,b,c\}} G^{pq}_{i-j} \vec{U}^{re,q}_{i-j} - B^{pq}_{i-j} \vec{U}^{im,q}_{i-j} \\ I^{im,p}_{i-j} = \dfrac{b^p_{i-j}}{2} U^{re,p}_i + \sum\limits_{q\in\{a,b,c\}} G^{pq}_{i-j} \vec{U}^{im,q}_{i-j} + B^{pq}_{i-j} \vec{U}^{re,q}_{i-j} \end{cases} \tag{12}$$

where $I^{re,p}_{i-j}$ and $I^{im,p}_{i-j}$ represent the p-phase real and imaginary currents at the $i-j$ branch, respectively.

Figure 1 shows the three phase unbalanced line model of the PDNs, where the missing phase line model is similar to the three-phase model and is not fully shown here.

3 EVENT-TRIGGERED MECHANISM

The basic working architecture of the PDN based on an event-triggered mechanism is shown in **Figure 2**. To be specific, the measurement at the current moment collected using the PMU and DRTU measurement devices are compared with the measurement of the latest transmission by the event-triggered mechanism. When the triggering condition is satisfied, the current measurement will be transmitted to the remote estimation center *via* the ICN, otherwise the measurement will not be transmitted. According to the zero-order hold strategy, the last transmitted measurement will participate in the state estimation process in the estimation center. Since the event-triggered mechanism is adopted, the measurement devices only provide useful information to the estimation center, and the data transmitted by the ICN will greatly decrease, which reasonably alleviates the burden on the channel. Thus, the probability of network-induced phenomenon is effectively reduced.

The triggering condition is as follows:

$$t^i_{r+1} = \inf_{k\in N} \{k > t^i_r | S_k > 0\}. \tag{13}$$

The specific expression of S_k is

$$S_k = \sigma^T_{i,k} \psi \sigma_{i,k} - \varepsilon_i y^T_{i,t^i_r} \psi y_{i,t^i_r} \tag{14}$$

where ψ is the weight matrix of the opposite and positive definite and is assumed to be a unit matrix in this article. $\sigma_{i,k}$ is the difference between the current measurement $y_{i,k}$ and the last transmitted value y_{i,t^i_r} (the latest accepted values for the estimate center), which is defined as

$$\sigma_{i,k} = y_{i,t^i_r} - y_{i,k}, \tag{15}$$

and the following expression is given by:

$$\delta_i = \varepsilon_i y^T_{i,t^i_r} \psi y_{i,t^i_r}. \tag{16}$$

When increasing the value of ε_i, the transmission frequency would decrease correspondingly. In engineering practice, the selection of ε_i should consider not only the network communication resources but also the system filtering performance. As such, the appropriate parameter selected can achieve a trade-off between energy conservation and the estimation performance of the distribution system. Then, the event-triggering function can be defined as follows:

$$f_i(\sigma_{i,k}, \delta_i) = \sigma^T_{i,k} \sigma_{i,k} - \delta_i. \tag{17}$$

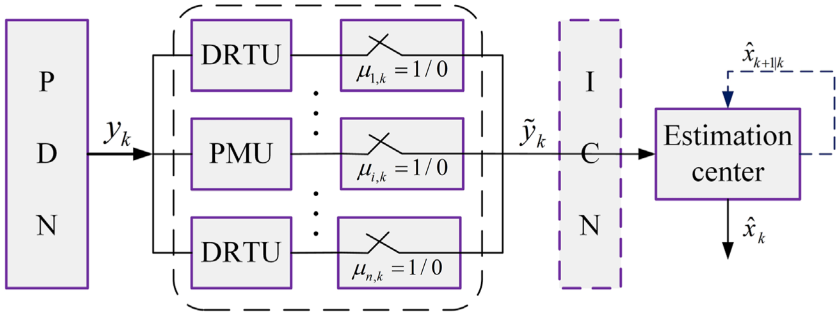

FIGURE 2 | Event-triggered mechanism.

The parameters $\mu_{i,k}$ are constructed to indicate whether the measurement is transmitted or not, and triggering logic variable is expressed as

$$\mu_{i,k}=\begin{cases}1, & f_i(\sigma_{i,k},\delta_i)>0\\ 0, & f_i(\sigma_{i,k},\delta_i)\leqslant 0\end{cases} \tag{18}$$

If $\mu_{i,k}=1$, the event triggering is executed. Otherwise, by the zero-order hold strategy, the latest triggered one would be used to the filtering process instead of $y_{i,k}$, so as to realize the measurement synchronization and the integrity of the measurement information. By **Equations 17**, **18**, the non-triggering error can be described as

$$\sigma_{i,k}=\begin{cases}0, & \mu_{i,k}=1\\ y_{i,t_r^i}-y_{i,k}, & \mu_{i,k}=0\end{cases} \tag{19}$$

The current measurement information received by the estimation center is

$$\tilde{y}_k=y_k+\sigma_k \tag{20}$$

where $\sigma_k=[\sigma_{1,k}^T,\sigma_{2,k}^T,\ldots,\sigma_{m,k}^T]^T$.

Let $\delta=\sum_{i=1}^{m}\delta_i$, then the formula is established as

$$\sigma_k^T\sigma_k\leqslant\delta. \tag{21}$$

The above results will be fully reflected in the design process of the filter.

Remark 1: The different measurement devices such as the PMUs and DRTUs are equipped at the buses of the PDNs. The diversity of measurements will bring great challenges to the setting of event-triggering threshold. Based on this challenge, we develop the event-triggered mechanism described above. This is a relative event-triggered mechanism, which is different from the absolute one in Bai et al. (2021b).

4 EVENT-TRIGGERED DUAL SET-MEMBERSHIP FILTER

4.1 Linearization Error Boundary

Actually, the linearization error boundary determined by the interval analysis method is too conservative, and its cumulative effect will also affect the accuracy and even lead to filter divergence. In addition, the Lagrange remainder of the linearized nonlinear function can be used to represent the linearization error, but the process of optimizing the Hessian matrix is more complex. In this article, the linearization error is limited by solving the dual form of semi-infinite programming, which not only avoids the solution of Hessian matrix but also overcomes the defects of the interval analysis method, and a more compact linearization error boundary can be obtained.

A lemma will first be introduced for the formula derivation in this section.

Lemma 1: Wang et al. (2021) The optimization problem of the ellipsoid can be expressed as

$$\begin{cases}\min\limits_{P,\hat{u}}\log\det(P)\\ s.t.(u-\hat{u})^TP^{-1}(u-\hat{u})\leqslant 1,\forall u\in\mathbb{C}\end{cases} \tag{22}$$

with

$$\begin{cases}\mathbb{C}\triangleq\{u:u=s(x),x\in\phi\}\\ \phi\triangleq\{x:(x-\hat{x})^T\bar{P}^{-1}(x-\hat{x})\leqslant 1\}.\end{cases} \tag{23}$$

Then, the optimal solution of **Eq. 22** is

$$P^*=\int_{\mathbb{C}}uu^Td\tau^*-u^*u^{*T} \tag{24}$$

where $\hat{u}^*=\int_{\mathbb{C}}ud\tau^*$ is the optimal solution to the following optimization problem:

$$\begin{cases}\max\limits_{\tau_i\geqslant 0}\log\det\left(\int_{\mathbb{C}\times\{1\}}\breve{u}\breve{u}^Td\tau\right)\\ s.t.\int_{\mathbb{C}\times\{1\}}d\tau=1\end{cases} \tag{25}$$

with $\breve{u}=[u^T,1]^T$, and **Eq. 25** is the dual problem of **Eq. 22**. For the proof of this lemma, please refer to Wang et al. (2021).

Next, we introduce the specific application of this lemma in this article. First, the Taylor expansion of the measurement equation is performed around $\hat{x}_{k+1|k}$.

$$g(x_{k+1})=g(\hat{x}_{k+1|k})+G_{k+1}(x_{k+1}-\hat{x}_{k+1|k})+\Delta g(x_{k+1}) \tag{26}$$

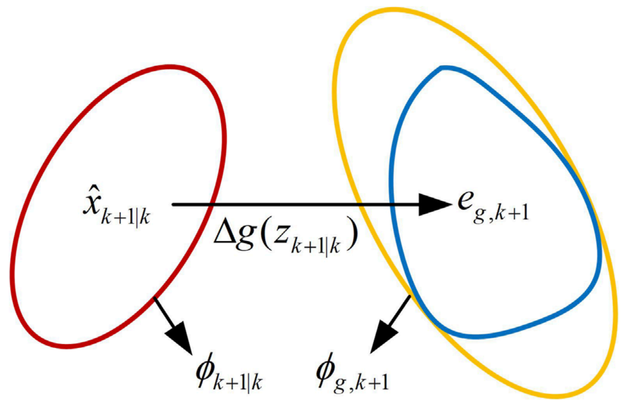

FIGURE 3 | The linearization error ellipsoid.

According to the properties of the ellipsoid, **Eq. 26** is equivalent to:

$$\mathrm{g}\left(\hat{x}_{k+1|k}+E_{k+1|k}z_{k+1|k}\right)=\mathrm{g}\left(\hat{x}_{k+1|k}\right)+G_{k+1}E_{k+1|k}z_{k+1|k}+\Delta \mathrm{g}\left(z_{k+1|k}\right) \tag{27}$$

where $\left\|z_{k+1|k}\right\|\leq 1$, $P_{k+1|k}=E_{k+1|k}E_{k+1|k}^{T}$. Thus, the higher-order linearization error can be expressed as

$$\begin{aligned}\Delta \mathrm{g}\left(z_{k+1|k}\right)&=\mathrm{g}\left(x_{k+1}\right)-\mathrm{g}\left(\hat{x}_{k+1|k}\right)-G_{k+1}\left(x_{k+1}-\hat{x}_{k+1|k}\right)\\&=\mathrm{g}\left(\hat{x}_{k+1|k}+E_{k+1|k}z_{k+1|k}\right)-\mathrm{g}\left(\hat{x}_{k+1|k}\right)-G_{k+1}E_{k+1|k}z_{k+1|k}.\end{aligned} \tag{28}$$

As shown in **Figure 3**, we try to find a compact ellipsoid to cover the higher-order remainder term, assuming that the outsourced ellipsoid of the higher-order remainder term is expressed as $\phi_{\mathrm{g},k+1}$. This article uses the nonlinear programming method to optimize the boundary of linearization error, which can get a tight boundary estimate. In general, it can be obtained from Lemma 1 that the linear programming **Eq. 25** is the dual form of the nonlinear programming **Eq. 22**. Therefore, in order to achieve a balance between the estimation accuracy and the calculation amount, the continuous system is discretized by the Monte Carlo sampling method. In this regard, the nonlinear programming is converted into a linear programming problem. The following expression is established:

$$\begin{aligned}\Delta \mathrm{g}\left(z_{k+1|k}\right)&\triangleq\left\{u|\left(u-\hat{u}_{\mathrm{g},k+1}\right)^{T}P_{\mathrm{g},k+1}^{-1}\left(u-\hat{u}_{\mathrm{g},k+1}\right)\leq 1\right\}\\&\triangleq\left\{u|u=\hat{u}_{\mathrm{g},k+1}+E_{\mathrm{g},k+1|k}z_{\mathrm{g},k+1|k},P_{\mathrm{g},k+1}\right.\\&\left.=E_{\mathrm{g},k+1|k}E_{\mathrm{g},k+1|k}^{T},\left\|z_{\mathrm{g},k+1|k}\right\|\leq 1\right\}\\&\in\phi_{\mathrm{g},k+1}\end{aligned} \tag{29}$$

where $\hat{u}_{\mathrm{g},k+1}$ and $P_{\mathrm{g},k+1}$ denote the center and shape matrix of the ellipsoid $\phi_{\mathrm{g},k+1}$, respectively.

A nonlinear programming method can be used to optimize the linearized error boundary, so the following nonlinear programming problem can be constructed:

$$\begin{cases}\min\limits_{P_{\mathrm{g},k+1},\hat{u}_{\mathrm{g},k+1}}\ \log\det\left(P_{\mathrm{g},k+1}\right)\\ s.t.\left(u-\hat{u}_{\mathrm{g},k+1}\right)^{T}P_{\mathrm{g},k+1}^{-1}\left(u-\hat{u}_{\mathrm{g},k+1}\right)\leqslant 1,\forall u\in\mathbb{C}\end{cases} \tag{30}$$

where $\mathbb{C}$ is defined as

$$\begin{cases}\mathbb{C}\triangleq\left\{u:u=h\left(x_{k+1}\right),x_{k+1}\in\phi_{k+1|k}\right\}\\ \phi_{k+1|k}\triangleq\left\{x_{k+1}:\left(x_{k+1}-\hat{x}_{k+1|k}\right)^{T}P_{k+1|k}^{-1}\left(x_{k+1}-\hat{x}_{k+1|k}\right)\leqslant 1\right\}\end{cases} \tag{31}$$

in which, $h(\cdot)$ is an arbitrary nonlinear continuous function, expressed here as a higher-order remainder term function.

The minimal volume of the linear error outsourcing ellipsoid can be obtained by solving the nonlinear programming problem. In order to make it more convenient, the continuous system is discretized by the Monte Carlo sampling method, and the discrete expression of the center and shape matrix of the ellipsoid are obtained by **Eqs. 32, 33**, which corresponds to **Eq. 24** under continuous form. Moreover, the approximate expression of **Eq. 25** is obtained, as shown in **Eq. 34**. Thus, an outsourcing compact ellipsoid with the linearization error is developed. The results obtained in this section will be used in the design of the dual set-membership filter. The specific process will be shown in detail in **Section 4.2**.

$$P_{\mathrm{g},k+1}=\sum\nolimits_{i=1}^{m}\tau_{i}u_{i}u_{i}^{T}-\hat{u}_{\mathrm{g},k+1}\hat{u}_{\mathrm{g},k+1}^{T} \tag{32}$$

with

$$\hat{u}_{\mathrm{g},k+1}=\sum\nolimits_{i=1}^{m}\tau_{i}u_{i} \tag{33}$$

where coefficients $\tau_{i}(i=1,\ldots,m)$ are obtained by solving the linear programming shown in the solution **Eq. 34**

$$\begin{cases}\max\limits_{\tau_{i}\geqslant 0}\ \log\det\left(\sum\nolimits_{i}^{m}\tau_{i}\breve{u}_{i}\breve{u}_{i}^{T}\right)\\ s.t.\sum\nolimits_{i}^{m}\tau_{i}=1.\end{cases} \tag{34}$$

By Lemma 1, we obtain the dual form of nonlinear programming and the continuous expressions of the center and shape matrix of the linearized error ellipsoid. Then, the continuous system is discretized by the Monte Carlo sampling method, and the semi-infinite programming problem is transformed into a finite programming problem, so the discrete expressions of the ellipsoid center and shape matrix are obtained.

Remark 2: Different from the UKF, the approximate probability distribution of the nonlinear function cannot be obtained directly, since we assume that the true state is restricted to the ellipsoid, rather than obeying a particular Gaussian distribution. Wang et al. (2021) avoids the process of Taylor expansion by directly solving the approximate distribution of the nonlinear measurement function values. But this will still inevitably produce large errors for strong nonlinear systems. Therefore, the method in this article strikes a balance between the computational quantity and the estimation accuracy.

4.2 Predictive and Update Steps

In this section, a set-membership filtering algorithm based on the event-triggered mechanism is proposed to solve the state estimation problem of the PDNs. And the real state is always confined to the set of state estimation. In order to deal with quadratic constraints such as event-triggered mechanism and external noises, RLMI technology is used to transform the externally bounded ellipsoid filtering problem into a convex optimization problem with linear matrix inequality constraints. The sufficient conditions for the existence of the estimated state set are strictly derived, and the filter gain parameters are easily obtained by solving the convex optimization problem(Boyd et al., 1994).

We begin by introducing two lemmas, which will be used in the proof of this section.

Lemma 2: (S-Procedure) (Bai et al., 2021a): Let $\hbar_0(\cdot)$, $\hbar_1(\cdot),\ldots,\hbar_p(\cdot)$ be the quadratic function of the variable $\chi \in \mathbb{R}^n$, $\hbar_i(\chi) = \chi^T M_i \chi (i = 0,1,\ldots,p)$, with $M_i = M_i^T$, if there exist $\lambda_1 \geqslant 0,\ldots,\lambda_p \geqslant 0$ such that $M_0 - \sum_{i=1}^{p} \lambda_i M_i \leqslant 0$, then the following is true: $\hbar_1(\chi) \leqslant 0,\ldots,\hbar_p(\chi) \leqslant 0 \rightarrow \hbar_0(\chi) \leqslant 0$.

Lemma 3: (Schur Complement Equivalence) (Bai et al., 2021a): For matrices H_1, H_2, H_3, where $S_1 = S_1^T \geqslant 0$, $H_2 = H_2^T \geqslant 0$, $H_3^T H_2^{-1} H_3 + H_1 \leqslant 0$, if and only if $\begin{bmatrix} -H_2 & H_3 \\ H_3^T & H_1 \end{bmatrix} < 0$ or $\begin{bmatrix} H_1 & H_3^T \\ H_3 & -H_2 \end{bmatrix} < 0$.

One-step state prediction value $\hat{x}_{k+1|k}$ is approximated by the Holt-Winters two-parameter exponential smoothing method. Based on the state estimate at k, one-step predicted ellipsoid $\phi_{k+1|k}$ is obtained by solving the semi-definite programming problem **Eq. 36**.

$$\phi_{k|k+1} = \left\{ x_{k+1} : \left(x_{k+1} - \hat{x}_{k+1|k} \right)^T P_{k+1|k}^{-1} \left(x_{k+1} - \hat{x}_{k+1|k} \right) \leqslant 1 \right\} \tag{35}$$

where $P_{k+1|k}$ is the desired optimization variable.

It should be noted that calculating the volume of the ellipsoidal set is more difficult than the trace of the matrix P_{k+1}. The trace of P_{k+1} is the sum of the semi-axes of the ellipsoid, by which the size of the ellipsoidal set can be reflected effectively. Therefore, the objective function **Eq. 36** is the trace function.

$$\begin{cases} \min\limits_{P_{k+1|k}, \lambda_1 \geqslant 0, \lambda_2 \geqslant 0} f\left(P_{k+1|k} \right) \\ s.t. \begin{bmatrix} \Xi_{k+1|k} & \Phi_{k+1|k}^T \\ \Phi_{k+1|k} & -P_{k+1|k} \end{bmatrix} < 0 \end{cases} \tag{36}$$

where

$$\Phi_{k+1|k} = \left[0, A_k E_k, I \right], \tag{37}$$

$$\Xi_{k+1|k} = \operatorname{diag}\left\{ \lambda_1 + \lambda_2 - 1, -\lambda_1 I, -\lambda_2 Q_k^{-1} \right\}. \tag{38}$$

Proof 1: In view of **Equation 4**, we can get one-step prediction state error

$$\begin{aligned} e_{k+1|k} = x_{k+1} - \hat{x}_{k+1|k} &= A_k E_k z_k + w_k \\ &= \Phi_{k+1|k} \zeta. \end{aligned} \tag{39}$$

Let, $\zeta = [1, z_k^T, w_k^T]^T$. Thus, $x_{k+1} \in \phi_{k+1|k}$ is equivalent to

$$\zeta^T \left[\Phi_{k+1|k}^T P_{k+1|k}^{-1} \Phi_{k+1|k} \right] \zeta \leq 1. \tag{40}$$

The following unequal conditions exist naturally:

$$\begin{cases} \|z_k\| \leq 1 \\ w_k^T Q_k^{-1} w_k \leq 1. \end{cases} \tag{41}$$

Eq. 41 is equivalent to

$$\begin{cases} \zeta^T \operatorname{diag}\{-1, I, 0\} \zeta \leq 0 \\ \zeta^T \operatorname{diag}\{-1, 0, -Q_k^{-1}\} \zeta \leq 0. \end{cases} \tag{42}$$

By means of Lemma 1, $\zeta^T [\Phi_{k+1|k}^T P_{k+1|k}^{-1} \Phi_{k+1|k}] \zeta \leq 1$ holds, if positive scalar λ_1, λ_2 exists such that

$$\begin{aligned} &\Phi_{k+1|k}^T P_{k+1|k}^{-1} \Phi_{k+1|k} - \operatorname{diag}\{1,0,0\} - \lambda_1 \operatorname{diag}\{-1, I, 0\} \\ &\quad - \lambda_2 \operatorname{diag}\{-1, 0, -Q_k^{-1}\} \leq 0. \end{aligned} \tag{43}$$

Equation 43 can be rewritten as

$$\Phi_{k+1|k}^T P_{k+1|k}^{-1} \Phi_{k+1|k} + \Xi_{k+1|k} \leq 0 \tag{44}$$

where

$$\Xi_{k+1|k} = \operatorname{diag}\left\{ \lambda_1 + \lambda_2 - 1, -\lambda_1 I, -\lambda_2 Q_k^{-1} \right\}. \tag{45}$$

By Lemma 2, **Equation 45** can be converted to the following formula:

$$\begin{bmatrix} \Xi_{k+1|k} & \Phi_{k+1|k}^T \\ \Phi_{k+1|k} & -P_{k+1|k} \end{bmatrix} < 0. \tag{46}$$

The proof is completed.

On the other hand, based on the proposed event-triggered mechanism, the estimates can be expressed by:

$$\hat{x}_{k+1} = A_k \hat{x}_k + B_k + K_{k+1} \left(\tilde{y}_{k+1} - \mathrm{g}\left(\hat{x}_{k+1|k} \right) \right) \tag{47}$$

where K_{k+1} is the filter gain matrix to be solved. In addition, the estimated ellipsoid ϕ_{k+1} is obtained by solving the semi-definite programming problem, based on the one-step state prediction value at k.

$$\phi_{k+1} = \left\{ x_{k+1} : (x_{k+1} - \hat{x}_{k+1})^T P_{k+1}^{-1} (x_{k+1} - \hat{x}_{k+1}) \leq 1 \right\} \tag{48}$$

The optimal variable P_{k+1} and the gain matrixes K_{k+1} can be obtained by solving the following optimization problem:

$$\begin{cases} \min\limits_{P_{k+1}, K_{k+1}, \lambda_3 \geqslant 0, \ldots, \lambda_7 \geqslant 0} f\left(P_{k+1} \right) \\ s.t. \begin{bmatrix} \Xi_{k+1} & \Phi_{k+1}^T \\ \Phi_{k+1} & -P_{k+1} \end{bmatrix} < 0 \end{cases} \tag{49}$$

where

$$\begin{aligned} \Phi_{k+1} = \big[&-K_{k+1} e_{\mathrm{g},k+1}, \left(I - K_{k+1} G_{k+1} \right) A_k E_k, I - K_{k+1} G_{k+1}, -K_{k+1} E_{\mathrm{g},k+1}, \\ &- K_{k+1}, -K_{k+1} \big] \end{aligned} \tag{50}$$

$$\begin{aligned} \Xi_{k+1} = \operatorname{diag}\big\{ &\lambda_3 + \lambda_4 + \lambda_5 + \lambda_6 + \lambda_7 \delta - 1, -\lambda_3 I, -\lambda_4 Q_k^{-1}, -\lambda_5 I, \\ &- \lambda_6 R_{k+1}^{-1}, -\lambda_7 I \big\} \end{aligned} \tag{51}$$

Proof 2: According to **Eq. 47**,

$$\begin{aligned} e_{k+1} &= x_{k+1} - \hat{x}_{k+1} \\ &= x_{k+1} - \hat{x}_{k+1|k} - K_{k+1} \left(G_{k+1} \left(x_{k+1} - \hat{x}_{k+1|k} \right) + e_{\mathrm{g},k+1} + E_{\mathrm{g},k+1} z_{\mathrm{g},k+1} \right. \\ &\quad \left. + v_{k+1} + \sigma_{k+1} \right) \\ &= \left(I - K_{k+1} G_{k+1} \right) \left(A_k E_k z_k + w_k \right) - K_{k+1} e_{\mathrm{g},k+1} \\ &\quad - K_{k+1} E_{\mathrm{g},k+1} z_{\mathrm{g},k+1} - K_{k+1} v_{k+1} - K_{k+1} \sigma_{k+1} \\ &= -K_{k+1} e_{\mathrm{g},k+1} + \left(I - K_{k+1} G_{k+1} \right) A_k E_k z_k + \left(I - K_{k+1} G_{k+1} \right) w_k \\ &\quad - K_{k+1} e_{\mathrm{g},k+1} - K_{k+1} E_{\mathrm{g},k+1} z_{\mathrm{g},k+1} - K_{k+1} v_{k+1} - K_{k+1} \sigma_{k+1} \\ &= \Phi_{k+1} \eta \end{aligned} \tag{52}$$

with

$$\eta = \left[1, z_k^T, w_k^T, z_{g,k+1}^T, v_{k+1}^T, \sigma_{k+1}^T\right]^T. \tag{53}$$

Thus, $x_{k+1} \in \phi_{k+1}$ is equivalent to $\eta^T[\Phi_{k+1}^T P_{k+1}^{-1} \Phi_{k+1}]\eta \leqslant 1$. The following conditions are naturally satisfied:

$$\begin{cases} \|z_k\| \leqslant 1 \\ w_k^T Q_k^{-1} w_k \leqslant 1 \\ \left\|z_{g,k+1}\right\| \leqslant 1 \\ v_{k+1}^T R_{k+1}^{-1} v_{k+1} \leqslant 1 \\ \sigma_{k+1}^T \sigma_{k+1} \leqslant \delta \end{cases} \tag{54}$$

which can be rewritten as follows:

$$\begin{cases} \eta^T \operatorname{diag}\{-1, I, 0, 0, 0, 0\}\eta \leqslant 0 \\ \eta^T \operatorname{diag}\{-1, 0, Q_k^{-1}, 0, 0, 0\}\eta \leqslant 0 \\ \eta^T \operatorname{diag}\{-1, 0, 0, I, 0, 0\}\eta \leqslant 0 \\ \eta^T \operatorname{diag}\{-1, 0, 0, 0, R_{k+1}^{-1}, 0\}\eta \leqslant 0 \\ \eta^T \operatorname{diag}\{-\delta, 0, 0, 0, 0, I\}\eta \leqslant 0. \end{cases} \tag{55}$$

It can be seen from Lemma 1 that **Eq. 48** is established if positive scalar $\lambda_3, \lambda_4, \lambda_5, \lambda_6, \lambda_7$ exists to make the following inequality hold:

$$\begin{aligned} &\Phi_{k+1}^T P_{k+1}^{-1} \Phi_{k+1} - \operatorname{diag}\{1, 0, 0, 0, 0, 0\} \\ &\quad - \lambda_3 \operatorname{diag}\{-1, I, 0, 0, 0, 0\} - \lambda_4 \operatorname{diag}\{-1, 0, Q_k^{-1}, 0, 0, 0\} \\ &\quad - \lambda_5 \operatorname{diag}\{-1, 0, 0, I, 0, 0\} - \lambda_6 \operatorname{diag}\{-1, 0, 0, 0, R_{k+1}^{-1}, 0\} \\ &\quad - \lambda_7 \operatorname{diag}\{-\delta, 0, 0, 0, 0, I\} \leqslant 0. \end{aligned} \tag{56}$$

Equation 45 is equivalent to

$$\Phi_{k+1}^T P_{k+1}^{-1} \Phi_{k+1} + \Xi_{k+1} \leqslant 0 \tag{57}$$

where

$$\begin{aligned} \Xi_{k+1} = \operatorname{diag}\{&\lambda_3 + \lambda_4 + \lambda_5 + \lambda_6 + \lambda_7\delta - 1, -\lambda_3 I, -\lambda_4 Q_k^{-1}, -\lambda_5 I, \\ &-\lambda_6 R_{k+1}^{-1}, -\lambda_7 I\}. \end{aligned} \tag{58}$$

Using Lemma 2, the following inequality relationship holds:

$$\begin{bmatrix} \Xi_{k+1} & \Phi_{k+1}^T \\ \Phi_{k+1} & -P_{k+1} \end{bmatrix} < 0. \tag{59}$$

The proof is completed.

Algorithm 1 | ET-DSMF Algorithm.

```
1:  Initialization: Set $\hat{x}_0$, $P_0$ and the maximum number of sampling $k_{\max}$, set $Q_k$, $R_{k+1}$ and triggering thresholds $\varepsilon_i (i = 1, 2, \ldots, m)$.
2:  Solve the optimization problem (19) to get $\hat{u}_{g,k+1}$ and $P_{g,k+1}$.
3:  on the basis of $\hat{x}_k$ and $P_k$, obtain predicted ellipsoid $\phi_{k+1|k}$ and $\lambda_i (i = 1, 2)$ by solving (24).
4:  With the obtained $\hat{x}_k$, $P_k$, and $\phi_{k+1|k}$ ,solving convex optimization problem (49) to obtain $K_{k+1}$, $P_{k+1}$ and $\lambda_i (i = 3, 4, \ldots, 7)$.
5:  With the obtained $\hat{x}_k$ and $K_{k+1}$, compute $\hat{x}_{k+1}$ by (47).
6:  Set $k = k + 1$, if $k > k_{\max}$, exit. Otherwise, go to step 2.
```

In order to more clearly show the filtering algorithm in this article, the ET-DSMF algorithm is summarized as in **Algorithm 1**.

Remark 3: It is worth mentioning that the filtering algorithms under the Kalman framework are studied based on the assumption that the noises obey Gaussian distribution (Yang and Li, 2009). However, because the distribution network is located at the end of the power system and there is serious electromagnetic interference, the above assumption is not in line with the actual project. In fact, compared with the statistical characteristics of noises, it is easier for us to know its boundaries. Fortunately, set-membership filtering can effectively deal with this unknown but bounded noises and provide an estimation set that always surrounds the real states.

Remark 4: In order to alleviate communication pressure and improve the induction phenomenon of measurement data in the transmission process, the event-triggered mechanism is integrated into the design of the set-membership filter. To tackle the effects of σ_k, we employ the prescribed triggering condition which can be rewritten as a quadratic constraint. Subsequently, by using S-procedure, this quadratic constraint can be easily dealt with and reflected in the obtained RLMIs. And the gain matrix and the filter of the optimal estimated ellipsoid are obtained by solving the convex optimization problem.

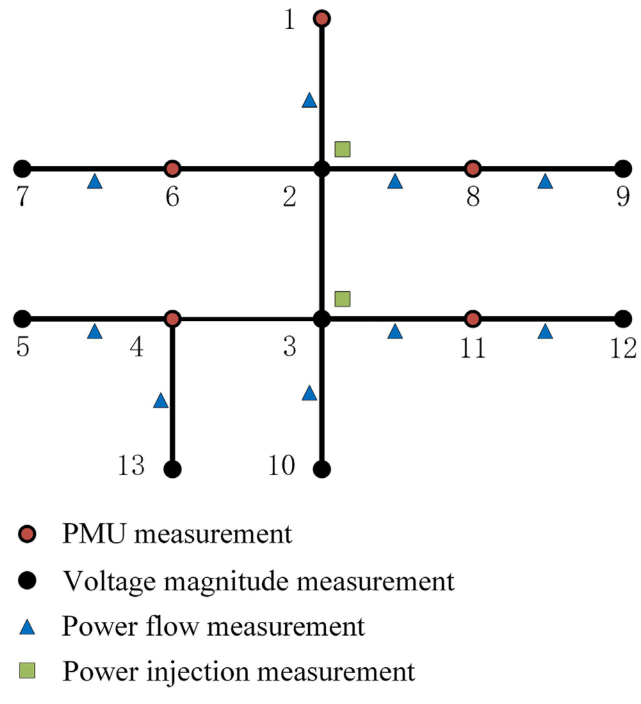

FIGURE 4 | IEEE 13 PDN test system.

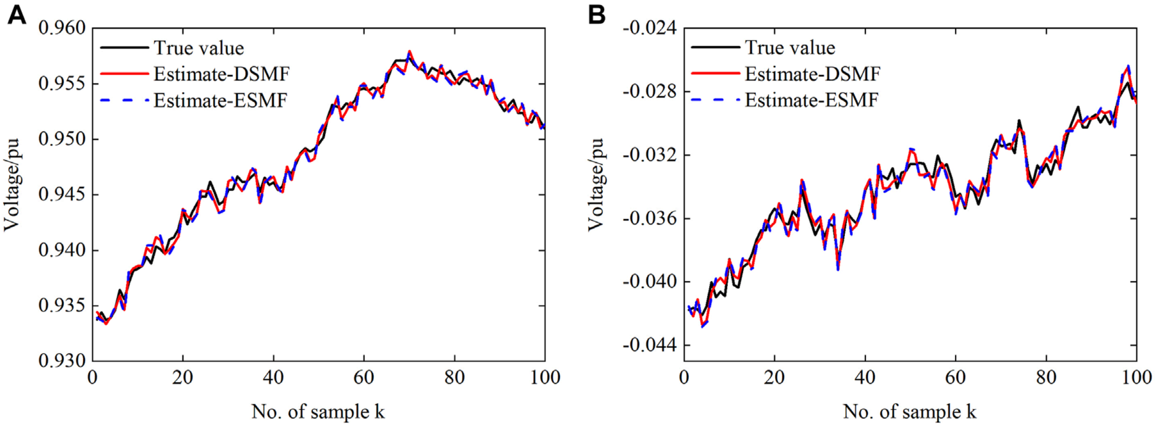

FIGURE 5 | The true and estimated values of a-phase at bus 4: **(A)** the real part of the voltage and **(B)** the imaginary part of the voltage.

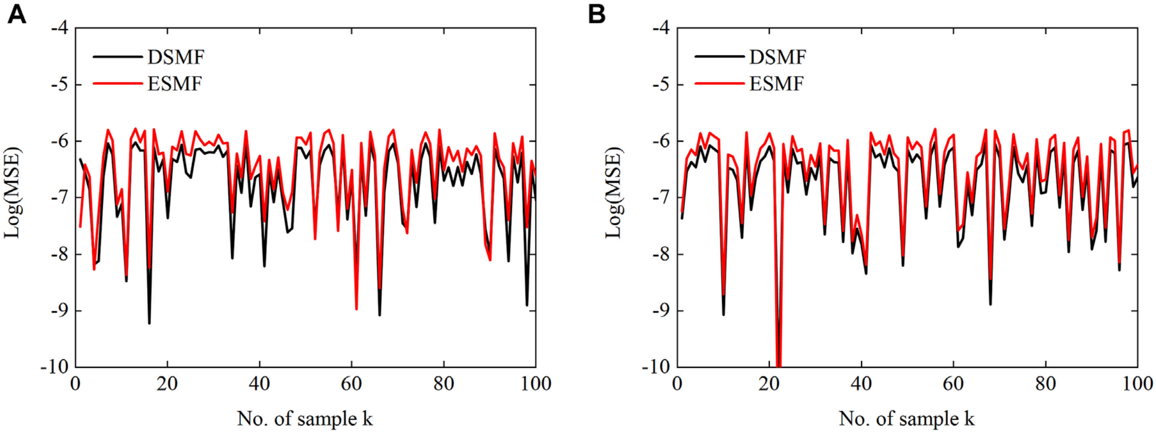

FIGURE 6 | Log(MSE) between the true and estimated values of a-phase at bus 4 for the DSMF and ESMF algorithms: **(A)** the real part of the voltage and **(B)** the imaginary part of the voltage.

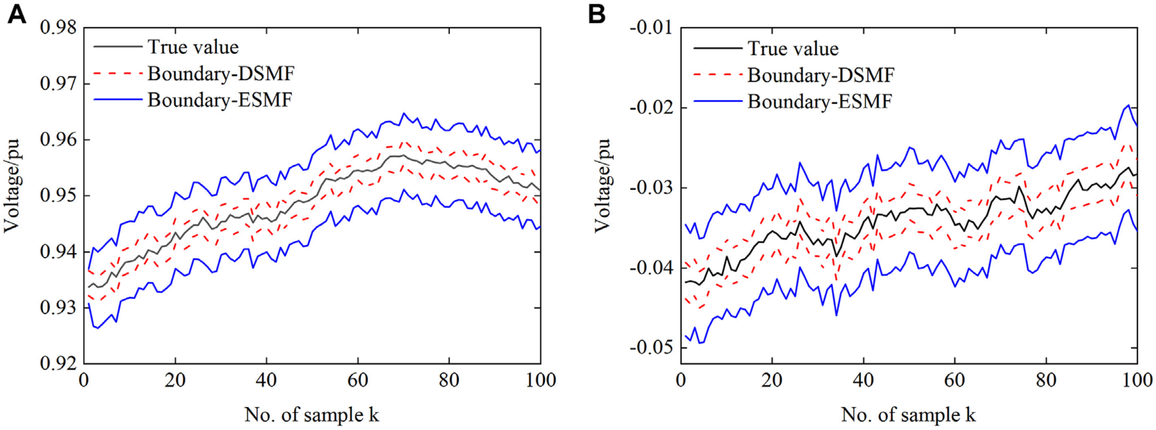

FIGURE 7 | Boundaries between the true and estimated values of a-phase at bus 4: **(A)** the real part of the voltage and **(B)** the imaginary part of the voltage.

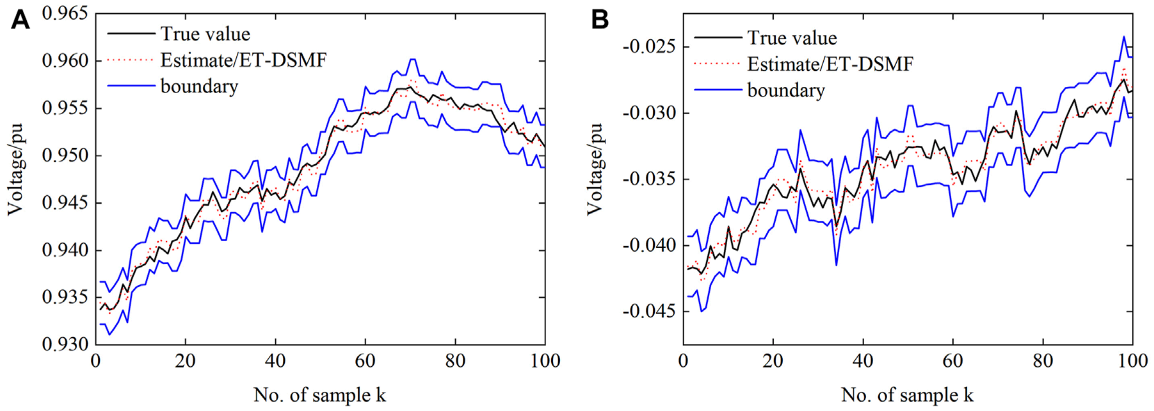

FIGURE 8 | The true and estimated values of a-phase at bus 4: **(A)** the real part of the voltage and **(B)** the imaginary part of the voltage.

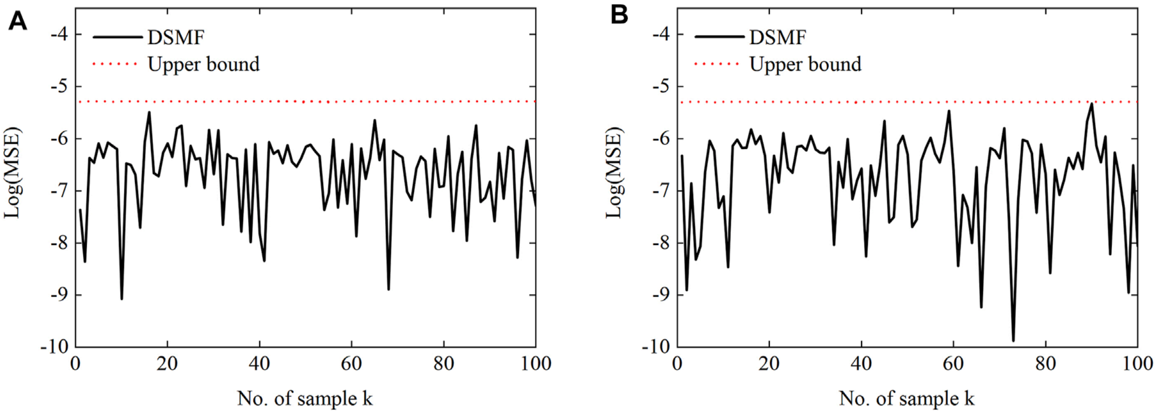

FIGURE 9 | Log(MSE) between the true and estimated values of a-phase at bus 4 for the ET-DSMF algorithm: **(A)** the real part of the voltage and **(B)** the imaginary part of the voltage.

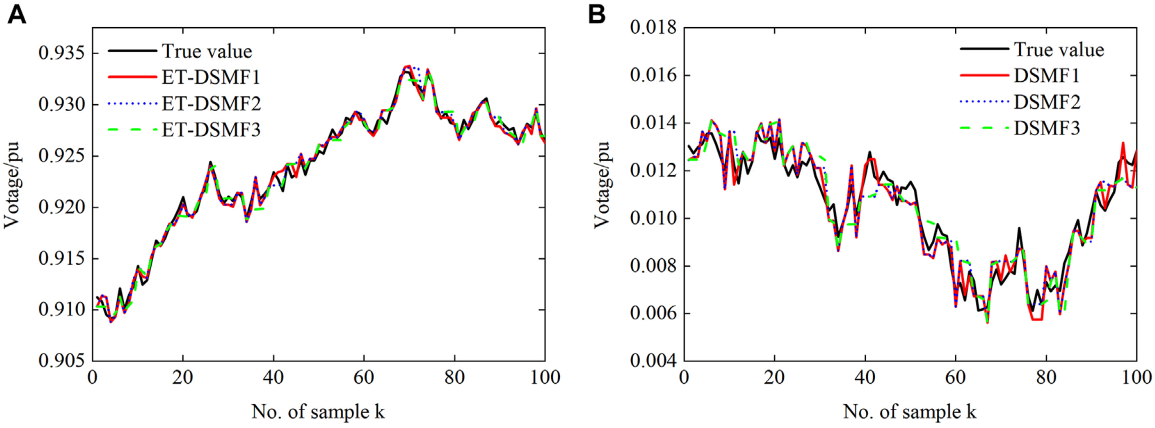

FIGURE 10 | The true and estimated values of c-phase at bus 4: **(A)** the real part of the voltage and **(B)** the imaginary part of the voltage.

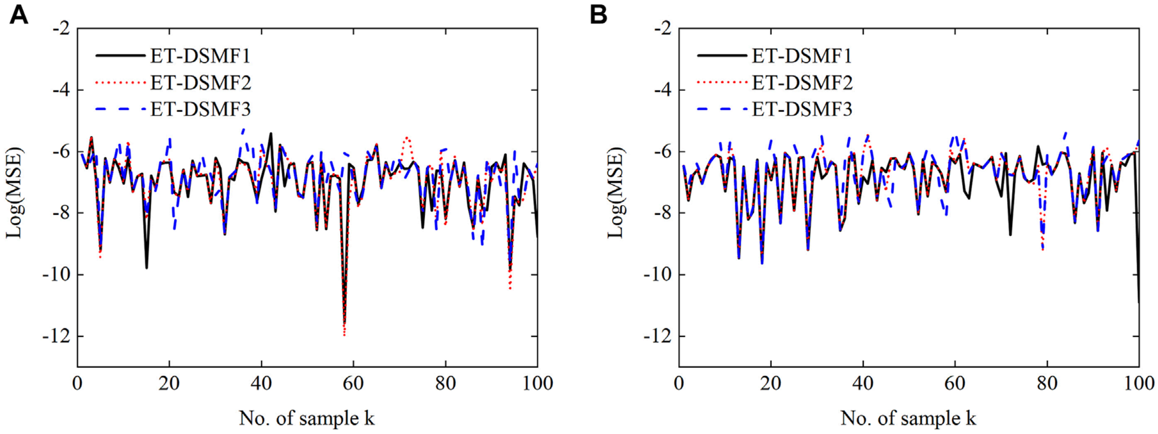

FIGURE 11 | Log(MSE) between the true and estimated values of c-phase at bus 4 for the ET-DSMF algorithm: **(A)** the real part of the voltage and **(B)** the imaginary part of the voltage.

5 SIMULATION

In this section, The IEEE 13 PDN test system is employed for simulation to verify the effectiveness of the ET-DSMF algorithm. The algorithm is implemented in MATLAB R2018b. The topology and the nominal data of the network are obtained from Kersting (1991). The measurement configuration is shown in **Figure 4**, where the PMUs are deployed at buses 1, 4, 6, 8, and 11. At the beginning, the power flow calculation result is taken as the real value of the state, and the measurement is obtained by superimposing the corresponding UBB noise on the power flow calculation result of the online test system. Moreover, the process equation is obtained by the Holt-Winters two-parameter exponential smoothing method with $\alpha = 0.9, \beta = 0.1$. Let the shape matrix of the initial state be $P_0 = 4\times10^{-3}I$. The process noise is set as $Q_k = 6\times10^{-3}$, and measurement noise parameters are set as $R_k^{PMU} = 2\times10^{-6}$ and $R_k^{DRTU} = 2\times10^{-4}$, respectively. Furthermore, the mean square error (MSE) is introduced in this article to more intuitively reflect the accuracy of the state estimation, i.e., $\mathrm{MSE}_i(k) = (1/k_{\max})\sum_{k=1}^{k_{\max}}(x_{i,k}-\hat{x}_{i,k})^2$, where $k_{\max}$ represents the number of samples. The transmission rate is defined as the number of transmission measurements divided by all sampling times and described by variables κ.

5.1 Comparison of Dual Set-Membership Filter and Extended Set-Membership Filter

Figures 5–7 show the performance of the DSMF and ESMF algorithms, taking the simulation results of a-phase at bus 4 as an example. It can be seen that both algorithms can achieve good estimation results. However, the MSE generated by the method proposed in this article is smaller. As shown in **Figure 7**, although the estimated boundaries obtained by the two algorithms can contain the real state, the proposed algorithm is less conservative owing to considering the compact linearization error ellipsoid. It is obvious that the boundary obtained by the DSMF algorithm is more compact than that obtained by the ESMF.

5.2 Verification of Event-Triggered Dual Set-Membership Filter Algorithm

Firstly, the event-triggering threshold is set as $\varepsilon_i = 5\times10^{-6}$. **Figure 8** shows the state estimation ellipsoid center and boundary of the ET-DSMF algorithm, where $\kappa = 83\%$. Although the estimation performance of the proposed algorithm degrades at a lower transmission rate, it ensures that the real state always resides in the estimation ellipsoid because the effective information is transmitted to the estimation center. In order to show the filtering results more clearly, **Figure 9** shows the MSEs

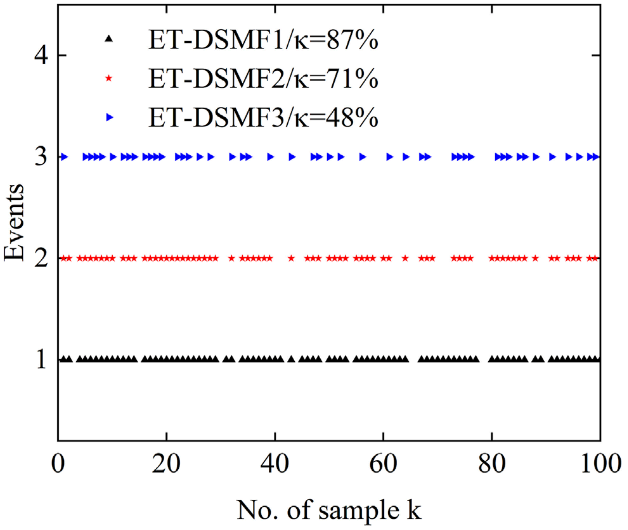

FIGURE 12 | Triggering sequences under different triggering threshold parameters.

generated by the proposed algorithm. It can be seen that the estimation error is always below the minimum upper bound and close to the upper bound, which further shows the low conservatism of the proposed algorithm.

5.3 Influence of Different Triggering Threshold Parameters

In order to verify the influence of the different triggering thresholds on the performance of the ET-DSMF algorithm, different triggering threshold parameters are selected, i.e., ET-DSMF1 with $\varepsilon_i = 4 \times 10^{-6}$, ET-DSMF2 with $\varepsilon_i = 6 \times 10^{-6}$, and ET-DSMF3 with $\varepsilon_i = 8 \times 10^{-6}$. **Figure 10** and **Figure 11** show the filtering curves and MSEs of c-phase at bus 4 under three different threshold parameters. In addition, to more clearly show the triggering time, the triggering sequences is shown in **Figure 12**. With the increase of the triggering threshold, the MSE of the ET-DSMF algorithm increases and the data transmission data decreases accordingly. Therefore, selecting the appropriate triggering threshold parameters can effectively alleviate the pressure of network communication and reduce the probability of network-induced phenomenon.

6 CONCLUSION

In this article, an event-triggered dual set-membership filtering algorithm is proposed. Firstly, considering the uncertainty caused by the linearization error, the approximate distribution range of linearization error is determined by the random sampling method, and the compact ellipsoid boundary of the linearization error is obtained by solving the dual problem of the semi-infinite programming, so as to reduce the conservatism of error boundary. Then, an event-triggered mechanism is introduced to reduce the communication burden. Finally, sufficient conditions for the existence of filter parameters are derived by lemmas, and the optimal state feasible set with ellipsoid as boundary is obtained by the semi-definite programming method. The simulation results show that the proposed method can still ensure good filtering performance even at a low transmission rate. In the future research, in order to further improve information transmission efficiency, we will integrate the dynamic event-triggered mechanism into the algorithm design of the PDNs set-membership state estimation. Moreover, in view of the extensive research on new energy grid connection, including wind and photovoltaic power generation, we will carry out distributed state estimation for the active PDNs combined with the algorithm proposed in this article.

DATA AVAILABILITY STATEMENT

The original contributions presented in the study are included in the article/Supplementary Material, and further inquiries can be directed to the corresponding author.

AUTHOR CONTRIBUTIONS

XB and XJ contributed to the conception and design of the study. MD performed the method analysis. GL wrote the first draft of the manuscript. XB, JL, and XZ wrote sections of the manuscript. All authors contributed to manuscript revision, read, and approved the submitted version.

REFERENCES

Alamo, T., Bravo, J. M., and Camacho, E. F. (2005). Guaranteed State Estimation by Zonotopes. *Automatica* 41, 1035–1043. doi:10.1016/j.automatica.2004.12.008

Bai, X., Wang, Z., Zou, L., and Cheng, C. (2018). Target Tracking for Wireless Localization Systems with Degraded Measurements and Quantization Effects. *IEEE Trans. Ind. Electron.* 65, 9687–9697. doi:10.1109/tie.2018.2813982

Bai, X., Wang, Z., Zou, L., and Zhang, Z. (2021a). Target Tracking for Wireless Localization Systems Using Set-Membership Filtering: A Component-Based Event-Triggered Mechanism. *Automatica* 132, 109795. doi:10.1016/j.automatica.2021.109795

Bai, X., Zheng, X., Ge, L., Qin, F., and Li, Y. (2021b). Event-triggered Forecasting-Aided State Estimation for Active Distribution System with Distributed Generations. *Front. Energ. Res.* 9, 327. doi:10.3389/fenrg.2021.707183

Becis-Aubry, Y., Boutayeb, M., and Darouach, M. (2008). State Estimation in the Presence of Bounded Disturbances. *Automatica* 44, 1867–1873. doi:10.1016/j.automatica.2007.10.033

Boyd, S., El Ghaoui, L., Feron, E., and Balakrishnan, V. (1994). *Linear Matrix Inequalities in System and Control Theory*. Philadelphia, PA: SIAM, Studies in Applied Mathematics.

Calafiore, G. (2005). Reliable Localization Using Set-Valued Nonlinear Filters. *IEEE Trans. Syst. Man. Cybern. A.* 35, 189–197. doi:10.1109/tsmca.2005.843383

Cerone, V., Lasserre, J.-B., Piga, D., and Regruto, D. (2014). A Unified Framework for Solving a General Class of Conditional and Robust Set-Membership Estimation Problems. *IEEE Trans. Automat. Contr.* 59, 2897–2909. doi:10.1109/TAC.2014.2351695

Ćetenović, D., Ranković, A., Zhao, J., Jin, Z., Wu, J., and Terzija, V. (2021). An Adaptive Method for Tuning Process Noise Covariance Matrix in Ekf-Based Three-phase Distribution System State Estimation. *Int. J. Electr. Power Energ. Syst.* 132, 107192. doi:10.1016/j.ijepes.2021.107192

Cheng, C., and Bai, X. (2021). Robust Forecasting-Aided State Estimation in Power Distribution Systems with Event-Triggered Transmission and Reduced Mixed Measurements. *IEEE Trans. Power Syst.* 36, 4343–4354. doi:10.1109/TPWRS.2021.3062386

Cheng, C., Bai, X., Zhang, Q., and Huang, C. (2018). Set-membership Filtering for Generator Dynamic State Estimation with Delayed Measurements. *Syst. Sci. Control. Eng.* 6, 35–43. doi:10.1080/21642583.2018.1531794

Dehghanpour, K., Wang, Z., Wang, J., Yuan, Y., and Bu, F. (2019). A Survey on State Estimation Techniques and Challenges in Smart Distribution Systems. *IEEE Trans. Smart Grid* 10, 2312–2322. doi:10.1109/TSG.2018.2870600

Ding, D., Wang, Z., and Han, Q.-L. (2020). A Set-Membership Approach to Event-Triggered Filtering for General Nonlinear Systems over Sensor Networks. *IEEE Trans. Automat. Contr.* 65, 1792–1799. doi:10.1109/TAC.2019.2934389

Fang, Z., Lin, Y., Song, S., Song, C., Lin, X., and Cheng, G. (2020). Active Distribution System State Estimation Incorporating Photovoltaic Generation System Model. *Electric Power Syst. Res.* 182, 106247. doi:10.1016/j.epsr.2020.106247

Ge, X., Han, Q.-L., and Wang, Z. (2019). A Dynamic Event-Triggered Transmission Scheme for Distributed Set-Membership Estimation over Wireless Sensor Networks. *IEEE Trans. Cybern.* 49, 171–183. doi:10.1109/TCYB.2017.2769722

Gubarev, V. F., and Melnichuk, S. V. (2015). Guaranteed State Estimation Algorithms for Linear Systems in the Presence of Bounded Noise. *J. Automat Inf. Scien* 47, 1–10. doi:10.1615/JAutomatInfScien.v47.i3.10

Hu, J., Wang, Z., Liu, G.-P., Zhang, H., and Navaratne, R. (2021). A Prediction-Based Approach to Distributed Filtering with Missing Measurements and Communication Delays through Sensor Networks. *IEEE Trans. Syst. Man. Cybern, Syst.* 51, 7063–7074. doi:10.1109/TSMC.2020.2966977

Ji, X., Yin, Z., Zhang, Y., Wang, M., Zhang, X., Zhang, C., et al. (2021). Real-time Robust Forecasting-Aided State Estimation of Power System Based on Data-Driven Models. *Int. J. Electr. Power Energ. Syst.* 125, 106412. doi:10.1016/j.ijepes.2020.106412

Jin, Z., Zhao, J., Chakrabarti, S., Ding, L., and Terzija, V. (2020). A Hybrid Robust Forecasting-Aided State Estimator Considering Bimodal Gaussian Mixture Measurement Errors. *Int. J. Electr. Power Energ. Syst.* 120, 105962. doi:10.1016/j.ijepes.2020.105962

Kersting, W. H. (1991). Radial Distribution Test Feeders. *IEEE Trans. Power Syst.* 6, 975–985. doi:10.1109/59.11923710.1109/59.119237

Kühn, W. (1998). Rigorously Computed Orbits of Dynamical Systems without the Wrapping Effect. *Computing* 61, 47–67. doi:10.1109/TAC.2019.2934389

Liu, S., Wang, Z., Wei, G., and Li, M. (2020). Distributed Set-Membership Filtering for Multirate Systems under the Round-Robin Scheduling over Sensor Networks. *IEEE Trans. Cybern.* 50, 1910–1920. doi:10.1109/TCYB.2018.2885653

Liu, X., Li, L., Li, Z., Chen, X., Fernando, T., Iu, H. H.-C., et al. (2017). Event-trigger Particle Filter for Smart Grids with Limited Communication Bandwidth Infrastructure. *IEEE Trans. Smart Grid* 9, 6918–6928. doi:10.1109/TSG.2017.2728687

Liu, Y., Zhao, Y., and Wu, F. (2016). Ellipsoidal State-bounding-based Set-membership Estimation for Linear System with Unknown-but-bounded Disturbances. *IET Control. Theor. Appl.* 10, 431–442. doi:10.1049/iet-cta.2015.0654

Martin, K. E., Hamai, D., Adamiak, M. G., Anderson, S., Begovic, M., Benmouyal, G., et al. (2008). Exploring the IEEE Standard C37.118-2005 Synchrophasors for Power Systems. *IEEE Trans. Power Deliv.* 23, 1805–1811. doi:10.1109/tpwrd.2007.916092

Mohammadrezaee, R., Ghaisari, J., Yousefi, G., and Kamali, M. (2021). Dynamic State Estimation of Smart Distribution Grids Using Compressed Measurements. *IEEE Trans. Smart Grid* 12, 4535–4542. doi:10.1109/TSG.2021.3071514

Peng, C., and Li, F. (2018). A Survey on Recent Advances in Event-Triggered Communication and Control. *Inf. Sci.* 457-458, 113–125. doi:10.1016/j.ins.2018.04.055

Ping, X., Yang, S., Ding, B., Raïssi, T., and Li, Z. (2020). Observer-based Output Feedback Robust Mpc *via* Zonotopic Set-Membership State Estimation for Lpv Systems with Bounded Disturbances and Noises. *J. Franklin Inst.* 357, 7368–7398. doi:10.1016/j.jfranklin.2020.05.014

Qing, X., Yang, F., and Wang, X. (2013). Extended Set-Membership Filter for Power System Dynamic State Estimation. *Electric Power Syst. Res.* 99, 56–63. doi:10.1016/j.epsr.2013.02.002

Qu, B., Wang, Z., and Shen, B. (2021). Fusion Estimation for a Class of Multi-Rate Power Systems with Randomly Occurring Scada Measurement Delays. *Automatica* 125, 109408. doi:10.1016/j.automatica.2020.109408

Scholte, E., and Campbell, M. E. (2003). A Nonlinear Set-Membership Filter for On-Line Applications. *Int. J. Robust Nonlinear Control.* 13, 1337–1358. doi:10.1002/rnc.856

Schweppe, F. (1968). Recursive State Estimation: Unknown but Bounded Errors and System Inputs. *IEEE Trans. Automat. Contr.* 13, 22–28. doi:10.1109/tac.1968.1098790

Tan, H., Shen, B., and Shu, H. (2021). Robust Recursive Filtering for Stochastic Systems with Time-Correlated Fading Channels. *IEEE Trans. Syst. Man. Cybern, Syst.* 1, 1. doi:10.1109/TSMC.2021.3062848

Vandenberghe, L., and Boyd, S. (1996). Semidefinite Programming. *SIAM Rev.* 38, 49–95. doi:10.1137/1038003

Wang, S., Zhao, J., Huang, Z., and Diao, R. (2018). Assessing Gaussian assumption of Pmu Measurement Error Using Field Data. *IEEE Trans. Power Deliv.* 33, 3233–3236. doi:10.1109/TPWRD.2017.2762927

Wang, X., Zhao, J., Terzija, V., and Wang, S. (2020). Fast Robust Power System Dynamic State Estimation Using Model Transformation. *Int. J. Electr. Power Energ. Syst.* 114, 105390. doi:10.1016/j.ijepes.2019.105390

Wang, Z., Shen, X., Liu, H., Meng, F., and Zhu, Y. (2021). Dual Set Membership Filter with Minimizing Nonlinear Transformation of Ellipsoid. *IEEE Trans. Automat. Contr.*, 1. doi:10.1109/TAC.2021.3081078

Wang, Z., Shen, X., Zhu, Y., and Pan, J. (2018). A Tighter Set-Membership Filter for Some Nonlinear Dynamic Systems. *IEEE Access* 6, 25351–25362. doi:10.1109/ACCESS.2018.2830350

Wei, G., Liu, S., Song, Y., and Liu, Y. (2015). Probability-guaranteed Set-Membership Filtering for Systems with Incomplete Measurements. *Automatica* 60, 12–16. doi:10.1016/j.automatica.2015.06.037

Yang, F., and Li, Y. (2009). Set-membership Filtering for Systems with Sensor Saturation. *Automatica* 45, 1896–1902. doi:10.1016/j.automatica.2009.04.011

Yu, W., Zamora, E., and Soria, A. (2016). Ellipsoid Slam: a Novel Set Membership Method for Simultaneous Localization and Mapping. *Auton. Robot* 40, 125–137. doi:10.1007/s10514-015-9447-y

Zhang, J., Bai, X., Zheng, X., Li, M., Qin, F., and Shi, Y. (2020a). Event-trigger Extended Set-Membership Filter for Power Distribution Network Dynamic State Estimation. *2020 Chinese Automation Congress*, 369–374. doi:10.1109/CAC51589.2020.9327219

Zhang, S., Liu, L.-G., and Li, H. (2020b). Gic Influence on Uhv Power Grids Based on Kalman Filter and Wams Data. *IEEE Access* 8, 202379–202386. doi:10.1109/ACCESS.2020.3036009

Zhang, Y., and Wang, J. (2020). Towards Highly Efficient State Estimation with Nonlinear Measurements in Distribution Systems. *IEEE Trans. Power Syst.* 35, 2471–2474. doi:10.1109/TPWRS.2020.2967173

Zhao, J., and Mili, L. (2017). Robust Unscented Kalman Filter for Power System Dynamic State Estimation with Unknown Noise Statistics. *IEEE Trans. Smart Grid* 10, 1215–1224. doi:10.1049/iet-gtd.2019.0031

Zhao, J., Netto, M., and Mili, L. (2017). A Robust Iterated Extended Kalman Filter for Power System Dynamic State Estimation. *IEEE Trans. Power Syst.* 32, 3205–3216. doi:10.1109/TPWRS.2016.2628344

Zou, L., Wang, Z., Hu, J., Liu, Y., and Liu, X. (2021). Communication-protocol-based Analysis and Synthesis of Networked Systems: Progress, Prospects and Challenges. *Int. J. Syst. Sci.* 1, 721. doi:10.1080/00207721.2021.1917721

Conflict of Interest: The authors declare that the research was conducted in the absence of any commercial or financial relationships that could be construed as a potential conflict of interest.

frontiers | Frontiers in Energy Research

ORIGINAL RESEARCH
published: 23 May 2022
doi: 10.3389/fenrg.2022.883004

Reducing Submodule Capacitance for Modular Multilevel Converter-Based Medium-Voltage Wind Power Converter

Jianhang Qian, Zhijie Liu, Ke-Jun Li, Liangzi Li and ZhongLin Guo*

School of Electrical Engineering, Shandong University, Jinan, China

This study presents a strategy to reduce the capacitance of the submodule (SM) capacitor of a modular multilevel converter-based medium-voltage wind power converter. The design of the SM capacitor of the modular multilevel converter (MMC) should consider the actual operating conditions, especially the influence of wind speed, because wind speed will affect the voltage ripple and voltage amplitude of the SM capacitor. In the traditional method, the capacitance design of the SM capacitor will be based on relatively high wind speed and leave a certain safety margin. However, in most cases, the system operates at the highest-frequency wind speed (HFWS). For the MMC-based wind energy conversion system, a constant capacitor voltage ripple (CCVR) control method is proposed. Using this method, the SM capacitor voltage ripple can be significantly reduced by injecting the second harmonic component of circulating current. In this way, the SM capacitor with smaller capacitance can be used. Finally, the effectiveness of the proposed method is validated in RT-Lab Platform.

Keywords: modular multilevel converter, most frequency wind speed, capacitor voltage ripple, wind energy conversion, circulating current

Edited by:
Sudhakar Babu Thanikanti,
Chaitanya Bharathi Institute of Technology, India

Reviewed by:
Mohamed Salem,
Universiti Sains Malaysia (USM), Malaysia
Nishant Kumar,
National University of Singapore, Singapore

****Correspondence:***
Zhijie Liu
liuzj@sdu.edu.cn

Specialty section:
This article was submitted to Smart Grids, a section of the journal Frontiers in Energy Research

Received: *24 February 2022*
Accepted: *19 April 2022*
Published: *23 May 2022*

Citation:
Qian J, Liu Z, Li K-J, Li L and Guo Z (2022) Reducing Submodule Capacitance for Modular Multilevel Converter-Based Medium-Voltage Wind Power Converter. Front. Energy Res. 10:883004. doi: 10.3389/fenrg.2022.883004

1 INTRODUCTION

Energy and environmental problems are tied to human development. Conventional energy is non-renewable and can cause environmental pollution. The development of renewable energy, especially wind energy, has attracted more and more attention (Li et al., 2018; Ghosh et al., 2020; Yang et al., 2022). With the continuous progress of wind power generation technology, the capacity of wind energy conversion systems is also gradually increasing. At present, the mainstream wind power generation system of offshore wind farms has reached the megawatt level (Cortes-Vega et al., 2021; Xue et al., 2021). Compared with small-capacity wind turbines, large-capacity wind turbines have obvious advantages, such as low maintenance cost and stronger ability to capture wind energy. During the past 30 years, the size and capacity of the wind energy conversion system have exponentially increased. Some manufacturers have even started to develop wind energy conversion systems with a capacity of 10MWs (Rebello et al., 2019).

Permanent magnet synchronous generators (PMSGs) and full-scale power converters have been widely adopted in the megawatt wind power generation system (Tao et al., 2019; Khan et al., 2019). The gearbox, which is a part of a wind turbine, can be gotten rid of. It is known that the gearbox is prone to overload and has a high damage rate. Therefore, this kind of wind energy conversion has many advantages, such as high efficiency, low noise, long lifetime, low maintenance cost, and so on (Hu et al., 2020).

However, with the continuous increment of the capacity, the traditional two-level and three-level converter cannot meet the needs of high-capacity wind power generation systems. The increment of capacity promotes the development of the voltage level, and the medium voltage level has become the mainstream voltage level for turbines with rated power greater than 3.0 MW (Khanzadeh et al., 2021).

Compared with the traditional two voltage source converters, MMC has the following significant advantages (Xiao et al., 2021; Dekka et al., 2017).

(1) The change rate of bridge arm voltage and current is low, which reduces the impact of IGBT and other semiconductor devices in the switching transient process and ensures their safe and stable operation.
(2) For MMC with high voltage and large capacity, the number of SMs is large, the waveform of voltage step wave is good, the quality is high, the harmonic component is very low, and there is no need for filter.
(3) The modular structure is easy to expand and transform and can meet the needs of increasingly complex power systems and various engineering needs in practice.

With the progress of related technologies, MMC has been widely used in offshore wind power generation and high-voltage direct current (HVDC) technology (Ronanki and Williamson, 2018).

However, different from the traditional two-level and three-level converters, the capacitor of the MMC is not directly connected to the DC bus. Its capacitor is installed in the submodule (SM) (Li et al., 2022). During the operation of the MMC, the arm current will pass through the SM capacitors. This will cause the fluctuation of the capacitor voltage. Normally, the capacitor voltage ripple should not increase 10% of the nominal capacitor voltage; otherwise, the overvoltage can result in the breakdown of semiconductors and capacitors (Liu et al., 2019). As a result, the capacitor with large capacitance is usually required in the MMC. The large capacitor can increase not only the cost but also the space of the converter.

In this study, a constant capacitor voltage ripple (CCVR) control for MMC-based medium-voltage wind power converters is proposed. It is found that the SM capacitor voltage ripple can be suppressed by injecting the second harmonic component of circulating current; in this way, the capacitance of the SM capacitor can be reduced. Therefore, the following work is done in this study.

1) Through the analysis of the wind farm, it is found that there exists the most-frequency wind speed (MFWS) in the wind farm, and the MMC-based wind energy conversion system operates at this wind speed most of the time (Groch and Vermeulen, 2019). However, the capacitance of the SM capacitor is selected and designed under the maximum wind speed, which will cause a waste of cost and volume. Based on this, a new method regarding the capacitance of SM capacitor selection and design is proposed, that is, the capacitance of the SM capacitor will be selected under the MFWS. But, when the wind speed increases, the voltage ripple of the SM capacitor will also rise, so there exists a certain risk.

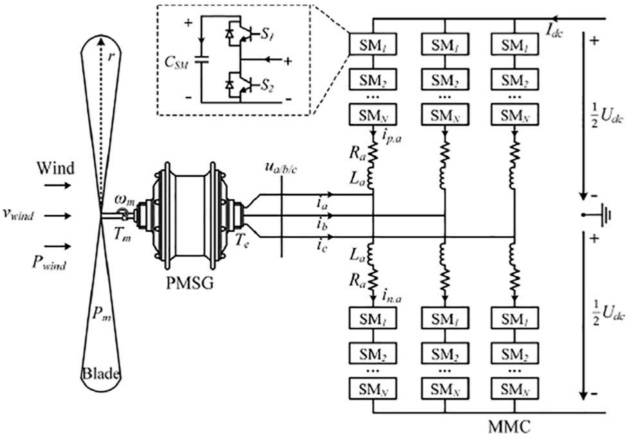

FIGURE 1 | Diagram of the MMC-based wind energy conversion system.

2) Injecting the second harmonic component of the circulating current into the MMC can reduce the voltage ripple of the SM capacitor, and the effect will be affected by the circulating current amplitude and phase angle. On the premise that the amplitude of the injected circulating current is fixed, the injection angle of the circulating current is changed, and it is found that under different wind speeds, each injected circulating current amplitude has an optimal angle. Under this optimal injection angle, the weakening effect on the SM capacitor voltage ripple is the largest.
3) Based on the above research conclusions, CCVR control for the MMC-based wind energy conversion system strategy is proposed. On the premise of the optimal injection phase angle, injecting the corresponding circulating current amplitude can keep the capacitor voltage ripple of the SM constant. Compared with the traditional method, the proposed method significantly reduces the SM capacitor voltage ripple. On the premise of the proposed method, the capacitance of the SM capacitor will be designed and selected under the MFWS, which greatly reduces the cost and volume of the equipment, and there is no need to worry about the SM capacitor damage caused by too high voltage ripple.

The rest of the article is organized as follows. The foundations of the MMC-based wind energy conversion system are explained in **Section 2**. The operation of wind farms is analyzed, and the concept of the most-frequency wind speed is put forward in **Section 3**. The relationship between circulating current injection and capacitor voltage fluctuation is analyzed in **Section 4**. **Section 5** analyzes the influence of the amplitude and phase angle of the circulating current on the SM capacitor voltage ripple. **Section 6** proposes a CCVR control for the MMC-based wind energy conversion system, and the effectiveness was analyzed using RT-Lab. The conclusions are summarized in Section 7.

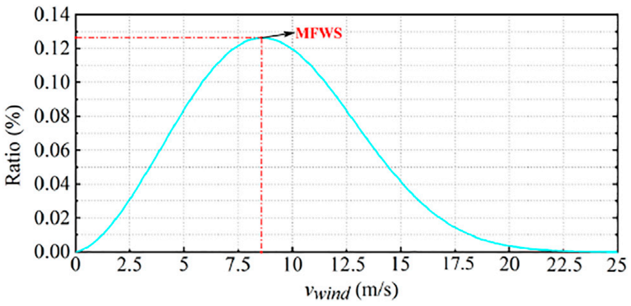

FIGURE 2 | Wind speed–frequency distribution.

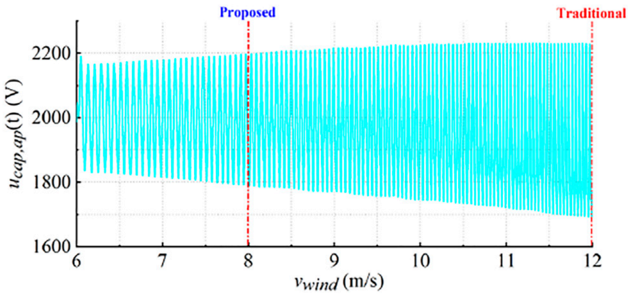

FIGURE 3 | Capacitor voltage under different wind speeds.

2 FOUNDATIONS

Figure 1 shows the diagram of the MMC-based wind energy conversion system. Under the action of blades, wind energy is converted into mechanical energy, which is then converted into electric energy through the PMSG. Finally, under the rectification of MMC, AC power is converted to DC power, and the electrical power is transferred from the PMSG to the DC bus (Singh et al., 1947; Ronanki and Williamson, 2018; Priya et al., 2019).

In **Figure 1**, v_{wind} is the wind speed. The wind energy determines the mechanical torque T_m and rotor speed ω_m of the PMSG. The output voltage and current of the PMSG are denoted by $u_a(t)$ and $i_a(t)$, respectively. The currents in the upper and lower arms of the MMC are denoted by $i_{p,a}(t)$ and $i_{n,a}(t)$, respectively, and $u_{cap.ap}(t)$ and $u_{cap.an}(t)$ are the capacitor voltage in the upper and lower arms, respectively.

In **Figure 1**, the wind speed is denoted by v_{wind}. The wind energy determines the mechanical torque T_m and rotor speed ω_m of the PMSG. Phase A is taken as an example. The output voltage and current of the PMSG are denoted by $u_a(t)$ and $i_a(t)$, respectively. The currents in the upper and lower arms of the MMC are denoted by $i_{p,a}(t)$ and $i_{n,a}(t)$, respectively. The capacitor voltage in the upper and lower arms is denoted by $u_{cap.ap}(t)$ and $u_{cap.an}(t)$, respectively.

The frequency of the MMC connected to the PMSG is affected by the number of poles in the generator and is also affected by the mechanical angular speed, that is,

$$\omega = \omega_r = p\omega_m, \tag{1}$$

where ω is the angular speed of the MMC; ω_r is the electrical angular speed of the rotor in the PMSG; p is the number of pole pairs.

The AC-side voltage and current of the MMC can be expressed as follows:

$$\begin{cases} u_a(t) = U_s \cos(\omega t + \alpha), \\ i_a(t) = I_s \cos(\omega t + \beta), \end{cases} \tag{2}$$

where U_s is the amplitude of the output voltage and α is the phase angle of the output voltage; I_s and β are the amplitude and the phase angle of the phase current.

In the wind energy conversion system, the relationship between the output current of the MMC and the electromagnetic torque of the PMSG can be expressed as in **Eq. 3**.

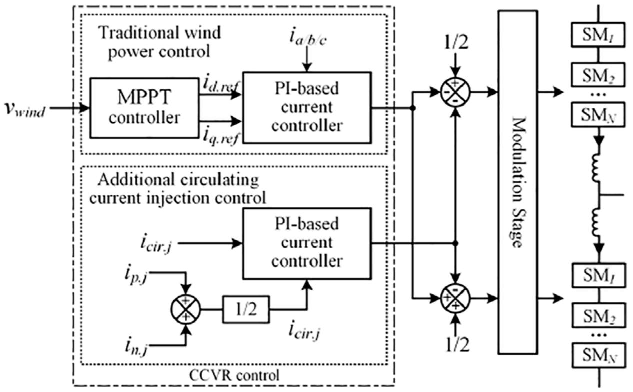

FIGURE 4 | CCVR control for the MMC-based wind energy conversion system.

$$T_e(t) = \frac{3}{2}p\left[\lambda_m i_q(t) - \left[L_d - L_q\right]i_d(t)i_q(t)\right], \tag{3}$$

where $i_d(t)$ and $i_q(t)$ denote the AC-side phase currents in the d-q frame.

From **Eq. 3**, the electromagnetic torque of the PMSG can be realized by controlling the output current of the MMC. To remove the coupling between the d-axis and q-axis currents, the d-axis current is controlled to be zero. Then **Eq. 3** can be simplified to **Eq. 4**.

$$\begin{cases} i_d = 0 \\ i_q = \dfrac{2T_e}{3p\lambda_m} \end{cases} \tag{4}$$

In **Eq. 4**, the electromagnetic torque is determined by the wind speed and the parameters of the wind turbine. Their relationship is shown in **Eq. 5** (Jae-Jung Jung et al., 2015):

$$T_e = \frac{\rho A v_{wind}^3}{2\omega_m} C_p\left(\lambda, \beta_{pit}\right), \tag{5}$$

where ρ is the air mass density; A is the area covered by the wind blades; v_{wind} denotes the wind speed; and C_p is the performance coefficient, which is determined by the pitch angle β_{pit} and the tip-to-speed ratio λ.

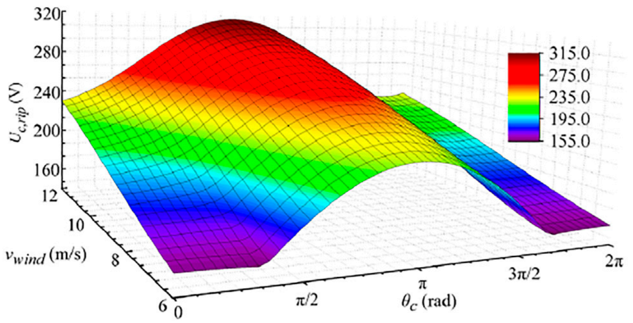

FIGURE 5 | Values of capacitor voltage ripple under the different wind speeds and the different phase angles of circulating current.

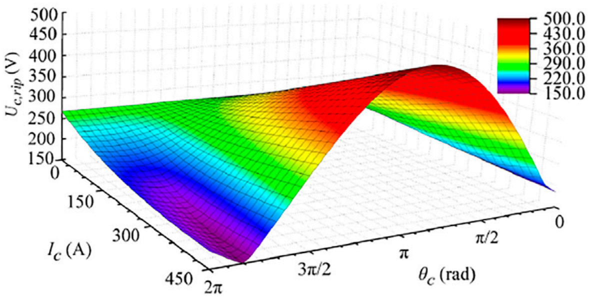

FIGURE 6 | Values of capacitor voltage ripple under the different phase angles and different amplitudes of circulating current.

To realize the maximum power point tracking (MPPT) of the wind energy system, C_p should be its maximum value, which is denoted by $C_{p.max}$. Thus, the reference value of output currents in the d-q frame can be derived, which is shown in **Eq. 6**.

$$\begin{cases} i_{d.ref} = 0 \\ i_{q.ref} = \dfrac{2K_{opt}v_{wind}^2}{3p\lambda_m} \end{cases}, \tag{6}$$

where

$$K_{opt} = \frac{\rho\pi r_{wind}^3 C_{p.max}}{2\lambda_{opt}}, \tag{7}$$

where r_{wind} is the radius of wind blades, and λ_{opt} is the optimum tip-to-speed ratio, which is a constant value and can be obtained from the manufacturer's data.

The arm current of the MMC is composed of the DC component, phase current component, and circulating current component, which is shown in **Eq. 8**:

$$\begin{cases} i_{p.a}(t) = \dfrac{I_{dc}}{3} - \dfrac{i_a(t)}{2} + i_{cir.a}(t) \\ i_{n.a}(t) = \dfrac{I_{dc}}{3} + \dfrac{i_a(t)}{2} + i_{cir.a}(t) \end{cases} \tag{8}$$

and

TABLE 1 | Parameters of the PMSG.

Parameter	Value
Rated power	5 MVA
Rated electrical frequency	25 Hz
Rated wind speed	12 m/s
D-axis inductance L_d	5.3 mH
Q-axis inductance L_q	12.5 mH
Maximum flux λ_m	20 Wb
Number of pole-pairs ρ	100
Rated wind speed	12 m/s

TABLE 2 | Parameters of the MMC.

Parameter	Value
Rated capacity	5 MVA
DC-line voltage U_{dc}	±4000 V
Number of SMs per arm N	4
SM capacitor C_{SM}	5,000 uF
Arm inductance L_a	3 mH
Carrier frequency f_c	2,500 Hz

$$\begin{cases} i_a(t) = I_s\cos(\omega t + \varphi) \\ i_{cir.a}(t) = I_c\cos(2\omega t + \theta_c) \end{cases}, \tag{9}$$

where I_s and φ are the amplitude and the phase angle of phase current, respectively. Ic and θc are the amplitude and the phase angle of the second harmonic circulating current, respectively.

The modulation signal of the MMC is as follows:

$$\begin{cases} S_{up,a}(t) = A_{dc} - A_1\cos(\omega t + \theta_1) - A_2\cos(\omega t + \theta_2) \\ S_{dn,a}(t) = A_{dc} + A_1\cos(\omega t + \theta_1) - A_2\cos(\omega t + \theta_2) \end{cases}, \tag{10}$$

where Adc is the DC component in the modulation signal; A1 and θ1 are the amplitude and the phase angle of the 1ω component in the modulation signal; and A_2 and θ_2 are the amplitude and the phase angle of the 2ω component in the modulation signal.

Taking the upper bridge arm as an example, the capacitor voltages can be derived by integrating the capacitor currents, which is as follows:

$$\begin{aligned} u_{cap.ap}(t) &= U_{cap.0} + \frac{1}{C_{SM}}\int i_{ap}(t)S_{up.a}(t)dt, \\ &= U_{cap.a.dc} + u_{cap.a.1\omega}(t) + u_{cap.a.2\omega}(t) + u_{cap.a.3\omega}(t), \end{aligned} \tag{11}$$

where Ucap.0 is the DC component in the capacitor voltage and CSM is the SM capacitor.

3 MECHANISM OF THE CONSTANT CAPACITOR VOLTAGE RIPPLE CONTROL METHOD

The design of the SM capacitor for the modular multilevel converter should consider the actual operating conditions,

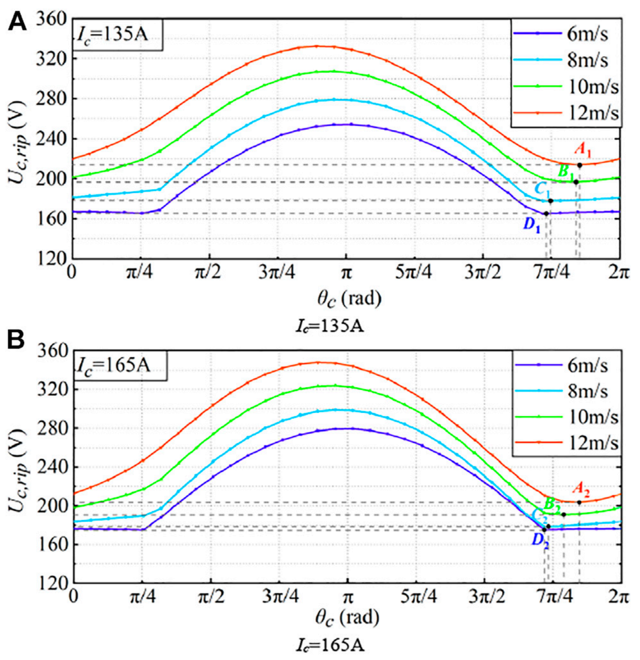

FIGURE 7 | Capacitor voltage ripple under different circulating current phase angles. **(A)** Ic = 165 A. **(B)** Ic = 135 A.

especially the influence of wind speed, because wind speed will affect the voltage ripple and voltage amplitude of the SM capacitor. In the traditional method, the design for the capacitance of the SM capacitor will be based on relatively high wind speed and leave a certain safety margin.

Figure 2 shows the wind speed fitting Weibull curve of a wind farm. It can be seen from the figure that the wind speed in this area is maintained at about 8 m/s most of the time. The wind speed with the highest frequency is defined as MFWS. In the traditional method, the capacitance of the SM capacitor is designed at the highest wind speed, but in the actual operating situation, the equipment operates at the MFWS most of the time, which will cause a waste. Based on this, a new capacitance of the SM capacitor design scheme is proposed, that is, the capacitance of the SM capacitor is selected under the MFWS instead of the highest wind speed, which will greatly reduce the volume and cost of the SM capacitor. However, doing so will create some problems.

Figure 3 shows the change of SM capacitor voltage under different wind speeds. From **Figure 3**, the voltage ripple of the SM capacitor will rise with the increase in wind speed. Suppose the maximum wind speed of a wind farm is 12 m/s and the most-frequency wind speed is 8 m/s. In the traditional method, the capacitance of the SM capacitor is selected and designed under the working condition of v_{wind} = 12 m/s, which can ensure the safe and reliable operation of the equipment. The proposed method is to select and design the capacitance of the SM capacitor under the working condition of v_{wind} = 8 m/s. However, it can be seen from the figure that if it is designed according to the working condition of 8 m/s, the voltage ripple of the SM capacitor will increase and the risk of capacitor breakdown will occur at the high wind speed. Therefore, certain measures need to be taken to avoid the risk of breakdown of the SM capacitor due to high voltage ripple.

Injecting the second harmonic component of the circulating current into the MMC can reduce the voltage ripple of the SM capacitor under certain conditions, so that the SM capacitor breakdown caused by the increase in voltage ripple can be avoided under the proposed method. The specific influence of the frequency doubling component of the injected circulating current on the capacitor voltage ripple will be discussed in the next section.

4 EFFECT OF CIRCULATING CURRENT ON CAPACITOR VOLTAGE RIPPLE

The basic wind power control can be realized based on **Eq. 6** and the proportional-integral (PI)-based current controller (Qingrui Tu et al., 2011), which is shown in **Figure 4**.

From the control block diagram shown in **Figure 4**, the CCVR control for the MMC is composed of two parts. They are the traditional wind power control and an additional circulating current injection control. The traditional wind power control is used to make the wind energy conversion system operate at the MPPT point to maximize conversion efficiency. The additional circulating current injection control is exclusive. Different from two-level converters, the arm current will pass through the SM capacitors in the MMC. With the effect of circular interaction, circulating currents will occur. These currents circulate inside the MMC, and they flow out from neither AC nor DC sides. Thus, the circulating current can provide a new control variable for improving the performance of the converter. The control of circulating current is similar to the control of output current. The reference value of the circulating current can be followed by using the PI-based current controller. Then, the problem is to calculate the appropriate value of the injected circulating current.

The reference value of the second harmonic component of circulating current will be calculated using the method proposed in the study by Liu et al. (2018). **Figure 5** and **Figure 6** show the variation of capacitor voltage ripple $U_{c,rip}$ under the influence of different factors. **Tables 1, 2** show the parameters of the MMC and the PMSG used in the numerical analysis. In **Figure 5**, the amplitude of circulating current, denoted by I_c, is 100A; the z-axis

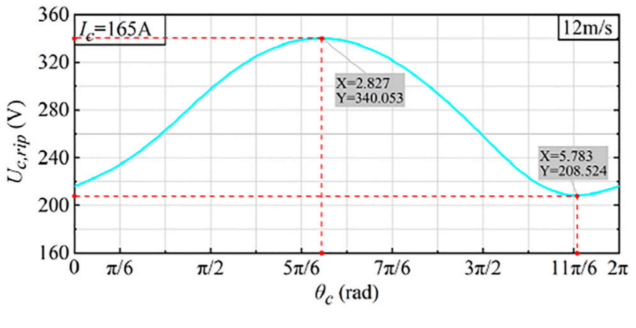

FIGURE 8 | Capacitor voltage ripple under different circulating current phase angles when v_{wind} = 12 m/s.

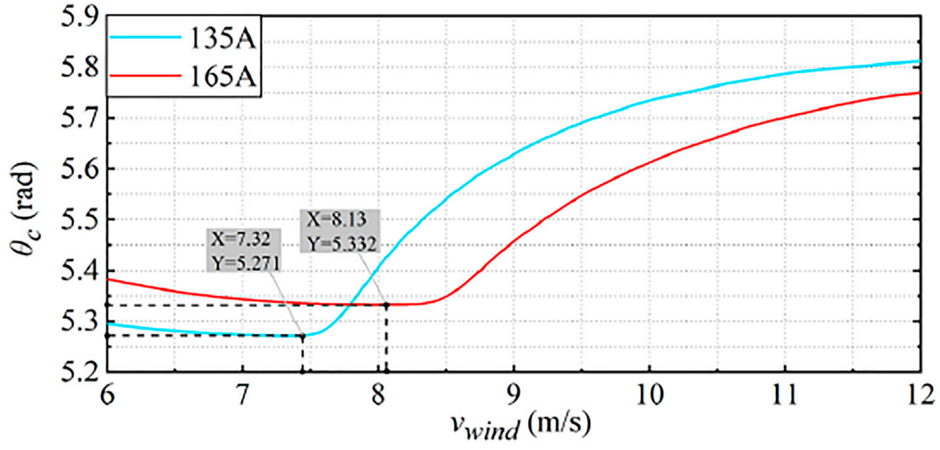

FIGURE 9 | Optimal circulating current phase angle under different wind speeds.

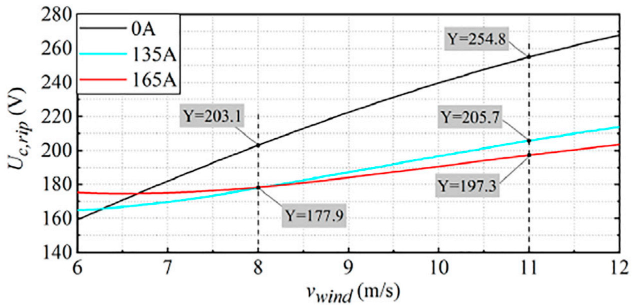

FIGURE 10 | Capacitor voltage ripple at optimal phase angle under different wind speeds.

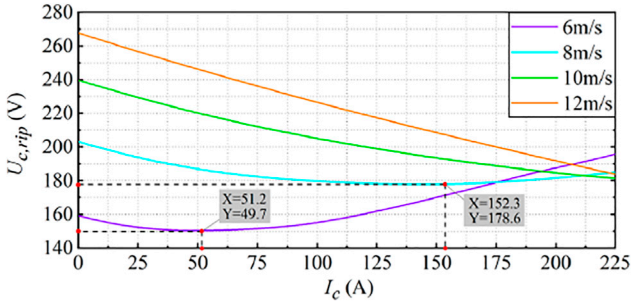

FIGURE 11 | Capacitor voltage ripple under different circulating current amplitudes.

shows the values of $U_{c,rip}$ with respect to the phase angle of circulating current and the wind speed. From **Figure 5**, changing the phase angle of the injected circulating current will have a great impact on the value of $U_{c,rip}$. This is because the injected circulating current can affect the phase angle of the harmonic components in capacitor voltage ripples. When the fundamental, 2nd, and 3rd harmonic components of the capacitor voltage reach the maximum at the same time, $U_{c,rip}$ will be large. On the contrary, when the fundamental component reaches its maximum and the 2nd and 3rd harmonic components reach their minimum at the same time, the 2nd and 3rd harmonic components can offset part of the fundamental component; hence, $U_{c,rip}$ can be smaller.

In **Figure 6**, v_{wind} = 12 m/s, and the z-axis shows variation of capacitor voltage ripple $U_{c,rip}$ under different phase angles and amplitudes of circulating current. With the increase in current amplitude, the influence of the circulating current on $U_{c,rip}$ becomes greater. In addition, there always exists a phase angle in every circulating current amplitude, which can make $U_{c,rip}$ smallest. In this study, this angle is defined as the optimum angle.

From **Figure 5** and **Figure 6**, the following two conclusions can be made.

1) The injected circulating current can either reduce or increase the fluctuation magnitude of the capacitor voltage ripple. Thus, there can be numerous reference values of circulating current for suppressing capacitor voltage ripples. There should be a rule to choose the appropriate reference value.
2) The value of θ_c is the key to determining the effect of the injected circulating current. It can be seen from **Figure 6** that the suppression effect occurs in a narrow interval. In other words, the angle of reference circulating current should be chosen precisely.

5 PHASE ANGLE AND AMPLITUDE ANALYSIS

5.1 Phase Angle Analysis

As mentioned earlier, every amplitude of circulating current has an optimum angle, which can make the injected circulating current have the best suppression effect on capacitor voltage ripples; hence, this optimum angle should be chosen as the phase angle of the reference circulating current.

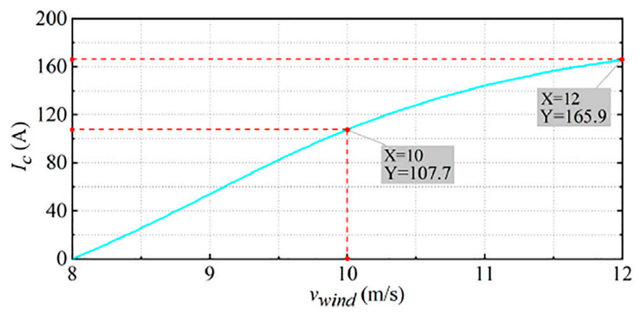

FIGURE 12 | Calculation results of circulating current amplitude.

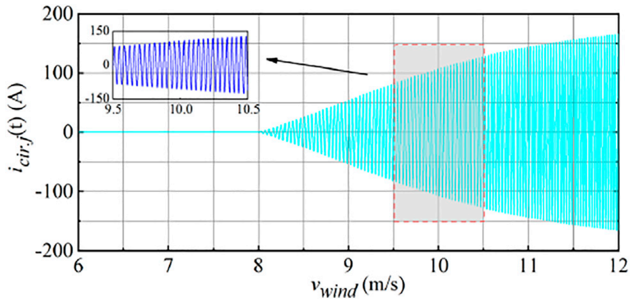

FIGURE 13 | Actual injection circulating current waveform.

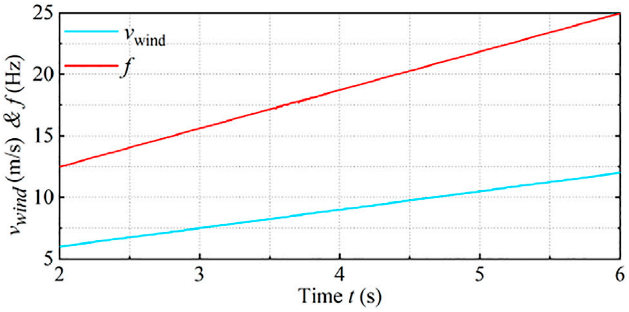

FIGURE 14 | Wind speed and system frequency.

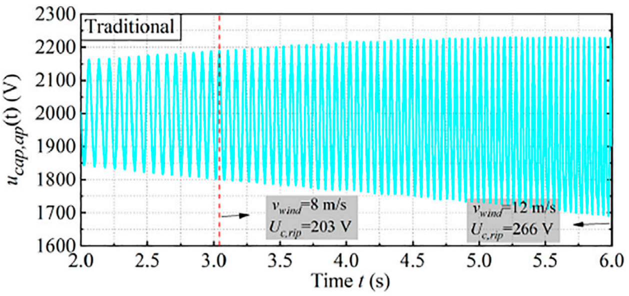

FIGURE 15 | Capacitor voltage under the traditional method.

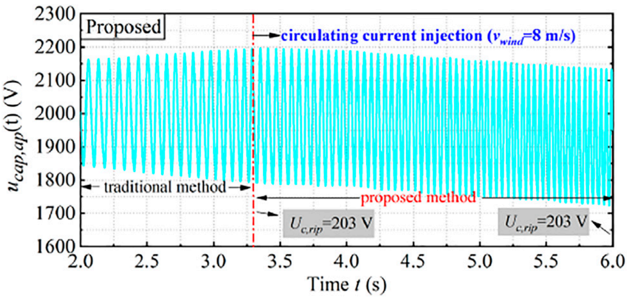

FIGURE 16 | Capacitor voltage under the proposed method.

This angle can be accurately obtained by following two steps. First, based on the steady-state analysis method proposed in the study by Liu et al. (2018), the values of $U_{c,rip}$ are calculated when the circulating current angle is changed from 0 to 2π. Second, the minimum value of $U_{c,rip}$ can be found, and the corresponding angle is the optimum angle.

Figure 7 shows the effect of the circulating current phase angle on capacitor voltage ripple under different wind speeds. In **Figure 7A**, A_1, B_1, C_1, and D_1 are the optimal injection phase angles at different wind speeds when the amplitude of injection circulating current is 135 A, respectively; A_2, B_2, C_2, and D_2 are the optimal injection phase angles at different wind speeds when the amplitude of injection circulating current is 165 A, respectively, in **Figure 7B**. The variation trend of capacitor voltage ripple under different circulating current phase angles can be seen from **Figure 7**, and there is an optimal injection phase angle under each wind speed and circulating current amplitude. Injecting circulating current under this phase angle can minimize the capacitor voltage ripple of the SM, and the phase angle is defined as the best phase angle under the corresponding wind speed and circulating current amplitude.

Figure 8 shows the capacitor voltage ripple under different circulating current phase angles at the wind speed of 12 m/s, when the circulating current amplitude is 165 A. It can be seen that the angle of injecting circulating current has an obvious influence on the capacitor voltage ripple. In **Figure 8**, when the circulating current phase angle is 5.783, the capacitor voltage ripple is suppressed to 208.524 V. Therefore, under the condition of v_{wind} = 12 m/s, when the circulating current amplitude is 165A, the corresponding optimal phase angle is 5.783.

Based on the steady-state analysis method described in the study by Liu et al. (2018), the variation of capacitor voltage ripple can be analyzed by changing the amplitude and phase angle of circulating current at different wind speeds. In this way, the optimal circulating current phase angle under different operating conditions can be determined.

Figure 9 shows the corresponding optimal phase angle under different wind speeds when the circulating current amplitude is 135 and 165 A. **Figure 9** also shows the variation trend of the circulating current phase angle; the change trend of the optimal phase angle decreases slowly at first and then increases to a certain extent. With the increase in circulating current amplitude, the wind speed at the corresponding turning point will also increase.

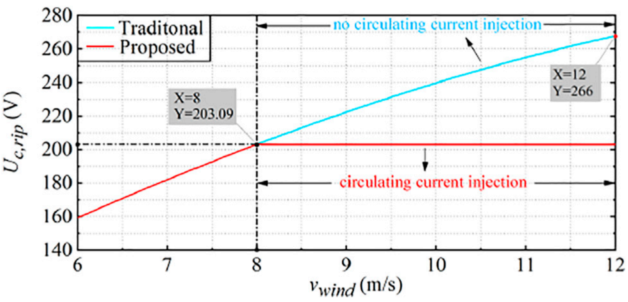

FIGURE 17 | Comparison of SM capacitor voltage ripple under the two methods.

Figure 10 shows the change of capacitor voltage ripple when injecting circulating current at the best phase angle. It can be seen from the figure that with the increase in wind speed, the effect of circulating current injection on the reduction of SM capacitor voltage ripple becomes more and more obvious, and the amplitude of circulating current will affect this effect. The effect of circulating current amplitude will be analyzed below.

5.2 Amplitude Analysis

The optimal phase angle of the circulating current injection under different wind speeds and amplitudes is analyzed. After determining the optimal phase angle, the difference of the amplitude of the injected circulating current will also affect the capacitor voltage ripple.

Figure 11 shows the variation of capacitor voltage ripple with the amplitude of injected circulating current at different wind speeds under the optimal circulating current injection angle. It can be seen from the figure that at low wind speed, if the amplitude of injected circulating current is too large, it will cause an increase in capacitor voltage ripple; this also explains why increasing the amplitude of the circulating current will increase the SM capacitor voltage ripple at the wind speed of 6 m/s in **Figure 10**.

Based on the phase angle analysis and amplitude analysis of injection circulating current, the following conclusions can be obtained:

1) Injecting appropriate circulating current will suppress the voltage ripple of the submodule capacitor. The variation of amplitude and phase angle of circulating current will affect the capacitor voltage ripple.
2) Each circulating current amplitude will have and only have a corresponding optimal injection phase angle at different wind speeds. When injecting circulating current at this phase angle, the capacitor voltage ripple will be minimized.
3) The variation of circulating current amplitude will affect the capacitor voltage ripple. By changing the amplitude of the injected circulating current, the desired capacitor voltage ripple of the SM will be obtained.

6 VERIFICATIONS

It can be seen from the previous section that the voltage ripple of the SM capacitor is affected by the phase angle and amplitude of the injection circulating current. The submodule capacitor voltage ripple can be controlled by changing the amplitude and phase angle of the injection circulating current. Based on this, a constant capacitor voltage ripple control method is proposed in this study. That is, on the premise of the optimal injection phase angle, the corresponding circulating amplitude is calculated to keep the capacitor voltage ripple constant.

Using this method, the SM capacitor can be designed and selected under the MFWS without worrying about the capacitor breakdown caused by the excessive voltage ripple of the SM capacitor, which can save the cost of the device and improve the reliability of the operation.

Simulations are conducted using RT-Lab to verify the effectiveness of the proposed method. The parameters of the PSMG and the MMC are shown in **Tables 1**, **2**, respectively. The rated capacity of the wind generation system is 5 MVA.

Figure 12 shows the calculation results of the required injection circulating current amplitude under the optimal phase angle. According to the method mentioned in the study by Liu et al. (2018), the circulating current amplitude to be injected and the optimal phase angle can be calculated quickly.

Figure 13 is the waveform diagram of the second harmonic component of circulating current $i_{cir,j}(t)$.

It can be seen that when v_{wind} is large, it is necessary to inject a large amplitude of circulating current to keep the SM capacitor voltage ripple constant, which is consistent with the results of **Figure 12**.

Figure 14 shows the wind speed and system frequency. The wind speed is 6 m/s at 2 s. Then, the wind speed is increased from 6 m/s to 12 m/s during $t = 2$ s to $t = 6$ s.

Figure 15 shows the capacitor voltage waveform under the traditional method. In **Figure 15**, the injected circulating current amplitude I_c is set to 0. This means that the circulating current is not injected. It can be seen that with the increase in wind speed, the voltage amplitude and voltage ripple of SM capacitor voltage will increase. When the wind speed reaches 12 m/s, the voltage amplitude and voltage ripple of the SM capacitor will also reach the maximum.

TABLE 3 | Comparison of different situations.

Case	Case 1	Case 2	Case 3
Suitable for medium voltage	No	Yes	Yes
Capacitance demand	Low	High	Low
Working conditions	Low voltage	Medium and high voltage	Medium and high voltage

Figure 16 shows the capacitor voltage waveform under the proposed method.

In **Figure 16**, when the wind speed reaches 8 m/s, the second harmonic component of circulating current is injected to keep the capacitor voltage ripple constant. It can be seen from the figure that from 8 m/s, with the increase in wind speed, the amplitude of the capacitor voltage of the SM decreases to a certain extent, and the voltage ripple always remains a constant value.

Figure 17 shows the specific variation of the SM capacitor voltage ripple under the two methods. It can be seen from the figure that in the traditional method, the injected circulating current amplitude I_c is set to 0. This means that the circulating current is not injected. It can be seen that the capacitor voltage ripple is 203.09 V when the wind speed is 8 m/s. The capacitor voltage ripple increases with the increment of wind speed. The capacitor voltage ripple is 266 V when the wind speed is 12 m/s, and it reaches the maximum at this time. In the proposed method, the circulating current is injected at 8 m/s to keep the capacitor voltage ripple at a constant value. From the figure, the capacitor voltage ripple is effectively reduced. The capacitor voltage ripple is 203.09 V when the wind speed is 8 m/s; when the wind speed increases to 12 m/s, the capacitor voltage ripple is also 203.09 V, which is reduced by 23.65% compared with the traditional method (Wang et al., 2016). It is obvious that the proposed method is effective.

In conclusion, based on the method proposed in this study, the capacitance of the SM capacitor can be designed and selected at the MFWS, and the damage of the SM capacitor caused by too high capacitor voltage amplitude and capacitor voltage ripple can be avoided. Compared with the traditional method, SM capacitors with smaller capacitance will be used, so it can save the cost and reduce the volume of equipment.

In order to highlight the improvement of the work done in this study, similar work in the relevant literature is selected for comparison, which is divided into four cases. Case 1 is a two-level voltage source converter (Lachichi et al., 2019), case 2 is a traditional MMC system (Wang et al., 2016), and case 3 is the method proposed in this study. The comparison results are shown in **Table 3**.

It can be seen from **Table 3** that the MMC can be more suitable for medium- and high-voltage DC technology scenarios and has lower switching loss compared than the two-level converter; the method proposed in this study has lower requirements than the traditional MMC operation mode for the capacitance of submodules, which can reduce the operation cost of equipment.

7 CONCLUSION

This study proposed a CCVR control for the MMC-based wind energy conversion system. This method reduces the ripple of SM capacitor voltage by injecting the second harmonic component of circulating current into the MMC so that the capacitance of the SM capacitor can be selected and designed under the MFWS. The specific conclusions are summarized as follows:

1. It is found that under the existing operating conditions, the capacitance design of the SM capacitor needs to be optimized. In this study, it is found that the voltage ripple of the SM capacitor can be significantly reduced by injecting the second harmonic component of circulating current. In this case, the design and selection for the capacitance of the SM capacitor will be carried out under the highest-frequency wind speed, and the cost and volume of the SM capacitor will be optimized.
2. The second harmonic component of circulating current injection will affect the voltage ripple of the submodule capacitor, and at different wind speeds, the amplitude of each injected circulating current has the corresponding optimal phase angle, so that when the circulating current is injected at this phase angle, the capacitor voltage ripple of the SM will be minimized.
3. A constant capacitor voltage ripple control method for the MMC-based wind energy conversion system is proposed; this method can significantly reduce the voltage ripple of the SM capacitor. The results show that the voltage ripple of the capacitor of the SM is significantly reduced by using the proposed method, that is, by 23.65%, compared with the traditional method under the working condition of v_{wind} = 12 m/s.

Based on the method proposed in this study, the SM capacitor with smaller capacitance will be used, so the cost, volume, and weight of the capacitor will be reduced.

DATA AVAILABILITY STATEMENT

The original contributions presented in the study are included in the article/Supplementary Material; further inquiries can be directed to the corresponding author.

AUTHOR CONTRIBUTIONS

Conceptualization: JQ and ZL; writing—original draft preparation: JQ and ZL; writing—review and editing: ZL, LL, and ZG; visualization: JQ; supervision: ZL; and funding acquisition: ZL. All authors have read and agreed to the published version of the manuscript.

FUNDING

This work is supported by the Natural Science Foundation of Shandong Province under Grant ZR2021QE158.

REFERENCES

Cortes-Vega, D., Ornelas-Tellez, F., and Anzurez-Marin, J. (2021). Nonlinear Optimal Control for PMSG-Based Wind Energy Conversion Systems. *IEEE Lat. Am. Trans.* 19 (7), 1191–1198. doi:10.1109/tla.2021.9461848

Dekka, A., Wu, B., Fuentes, R. L., Perez, M., and Zargari, N. R. (2017). Evolution of Topologies, Modeling, Control Schemes, and Applications of Modular Multilevel Converters. *IEEE J. Emerg. Sel. Top. Power Electron.* 5 (4), 1631–1656. doi:10.1109/jestpe.2017.2742938

Ghosh, S., Isbeih, Y. J., Bhattarai, R., Moursi, M. S. E., El-Saadany, E. F., and Kamalasadan, S. (2020). A Dynamic Coordination Control Architecture for Reactive Power Capability Enhancement of the DFIG-Based Wind Power Generation. *IEEE Trans. Power Syst.* 35 (4), 3051–3064. doi:10.1109/tpwrs.2020.2968483

Groch, M., and Vermeulen, H. J. (2019). Modeling High Wind Speed Shut-Down Events Using Meso-Scale Wind Profiles and Survival Analysis. *IEEE Trans. Power Syst.* 34 (6), 4955–4963. doi:10.1109/tpwrs.2019.2921940

Hu, C., Tong, Y., Jing, J., and Zhao, C. (2020). Research on Steady State Control Strategies of Wind Farm Integration by VSC-LCC Hybrid HVDC Transmission. *Energy Rep.* 6, 985–991. doi:10.1016/j.egyr.2020.11.088

Jae-Jung Jung, J. -J., Seung-Ki Sul, H. -J., and Sul, S. -K. (2015). Control Strategy for Improved Dynamic Performance of Variable-Speed Drives with Modular Multilevel Converter. *IEEE J. Emerg. Sel. Top. Power Electron.* 3 (2), 371–380. doi:10.1109/jestpe.2014.2323955

Khan, M. S. U., Maswood, A. I., Tariq, M., Tafti, H. D., and Tripathi, A. (2019). Parallel Operation of Unity Power Factor Rectifier for PMSG Wind Turbine System. *IEEE Trans. Ind. Appl.* 55 (1), 721–731. doi:10.1109/tia.2018.2870820

Khanzadeh, B., Okazaki, Y., and Thiringer, T. (2021). Capacitor and Switch Size Comparisons on High-Power Medium-Voltage DC–DC Converters with Three-phase Medium-Frequency Transformer. *IEEE J. Emerg. Sel. Top. Power Electron.* 9 (3), 3331. doi:10.1109/JESTPE.2020.2999726

Lachichi, A., Junyent-Ferre, A., and Green, T. C. (2019). Comparative Optimization Design of a Modular Multilevel Converter Tapping Cells and a 2L-VSC for Hybrid LV Ac/dc Microgrids. *IEEE Trans. Ind. Appl.* 55 (3), 3228–3240. doi:10.1109/tia.2019.2897263

Li, W., Chao, P., Liang, X., Xu, D., and Jin, X. (2018). An Improved Single-Machine Equivalent Method of Wind Power Plants by Calibrating Power Recovery Behaviors. *IEEE Trans. Power Syst.* 33 (4), 4371–4381. doi:10.1109/tpwrs.2017.2771323

Li, Z., Bo, L., Bai, J., Yang, B., and Zhu, D. (2022). Suppression Control Strategy of MMC Sub-module Capacitor Voltage in Variable-Frequency Situation. *Energy Rep.* 8, 1191–1206. doi:10.1016/j.egyr.2021.12.055

Liu, Z., Li, K.-J., Wang, J., Javid, Z., Wang, M., and Sun, K. (2019). Research on Capacitance Selection for Modular Multi-Level Converter. *IEEE Trans. Power Electron.* 34 (9), 8417–8434. doi:10.1109/tpel.2018.2886219

Liu, Z., Li, K., Sun, Y., Wang, J., Wang, Z., Sun, K., et al. (2018). A Steady-State Analysis Method for Modular Multilevel Converters Connected to Permanent Magnet Synchronous Generator-Based Wind Energy Conversion Systems. *Energies* 11 (2), 461. doi:10.3390/en11020461

Priya, M., Ponnambalam, P., and Muralikumar, K. (2019). Modular-multilevel Converter Topologies and Applications - a Review. *IET Power Electron.* 12 (2), 170–183. doi:10.1049/iet-pel.2018.5301

Qingrui Tu, Q., Lie Xu, Z., and Xu, L. (2011). Reduced Switching-Frequency Modulation and Circulating Current Suppression for Modular Multilevel Converters. *IEEE Trans. Power Deliv.* 26 (3), 2009–2017. doi:10.1109/tpwrd.2011.2115258

Rebello, E., Watson, D., and Rodgers, M. (2019). Performance Analysis of a 10 MW Wind Farm in Providing Secondary Frequency Regulation: Experimental Aspects. *IEEE Trans. Power Syst.* 34 (4), 3090–3097. doi:10.1109/tpwrs.2019.2891962

Ronanki, D., and Williamson, S. S. (2018). Modular Multilevel Converters for Transportation Electrification: Challenges and Opportunities. *IEEE Trans. Transp. Electrific.* 4 (2), 399–407. doi:10.1109/tte.2018.2792330

Singh, B., Kumar, N., and Panigrahi, B. K. Steepest Descent Laplacian Regression Based Neural Network Approach for Optimal Operation of Grid Supportive Solar PV Generation. *IEEE Trans. Circuits Syst. II Express Briefs* 68 (6), 1947

Tao, S., Zhao, L., Liao, K., and Liu, Y. (2019). Probability Assessment of Characteristics of Sub-synchronous Oscillation in D-PMSG-Based Wind Power Generation System. *IEEE Access* 7, 133159–133169. doi:10.1109/access.2019.2941909

Wang, M., Hu, Y., Zhao, W., Wang, Y., and Chen, G. (2016). Application of Modular Multilevel Converter in Medium Voltage High Power Permanent Magnet Synchronous Generator Wind Energy Conversion Systems. *IET Renew. Power Gener.* 10 (6), 824–833. doi:10.1049/iet-rpg.2015.0444

Xiao, H., Sun, K., Pan, J., Li, Y., and Liu, Y. (2021). Review of Hybrid HVDC Systems Combining Line Communicated Converter and Voltage Source Converter. *Int. J. Electr. Power & Energy Syst.* 129, 2021. doi:10.1016/j.ijepes.2020.106713

Xue, T., Lyu, J., Wang, H., and Cai, X. (2021). A Complete Impedance Model of a PMSG-Based Wind Energy Conversion System and its Effect on the Stability Analysis of MMC-HVDC Connected Offshore Wind Farms. *IEEE Trans. Energy Convers.* 36 (4), 3449–3461. doi:10.1109/tec.2021.3074798

Yang, D., Jin, Z., and Zheng, T. (2022). An Adaptive Droop Control Strategy with Smooth Rotor Speed Recovery Capability for Type III Wind Turbine Generators. *Int. J. Electr. Power. Energy Syst.* 135, 2022. doi:10.1016/j.ijepes.2021.107532

Conflict of Interest: The authors declare that the research was conducted in the absence of any commercial or financial relationships that could be construed as a potential conflict of interest.

NOMENCLATURE

MMC Modular multilevel converter

CCVR Constant capacitor voltage control

SM Submodule

MFWS Most frequency wind speed

PMSG Permanent magnet synchronous generator

HVDC High-voltage direct current

Symbols

v_{wind} Wind speed

T_m Mechanical torque of PMSG

ω_m Rotor speed of PMSG.

$u_a(t)$, $i_a(t)$ Output voltage and current of PMSG

$i_{p,a}(t)$, $i_{n,a}(t)$ Instantaneous value of the upper and lower arm currents in phase A, respectively

$u_{cap.ap}(t)$, $u_{cap.an}(t)$ Instantaneous value of the upper and lower capacitor voltages in phase A, respectively

ω Angular speed of MMC

P Number of pole pairs

U_s Amplitude of the output voltage

α Phase angle of the output voltage

I_s Amplitude of the phase currentAmplitude of phase current

β Phase angle of the phase current

$i_d(t)$, $i_q(t)$ Instantaneous value of the ac-side phase currents in d-q frame

$T_e(\mathrm{t})$ Electromagnetic torque of PMSG

L_d, L_q D-axis and q-axis inductance

P Air mass density

A Area covered by the wind blades

C_p Performance coefficient

β_{pit} Pitch angle

λ Tip-speed ratio

$i_{d.ref}$, $i_{q.ref}$ Reference value of output currents in the d-q frame

r_{wind} Radius of wind blades

λ_{opt} Optimum tip-speed ratio

$\mathrm{I_s}$ Amplitude of the phase currentAmplitude of phase current

φ Phase angle of phase current

abrIc Amplitude of the second harmonic circulat-ing current

θc Phase angle of the second harmonic circulat-ing current

Adc Dc component in the modulation signal

A1 Amplitude of 1ω component in the modulation signal

θ1 Phase angle of 1ω component in the modulation signal.

A2 Amplitude of 2ω component in the modulation signal

θ2 Phase angle of 2ω component in the modulation signal

Ucap 0 Dc component in the capacitor voltage

CSM Submodule capacitor of MMC

frontiers | Frontiers in Energy Research

ORIGINAL RESEARCH
published: 25 May 2022
doi: 10.3389/fenrg.2022.908207

A Study of Dynamic Equivalence Method for Multiple Wind Farms in Urban Power Grids

Lin Zhu[1]*, **Shiyu Huang**[1], **Zhigang Wu**[1]*, **Yonghao Hu**[1], **Mengjun Liao**[2] **and Min Xu**[2]

[1]School of Electric Power Engineering, South China University of Technology, Guangzhou, China, [2]Electric Power Research Institute of China Southern Power Grid, Guangzhou, China

As the number of wind farms (WFs) in urban power grids gradually increases, their dynamic equivalence is needed for stability analysis. This paper proposes a dynamic equivalence method for distributed multiple wind farms in an urban power grid. The key idea is to characterize wind farms dynamics and then use them for coherence by considering the differences between doubly-fed induction generators (DFIG) and permanent magnet direct-drive synchronous generators (PMSG). The mathematical-physical models and operational control characteristics are firstly analyzed to find the essential attributes representing the dynamic characteristics. Then we introduce the similarity based on the dynamic timing warping (DTW) distances, which help construct the clustering index for coherency wind farms. Meanwhile, comprehensive constraints, which ensure the consistency of the urban power grid topology, are adequately considered. Finally, the parameters of coherent wind farms are aggregated based on the clustering groups. The proposed method is validated in an urban grid by the time-domain simulation.

Keywords: urban power grid, dynamic equivalence, dynamic timing warping, doublyfed induction generator, permanent magnet direct-drive synchronous generator

Edited by:
Kaiqi Sun,
Shandong University, China

Reviewed by:
Zhijun Qin,
Guangxi University, China
Rui Wang,
Northeastern University, China
Hongjie Jia,
Tianjin University, China

***Correspondence:**
Lin Zhu
zhul@scut.edu.cn
Zhigang Wu
epzgwu@scut.edu.cn

Specialty section:
This article was submitted to Smart Grids, a section of the journal Frontiers in Energy Research

Received: *30 March 2022*
Accepted: *29 April 2022*
Published: *25 May 2022*

Citation:
Zhu L, Huang S, Wu Z, Hu Y, Liao M and Xu M (2022) A Study of Dynamic Equivalence Method for Multiple Wind Farms in Urban Power Grids. Front. Energy Res. 10:908207. doi: 10.3389/fenrg.2022.908207

INTRODUCTION

Wind power has maintained an upward trend in past decades because of its advantages, such as sustainability and environmental benefits. A higher wind power penetration demand in the urban power grid is in the corner, which leads to a growing capacity and a wide spatial distribution, then brings new challenges to the safe and stable operation of the grid. For example, stability analyses based on accurate and adequate modeling are significant. However, one-to-one high accuracy modeling of all wind turbines in large-scale grids causes dimensional disasters, resulting in an enormous computational burden and time-consuming. In order to balance the accuracy and the complication, the dynamic equivalence method for wind power is drawing attention (Weng and Xu, 2012; Dorfler and Bullo, 2013; Joe and Juan, 2020).

The traditional dynamic equivalence primarily aims at synchronous generators (Joe and Juan, 2020). The dynamic equivalence can dramatically reduce the scale of the power system while ensuring that the relevant dynamic characteristics of the retained system and the original system are essentially the same (Weng and Xu, 2012). Usually, the modeling of the synchronous generators section greatly affects the accuracy of the dynamic equivalence. A widely used method in large power systems is the coherency-based dynamic equivalence, which compares rotor angles of various synchronous generators suffering contingencies and considers their comparable tendencies and responses as a coherent criterion. Therefore, in order to obtain a reasonable equivalent model of synchronous generators, researchers cluster various groups based on synchronous generators' coherencies and then make parameters aggregation of the equivalent generator.

However, there is an evident gap when directly applying this traditional dynamic equivalent method to grids with high penetration of wind power. One reason lies in random and intermittent natures of wind energy, and the other is the significant difference in wind turbine types (Zhu et al., 2020a). These reasons make it challenging to cluster wind farms.

Currently, wind power dynamic modeling studies are limited inside wind farms. Dynamic equivalences of wind farms are divided into two categories: "single-machine" wind farm aggregation method and "multi-machine" method, depending on whether one or more machines are used to represent the wind farm (Muljadi and Parsons, 2006). The single-machine method uses one equivalent machine to replace the wind farm (Fernández et al., 2008; García-Gracia et al., 2008; Fernández et al., 2009). A wind farm consisting of the same type of wind turbine is equivalent to one expansion turbine. However, there is an error when the wind farm spans a wild area, and equivalence into a single wind turbine cannot act the dynamic characteristics. Then, the multi-machine method is proposed to overcome these drawbacks. Wind turbines are clustered into different groups considering the turbine types and operating conditions, then aggregates the turbines in each group separately. For example, considering the composition of DFIGs, converter controllers and crowbar protection are proposed for clustering (Fang and Wu, 2016). Early studies of wind turbine clustering are based on steady-state operation as the indicators, such as wind speed (Meng et al., 2013) and wake effect (Tian et al., 2017). However, wind speed does not accurately characterize the operating state of wind farms, which may lead to errors. Artificial algorithms have recently been applied to cluster wind turbines, including the density peak clustering algorithm, K-means, and fuzzy clustering algorithms (Zou et al., 2015; Liu et al., 2019). The references above mainly concentrated on DFIG. Recently, the dynamic equivalence of PMSG also has attracted attention (Wang et al., 2020; Wang et al., 2021a). Besides, Ref (Wang et al., 2021b) proposes an artificial algorithm to build dynamic equivalent models of DFIG and PMSG, but different indicators need to be extracted using algorithms to cluster for different models. However, these algorithms must be trained with datasets, which is time-consuming.

After the clustering of wind farms, the next step is to perform parameter aggregation of coherent wind turbines, which can identify parameters for an equivalent model and ensure that the accuracy of the dynamic responses is comparable to that of the original system. Currently, the capacity-weighted average method (Zhou et al., 1109) and the parameter identification method (Zin et al., 2003; Shao et al., 2021) are mainly used for parameter aggregation.

The dynamic equivalence for various wind farms, especially in an urban grid, is an aspect that has not been widely studied in earlier work. Some scholars have been interested in dynamic equivalence among multiple wind farms. Ref (Wang et al., 2018) gives the basis for clustering of doubly-fed wind turbines from different perspectives. Then the index of the similarity achieves clustering by the similarity of the output power characteristics of the point of common coupling (PCC). The coherency idea of synchronous generators is utilized for reference. Ref (Zhu et al., 2020b) constructs a clustering index based on the equivalent power angle in multiple scenarios, trying to discern the coherency between wind farms from a data-driven perspective. However, the proposed equivalent power angle is difficult to obtain directly during operation and only applies to doubly-fed wind farms.

The above approaches are inappropriate in urban power grids where wind turbines and farms are distributed broadly. In addition to wind randomness and model differences of various turbines, constraints in the urban grid need to be considered, such as the dispersion of the wind farm distribution. These reasons make it difficult to build a rational model of various wind farms. Therefore, this paper focuses on the equivalent modeling of wind farms in urban power grids.

The major influencing factors of the dynamic characteristics of wind turbines can be classified into three categories: 1) the type of the turbine, the control methods, and corresponding parameters; 2)the steady-state operation of the turbine representing a stable equilibrium point; 3)and the contingencies. The two most commonly used wind energy conversion systems in urban power grids are doubly-fed induction generators (DFIG) and permanent magnet direct-drive synchronous generators (PMSG). They have considerable differences, cannot be clustered into a group, and need to be studied separately. After separating multiple wind farms in the urban power grid according to the turbine types, it is also necessary to consider the consistency of the static and dynamic characteristics. The clustering of wind farms needs to be constrained by comprehensive conditions, such as urban geographic topology, terrain differences, and short-circuit capacity.

In order to address the abovementioned challenges, this paper focuses on attracting the key attributes that can characterize wind farms' dynamics and suit different wind turbine models. We construct a comprehensive constraint, especially considering the geographic topology of the urban power grids. We introduce the similarity based on the dynamic timing warping (DTW) distances and derive the similarity index for clustering the coherent wind farms. It is convenient to quantify the similarity for loop comparison and get the optimal clustering effect. We adopt a two-stage cluster based on the proposed index that satisfies both steady-state and dynamic consistency. After the clustering, the wind farm parameters are aggregated using an active power-weighted method (Zhu et al., 2020b).

The remainder of this paper is organized as follows. **Section 2** finds attributes that characterize the wind farms in urban power grids separately by analyzing models. **Section 3** introduces the similarity based on the dynamic timing warping (DTW) distances and constructs the similarity index for clustering the coherent wind farms. **Section 4** provides an overview of the dynamic equivalence process for multiple wind farms in urban power grids. Furthermore, in **Section 5**, the effectiveness of the dynamic equivalence method for multiple wind farms in urban power grids is demonstrated by case studies.

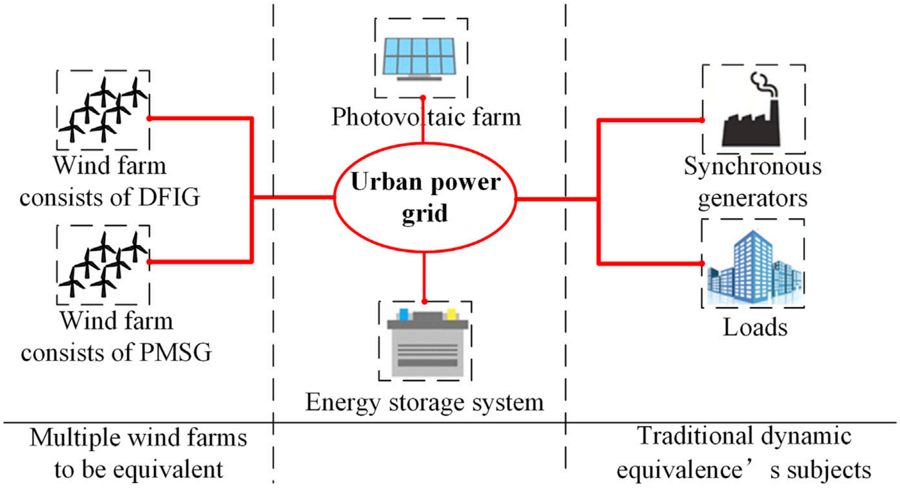

FIGURE 1 | Schematic structure of WFs in urban power gird.

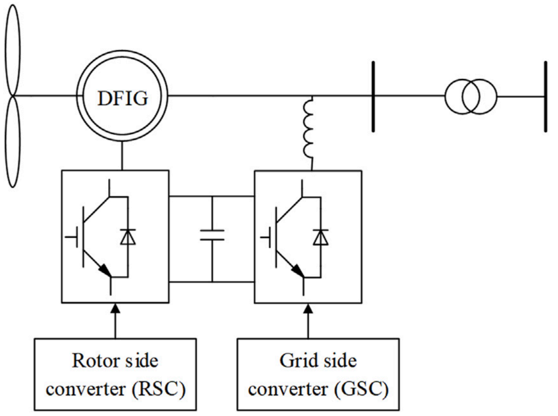

FIGURE 2 | Basic structural diagram of a doubly fed induction generator.

ATTRIBUTES OF MULTIPLE WIND FARMS FOR CLUSTERING

Figure 1 illustrates the simplified schematic structure of an urban power grid in which cleaner alternatives, primarily-wind turbines, and photovoltaics, are effectively addressed. We focus on DFIG and PMSG in this section and aim to find the key attributes of wind farms' dynamic characteristics from the working principle and mathematical-physical model separately. Some assumptions are made considering urban power grids' profiles, configurations, and operational data.

1) A wind farm in an urban power grid is internally composed of the same model. Thus, the wind farms are expanded into a single wind turbine with equivalent capacity.
2) The controller and other parameters of the same model are the same.

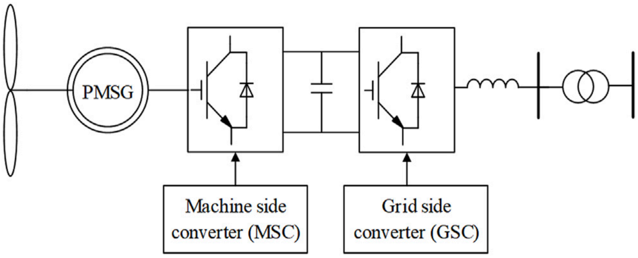

FIGURE 3 | Basic structural diagram of a permanent magnet wind power generator.

3) Wind turbines have the same control strategy within one wind farm.

Doubly Fed Induction Generator

A typical structure of a DFIG is shown in **Figure 2**.

The voltage equation and the flux-linkage equation of DFIG in the stator three-phase stationary coordinate system can be expressed as follows:

$$\begin{cases} u_{sd} = R_s i_{sd} + p\psi_{sd} - \omega_s \psi_{sq} \\ u_{sq} = R_s i_{sq} + p\psi_{sq} - \omega_s \psi_{sd} \end{cases} \tag{1}$$

$$\begin{cases} u_{rd} = R_r i_{rd} + p\psi_{rd} - s_{slip}\omega_s \psi_{rq} \\ u_{rq} = R_r i_{rq} + p\psi_{rq} - s_{slip}\omega_s \psi_{rd} \end{cases} \tag{2}$$

$$\begin{cases} \psi_{sd} = L_s i_{sd} + L_m i_{rd} \\ \psi_{sq} = L_s i_{sq} + L_m i_{rq} \end{cases} \tag{3}$$

$$\begin{cases} \psi_{rd} = L_m i_{sd} + L_r i_{rd} \\ \psi_{rq} = L_m i_{sq} + L_r i_{rq} \end{cases} \tag{4}$$

where, u_s, i_s, ψ_s represent the stator voltage, stator current and stator flux vectors; u_r, i_r, ψ_r represent the reduction voltage,

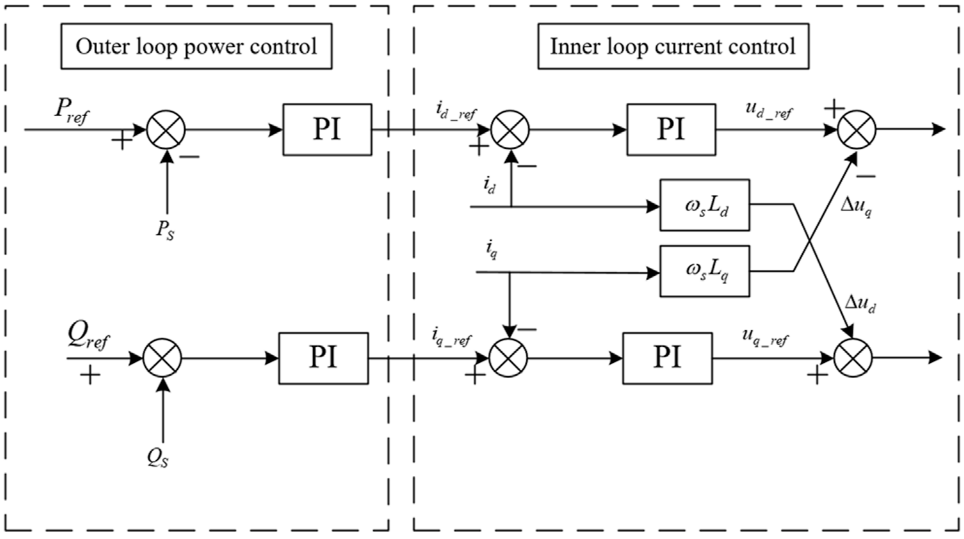

FIGURE 4 | Control block diagram of the rotor side converter and machine side converter.

reduction current and reduction flux vectors. *d*,*q* denote the *dq* components respectively.

Permanent Magnet Direct-Drive Synchronous Generator

A typical structure of a PMSG is shown in **Figure 3**.

PMSGs do not have rotor excitation windings, so only the stator voltage equation needs to be considered. The voltage equation and the flux-linkage equation of PMSG in the stator three-phase stationary coordinate system can be expressed as follows:

$$\begin{cases} \boldsymbol{u_d} = \dfrac{d\boldsymbol{\psi_d}}{dt} - \boldsymbol{\omega_e \psi_q} - \boldsymbol{R_s i_d} \\ \boldsymbol{u_q} = \dfrac{d\boldsymbol{\psi_q}}{dt} - \boldsymbol{\omega_e \psi_d} - \boldsymbol{R_s i_q} \end{cases} \tag{5}$$

$$\begin{cases} \boldsymbol{\psi_d} = -\boldsymbol{L_d i_d} + \boldsymbol{\psi_0} \\ \boldsymbol{\psi_q} = -\boldsymbol{L_q i_q} \end{cases} \tag{6}$$

where, u, i, ψ represent the stator voltage, stator current and stator flux vectors; L represents equivalent inductance; R_s represents the stator resistance, ω_e represents angular velocity. *d*,*q* denote the *dq* components respectively.

Wind Turbine Control Model

The converter models of the two types of wind turbines are the same since both sides of the converter are connected in a back-to-back structure. The converters on both sides are decoupled in the d-q coordinate system through their control loops and the DC link. Thus, we enable the conversion from the ac component in three-phase stationary coordinates to the DC component in d-q-0 coordinates, making the problem easier to analyze.

The overall control block diagram of the rotor side converter and machine side converter of the wind turbines is shown in **Figure 4**. The converter is controlled by a double closed-loop structure of outer loop control and inner loop control together. In the outer loop power control, the input active power (P_{ref}) is obtained through the maximum power control. The reactive power is obtained as its input, and the inner loop current input is adjusted through PI controller to obtain the rotor side and machine side current values i_{rd_ref} and i_{rq_ref}. In the inner loop current control, the current inputs are compared with their actual values i_{rd} and i_{rq} respectively, and adjusted by the PI controller. The variable voltage compensations Δu_{rd} and Δu_{rq} measured by the rotor are superimposed on the voltage quantities u_{rd} and u_{rq} on the rotor side and machine side to achieve decoupling.

The overall control block diagram of the grid side converter is shown in **Figure 5**. The control process of the grid side converter is similar. It is also controlled by a double closed loop structure similar to the rotor side converter. In the outer loop power reactive control, the DC voltages U_{dc_ref} and Q_{g_ref} are used as inputs to the grid side converter. And they pass through the PI controller, respectively, thus obtaining the input quantities i_{gd_ref} and i_{gq_ref} for the inner loop current control. In the inner loop current control, the input currents are compared with the actual currents i_{gd} and i_{gq}. Then through the PI controller, a superimposed voltage quantities u_{gd}, u_{gq} on the net side to achieve decoupling.

Attributes for Coherency Clustering

Take a DFIG as an example. When the grid voltage dip fault occurs, the composition contains DC attenuation components, rotor frequency attenuation components, and positive/negative sequence components that can affect the dynamic characteristics of the DFIG.

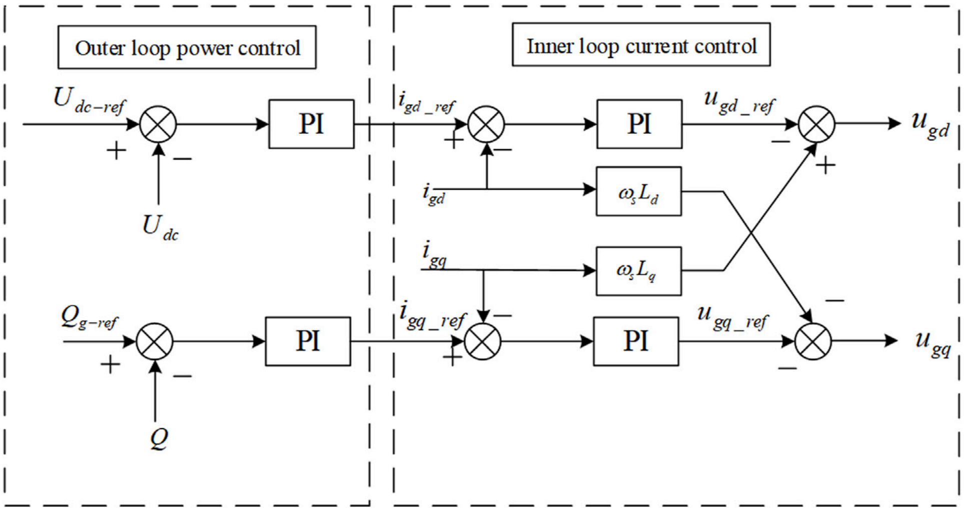

FIGURE 5 | Control block diagram of the grid side converter.

Assuming that a fault occurs in the grid at t = 0, resulting in a voltage drop, for any grid voltage drop type, the port voltage of the turbine can be expressed as a combination of positive sequence voltage and negative sequence voltage after the fault instant.

$$\begin{cases} \dot{V}_{s,0} e^{j\omega_s t} & ,t<0 \\ \dot{V}_{s,1} e^{j\omega_s t} + \dot{V}_{s,2} e^{-j\omega_s t} & ,t \geq 0 \end{cases} \tag{7}$$

where, $V_{s,0}$ is the pre-fault port stability voltage; $V_{s,1}$ and $V_{s,2}$ is related to the topology among the fault type, the fault point and the port voltage.

The equation for the stator fault current is shown below. These equations show that the short-circuit current is correlated with the rotor speed and the degree of voltage dip for DFIG in the same area under the same fault.

$$\begin{aligned} I_S = {} & \left(\frac{\dot{\psi}_{s,0}}{L_s'} - \frac{\dot{V}_{s,1}}{j\omega_s L_s'} - \frac{\dot{V}_{s,2}}{j\omega_s L_s'} \right) e^{-\frac{1}{T_s'}} - k_r \frac{\dot{\psi}_{s,0}}{L_s'} e^{\left(-\frac{1}{T_s'} + j\omega_r \right) t} + \frac{\dot{V}_{s,1}}{j\omega_s L_s'} e^{j\omega_s t} \\ & - \frac{\dot{V}_{s,2}}{j\omega_s L_s'} e^{-j\omega_s t} \end{aligned} \tag{8}$$

where ω_s and ω_r are stator speed and rotor speed, respectively; $\dot{\psi}_{s,0}$ is stator flux linkage; L_s' represents stator transient inductance.

From the wind turbine perspective, the rotor speed variation represents the transient response characteristics during the electromagnetic transient process of DFIG ignoring the mechanical motion. However, in the operation of the urban power grid, the wind turbine is connected to the main grid through power electronics. The rotor angle variation curve cannot be directly obtained. We provide a clustering indicator in practical applications.

The active power output of DFIG is shown as follow:

$$P_s = -Re\left[\frac{3}{2} \dot{U}_s \dot{I}_s^* \right] = -\frac{3}{2} Re\left[R_s I_s^2 + j\omega_s \dot{\psi}_s \dot{I}_s^* \right] \approx \frac{3}{2} \omega_s Im\left[\dot{\psi}_s \dot{I}_s^* \right] \tag{9}$$

$$P_r = -Re\left[\frac{3}{2} \dot{U}_r \dot{I}_r^* \right] = -\frac{3}{2} Re\left[R_r I_r^2 + j\omega_r \dot{\psi}_r \dot{I}_r^* \right] \approx \frac{3}{2} \omega_r Im\left[\dot{\psi}_r \dot{I}_r^* \right] \tag{10}$$

$$P = P_s + P_r \tag{11}$$

where P_s and P_r represent stator and rotor output active power, P represents overall active power output. Form the equation, the result that the output real-time active power P can be approximated as a classification indicator instead of the rotor angle.

In contrast to DFIG, PMSG is connected to the grid through full-scale back-to-back converters. The machine side converter (MSC) controls the speed and power of the generator, and the grid side converter (GSC) realizes the conversion of mechanical energy to electrical energy. A DC filter capacitor between the two converters decouples between the machine side converter and the network side converter, separating the generator from the grid.

When the voltage of PCC falls from e_{gd} to e_{gd}', while the output power maintains the same. The active current of GSC changes from i_{gd} to i_{gd}' based on power equilibrium, as shown following:

$$P_{dc} = \frac{3}{2} e_{gd} i_{gd} = \frac{3}{2} e_{gd}' i_{gd}' \tag{12}$$

However, the instantaneous current is i_{gd}'' because of PI regulator, and $i_{gd}'' < i_{gd}'$, shown as follow:

$$P_{dc} = \frac{3}{2} e_{gd} i_{gd} > \frac{3}{2} e_{gd}' i_{gd}'' \tag{13}$$

Considering the power equilibrium:

$$P_{dc} = \frac{3}{2} e_{gd}' i_{gd}'' + \Delta P \tag{14}$$

$$\boldsymbol{I_{dc}U_{dc}} = \frac{3}{2}\boldsymbol{u_{dc}i_{dc}} + \boldsymbol{C}\frac{\boldsymbol{dU_{dc}}}{\boldsymbol{dt}}\boldsymbol{U_{dc}} = \boldsymbol{I_{dc}U_{dc}} + \boldsymbol{C}\frac{\boldsymbol{dU_{dc}}}{\boldsymbol{dt}}\boldsymbol{U_{dc}} \tag{15}$$

From the equation, it can be seen that the extra power ΔP is stored in the DC filter capacitor. While the controller parameters of PMSGs are the same, the output characteristic is correlated with PCC voltage.

The wind farm dynamic equivalent model aims to study the external characteristics of the wind farm, which are closely related to the control characteristics of its converter. For example, the grid side converter is controlled by a constant DC voltage U_{dc}, and the active power from the machine side converter is related to the inverter side by maintaining U_{dc}.

The mathematical model of the net-side converter can be expressed as:

$$\begin{cases} \boldsymbol{L}\dfrac{\boldsymbol{di_{sd}}}{\boldsymbol{dt}} = -\boldsymbol{U_{sd}} - \boldsymbol{Ri_{sd}} + \boldsymbol{\omega Li_{sq}} + \boldsymbol{U_{gd}} \\ \boldsymbol{L}\dfrac{\boldsymbol{di_{sq}}}{\boldsymbol{dt}} = -\boldsymbol{Ri_{sq}} + \boldsymbol{\omega Li_{sd}} + \boldsymbol{U_{gq}} \end{cases} \tag{16}$$

where U_{sd} is the voltage of the grid connected on the network side, U_{gd} and U_{gq} are grid side converter output voltage, i_{sd} and i_{sq} are grid side converter output current, ω represents angular frequency, R and L are the AC side line resistance and filter inductor, respectively.

Neglecting the losses in the DC link and the converter, the active and reactive power output from the grid side can be expressed as:

$$\begin{cases} \boldsymbol{P_s} = \dfrac{3}{2}\left(\boldsymbol{U_{sd}i_{sd}} + \boldsymbol{U_{sq}i_{sq}}\right) = \dfrac{3}{2}\boldsymbol{U_{sd}i_{sd}} = \boldsymbol{U_{dc}i_{dc}} \\ \boldsymbol{Q_s} = \dfrac{3}{2}\left(\boldsymbol{U_{sq}i_{sd}} + \boldsymbol{U_{sd}i_{sq}}\right) = -\dfrac{3}{2}\boldsymbol{U_{sd}i_{sq}} \end{cases} \tag{17}$$

where P_s and Q_s are active power and reactive power output to the network side, respectively.

The active power input to the grid from the grid side converter is related to the DC voltage. In order to stabilize the DC voltage, the output of the DC voltage controller can be used as the reference value of the d-axis current component to realize the control of the DC voltage. From the equation, we can infer that the active power output from the PMSG can characterize the variation of the DC voltage. As analyzed above, the DC voltage is positively correlated with the voltage value of PCC. The active power can characterize the output characteristics of the PMSG. Therefore, the dynamic coherency of PMSG can be measured by considering both the degree of voltage dip at the PCC and the generator output active power.

According to the above analysis, although the operating principles and mathematical-physical models of DFIG and PMSG are significantly different, they can be clustered using the same indicators. From the grid side, the PCC voltage transient curve of the wind turbine affects its dynamic characteristics; from the wind turbine side, the active power is used to characterize its output characteristics. Combining these two indicators, we can use the same indicators to classify different types of wind turbines by the same regulation, respectively.

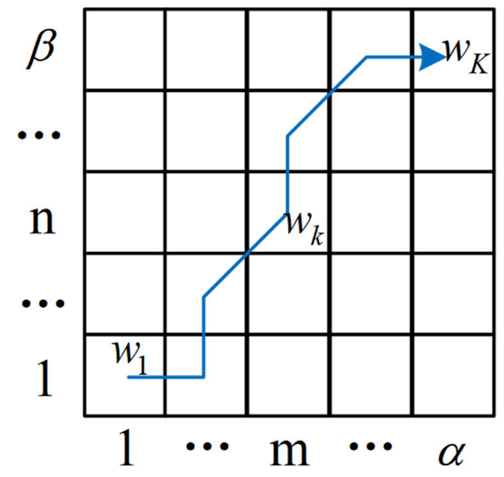

FIGURE 6 | Principle diagram of warping path. The warping path needs to satisfy the following constraints.

AN INDEX OF THE SIMILARITY FOR ATTRIBUTES

For synchronous generators, the swings of their rotors under different disturbances can act as the criterion for coherent identification, as shown in following equation.

$$\max_{t\in[0,\tau]}\left|\boldsymbol{\Delta\delta_i(t)} - \boldsymbol{\Delta\delta_j(t)}\right| \leq \boldsymbol{\varepsilon} \tag{18}$$

where $\Delta\delta_i(t)$ is the relative power angle of synchronous generator i, $\Delta\delta_j(t)$ is the relative power angle of synchronous generator j. The similarity is measured by the Euclidean distance in two time series. Within the simulation calculation time $t \in [0, \tau]$, if the relative rotor angle deviation of the two machines is not greater than a given criterion ε (>0) at any moment, the two machines are judged to be coherency in the τ time interval.

This criterion cannot apply directly to wind farms because converters play crucial roles in energy conversion and separate wind generators and grids. However, the core idea is still attractive since swings of rotors can represent generators dynamics, and a 5°to 10°deviation is considered acceptable for a coherent group. We have the notion of inherent attributes for wind farms and then introduce an index of similarity to utilize fully.

The dynamic characteristics of wind farms have temporal deviations, but the overall profiles can have a similarity. To describe this character, this paper introduces the dynamic timing warping (DTW) to measure the time series and derive an index of similarity.

There are two trajectory time series $X = [x_1, x_2, \ldots, x_\alpha]$ and $Y = [y_1, y_2, \ldots, y_\beta]$, where α and β are the lengths of the two sequences. First, define a distance matrix D of order $\alpha \times \beta$, where the elements of row m and column n are expressed as $d(m, n) = (x_m - y_n)^2$.

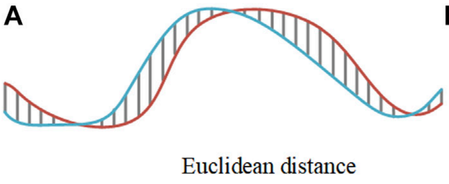

FIGURE 7 | Difference between DTW distance and Euclidean distance. **(A)** Euclidean distance; **(B)** DTW distance.

Define the warping path W as shown in the following equation to represent an alignment or mapping of sequences X and Y, as shown in **Figure 6**.

$$\boldsymbol{W} = [\boldsymbol{w}_1, \ldots, \boldsymbol{w}_k, \ldots, \boldsymbol{w}_K] \tag{19}$$

1) Boundedness constraint. The starting point of the path is $w_1 = (1, 1)$, and the ending point is $w_K = (\alpha, \beta)$.
2) Continuity and monotonicity constraints. If $w_k = (m, n)$, then the forward direction of w_{k+1} must be one of $(m + 1,\ n)$, $(m,\ n + 1)$ and $(m + 1,\ n + 1)$.

Although many paths are satisfied with the above constraints, the one with the smallest cumulative distance is determined as the DTW distance between sequences X and Y. The cumulative distance $r(m,\ n)$ is derived as follows:

$$\begin{cases} r(\boldsymbol{m},\boldsymbol{n}) = d(\boldsymbol{m},\boldsymbol{n}) + min\{\boldsymbol{r}(\boldsymbol{m}-1,\boldsymbol{n}), \boldsymbol{r}(\boldsymbol{m}-1,\boldsymbol{n}-1), \boldsymbol{r}(\boldsymbol{m},\boldsymbol{n}-1)\} \\ \boldsymbol{r}_{\boldsymbol{DTW}} = min\{\boldsymbol{r}(\boldsymbol{m},\boldsymbol{n})\} \end{cases} \tag{20}$$

where $r_{DTW}(X, Y)$ is the DTW distance between sequences X and Y.

As shown in the following figure, **Figure 7A** shows the scenario when the Euclidean distance is used to measure the distance of two time series containing oscillations, while **Figure 7B** shows the application of DTW distance. It is straightforward to see that the DTW distance better measures the similarity in the oscillate time series.

Although the DTW distance can roughly determine whether the dynamic characteristics of the wind farms are consistent with each other, there is still a need for a quantitative index for a more precise clustering. The transient voltage at PCC and active power are sampled to calculate the DTW distance to describe the difference. A larger DTW distance implies a lower degree of similarity, while a smaller DTW distance implies a higher degree of similarity. Some issues have emerged. For example, the units of active power and transient voltage at PCC are not the same, and also the fluctuation range in case of faults is not the same. Therefore, before performing the DTW distance calculation, we normalize the two-time series within the interval [0,1], respectively, which helps quantify the index for clustering.

Considering the weights of the active power and the transient voltage at PCC during the dynamic process, the combined DTW distance of the two indicators can be written as follow:

$$\begin{cases} \boldsymbol{D} = \boldsymbol{\alpha d_P} + \boldsymbol{\beta d_U} \\ \boldsymbol{\alpha} + \boldsymbol{\beta} = 1 \end{cases} \tag{21}$$

Where d_P and d_U represent DTW distance of active power and transient voltage at PCC; α and β represent weights of active power and transient voltage at PCC, which can be determined on a situational basis.

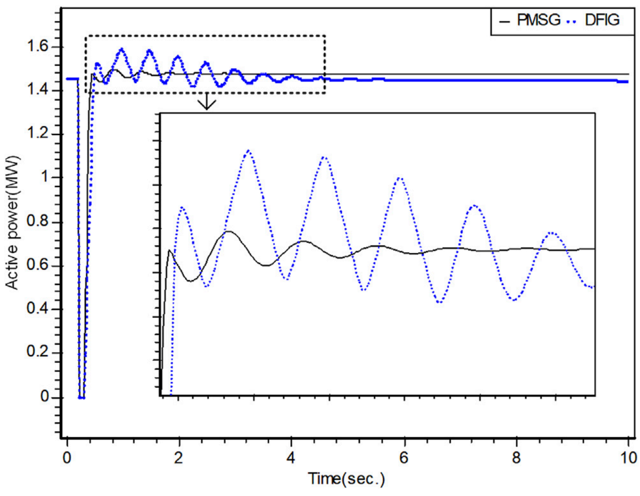

FIGURE 8 | Active power of DFIG and PMSG.

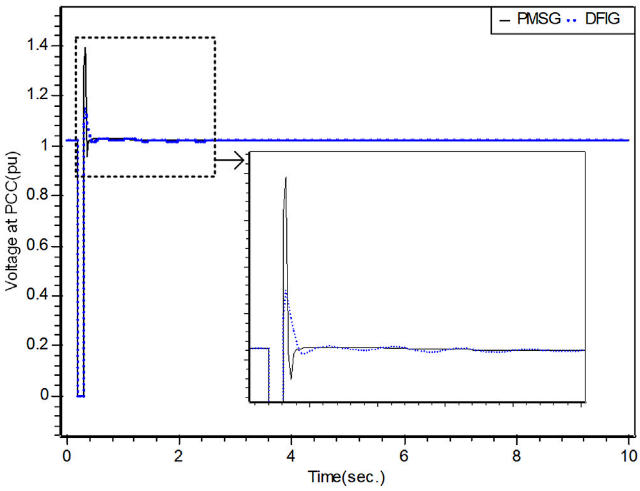

FIGURE 9 | Voltages at PCC of DFIG and PMSG.

It is usually considered that voltage and active power are weighted equally, which we need simulation results to validate. Separate commercial models of the two wind turbines are used to build a single machine infinite bus system to compare their output characteristics. When the same three-phase short-circuit fault occurs, the voltage at PCC and active power of PMSG and DFIG without low-voltage ride-through protection and crowbar protection are shown in **Figure 8** and **Figure 9**.

The active power fed into the grid by the PMSG decreases to zero and stays during the fault. After the fault ends, the active output rises instantly above the rated value and resumes stable operation after an oscillation. It is mainly because after a three-phase short-circuit fault occurs, the PMSG inverter controls the d-axis voltage to track the grid voltage down to zero, so the active power output drops rapidly. The voltage will be restored after the fault is cleared, and the outlet current cannot change abruptly. As to DFIG, the current fluctuation is relatively large, causing the active power to fluctuate above the rated value at the instant.

Although the output characteristics are different, the general profile is similar. DFIG and PMSG have similar control strategies. At the same time, the grid itself has certain limitations, such as low voltage ride-through and other control measures, which will limit the output characteristics to a certain safety range. Therefore, in the paper, the same weights are used to calculate the combined DTW distance of PMSG and DFIG. Thus, the combined DTW distance *D*, considering both indicators, can be calculated as follow:

$$\boldsymbol{D} = 0.5\boldsymbol{d_P} + 0.5\boldsymbol{d_U} \tag{22}$$

Usually, we focus on the transient characteristic profile within 10s after the fault. The frequency is 50 Hz, which means 500 cycles are sampled for 10 s. The sampling step is typically 0.5 to 1 cycle. In order to save some computation time and reduce the cumulative error, the sampling step used in this paper is 1 cycle, so there are 500 sampling points. In this paper, we cluster the two wind farms into the same group when the combined DTW distance obtained from 500 sampling points is less than 15%, which means less than 75.

PROCESS FOR EQUIVALENCE MODELLING OF WIND FARMS

In order to obtain a reliable equivalent model, there are two processes of dynamic equivalence of multiple wind farms in an urban power grid: coherency clustering and aggregation of coherent wind farms. This section provides an overview of the process of dynamic equivalence of multiple wind farms in urban power grids.

The above sections have discussed the attributes representing the characteristics of wind farms and the index of wind farms' similarity, respectively. This paper put the comprehensive constraints for wind farms in an urban power grid for the subsequent aggregation of wind farms and network simplification.

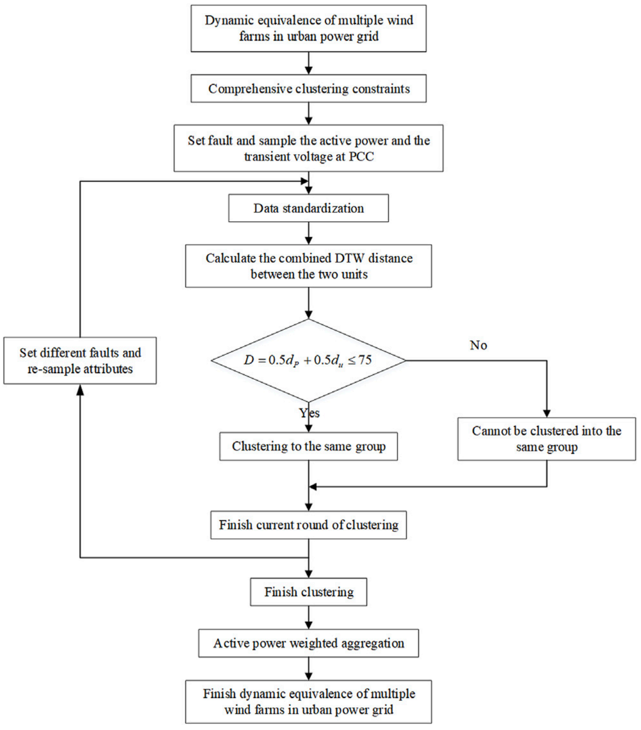

FIGURE 10 | Process flow chart of dynamic equivalence among WFs.

1) Since the models of DFIG and PMSG have large differences, wind farms of different types are not clustered into one group.
2) Considering geographic locations and topology constraints, we select 220 kV voltage level stations as the source. The wind farms in different topology regions can not be clustered into one group.
3) If two groups of wind farms belong to the same topological region, they may be clustered into one group only if the oscillations are similar.

Deviations in the power flow before and after dynamic equivalence and excessive connection lines can be greatly avoided with the above constraints.

After confirming the steady-state consistency, the active power and voltage at PCC are used as characteristics for clustering, as described above. It meets the steady-state and dynamic consistency requirements simultaneously and reduces the comparison workload, saving much time. After the fault, the transient characteristic data of 10 s are collected by continuously setting different faults.

In the collected data, oscillations and noises are inevitable. Since the DTW distance is sensitive to noises, it may not correctly identify the peak and trough. The wavelet transform (WT) is used to reduce noises. A relatively smooth time series can be obtained to meet the data requirements of the DTW distance. The wavelet-based threshold noise removal method is used to process the signal noises, which can effectively filter out the noises and guarantee the maximum effective signal without loss.

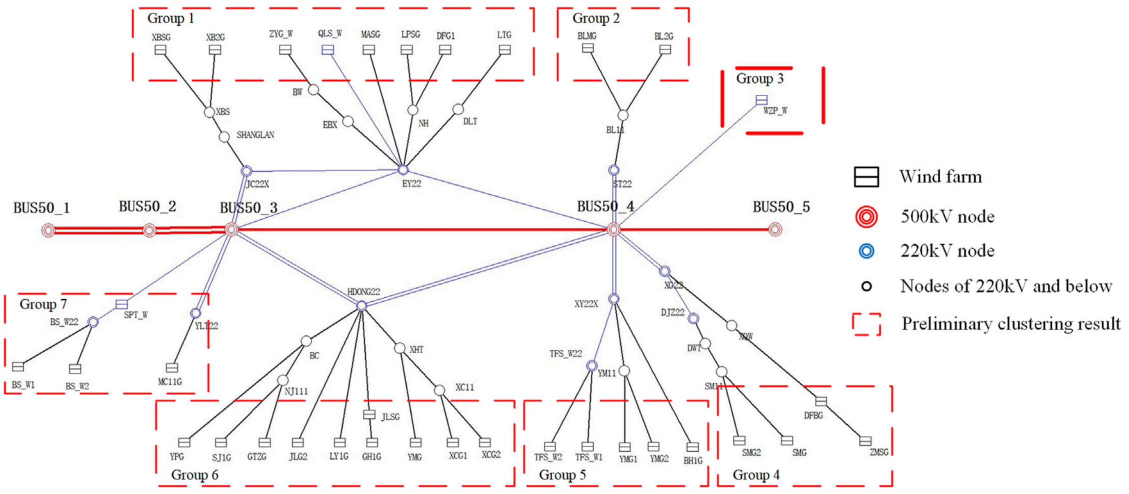

FIGURE 11 | Geographical wiring diagram of WFs.

After processing the noise by wavelet transform, the collected data are normalized within the interval [0,1]. The DTW distance measures the similarity between the active power and the transient voltages at PCC of the wind farms. Setting the active power and the transient voltage at PCC to be of equal importance, **Equation 22** obtains the combined DTW distance. If the combined DTW distance is less than 75, we can cluster the two wind farms into a group and vice versa.

The index for similarity proposed in this paper is straightforward to access. The initial coherent groups are decided by setting one fault. However, with different fault types and fault locations, the similarity of the output characteristics of the wind farms changes. Setting only one type of fault perturbation does not give accurate cluster results. Different faults should occur, and secondary clustering is performed based on the initial group for better accuracy.

After clustering, the wind farms in the same group need to be aggregated into one equivalent model. Reference literature (Zhu et al., 2020b) has proposed a parameter aggregation method based on active power weights. This method is easy to implement and has good accuracy, then is used here.

The flow chart of the dynamic equivalence of multiple wind farms within urban power grids is shown in **Figure 10**.

CASE STUDY

We take an urban power grid integrated with many WFs in Yunnan province, China. As a relatively rich wind resource area, this grid contains 34 wind farms. It is representative of an urban power grid with multiple wind farms.

Equivalent Modelling of A Study System

The topology of the system is shown in **Figure 11**. In order to satisfy the steady-state consistency before and after dynamic equivalence, preliminary groups are necessary, as shown by the wind farms divided by the red boxes in **Figure 11**. Thus, the preliminary results of clustering for these WFs can be obtained.

A further cluster based on the consistency of the dynamic response is carried out. As mentioned above, active power and transient voltage at PCC are selected as the clustering indicators.

We show the results of the case. For the initial clustering, a three-phase fault occurs in line BUS50-3- BUS50-4 at 2 s and disappears at 2.1 s. The DTW distances of WFs in Group 1 are shown in **Table 1**. According to the table, the DTW distance between QLS_W and all the rest of the wind farms is less than 75. Therefore, all WFs within Group 1 are coherent. As to WFs in Group 2, BL2G does not contribute to the power, should not be in this group. Furthermore, Group 3 contains only one wind farm and does not require further clustering. According to **Table 2**, we can learn that in Group 4, the combined DTW of ZMSG and DFBG is 9.58, which is less than 75 and can be divided into a group. The combined DTW of SMG and SMG2 is 49.62, which is less than 75 and can be divided into a group. In Group 5, as shown in **Table 3**, TFS_W1 coheres with TFS_W2, while YMG1, YMG2, and BH1G can be clustered in one group. According to **Table 4**, the DTW distance between LYG1 and all the rest of the wind farms, except XCG2, is less than 75. Therefore, all WFs in Group 6 are coherent. In Group 7, SPT_W, as shown in **Table 5**, cohere with BS_W1 and BS_W2, but has differences with MC11G. Therefore, MC11G forms a group by itself.

Setting only one fault perturbation does not give accurate cluster results. Different faults should occur for a double-check, and secondary clustering is performed based on the initial group for better accuracy. The final results of the clustering are shown in **Figure 12**.

In this case, the wind farms are divided into 10 groups, which is about 70% less than the original 34 wind farms. This method will greatly simplify the wind power simulation scale of the original system.

TABLE 1 | Results of combined DTW distance in Group 1.

WFs	d_u	d_P	Combined DTW	Coherent Identification
(QLS_W, XBSG)	5.3044	4.5336	4.919	Yes
(QLS_W, XB2G)	5.3446	4.4707	4.9076	Yes
(QLS_W, ZYG_W)	5.0485	3.7467	4.3976	Yes
(QLS_W, MASG)	5.3323	1.8773	3.6048	Yes
(QLS_W, LPSG)	5.4003	5.0813	5.2408	Yes
(QLS_W, DFG1)	5.3811	6.5993	5.9902	Yes
(QLS_W, LTG)	5.1349	1.9740	3.5545	Yes

TABLE 2 | Results of combined DTW distance in Group 4.

WFs	d_u	d_P	Combined DTW	Coherent Identification
(ZMSG, DFBG)	18.1024	1.0639	9.58315	Yes
(ZMSG, SMG)	135.0864	193.3582	164.2223	No
(ZMSG, SMG2)	222.0397	180.1788	201.1093	No
(SMG, SMG2)	86.8143	12.4270	49.62065	Yes

TABLE 3 | Results of combined DTW distance in Group 5.

WFs	d_u	d_P	Combined DTW	Coherent Identification
(TFS_W1, TFS_W2)	0.0	0.0	0.0	Yes
(TFS_W1, YMG2)	79.2881	83.2881	81.2881	No
(TFS_W1, YMG1)	89.7404	81.9162	85.8283	No
(TFS_W1, BH1G)	86.8143	69.4921	78.1532	No
(YMG1, YMG2)	3.1420	7.8117	5.47685	Yes
(YMG1, BH1G)	3.1439	101.6374	52.39065	Yes

TABLE 4 | Results of combined DTW distance in Group 6.

WFs	d_u	d_P	Combined DTW	Coherent Identification
(LYG1, JLG2)	27.6179	81.6051	54.6115	Yes
(LYG1, JLSG)	20.779	100.5710	60.675	Yes
(LYG1, GH1G)	34.7910	166.9633	50.87715	Yes
(LYG1, YMG)	18.6290	94.8490	56.739	Yes
(LYG1, XCG1)	19.3115	23.7622	21.53685	Yes
(LYG1, GTZG)	37.3447	128.8303	68.0875	Yes
(LYG1, SJ1G)	30.8365	147.7707	69.3036	Yes
(LYG1, YPG)	17.7426	3.3723	10.55745	Yes

TABLE 5 | Results of combined DTW distance in Group 7.

WFs	d_u	d_P	Combined DTW	Coherent Identification
(SPT_W, BS_W1)	0.9157	26.0552	13.48545	Yes
(SPT_W, BS_W2)	0.9157	26.0552	13.48545	Yes
(SPT_W, MC11G)	466.4171	32.4362	249.4267	Yes

Equivalent Effect Verification

It is necessary to verify the effect of wind farms' dynamic equivalence compared with the original system. Besides preliminary and final results, the undesirable clustering results are also compared to verify the importance of rational clustering. After clustering and aggregating wind farms in each group,

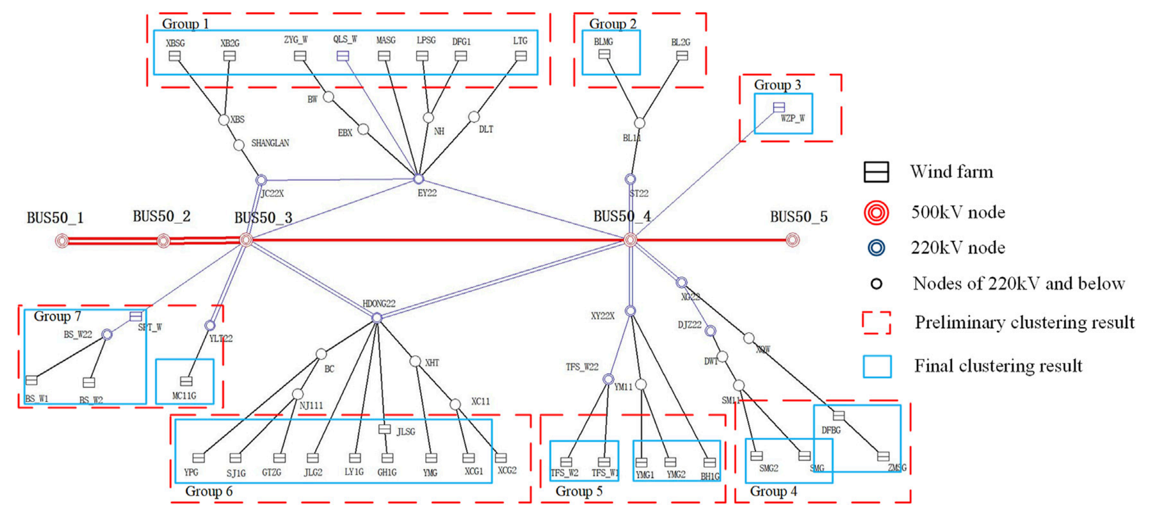

FIGURE 12 | Results of clustering among WFs.

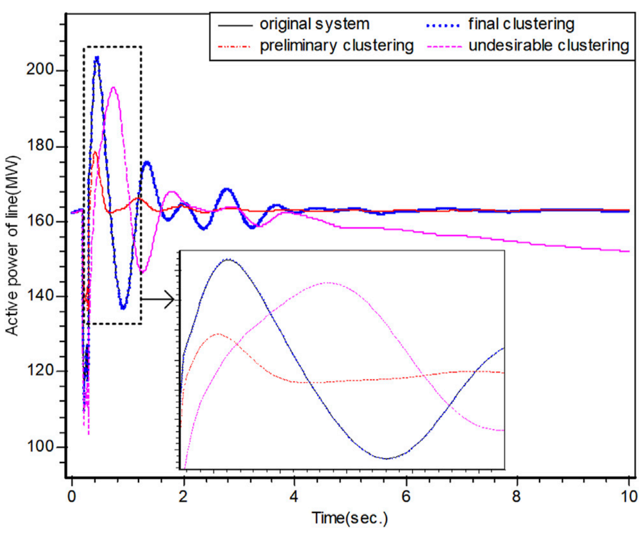

FIGURE 13 | Active power of line SHANGLAN to JC22X.

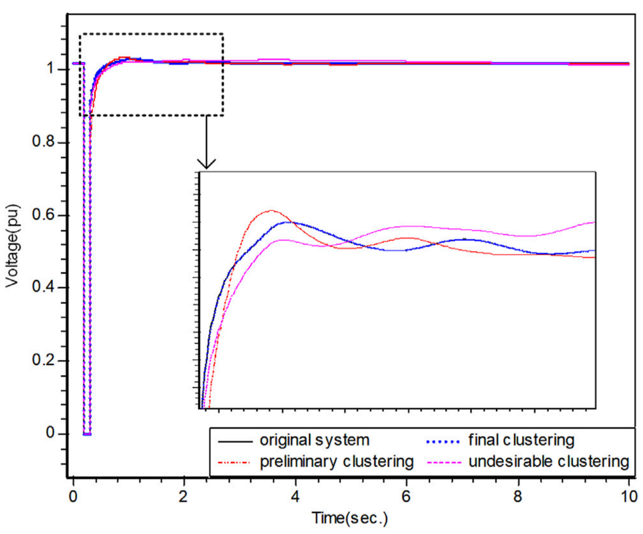

FIGURE 14 | Voltage of bus BUS50_4.

comparisons of the dynamic equivalence are shown in **Figure 13** and **Figure 14**.

It can be seen in the figures that the active power is sensitive to the clustering results, while the bus voltages do not have major differences. However, tracks of the original system and final clustering results maintain a high degree of overlap. The preliminary clustering results are better than the undesirable ones, but still have more considerable inaccuracy than the final ones in **Figure 13**.

This result successfully indicates that the proposed method can maintain the dynamic characteristics of the original system. Therefore, the index proposed in this paper is reasonable and precise. With the proposed method, the scale of the grid can be reduced while retaining high fidelity. The equivalent system will save time in the modeling and simulation of dynamic analysis.

CONCLUSION

This paper proposed a new dynamic equivalence method for multiple wind farms in an urban power grid. From the mathematical-physical models and operational control characteristics of DFIG and PMSG, the active power and the transient voltage at PCC are found as the clustering attributes. Thus, we introduce DTW distance to measure the similarity among wind farms. The clustering results of the index quantify the coherency between wind farms in a more refined way. The dynamic-state consistency and the steady-state consistency are both taken into account. Comprehensive clustering constraints ensure that the power flow and the basic structure of the urban power grid remain unchanged. The proposed method is validated to effectively reduce the power system size and the number of wind farms. The transient characteristics, including power and voltage of the aggregated system, are consistent with the ones in the original system. Simulation results prove the feasibility and accuracy of the proposed method.

This work mainly focuses on the dynamic clustering of wind farms in an urban power grid. The attributes with high correlation can be determined by analyzing the working principle for clustering and modeling. The method can also be extended to resources containing converters such as PV in our future work.

DATA AVAILABILITY STATEMENT

The original contributions presented in the study are included in the article/Supplementary Material, further inquiries can be directed to the corresponding authors.

AUTHOR CONTRIBUTIONS

LZ and SH conceived of the presented idea. ZW contributed significantly to analysis and manuscript preparation. MX carried out the experiments. YH verified the analytical methods. ML and MX encouraged LZ and SH to investigate the dynamic equivalence of multiple wind farms and supervised the findings of this work. ZW and YH took the lead in writing the manuscript. All authors discussed the results and contributed to the final manuscript.

FUNDING

This work is supported by Guangdong Provincial Key Laboratory of Intelligent Operation and Control for New Energy Power System (No. GPKLIOCNEPS-2021-KF-01).

REFERENCES

Dorfler, F., and Bullo, F. (2013). Kron Reduction of Graphs with Applications to Electrical Networks. *IEEE Trans. Circuits Syst. I* 60, 150–163. doi:10.1109/tcsi.2012.2215780

Fang, R., and Wu, M. B. I. (2016). Dynamic Equivalence of Wind Farm Considering Operational Condition of Wind Turbines. Rohde \& Schwarz; Springer, 827–830. IEEE; MEDs Technologies; CST; Infineon; Rolls Royce; Plexim; Keysight Technologies.

Fernández, L. M., García, C. A., Saenz, J. R., and Jurado, F. (2009). Equivalent Models of Wind Farms by Using Aggregated Wind Turbines and Equivalent Winds. *Energy Convers. Manag.* 50, 691–704.

Fernández, L. M., Jurado, F., and Saenz, J. R. (2008). Aggregated Dynamic Model for Wind Farms with Doubly Fed Induction Generator Wind Turbines. *Renew. Energy* 33, 129–140.

García-Gracia, M., Comech, M. P., Sallán, J., and Llombart, A. (2008). Modelling Wind Farms for Grid Disturbance Studies. *Renew. ENERGY* 33, 2109–2121. doi:10.1016/j.renene.2007.12.007

Joe, H. C., and Juan, J. S. (2020). *Power System Modeling, Computation, and Control*. IEEE, 563–575.

Liu, M., Pan, W., Zhang, Y., Zhao, K., Zhang, S., and Liu, T. (2019). A Dynamic Equivalent Model for DFIG-Based Wind Farms. *IEEE Access* 7, 74931–74940. doi:10.1109/access.2019.2918359

Meng, Z., Xue, F., and Li, X. (2013). Wind Speed Equalization-Based Incoming Wind Classification by Aggregating DFIGs. *J. Mod. Power Syst. Clean. Energy* 1, 42–48. doi:10.1007/s40565-013-0007-1

Muljadi, E., and Parsons, B. (2006). Comparing Single and Multiple Turbine Representations in a Wind Farm Simulation. *Preprint* 0003–01.

Shao, H., Cai, X., Yan, H., Zhou, J., Qin, Y., and Zhang, Z. (2021). PMSM Wind Farm Aggregation Algorithm Based on Power Equivalence Principle. *Front. Energy Res.* 9. 10-07 2021. doi:10.3389/fenrg.2021.771009

Tian, J., Zhou, D., Su, C., Chen, Z., and Blaabjerg, F. (2017). Reactive Power Dispatch Method in Wind Farms to Improve the Lifetime of Power Converter Considering Wake Effect. *IEEE Trans. Sustain. Energy* 8, 477–487. doi:10.1109/tste.2016.2607146

Wang, B., Zhu, L., and Chen, D. (2018). Mechanism Research on the Influence of Large Scale Wind Power Integration on Power System Angle Stability. *Energy Procedia* 145, 295–300. doi:10.1016/j.egypro.2018.04.054

Wang, T., Gao, M., Mi, D., Huang, S., and Wang, Z. (2020). Dynamic Equivalent Method of PMSG-Based Wind Farm for Power System Stability Analysis. *IET Gener. Transm. & Distrib.* 14, 3488–3497. doi:10.1049/iet-gtd.2020.0006

Wang, T., Huang, S., Gao, M., and Wang, Z. (2021). Adaptive Extended Kalman Filter Based Dynamic Equivalent Method of PMSG Wind Farm Cluster. *IEEE Trans. Ind. Appl.* 57, 2908–2917. doi:10.1109/tia.2021.3055749

Wang, Y., Li, Y. G., Xie, H., Wu, B. Y., and Yang, Y. N. (2021). Cluster Division in Wind Farm through Ensemble Modelling. *IET Renew. Power Gener.* 16 (7), 1299–1315. doi:10.1049/rpg2.12276

Weng, H., and Xu, Z. (2012). Dynamic Reduction of Large-Scale AC/DC Power Systems via Retaining the Trunk Network. *Int. J. Electr. Power & Energy Syst.* 43, 1332–1339. doi:10.1016/j.ijepes.2012.07.002

Zhou, Y., Zhao, L., Matsuo, I. B. M., and Lee, W. A Dynamic Weighted Aggregation Equivalent Modeling Approach for the DFIG Wind Farm Considering the Weibull Distribution for Fault Analysis. *IEEE Trans. Industry Appl.* 55, 5514–5523. doi:10.1109/tia.2019.2929486

Zhu, L., Zhang, J., Zhong, D., Wang, B., Wu, Z., Xu, M., et al. (2020). A Study of Dynamic Equivalence Using the Similarity Degree of the Equivalent Power Angle in Doubly Fed Induction Generator Wind Farms. *IEEE Access* 8, 88584–88593. doi:10.1109/access.2020.2993115

Zhu, L., Zhong, D., Wang, B., Lin, R., and Xu, M. (2020). Understanding Subsynchronous Oscillation in DFIG-Based Wind Farms with Rotor-Side Converter Control Based on the Equivalent RLC Model. *IEEE Access* 8, 65371–65382. doi:10.1109/access.2020.2983727

Zin, A., Kok, B. C., Mustafa, M. W., Lo, K. L., and Ariffin, A. B. I. (2003). "Time Domain Dynamic Aggregation of Generating Unit Based on Structurepreserving Approach," . Malaysia Sect; Energy Commiss in Proceedings. National Power Engineering Conference, 2003 (IEEE), 154–160}. IEEE Power Engn Soc, Malaysia Chapter.

Zou, J., Peng, C., Xu, H., and Yan, Y. (2015). A Fuzzy Clustering Algorithm-Based Dynamic Equivalent Modeling Method for Wind Farm with DFIG. *IEEE Trans. Energy Convers.* 30, 1329–1337. doi:10.1109/tec.2015.2431258

Conflict of Interest: The authors declare that the research was conducted in the absence of any commercial or financial relationships that could be construed as a potential conflict of interest.

frontiers | Frontiers in Energy Research

ORIGINAL RESEARCH
published: 26 May 2022
doi: 10.3389/fenrg.2022.905359

LSTM-RNN-FNN Model for Load Forecasting Based on Deleuze's Assemblage Perspective

Jie Xin[1]*, Zhenyu Wei*[2]**, Yujie Dong*[3] *and Wan Ni*[1]***

[1]*School of Journalism and Communication, Shandong University, Jinan, China,* [2]*Department of Electrical and Electronic Engineering, The University of Tokyo, Bunkyo, Japan,* [3]*School of Management, Shandong University, Jinan, China*

Reliable load forecasting is essential for electricity generation and even for people's lives. However, the existing load forecasting theories cannot match the requirements of complex systems (e.g., smart grids). Deleuze's metaphysical complexity theory is seen as the theoretical foundation for comprehending complex systems, and thus, a new perspective based on Deleuze's assemblage concept is given. According to the assemblage perspective, the electrical load is a quantitative representation of the mutual becoming of people and electricity, and load forecasting is an attempt to control this continuous process of deterritorialization and reterritorialization. We built an LSTM-RNN-FNN model for load forecasting based on the assemblage perspective, and the assessment results demonstrated that the model has high prediction performance. Furthermore, the performance of adding the temperature parameter into the network is also tested, while the correlation between the temperature and load is not strong enough and may not be suitable for load prediction. The assemblage perspective has significant implications for future load forecasting and potentially smart grid research.

Keywords: load forecasting, assemblage, neural networks, LSTM-RNN-FNN, Deleueze

OPEN ACCESS

Edited by:
Huangqing Xiao,
South China University of Technology, China

Reviewed by:
Shengyuan Liu,
Zhejiang University, China
Fan Yang,
King's College London, United Kingdom

****Correspondence:***
Wan Ni
niwan@sdu.edu.cn
Zhenyu Wei
wei@streamer.t.u-tokyo.ac.jp

Specialty section:
This article was submitted to Smart Grids, a section of the journal Frontiers in Energy Research

Received: *27 March 2022*
Accepted: *14 April 2022*
Published: *26 May 2022*

Citation:
Xin J, Wei Z, Dong Y and Ni W (2022) LSTM-RNN-FNN Model for Load Forecasting Based on Deleuze's Assemblage Perspective. Front. Energy Res. 10:905359. doi: 10.3389/fenrg.2022.905359

1 INTRODUCTION

1.1 Background

Electricity is an enthralling subject to investigate, and it is an infrastructure in many ways. Since the end of the 19th century, electricity has been the foundation of modernity's experience. Currently, electricity powers a plethora of supplementary equipment and services on which modern lifestyles rely. Worldwide electricity usage will account for about 20% of the total energy consumption in 2021 (Zhang and Li, 2021).

With the increasing reliance of human existence on power, electricity production planning is becoming increasingly vital. Because electricity is difficult to store, it is usually required to consume it shortly after it is generated. As a result, dependable load forecasting is the essential foundation for directing power generation. Unreliable projections, on the other hand, might have catastrophic implications. Overestimation of future electricity use will result in waste of primary energy and power producing facilities, whereas underestimation would result in power shortages, which will have a direct impact on people's daily lives.

Currently, a variety of methods have been developed to predict the load of the power grid, such as the time series method, regression method, exponential smoothing, random forest, and others (Kamel and Baharudin, 2007; Singh et al., 2012; Dodamani et al., 2015; Lahouar and Slama, 2015). However, these traditional methods have some different defects. For example, for the time series method, factors affecting the load change are not considered, and the uncertain factors (such as weather (Pan et al., 2021) and holidays) are not sufficiently considered. When the weather changes greatly or encounters holidays, the prediction error of the model is large. As a result, different neural networks (NNs) such as the conventional neural network (CNN) and recurrent neural network (RNN) are utilized to forecast the load value, obtain better results, and also used for smart grids Zhang et al. (2010); Zheng et al. (2017); Kuo and Huang (2018); Mohammad and Kim (2020).

However, because future electricity consumption is a reflection of human social activities, it will be influenced by a variety of factors, including political conditions, the economy (Lin and Liu, 2016), human activities, population behavior (Hussain et al., 2016), climate factors (Hernández, 2013), and other external factors influencing electrical consumption forecasting accuracy. Forecasting electricity is complex and fraught with uncertainty.

1.2 Literature Review *and* Motivation

At present, there are several ways for predicting load, which may be broadly classified as the Markov chain or autoregressive techniques (Dodamani et al., 2015; Kamel and Baharudin, 2007; Li and Niu, 2009; Baharudin and Kamel, 2008). However, contemporary load forecasting research is still centered on cybernetics and views the power grid as an independent technology and facility that can no longer match the needs of complex systems (e.g., smart grids) (Xiao et al., 2021; Sun et al., 2021b,c,d). User demand, from the perspective of smart grids, is simply another managed resource that will aid in balancing supply and demand and ensuring system dependability. Furthermore, the availability of intermittent clean energy sources such as wind, solar, and water energy adds to the issues of smart grid stability (Sun et al., 2021a; Yang et al., 2022). As a result, the smart grid should be considered as part of a wider, unpredictable system that incorporates the natural environment and a huge number of users. Therefore, we require a new theory to guide power forecasting research in the context of smart grids.

Deleuze's metaphysical complexity theory gives a theoretical foundation for comprehending complex systems. Electricity's material-social entanglements have been included into concepts of modernity and progress by a significant number of anthropologists. Winther (2008) investigates the influence of electricity reaching rural populations in Africa based on the ethnographic fieldwork in Zanzibar at various moments in time. Howe and Boyer (2015) discovered that the material politics of electricity flow through state power in their research of wind energy and the energy transition in Mexico. Akhil Gupta's research (Gupta, 2015) on electricity and class examines the link between the global South's developing middle class and rapidly growing power demand. Anusas and Ingold (2015) pondered whether we must think more expansively about electricity as a phenomenon of matter and life.

Despite the fact that electricity prediction is impacted by various human, political, economic, and social elements, no one has yet integrated the material-social entanglements of electricity into the field of electrical load forecasting study.

1.3 Contribution

This research chooses to analyze and model electricity forecasting from a novel perspective in order to bridge the gap between the literature and motivation stated previously. The major study contents of this article are separated into three parts: first, we described how to comprehend electricity forecasting using Deleuze's metaphysical complexity theory; second, we designed a neural network model using this theory; and finally, we assessed the model. The article's primary contributions are as follows:

1) Based on Deleuze's theory, a new approach to understanding electric demand and load forecasting is offered. According to this line of thought, the electrical load is a quantitative description of the mutual becoming of people and electricity, whereas load forecasting is an attempt to control this constant deterritorialization and reterritorialization process.
2) A neural network model using Deleuze's theoretical guidance is created. In this article, an LSTM-RNN-FNN model is utilized to predict the load in future 5 h based on the load value in the last 24 h and the current temperature. The result indicates that current architecture can do such a job very well.
3) We assessed the model. Here, the performance of the networks with different superparameters and datasets is also tested for the reference of subsequent researchers when selecting the parameters.

The rest of this article is organized as follows: In **Section 2**, we introduced Deleuze's concept of assemblage and the understanding of load forecasting from the assemblage perspective after a criticism of three typical perspectives (separate, embedded, and articulation perspectives). **Section 3** proposes the LSTM-RNN-FNN model based on the assemblage perspective, and **Section 4** evaluates the model using different superparameters and datasets. **Section 5** discusses the assessment results and the potential future study directions. **Section 6** concludes this article.

2 DELEUZE-STYLE THINKING PARADIGM ABOUT THE ELECTRICAL LOAD

Deleuze was one of the first philosophers to attempt to conceptualize in terms of the new electronic information environment, criticizing cybernetics' systematicity, and advocating for "open systems" of operation, code, power, and flow (Boyer, 2015). We suggested a new way of thinking about electricity forecasting based on Deleuze's concept of "assemblage." (Wise, 2013) In this section, we discussed and critiqued three typical perspectives on understanding electrical grids or, more broadly, human-technology relations and then presented Deleuze's concept of "assemblage" and how this concept should be used to comprehend the grid and load forecasts.

2.1 Criticism of Three Typical Perspectives

2.1.1 Separate Perspective

It is very common to think of people and technology as separate entities. In this view, both humans and technology are assumed to be distinct and interacting special things. People may be surrounded by numerous forms of technology; however, technologies are completely external to individuals and are only seen as tools. This perspective is very prevalent in the study of electricity. Therefore, when the smart grid enters the field of study, in other words, when the grid as a technology and humans begin to converge, individuals who share this perspective get rather nervous. This perspective has prompted a never-ending debate between the technological and social determinism.

2.1.2 Embedded Perspective

The second point of view says that technology and people cannot be isolated from their surroundings and that we should look at the interaction between people and technology in context rather than thinking about a technology in isolation. This research route offers two benefits: first, it is intuitive; second, humans and technology are both constrained. This approach views technological or social determinism as environmental rather than universal, in which people and technology are embedded (Howard, 2004). This perspective is also prevalent in the study of electricity, and terms such as electric ecology/ecosystem are rooted on it. However, it must be recognized that "embedded" implies that it can be "disembedded"; thus, this approach continues to believe that technology and humans are different and independent entities.

2.1.3 Articulation Perspective

The concept of articulation, which maintains that distinct pieces may be connected (articulated) or separated to generate completeness and identities, is the third perspective of perceiving. Historically, any articulation is unintentional. Articulation must be created, sustained, modified, and destroyed in specific practices. From this perspective, we may pose the following questions about the grid: how does the grid articulate to specific functions and uses, people, ideas and discourses, and practices? What articulations does the grid itself consist? Many anthropological studies have used this approach to better understand topics such as relationships between electrical and social power, human daily life (Winther and Wilhite, 2015), culture, and economics (Özden-Schilling, 2015).

2.2 Deleuze's Assemblage Concept

Assemblage, as defined by Deleuze, is a concept that deals with contingency and the roles of structure, organization, and change. Assemblage is a process of arranging, structuring, and fitting together, not a static term. An assemblage is also not a random collection of objects. It is a whole that reflects a certain identity and announces the scope of territorialization. An assemblage is some kind of "becoming [1]" that brings the elements together.

The assemblage may be a more complicated mode of articulation, yet there are several distinctions between the assemblage and articulation. First, the assemblage is dynamic, stressing the "process," but articulation highlights the complexity of the relationship between the static elements. Second, the assemblage's dynamics imply that rather than merely items, practices, and symbols articulated into a structure, extra aspects that characterize the process (e.g., speed) are brought into the territorialization of the assemblage. Third, an assemblage is territorialization that extracts something from the environment and draws it into the relation with other environments, rather than merely an environment, a clump of space-time, or an articulation of elements. Assemblages also disperse (deterritorialization), with the elements moving into different relations and configurations (reterritorialization). Then, the assemblage is assembled again, and the elements are reterritorialized at the same moment but in a different way.

2.3 Rethinking Load Forecasting From the Assemblage Perspective

Using Deleuze's concept of "assemblage," we may gain a fresh understanding of people's relationship with electricity. Everyone's power use may be regarded as the becoming of an appliance-grid-generator (AGG) assemblage. On the route to inventing this assemblage, people are becoming electricity, and electricity is becoming people. This pair of mutual becoming relationships is quantitatively described as the electrical load. The load at each moment indicates territorialization, and the change of load at each subsequent moment signifies deterritorialization of this moment and reterritorialization of the following moment.

Understanding the electrical load forecasting from the assemblage perspective has unparalleled advantages. First, this perspective challenges the previous belief that electricity is a separate entity, combining electricity and people. Second, the assemblage perspective emphasizes dynamics and changes, which allow researchers to make more accurate predictions. Furthermore, the assemblage's continual deterritorialization and reterritorialization means that it is constantly being created, opening up an infinite number of possibilities for load forecasting research. Researchers can develop more specific models to deal with various situations by emphasizing/removing one or more elements.

However, Deleuze reminds us that focusing solely on the usage of electricity by individuals or organizations prevents such specific assemblages from exhibiting a larger set of functions or principles. These functions or principles are referred to as the "abstract machine" by Deleuze and Guattari (1988). Deleuze (2017) envisions a new abstract machine, "society of

---

[1] "Becoming" is one of Deleuze's most important concepts. Deleuze believes that the world is nothing more than a stream of becoming and that all existence is nothing more than a relatively stable moment in the stream of "becoming-life." With the help of the concept of becoming, he rejects the concept of human beings as the basic existence, affirming that all kinds of existences in the world have multiple existence values and meanings. He supports the dynamic view of becoming and vitality theory's multiple perspectives

control," in his last articles: "We're moving toward control societies that no longer operate by confining people but through continuous control and instant communication." Electricity has been demonstrated as a control in the work of McDonald (2012) and Von Schnitzler (2013), and as a communication, the change in electrical load precisely describes the flow of control, and the forecast of the electric load should be regarded as our attempt to control this flow. We used to rely on the negative feedback regulation of the load, which means that the regulation to keep the flow under control of the grid will always be slower than the rate of change of the load, but now (in this research), we rely on the assemblage called neural networks, or more specifically, a multi-layered data-perceptron assemblage consisting of a large amount of data and multiple perceptrons.

3 ARCHITECTURE OF NEURAL NETWORKS

The electrical load reflects the becoming flow of the AGG assemblage and attempts to predict that the electrical load is based on the historical situation of the becoming flow. Therefore, it is necessary to extract the relationship between the load in different time series. In this article, a neural network is developed in order to predict the grid load for the next 5 h based on the grid load 24 h before and the current temperature. As a result, the long short-term memory recurrent neural network (LSTM-RNN) architecture is taken into consideration, which is thought to be good at predicting based on time series.

3.1 Recurrent Neural Network and Long Short-Term Memory

3.1.1 Recurrent Neural Networks

With the development of the machine learning technology, all kinds of architecture have been invented and developed in order to adapt to the needs of different types of tasks (Cho et al., 2014; Girshick, 2015; Schwing and Urtasun, 2015; Sindagi and Patel, 2018; Sherstinsky, 2020; Kattenborn et al., 2021). Recurrent neural networks (RNNs) are a classical architecture that is often used to process data sequences such as speech recognition and sales forecasting.

The comparison of the characteristics of the RNN and ordinary neural networks is shown in the following **Figures 1A, B**, which indicates that the output of the RNN at each moment depends not only on the input at that moment but also on the system state, and the main difference is that the RNN relies on the state of the entire scene more than the original network does.

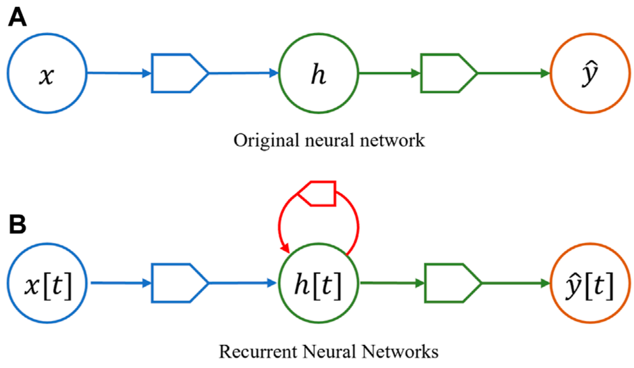

FIGURE 1 | Overview of comparison between the original networks and recurrent neural networks. **(A)** is the original network, and **(B)** represents simple architecture of the RNN.

The classical architecture of RNN is shown in **Figure 2**. It can be observed that the output value at this moment is not only controlled by the input value at this moment x_{t_i} but also receives the influence of the output value $S_{t_{i-1}}$ at the previous moment. During the training process, with the continual update of the weight matrix, the error between prediction and target data will be decreased, which means that the neural networks gradually fit the intrinsic connections between the datasets.

3.1.2 Long Short-Term Memory

Even though the RNN solves the problem about how can the neural networks datasets learn with time series, it still has certain defects. Over time scales, the RNN network does take into account the effect of the previous moment's output. However, in most cases, data from more distant moments have little effect on the present moment; as a result, introducing the effect of too far moments in a neural network may degrade its performance.

In order to overcome the negative effects of too distant a point in time, the long short-term memory (LSTM) network is developed and generally accepted by researchers. LSTMs are a special kind of RNN, capable of learning long-term dependencies based on the addition of the gate mechanism. The LSTM-RNN usually contains forgotten, input, and output gates and introduced the concept of cell state. These kinds of mechanisms allow LSTM-RNN to be made to switch between remembering the recent information and information from a long time ago, letting the data decide for itself which information to keep and which to forget. LSTM has stronger temporal correlation, allowing the neural network to obtain the relationship between the parameters from previous data, which is very helpful for the data prediction job. An original graph of architecture of LSTM networks is provided in following **Figure 3** (Yu et al., 2019), which contains extra forget gate per LSTM block to reduce the weight of values at distant time points.

3.2 Overview of the Proposed Framework

3.2.1 Architecture

The full architecture of the hybrid deep neural network used in this article is shown in **Figure 4**. The inputs are the information of the load value in the past few hours and the current temperature, and the outputs represent the prediction of the future load values. The current network contains two major parts: the LSTM-RNN and fully connected neural network (FNN).

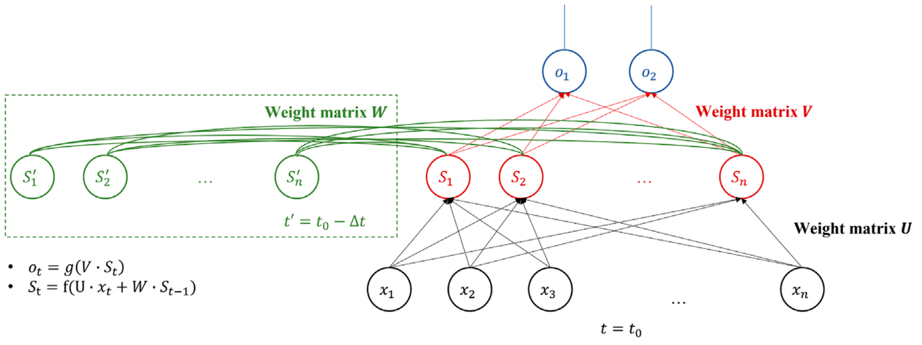

FIGURE 2 | Classical architecture of recurrent neural networks; the output at a certain time is affected by both the current input and previous output.

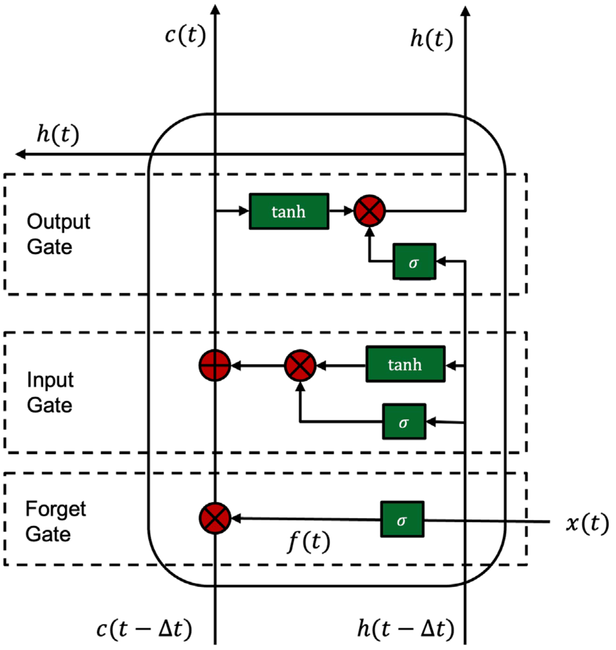

FIGURE 3 | Architecture of LSTM block.

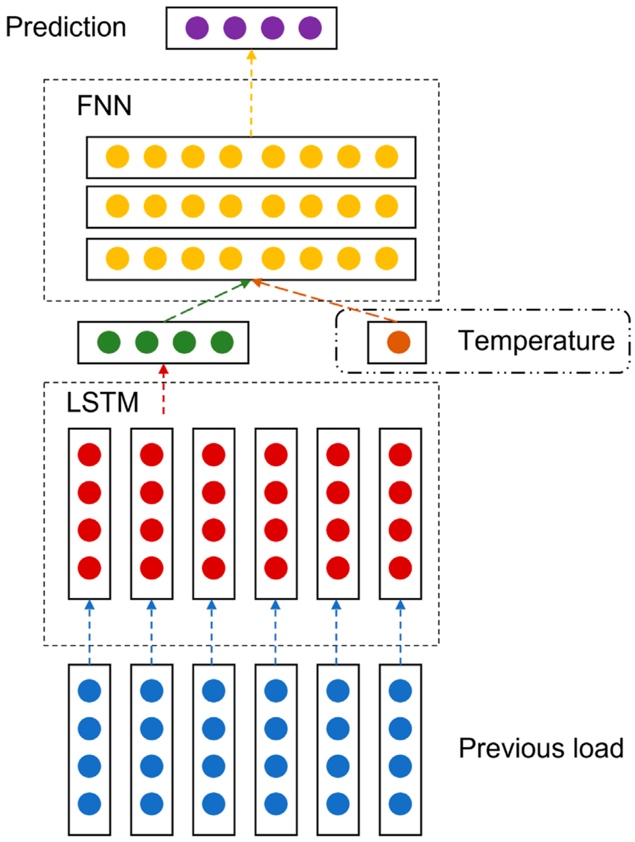

FIGURE 4 | Overview of the architecture of the LSTM-FNN used in this article; the double-dot-dash line around the temperature means participation or nonparticipation of temperature parameters.

In the process of preparing for the datasets, null values are checked, and the load data are split into training and test datasets, which relatively contain 70 and 30% data points in the whole file, respectively. The LSTM-RNN is used to extract the relationship between the load in different time series, and the FNN part is utilized to perform feature fusion, which means fusion of time series with temperature features. The output of the LSTM-RNN will be combined and sent to FNN layers and then used to calculate the final predicted values.

3.2.2 Loss Function

In this article, in order to train and test the performance of the network, different loss functions are utilized, which is called the mean square error and the mean absolute percentage error. The error measure is defined as follows:

$$MAE = \frac{1}{N}\sum_{L=1}^{N}|\hat{y} - y|$$
$$MAPE = \frac{1}{N}\sum_{L=1}^{N}|\frac{\hat{y} - y}{y}| \tag{1}$$

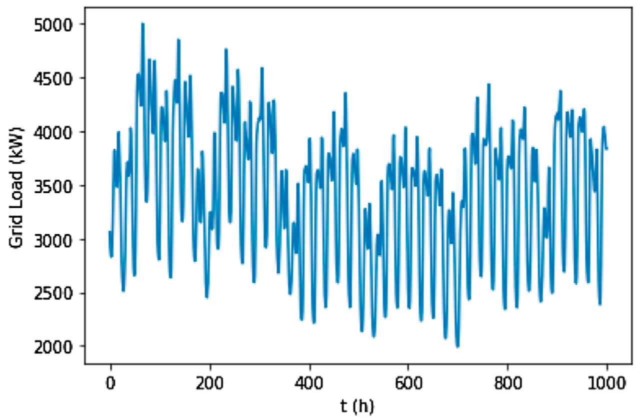

FIGURE 5 | Example of load in the training dataset in 1,000 h.

where $\hat{y}$ is the predicted load value, and y is the real load value in future several hours.

In order to improve the performance, the Huber Loss function is also used as the train loss function, which is defined as follows:

$$L_\sigma(\hat{y}, y) = \begin{cases} \frac{1}{2}(\hat{y}-y)^2, & \text{for } |\hat{y}-y| \le \delta \\ \delta|\hat{y}-y| - \frac{1}{2}\delta^2, & \text{for others} \end{cases}, \qquad (2)$$

where δ is a super parameter and can be defined by researchers.

This function is quadratic for small values of a and linear for large values, with equal values and slopes of the different sections at two points where $|\hat{y}-y| = \delta$. Comparing with the MSE loss function, the Huber loss function is more robust to outliers, and often has better performance than the general loss function.

4 MERICS

The network is established for predicting the real grid load in the real word. In this section, the performance of the network is tested and provided.

4.1 Datasets Description

In this article, the electric load dataset in the Tetouan city in the Morocco and GEF2017 datasets was used. For the dataset in Tetouan city, it provides loads of data of Tetouan city of the whole year of 2017, and for GEF2017 dataset, it provides the load data from the year of 2003–2009. An example of training datasets is shown **Figure 5**.

4.2 Test Performance Without Temperature

The classical performance of the current network is shown in **Figure 6**, where it can be observed that both the datasets can be fitted by the current neural network. The average test MAPE loss of the Tetouan database is about 0.64% while 4.32% with the GEF2017 database. The difference between two different databases is probably caused by the length of the datasets. For the larger datasets, it seems more difficult to analyze the intrinsic pattern of the load value for the LSTM network.

In order to find networks with better performance, different superparameters of the number of hidden layers and hidden sizes are tested by using both the datasets, and the MAPE is shown in **Figure 7**:

Figure 7 indicates that the increase in the hidden size has positive influence on reducing the error, but after the hidden size larger than 64 is reached, this effect will be diminished, and the train time and calculation time will also be increased while increasing such size; as a result, 64 might be the best choice to balance the time consumption with accuracy. However, for the hidden layers, networks with only one LSTM layer have better performance than others, which means more complex networks are less effective. The probable reason is that when the complexity of the network increases, the risk of overfitting increases accordingly, which is particularly serious in large datasets. However, in order to guarantee the fitting ability of the neural network, we assumed that two LSTM layers are the best choice at present, according to the result.

4.3 Adding Temperture Into Consideration

In order to test the influence of the temperature of the load value, shown in **Figure 4**, the temperature parameter is added into the neural network by being combined with the output of the LSTM part. However, the MAPE loss seems increased if we do not increase the number of epochs because of the increase in the complexity of the model. As a result, the number of epochs is also changed in order to get higher accuracy. The MAPE of different epochs using the Tetouan datasets can be shown by **Figure 8**.

Figure 8 indicates that after adding the temperature parameter into the network, more epochs are needed to get the best performance, while too many epochs will also increase the risk of overfitting; this causes the increase of MAPE in epoch = 200 in both the datasets. In addition, comparing with the original network, after adding the temperature, the forecast performance of the networks slightly declines rather than increase, which means the addition of the temperature is a negative performance of the networks. This could mean that the relationship between weather and electricity load is very uncertain for the networks to forecast.

5 DISCUSSION

An assemblage takes materials from the environment and arranges them in a unique way. "An assemblage, in this sense, is a veritable invention." (Deleuze and Guattari, 1988) Therefore, a larger assemblage (which must be part of a smart grid) can be invented, consisting of a combination of the AGG assemblage and neural networks. In this assemblage, people's historical electricity usage is becoming load forecasts. This assemblage also explains the performance degradation caused by adding temperature as a

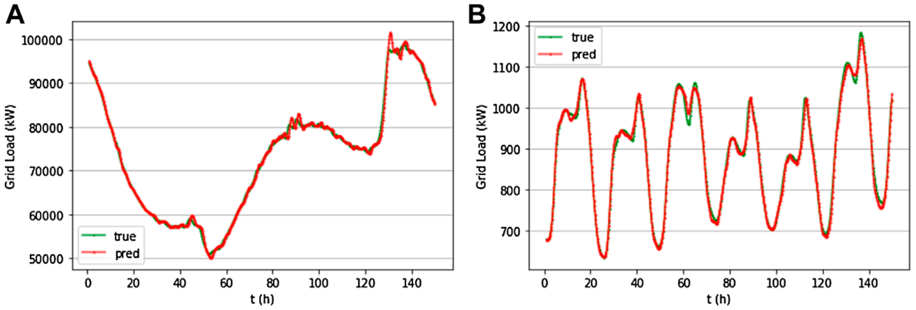

Prediction of Tetouan city database

Prediction of GEF2017 database

FIGURE 6 | Prediction and true load value of different databases. **(A)**Result of the Tetouan database. **(B)** Result of the GEF2017 database.

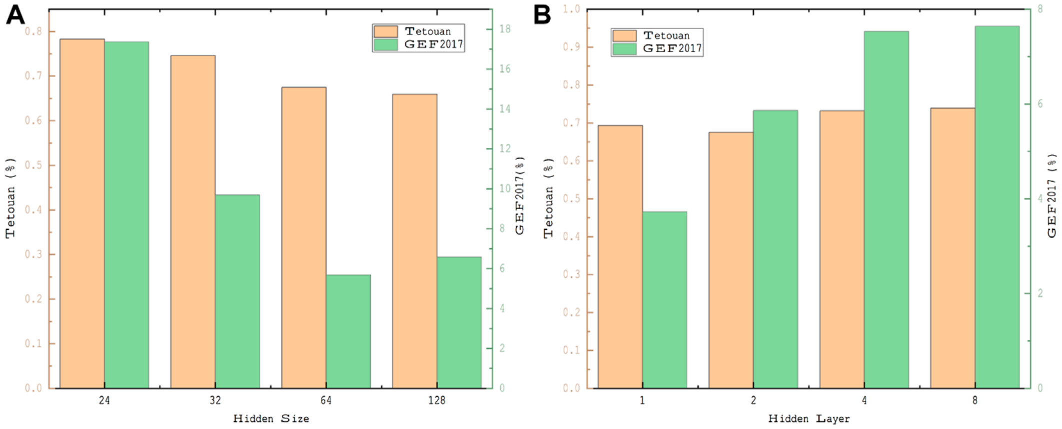

MAPE of different hidden size of LSTM

MAPE of different number of hidden layers of LSTM

FIGURE 7 | Mean absolute percentage error with different networks with different superparameters. **(A)** Different hidden sizes (with hidden layers = 2). **(B)** Different numbers of hidden layers (with hidden size = 64).

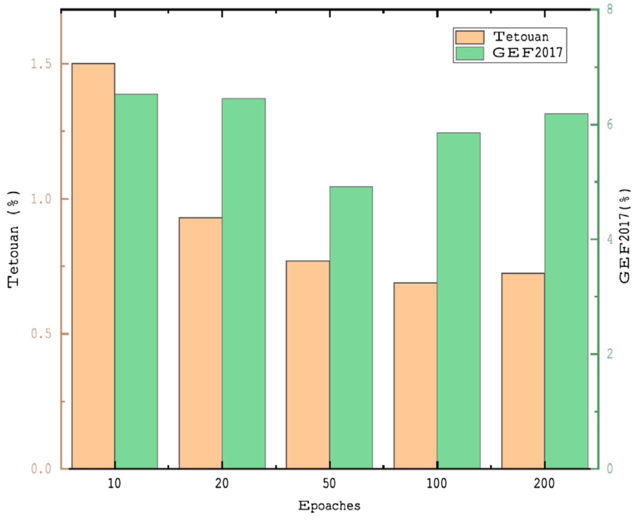

FIGURE 8 | Mean absolute percentage error with different number of epochs under hidden layers = 2 and hidden size = 64.

variable to the neural network. Temperature is a factor that affects people's electrical behaviors (Valor et al., 2001). Thus, adding temperature may be considered as a double-count.

Actually, the relationship between the load value and temperature is not stable and even chaotic under some conditions. For example, the temperature-load relationship will be different in summer and winter, or in weekday and weekends. If we want to use the neural network to reflect it, it may get lost sometimes, causing the decrease in the performance.

Meanwhile, in the larger assemblage, the load forecasting results are utilized to "optimize" the grid, which in turn affects human behaviors. This mutual becoming constitutes a deconstruction of the time series. The forecast of the future is becoming the present, and it all points to the past. Attempting to control the flow of the control instead causes it to control itself.

Furthermore, we are constantly entangled and constructed by multiple assemblages. Therefore, Deleuze cautions us not to oversimplify the assemblage. The distinction between conventional and renewable energy sources, for example, is a more vivid description of the power producing assemblage in Howe and Boyer's study (Howe and Boyer, 2015).Similarly, future study on electric load forecasting can be more specific and accurate by combining different assemblages or by the constant becoming and destruction of the assemblages.

6 CONCLUSION

Unlike previous research on electric load forecasting, we presented a novel pattern of thinking based on Deleuze's assemblage concept in this article. From the perspective of the assemblage, the electrical load is regarded as a quantitative description of the mutual becoming of people and electricity (i.e., a constant deterritorialization and reterritorialization process), whereas load forecasting is an attempt to control the aforementioned process. Depending on the assemblage perspective, an LSTM-RNN-FNN model is utilized to predict the load in future 5 h based on the load value in the last 24 h and the current temperature. The outcome of evaluating multiple superparameters and datasets reveals that the current architecture can conduct forecast job quite effectively. We believed that the proposed LSTM-RNN-FNN model will aid in electric load forecasting and that the assemblage perspective on which we rely will give new inspiration for future electric load forecasting and potentially smart grid research. By adding or removing the elements in the assemblage or constructing new assemblages, future research could delve more into the impact of smart grid, natural environment, and human and societal factors on the accuracy of electric load forecasting.

DATA AVAILABILITY STATEMENT

The original contributions presented in the study are included in the article/Supplementary Material further inquiries can be directed to the corresponding authors.

AUTHOR CONTRIBUTIONS

Conceptualization: JX, ZW, and WN; writing—original draft preparation: JX and ZW; writing—review and editing: JX, ZW, and YD; visualization: ZW; supervision: WN; funding acquisition: WN. All authors have read and agreed to the published version of the manuscript.

REFERENCES

Anusas, M., and Ingold, T. (2015). The Charge against Electricity. *Cult. Anthropol.* 30, 540–554. doi:10.14506/ca30.4.03

Baharudin, Z., and Kamel, N. (2008). "Autoregressive Method in Short Term Load Forecast," in 2008 IEEE 2nd International Power and Energy Conference (Johor Bahru, Malaysia: IEEE), 1603–1608. doi:10.1109/pecon.2008.4762735

Boyer, D. (2015). Anthropology Electric. *Cult. Anthropol.* 30, 531–539. doi:10.14506/ca30.4.02

Cho, K., Van Merriënboer, B., Gulcehre, C., Bahdanau, D., Bougares, F., Schwenk, H., et al. (2014). Learning Phrase Representations Using Rnn Encoder-Decoder for Statistical Machine Translation. *arXiv Prepr. arXiv:1406.1078*. doi:10.3115/v1/d14-1179

Deleuze, G., and Guattari, F. (1988). *A Thousand Plateaus: Capitalism and Schizophrenia*. London, UK: Bloomsbury Publishing.

Deleuze, G. (2017). *Postscript on the Societies of Control*. Oxfordshire, England, UK: Routledge.

Dodamani, S., Shetty, V., and Magadum, R. (2015). "Short Term Load Forecast Based on Time Series Analysis: A Case Study," in 2015 International Conference on Technological Advancements in Power and Energy (TAP Energy) (Kollam, India: IEEE), 299–303. doi:10.1109/tapenergy.2015.7229635

Girshick, R. (2015). "Fast R-Cnn," in Proceedings of the IEEE international conference on computer vision, 1440–1448. doi:10.1109/iccv.2015.169

Gupta, A. (2015). An Anthropology of Electricity from the Global South. *Cult. Anthropol.* 30, 555–568. doi:10.14506/ca30.4.04

[Dataset] Hernández, D. (2013). *Energy Insecurity: A Framework for Understanding Energy, the Built Environment, and Health Among Vulnerable Populations in the Context of Climate Change*.

Howard, P. N. (2004). *Embedded Media: Who We Know, what We Know, and Society Online Philip N.* howard: university of washington steven jones, university of illinois-chicago.

Howe, C., and Boyer, D. (2015). Aeolian Politics. *Distinktion J. Soc. Theory* 16, 31–48. doi:10.1080/1600910x.2015.1022564

Hussain, A., Rahman, M., and Memon, J. A. (2016). Forecasting Electricity Consumption in pakistan: The Way Forward. *Energy Policy* 90, 73–80. doi:10.1016/j.enpol.2015.11.028

Kamel, N., and Baharudin, Z. (2007). "Short Term Load Forecast Using Burg Autoregressive Technique," in 2007 International Conference on Intelligent and Advanced Systems (Kuala Lumpur, Malaysia: IEEE), 912–916. doi:10.1109/icias.2007.4658519

Kattenborn, T., Leitloff, J., Schiefer, F., and Hinz, S. (2021). Review on Convolutional Neural Networks (Cnn) in Vegetation Remote Sensing. *ISPRS J. Photogrammetry Remote Sens.* 173, 24–49. doi:10.1016/j.isprsjprs.2020.12.010

Kuo, P.-H., and Huang, C.-J. (2018). A High Precision Artificial Neural Networks Model for Short-Term Energy Load Forecasting. *Energies* 11, 213. doi:10.3390/en11010213

Lahouar, A., and Ben Hadj Slama, J. (2015). Day-ahead Load Forecast Using Random Forest and Expert Input Selection. *Energy Convers. Manag.* 103, 1040–1051. doi:10.1016/j.enconman.2015.07.041

Li, Y.-z., and Niu, J.-c. (2009). "Forecast of Power Generation for Grid-Connected Photovoltaic System Based on Markov Chain," in 2009 Asia-Pacific Power and Energy Engineering Conference (Wuhan, China: IEEE), 1–4. doi:10.1109/appeec.2009.4918386

Lin, B., and Liu, C. (2016). Why Is Electricity Consumption Inconsistent with Economic Growth in china? *Energy Policy* 88, 310–316. doi:10.1016/j.enpol.2015.10.031

McDonald, D. A. (2012). *Electric Capitalism: Recolonising Africa on the Power Grid*. Oxfordshire, England, UK: Routledge.

Mohammad, F., and Kim, Y.-C. (2020). Energy Load Forecasting Model Based on Deep Neural Networks for Smart Grids. *Int. J. Syst. Assur Eng. Manag.* 11, 824–834. doi:10.1007/s13198-019-00884-9

Özden-Schilling, C. (2015). Economy Electric. *Cult. Anthropol.* 30, 578–588.

Pan, G., Hu, Q., Gu, W., Ding, S., Qiu, H., and Lu, Y. (2021). Assessment of Plum Rain's Impact on Power System Emissions in Yangtze-Huaihe River Basin of China. *Nat. Commun.* 12, 6156. doi:10.1038/s41467-021-26358-w

Schwing, A. G., and Urtasun, R. (2015). Fully Connected Deep Structured Networks. *arXiv Prepr. arXiv:1503.02351*.

Sherstinsky, A. (2020). Fundamentals of Recurrent Neural Network (Rnn) and Long Short-Term Memory (Lstm) Network. *Phys. D. Nonlinear Phenom.* 404, 132306. doi:10.1016/j.physd.2019.132306

Sindagi, V. A., and Patel, V. M. (2018). A Survey of Recent Advances in Cnn-Based Single Image Crowd Counting and Density Estimation. *Pattern Recognit. Lett.* 107, 3–16. doi:10.1016/j.patrec.2017.07.007

Singh, A. K., Khatoon, S., Muazzam, M., and Chaturvedi, D. (2012). "Load Forecasting Techniques and Methodologies: A Review," in 2012 2nd International Conference on Power, Control and Embedded Systems (Allahabad, India: IEEE), 1–10. doi:10.1109/icpces.2012.6508132

Sun, K., Li, K.-J., Zhang, Z., Liang, Y., Liu, Z., and Lee, W.-J. (2021a). An Integration Planning for Renewable Energies, Hydrogen Plant and Logistics Center in the Suburban Power Grid. *IEEE Trans. Industry Appl.* 58, 2771. doi:10.1109/TIA.2021.3111842

Sun, K., Qiu, W., Yao, W., You, S., Yin, H., and Liu, Y. (2021b). Frequency Injection Based Hvdc Attack-Defense Control via Squeeze-Excitation Double Cnn. *IEEE Trans. Power Syst.* 36, 5305–5316. doi:10.1109/tpwrs.2021.3078770

Sun, K., Xiao, H., and Liu, Y. (2021c). Optimized Allocation Method of the Vsc-Mtdc System for Frequency Regulation Reserves Considering the Cost. *CSEE J. Power Energy Syst.* 8, 53. doi:10.17775/CSEEJPES.2020.05800

Sun, K., Xiao, H., Pan, J., and Liu, Y. (2021d). Vsc-hvdc Interties for Urban Power Grid Enhancement. *IEEE Trans. Power Syst.* 36, 4745–4753. doi:10.1109/tpwrs.2021.3067199

Valor, E., Meneu, V., and Caselles, V. (2001). Daily Air Temperature and Electricity Load in spain. *J. Appl. Meteor.* 40, 1413–1421. doi:10.1175/1520-0450(2001)040<1413:datael>2.0.co;2

Von Schnitzler, A. (2013). Traveling Technologies: Infrastructure, Ethical Regimes, and the Materiality of Politics in south africa. *Cult. Anthropol.* 28, 670–693. doi:10.1111/cuan.12032

Winther, T. (2008). *The Impact of Electricity: Development, Desires and Dilemmas*. New York, NY, USA: Berghahn Books.

Winther, T., and Wilhite, H. (2015). Tentacles of Modernity: Why Electricity Needs Anthropology. *Cult. Anthropol.* 30, 569–577. doi:10.14506/ca30.4.05

Wise, J. (2013). "Assemblage," in *Gilles Deleuze: Key Concepts* (Buckinghamshire, UK: Acumen Publishing Limited), 91–102.

Xiao, H., Sun, K., Pan, J., Li, Y., and Liu, Y. (2021). Review of Hybrid Hvdc Systems Combining Line Communicated Converter and Voltage Source Converter. *Int. J. Electr. Power & Energy Syst.* 129, 106713. doi:10.1016/j.ijepes.2020.106713

Yang, D., Jin, Z., Zheng, T., and Jin, E. (2022). An Adaptive Droop Control Strategy with Smooth Rotor Speed Recovery Capability for Type Iii Wind Turbine Generators. *Int. J. Electr. Power & Energy Syst.* 135, 107532. doi:10.1016/j.ijepes.2021.107532

Yu, Y., Si, X., Hu, C., and Zhang, J. (2019). A Review of Recurrent Neural Networks: LSTM Cells and Network Architectures. *Neural Comput.* 31, 1235–1270. doi:10.1162/neco_a_01199

Zhang, H.-T., Xu, F.-Y., and Zhou, L. (2010). "Artificial Neural Network for Load Forecasting in Smart Grid," in 2010 international conference on machine learning and cybernetics (Qingdao, China: IEEE), 3200–3205. doi:10.1109/icmlc.2010.5580713

Zhang, X., and Li, R. (2021). A Novel Decomposition and Combination Technique for Forecasting Monthly Electricity Consumption. *Front. Energy Res.* 2021, 773. doi:10.3389/fenrg.2021.792358

Zheng, J., Xu, C., Zhang, Z., and Li, X. (2017). "Electric Load Forecasting in Smart Grids Using Long-Short-Term-Memory Based Recurrent Neural Network," in 2017 51st Annual Conference on Information Sciences and Systems (CISS) (Baltimore, MD, USA: IEEE), 1–6. doi:10.1109/ciss.2017.7926112

Conflict of Interest: The authors declare that the research was conducted in the absence of any commercial or financial relationships that could be construed as a potential conflict of interest.

frontiers | Frontiers in Energy Research

ORIGINAL RESEARCH
published: 27 May 2022
doi: 10.3389/fenrg.2022.906047

Comprehensive Decision-Making Method for DC Transformation Object of Medium Voltage AC Distribution Network

Fengxue Wang, Yangsen Ou, Xi Xin and Moyuan Yang*

School of Electric Power, South China University of Technology, Guangzhou, China

The trend of DC development in the medium voltage AC distribution network is obvious. However, due to the constraints of reliability, cost, and power quality, not every AC distribution network is suitable for DC transformation. As for the AC distribution network suitable for DC transformation, it is necessary to solve the problems of multivariable constraint solutions and the demand for sorting and optimizing multi-schemes in DC transformation. Therefore, this study proposes a comprehensive decision-making method for the DC transformation object of the medium voltage AC distribution network. Firstly, a comprehensive evaluation index system for DC transformation is established from four aspects: improving power supply reliability, technical requirements, social benefits, and economic benefits. Among them, the reliability of power supply mainly examines the completion degree of the target. In terms of the technical requirements of DC transformation, it is necessary to consider the constraints of AC transformation and the driving force of DC transformation. As for the social benefits, it reflects the indirect demand for DC transformation, which reflects social development. In terms of economic benefits, it pays attention to the transformation cost and input–output ratio. Then, the combined optimization model is used to solve the index's comprehensive weight based on the subjective and objective weight model. Moreover, the comprehensive evaluation value of the transformation object is determined by the double-base point method. The scheme optimization model is used to determine the final transformation scheme to guide the power grid enterprises to prioritize the DC transformation projects. Finally, several medium-voltage distribution networks in Guangzhou, Guangdong province, China, are taken as examples to verify the effectiveness of the proposed method.

Keywords: urban distribution network, DC transformation, optimization of object, comprehensive decision making, comprehensive evaluation index system

OPEN ACCESS

Edited by:
Ke-Jun Li,
Shandong University, China

Reviewed by:
Ying Sun,
Shandong University, China
Zhijie Liu,
Shandong University, China

****Correspondence:***
Yangsen Ou
1400166077@qq.com

Specialty section:
This article was submitted to
Smart Grids,
a section of the journal
Frontiers in Energy Research

Received: *28 March 2022*
Accepted: *20 April 2022*
Published: *27 May 2022*

Citation:
Wang F, Ou Y, Xin X and Yang M (2022) Comprehensive Decision-Making Method for DC Transformation Object of Medium Voltage AC Distribution Network.
Front. Energy Res. 10:906047.
doi: 10.3389/fenrg.2022.906047

1 INTRODUCTION

The traditional AC distribution network faces the following difficulties: 1) because of the rapid growth of urban power supply load, the load demand and pressure of power supply reliability increase; 2) the continuous development of high-tech industries has higher requirements for power quality; and 3) the reform of the new energy system has led to a continuous surge in urban renewable energy penetration, which puts forward higher requirements for the ability of the grid to absorb clean energy. However, the traditional AC transformation has technical bottlenecks in solving these new problems: 1) under the constraints of space resources, it is difficult to meet the higher requirements of high-density urban loads for power supply capacity; 2) it is difficult to meet the requirements of safe, flexible, and efficient access of renewable energy under the constraints of frequency, phase, and angle; 3) under short-term interruption constraints of power outage transfer, it is difficult to meet the requirements of sensitive loads for uninterrupted high-quality power supply; 4) it is difficult to meet the requirements of the distribution network for closed-loop operation power accommodation under open-loop operation constraints; and 5) under the constraints of the technology level of current distribution equipment, it is difficult to meet the requirements of the distribution network for capacity expansion without exceeding the short-circuit current. The above technical bottlenecks make the DC transformation an important consideration. How to select the object of DC transformation and determine its sequence has become the first consideration. Therefore, this study focuses on the decision-making method for the DC transformation object of the medium voltage AC distribution network.

In the DC transformation, the bipolar three-wire DC distribution network system has more advantages than the urban AC distribution network: 1) the power supply capacity can be increased to about 1.6 times of the original (Rentschler et al., 2018), which is conducive to greatly improving the power supply capacity under the condition of limited space resources and solving the demand problem of rapid load growth; 2) according to the active power dispatching instruction of the system, the converter can realize the power fusion under the closed-loop operation and improve the power supply reliability; 3) through the fast controllability of power electronic equipment and the rational allocation of energy storage devices, high quality power supply of important loads can be realized (Wang et al., 2020), which can solve the problems of the development of high-tech industries; 4) compared with AC, DC grids do not have the frequency and phase angle problem, which can solve the problem of clean energy access; and 5) the current control effect of the inverter can significantly inhibit the short-circuit current. Based on the above analysis, this study determines the means of DC transformation: transforming the urban AC distribution network into a bipolar three-wire DC distribution network system.

Under the limited investment conditions, how to formulate a reasonable DC transformation and investment plan is the concern of power supply enterprises. At present, there are few studies on the DC transformation of urban distribution networks. Rentschler et al. (2018) analyzed the advantages of power supply capacity in DC transformation of the urban distribution network. Chen et al. (2019) comparatively analyzed three DC distribution application scenarios and showed that DC transformation can effectively reduce transmission loss and meet the needs of green power grid development. Cui et al. (2019) proposed an AC/DC party-line power distribution scheme based on Z-type transformer and showed the feasibility and technical advantages of the scheme. Li et al. (2020) used empirical mode decomposition (EMD) for data preprocessing and then evaluated the DC power quality after transformation based on the neural network. Huang et al. (2020) evaluated the DC transformation scheme of the power grid in a large city based on the analytic hierarchy process and entropy weight method. However, all the above studies evaluated the DC transformation of a single distribution network, lacking the basis for selecting this single distribution network for DC transformation. Moreover, the influence of the AC transformation bottleneck on the optimization of DC transformation objects of the urban distribution network is not considered.

In order to formulate a reasonable DC transformation strategy, it is necessary to make comprehensive decisions on multiple urban distribution networks and optimize the distribution network that can give full play to the advantages of DC transformation and maximize the comprehensive benefits of DC transformation. The comprehensive decision-making of urban distribution network transformation objects is an optimization problem, including the establishment of comprehensive evaluation indexes and the optimization of objects under the comprehensive decision-making model. At present, there are a few studies on comprehensive decision-making of distribution network transformation objects. Zhao and Li (2021) proposed evaluation indexes based on the pressure-state-response (PSR) model, combined with principal component analysis and correlation analysis to screen redundant indexes, thus constructing a dynamic energy efficiency index system to evaluate and transform the energy efficiency of industrial park users. Chen et al. (2020) considered the economy and efficiency of social capital participating in the operation of the distribution network, which can make comprehensive decisions on the transformation objects and planning schemes of the distribution network. However, there is still a lack of research on the comprehensive decision-making of DC transformation objects in the urban distribution network. Zhao and Li (2021) and Chen et al. (2020) mentioned that the research subjects are traditional AC transformation objects. Without considering the characteristics of DC transformation, they cannot reflect the direct demand for DC transformation, which can have the driving force by replacing the AC transformation constraints in the urban distribution network, or the indirect demand for DC transformation, which is driven by social development.

At present, the research on decision-making methods mainly focuses on the analytic hierarchy process (AHP) (Huang et al., 2020), interval-valued intuitionistic fuzzy method (De Miguel et al., 2016; Ma and Zhang, 2020), and entropy weight method (Zhao and Li, 2021; Wang et al., 2017; Hu et al. 2020), among others. However, the above methods have some shortcomings in practical engineering: 1) the analytical method ignores the fuzziness and uncertainty of decision-makers; 2) the process of establishing interval-valued intuitionistic fuzzy judgment matrix and the consistency test is complicated, and experts' risk attitude is not considered

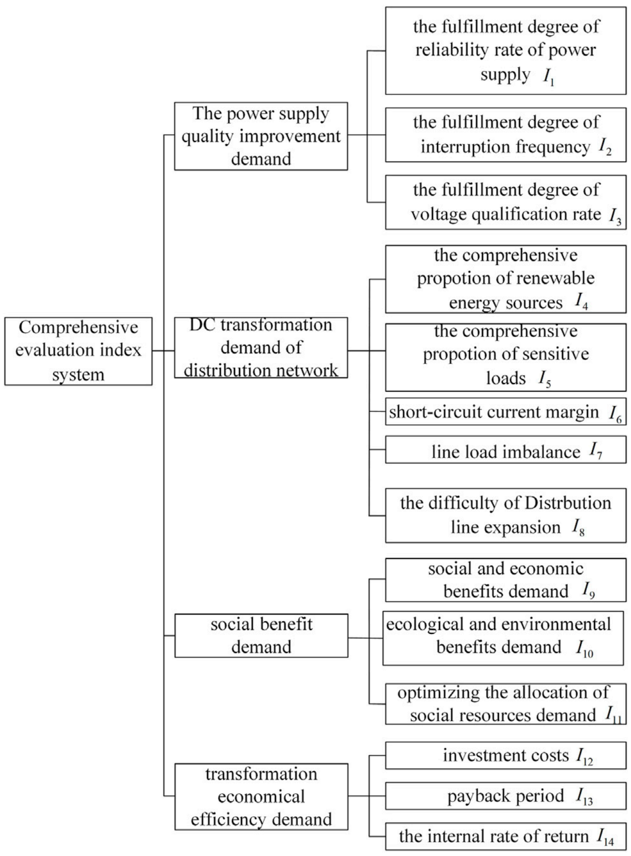

FIGURE 1 | Comprehensive evaluation index system of DC transformation object of the urban distribution network.

effectively; 3) the entropy weight method ignores the value information brought by the correlation and conflict of index data; and 4) there is a lack of effective integration of subjective and objective value information.

According to the above problems, this study proposes a comprehensive decision-making method for the DC transformation object of the urban distribution network, which can make a decision by constructing an evaluation index system, solving the index weight, and determining the comprehensive evaluation value. Firstly, this study constructs a comprehensive evaluation index system of DC transformation objects of the urban distribution network from four aspects: power supply quality improvement demand, DC transformation demand, social benefit demand, and transformation economical efficiency demand. Then, the improved G2 method and the improved criteria importance through the intercriteria correlation weight method (CRITIC) are used to solve the comprehensive weight through the relative entropy combinatorial optimization model, and the comprehensive evaluation value of the object is calculated based on the double-base point method. Combined with the scheme selection model, the optimal scheme is determined to arrange the investment in DC transformation reasonably. Finally, the effectiveness of the method is verified by an example.

2 COMPREHENSIVE EVALUATION INDEX SYSTEM

In order to determine the construction priority of DC transformation objects of the urban distribution network, this study establishes a comprehensive evaluation index system, considering the power supply quality improvement demand, DC transformation demand, social benefit demand, and transformation economical efficiency demand. The structure of this system is shown in **Figure 1**. The index system aims to guide the optimization of DC transformation objects of the urban distribution network and maximize the comprehensive benefits of DC transformation investment.

2.1 The Power Supply Quality Improvement Demand

Improving power supply reliability is the main task of traditional distribution network transformation. In practical engineering, the average reliability rate of power supply and system average interruption frequency index are the main indexes, reflecting the continuity of power supply. In addition, the quality of voltage directly affects the power supply availability and cannot be ignored in the distribution network transformation.

Accordingly, this study uses the power supply quality (Zhao and Li, 2021) covering the above two aspects to characterize the continuous availability of power supply in the distribution network. The power supply quality in this study is comprehensively characterized by the average reliability rate of power supply, the system average interruption frequency index, and the voltage qualification rate (Chen et al., 2020; De Miguel et al., 2016). In the actual planning, it is necessary to consider the matching degree between the current situation of power supply quality and the target level to guide the optimization of the transformation objects. Therefore, this study introduces the fulfillment degree of reliability rate of power supply I_1, the fulfillment degree of interruption frequency I_2, and the fulfillment degree of voltage qualification rate I_3, which can reflect the demand for power supply quality improvement in the distribution network. The definition is as follows:

$$\begin{cases} I_1 = \left(R_{\mathrm{ASAI-1}} / R_{\mathrm{ASAI-T}}\right) \times 100\% \\ I_2 = \left(R_{\mathrm{SAIFI-T}} / R_{\mathrm{SAIFI-1}}\right) \times 100\% \\ I_3 = \left(R_{\mathrm{VQR-1}} / R_{\mathrm{VQR-T}}\right) \times 100\% \end{cases} \tag{1}$$

In this formula, $R_{\mathrm{ASAI\text{-}1}}$, $R_{\mathrm{SAIFI\text{-}1}}$, $R_{\mathrm{VQR\text{-}1}}$ and $R_{\mathrm{ASAI\text{-}T}}$, $R_{\mathrm{SAIFI\text{-}T}}$, $R_{\mathrm{VQR\text{-}T}}$ are the current and target values of the average reliability rate of power supply, system average interruption frequency, and voltage qualification rate of the distribution network, respectively.

The above target values are different from different power supply zones. Usually, the power supply enterprises formulate corresponding planning objectives according to the five types of power supply zones and can be selected according to the actual situation in engineering application.

2.2 DC Transformation Demand of the Distribution Network

In addition to the power supply quality improvement demand, the comprehensive decision-making method of DC transformation objects in the urban distribution network also needs to focus on the DC demand of the urban distribution network. In this regard, from the source-load characteristics, network-side security, and the construction conditions of distribution lines, this study sets up five DC transformation demanding indicators of the distribution network to reflect the different planning areas and different transformation demands of different scenes. The indicators are shown in **Figure 1**.

The comprehensive proportion of renewable energy sources (RES) and the comprehensive proportion of sensitive loads reflect the DC demand of source-load characteristics in the distribution network, which is from the two aspects of the safe and efficient access demand for RES and the high power supply quality demand for sensitive loads. Short-circuit current margin and line load imbalance reflect the DC demand of network-side security from two aspects of the constraint of substation capacity expansion and the incoordination of line development. From the perspective of spatial resource constraints, the difficulty of distribution line expansion reflects the limited expansion of AC lines with different planning objects and the demand for DC lines with high transmission capacity. The above indicators establish an evaluation system from the three dimensions of source, network, and load, which comprehensively reflects the DC demand for the urban distribution network.

2.2.1 DC Transformation Demand Based on Source and Load Characteristics

Compared with AC, there is no synchronization problem and power quality problem caused by frequency and phase angle in DC distribution, and the reasonable configuration of voltage source converter can effectively play a role in power quality control, which satisfies the demand for renewable energy development for flexible and efficient access, as well as the demand for sensitive load development for high power quality (Wang et al., 2020; Wang et al., 2017). Therefore, this study sets the comprehensive proportion of RES and sensitive load to reflect the DC transformation demand of source and load characteristics for the urban distribution network.

The comprehensive proportion index of RES is defined as

$$.\quad \begin{cases} I_4 = \left(\alpha_{\mathrm{RES}} \dfrac{\sum P_{\mathrm{RES.0}}^{\mathrm{N}i}}{P_{\mathrm{L.0}}^{\max}} + \beta_{\mathrm{RES}} \dfrac{\sum P_{\mathrm{RES.1}}^{\mathrm{N}i}}{P_{\mathrm{L.1}}^{\max}} \right. \\ \qquad \left. + \gamma_{\mathrm{RES}} \dfrac{\sum P_{\mathrm{RES.2}}^{\mathrm{N}i}}{P_{\mathrm{L.2}}^{\max}} \right) \times 100\% \\ \alpha_{\mathrm{RES}} + \beta_{\mathrm{RES}} + \gamma_{\mathrm{RES}} = 1 \end{cases} \tag{2}$$

In this formula, $P_{\mathrm{RES.0}}^{\mathrm{N}i}$, $P_{\mathrm{RES.1}}^{\mathrm{N}i}$, $P_{\mathrm{RES.2}}^{\mathrm{N}i}$ are the statistical region's current, short-term, and medium-term rated active power of the type i RES, respectively. $P_{\mathrm{L.0}}^{\max}$, $P_{\mathrm{L.0}}^{\max}$, $P_{\mathrm{L.0}}^{\max}$ are the statistical region's current, short-term, and medium-term load peak, respectively. α_{RES}, β_{RES}, γ_{RES} are the statistical region's current, short-term, and medium-term weight coefficient of RES proportion in comprehensive proportion. According to the specific situation, they can be given by experts. In this study, they are set to 0.3, 0.4, and 0.3, respectively.

Sensitive loads refer to the user loads that cannot work normally or causes serious losses when the voltage drops instantaneously or breaks shortly (Hu et al., 2020). This kind of loads has high requirements for voltage quality and power supply reliability. The comprehensive proportion index of sensitive loads I_5 in this study reflects the demand degrees of loads for the DC distribution network with high power supply quality, which is defined as

$$.\quad \begin{cases} I_5 = \left(\alpha_{\mathrm{SL}} \dfrac{\sum P_{\mathrm{SL.0}}^{\mathrm{N}j}}{P_{\mathrm{L.0}}^{\max}} + \beta_{\mathrm{SL}} \dfrac{\sum P_{\mathrm{SL.1}}^{\mathrm{N}j}}{P_{\mathrm{L.1}}^{\max}} \right. \\ \qquad \left. + \gamma_{\mathrm{SL}} \dfrac{\sum P_{\mathrm{SL.2}}^{\mathrm{N}j}}{P_{\mathrm{L.2}}^{\max}} \right) \times 100\% \\ \alpha_{\mathrm{SL}} + \beta_{\mathrm{SL}} + \gamma_{\mathrm{SL}} = 1 \end{cases} \tag{3}$$

In this formula, $P_{\mathrm{SL.0}}^{\mathrm{N}i}$, $P_{\mathrm{SL.0}}^{\mathrm{N}i}$, $P_{\mathrm{SL.0}}^{\mathrm{N}i}$ are the statistical region's current, short-term, and medium-term rated power of the type j RES, respectively, and α_{SL}, β_{SL}, γ_{SL} are the current, short-term, and medium-term weight coefficient of sensitive load proportion in comprehensive proportion. According to the specific situation, they can be given by experts. In this study, they are set to 0.3, 0.4, and 0.4, respectively.

2.2.2 DC Transformation Demand Based on Network-Side Security

According to the security constraints of the heterogeneity of short-circuit current level and line load development on the AC distribution network capacity expansion, this study sets short-circuit current margin and line load imbalance index to reflect the DC transformation demand of network-side security.

In the traditional AC distribution network, substation capacity expansion improves the power supply capacity to meet the demand for growing loads, which may lead to excessive short-circuit current of the distribution network and difficult selection of circuit breakers and even affect the safety of the whole network. If the line is expanded by the DC transformation, the short-circuit current will not be significantly increased due to the current control effect of the inverter, which is conducive to the short-circuit current control of the AC system (Wang et al., 2020).

In addition, due to the open-loop operation mode of the traditional AC distribution network, the heterogeneity of line load development will significantly affect the load transfer capacity, reduce the reliability of power supply, and cause a crisis in the safety of the distribution network. However, AC lines are interconnected through DC transformation, and the power flow control ability of the converter can effectively balance the line load rate and maintain the benign development of distribution network lines.

The short-circuit current margin I_6 and line load imbalance I_7 are set to reflect the DC transformation demand of network-side security, which are defined as

$$I_6 = \left(1 - \frac{I_{\mathrm{F}}^{\max}}{I_{\mathrm{F}}^{\mathrm{CL}}}\right) \times 100\% \tag{4}$$

In the formula, $I_{\mathrm{F}}^{\max}$ is the short-circuit current peak value of the distribution network; $I_{\mathrm{F}}^{\mathrm{CL}}$ is the short-circuit current control level of the distribution network; and the medium voltage distribution network is generally 20 kV:

$$I_7 = 1 - \left(-\frac{1}{\ln L}\sum \frac{\eta_{\mathrm{LLR}l}}{\sum \eta_{\mathrm{LLR}l}} \ln \frac{\eta_{\mathrm{LLR}l}}{\sum \eta_{\mathrm{LLR}l}}\right) \tag{5}$$

In the formula, L is the line return; $\eta_{\mathrm{LLR}l}$ is the load rate for the circuit l; and $\frac{1}{\ln L}\sum \frac{\eta_{\mathrm{LLR}l}}{\sum \eta_{\mathrm{LLR}l}} \ln \frac{\eta_{\mathrm{LLR}l}}{\sum \eta_{\mathrm{LLR}l}}$ is the information entropy for line load rate. The index reflects the unbalanced degree of line loads with the concept of entropy. Besides, the larger the index value, the more unbalanced the line load.

2.2.3 DC Transformation Demand Based on Construction Conditions of Distribution Lines

The national standard GB 50217 points out that the selection of cable path should be convenient for laying and maintenance and ensure the shortest path under the condition of meeting the safety requirements (Liao et al., 2016). The DC transformation of AC lines into bipolar three-line DC lines can increase the power supply capacity to about 1.6 times the original. In the complex areas of the underground pipe network, such as the urban center, it can effectively reduce the laying path of cable lines and the late operation and maintenance and reduce the influence of cable line laying and maintenance on the complex underground pipe network. It has the advantages of construction and maintenance and economic advantages. On the contrary, when using overhead lines, the high transmission capacity of DC distribution lines can also effectively reduce the occupied corridor of overhead lines. In the urban center area with the high land price and difficult new corridors, DC overhead lines will play obvious economic and construction advantages. Therefore, this study sets the difficulty of distribution line expansion (index I_8) to reflect the demand for space resource constraints for the DC distribution network. The index I_8 in this study is defined as

$$I_8 = \left(I_8^{\mathrm{pipe}} + I_8^{\mathrm{line}}\right)/2 \tag{6}$$

In the formula, I_8^{pipe} is the complexity of the underground pipe network and I_8^{line} is the difficulty of the construction of the overhead line corridor. In addition, the indexes I_8^{pipe} and I_8^{line} in this study are defined as qualitative indexes, which can be obtained by the Delphi-gold segmentation cloud generation method (Okoli and Pawlowski, 2004). Its calculation is shown in **Supplementary Table SA2**.

2.3 Social Benefit Demand

Social benefit demand is the indirect demand for social development for DC transformation of urban distribution network, including social and economic benefits demand, ecological and environmental benefits demand, and optimizing the allocation of social resources demand.

Social and economic benefit demand refers to the indirect promotion effect of DC transformation on social and economic development, which is characterized by the ratio of gross domestic product (GDP) of loads to total electricity consumption, reflecting the social and economic value of unit electricity consumption. The social and economic benefit demand is defined as

$$I_9 = \frac{M_{\mathrm{GDP}}}{E_{\mathrm{year}}} \tag{7}$$

In the formula, E_{year} is the total power consumption of loads in the distribution network in 1 year.

The safe and efficient consumption of RES after DC transformation of the distribution network can effectively reduce the emissions of SO_2 and NO_x and dust from coal-fired power plants (SO_2, NO_x and dust are the main causes of acid rain and PM2.5 in urban areas). According to the main composition of primary energy in the region, where the distribution network is located, and the degree of regional requirements for ecological environment protection and governance, the ecological environment benefit demand for DC transformation is determined. The ecological environment benefit demand (index I_{10}) in this study is defined as a qualitative index obtained by the Delphi-gold segmentation cloud generation method. The specific calculation is shown in **Supplementary Table SA3**.

The DC transformation of the distribution network can directly or indirectly promote the development of related industries to promote social employment (State Grid Corporation of China estimates that every 100 million RMB investment will increase 700 people's employment) and play the employment benefits (Liu et al., 2019). In addition, the large-scale consumption of RES after DC transformation can alleviate the transportation and scheduling problem of primary energy to a certain extent and alleviate the pressure of land and water transportation (State Grid Corporation of China, 2017). In addition, the DC transformation also plays a positive role in promoting technological upgrading and innovation, ensuring the power market. According to the local labor, traffic, and other conditions, optimizing the allocation of social resources demand is determined. Like the ecological environment benefit demand, optimizing the allocation of social resources demand (index I_{11}) is also a qualitative index. Its specific calculation is shown in **Supplementary Table SA4**.

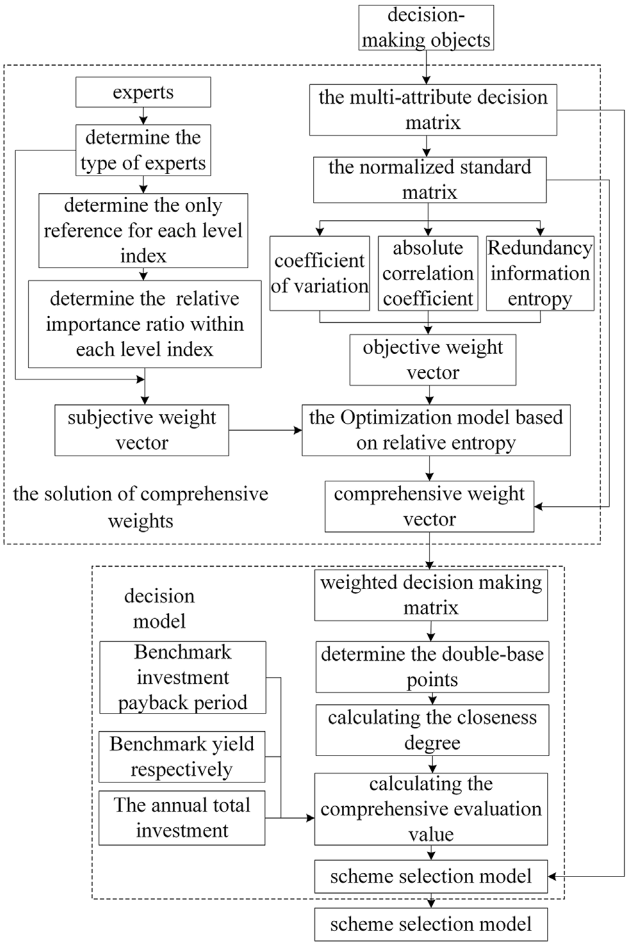

FIGURE 2 | Comprehensive decision process.

2.4 Transformation Economical Efficiency Demand

The transformation economical efficiency demand of the urban distribution network is the effective control of the cost of transformation investment, financial anti-risk ability, and capital efficiency under the premise of reaching the target level of power supply quality, power supply capacity, and RES access capacity, which means meeting the established transformation goal. In this study, the economic indicators of the DC transformation include investment costs, the payback period, and the internal rate of return (Ministry of Construction of the People's Republic of China, 2007). Among them, the investment cost is defined as

$$I_{12} = G_1 + G_2 \tag{8}$$

In the formula, G_1 is the cost of equipment purchase, installation, and debugging fees and G_2 is the fees for the research and design of new projects and the land renovation and construction.

3 THE COMPREHENSIVE DECISION-MAKING MODEL

In this study, a comprehensive decision-making model is designed to optimize the DC transformation objects of the urban distribution network. The steps are as follows: 1) compute the comprehensive weight based on the subjective and objective weight model; 2) solve the comprehensive value of the evaluation objects based on the double-base point method; and 3) constrained by the industry benchmark of total annual investment and financial-economic indicators, the final scheme is determined with the maximum total evaluation value of the scheme as the optimization objective. The process of comprehensive decision-making is shown in **Figure 2**.

3.1 The Solution of Comprehensive Weights

The comprehensive decision-making of DC transformation objects in the urban distribution network is a complex multi-index evaluation and optimization problem (Shen et al., 2019). The rationality of index weight is crucial to the evaluation results. A simple subjective or objective weight model has one-sidedness and little credibility (Wang et al., 2021). Therefore, this study combines the subjectivity and objectivity of the improved G2 method and the improved CRITIC method to optimize the combination weighting through the relative-entropy model.

3.1.1 Preprocessing the Indicators

Assuming that p evaluation objects have common q evaluation indexes $\boldsymbol{I} = \{\mathrm{I}_1, \mathrm{I}_2, \cdots, \mathrm{I}_q\}$ and the corresponding index value of the object S_i is x_{ij} ($i = 1, 2, \cdots, p$, $j = 1, 2, \cdots, q$), the multi-attribute decision matrix $\boldsymbol{X} = [x_{ij}]_{p\times q}$ composed of q indexes of p objects is preprocessed to obtain the normalized standard matrix $\boldsymbol{C} = [c_{ij}]_{p\times q}$, and there is

$$c_{ij} = \begin{cases} \dfrac{x_{ij} - \min\limits_{j} \boldsymbol{X}}{\max\limits_{j} \boldsymbol{X} - \min\limits_{j} \boldsymbol{X}}, I_j \in \boldsymbol{I}_{\text{benefit}} \\ \dfrac{\max\limits_{j} \boldsymbol{X} - x_{ij}}{\max\limits_{j} \boldsymbol{X} - \min\limits_{j} \boldsymbol{X}}, I_j \in \boldsymbol{I}_{\text{cost}} \end{cases} \tag{9}$$

In this formula, $\boldsymbol{I}_{\text{benefit}}$ and $\boldsymbol{I}_{\text{cost}}$ are the indicator set of efficiency and cost, respectively.

3.1.2 Improved G2 Method

The G2 method is a function-driven subjective weighting method. This method judges the importance of indicators according to expert experience, which can effectively consider the fuzziness of expert experience and the risk state of expert individuals. It is particularly practical in dealing with uncertain decision-making problems (Xie et al., 2010).

In this study, the improved G2 method is introduced on the basis of the original G2 method. The comprehensive decision-making index system is divided into the target layer, criterion layer, and index layer, and the hierarchical structure is shown in **Figure 1**. Let an upper index be described by the corresponding lower index set $\{I'_1, I'_2, \cdots, I'_o\}$, and the steps of the improved G2 method are as follows:

(1) First, determine the least important indicators in the index set, denoted as I'_{ho} $(h = 1, 2, \cdots, o)$, and reorder the index set as $\{I'_{h1}, I'_{h2}, \cdots, I'_{ho}\}$ according to the order relation method.
(2) Then, $D_{h'}$, as the ratio of the importance of the indicator $I'_{hh'}$ $(h' = 1, 2, \cdots, o-1)$ to the sole reference I'_{ho}, is determined:

$$\frac{I'_{hh'}}{I'_{ho}} \Leftrightarrow \begin{cases} D_{h'} = a_{h'}\,,\ d_{1h'} = d_{2h'} \\ D_{h'} = \left[d_{1h'}, d_{2h'}\right]\,,\ d_{1h'} < d_{2h'} \end{cases} \tag{10}$$

If $d_{1h'} = d_{2h'}$, the value of $D_{h'}$ is $a_{h'}$; if $d_{1h'} < d_{2h'}$, the value of $D_{h'}$ is within the interval $[d_{1h'}, d_{2h'}]$; and $\forall h'$ always satisfies the $1 \le d_{1h'} \le d_{2h'}$.

(3) After that, the index weight $u_{h'}$ is calculated according to the ratio of importance:

$$u_{h'} = R_{h'} \Big/ \sum_{h'=1}^{o} R_{h'}, R_{h'} = \begin{cases} a_{h'}\,, d_{1h'} = d_{2h'} \\ \delta^{\varepsilon}_{(D_{h'})}\,,\ d_{1h'} < d_{2h'} \end{cases} \tag{11}$$

In this formula, $\delta^{\varepsilon}_{(D_{h'})} = m(D_{h'}) + \varepsilon l(D_{h'})$ is the interval mapping function with the risk attitude of experts. In the mapping, $m(D_{h'}) = (d_{2h'} + d_{1h'})/2$, $l(D_{h'}) = d_{2h'} - d_{1h'}$ are the width and median of the interval $D_{h'}$, respectively; as for the risk state factor ε, conservative experts take $-0.5 \le \delta \le 0$; neutral experts take $\varepsilon = 0$; risk experts take $0 \le \varepsilon \le 0.5$; and $h' = 1, 2, \cdots, o-1, o$. If $h' = o$, then $R_{h'} = a_{h'} = 1$.

(4) Finally, the weight obtained is multiplied layer by layer to get the subjective weight vector $\boldsymbol{U} = [u_j]_{1\times q}$ of the final improved G2 method.

3.1.3 Improved CRITIC Method

The CRITIC method (Lin et al., 2018) is a new weighting method for solving weights based on objective data. This method can consider both the comparative strength between transformation objects and the degree of conflict between evaluation indexes so that the weight is objective and accurate. Among them, the contrast intensity reflects the difference of different objects in the same index, which is quantified by standard deviation. The degree of conflict reflects the correlation between different indicators and is quantified by the correlation coefficient.

In this study, the original CRITIC method is improved as follows: 1) the contrast strength between indicators is reflected by the coefficient of variation, and the defects that standard deviation is susceptible to dimension and the mean value are corrected. 2) The absolute value of the correlation coefficient reflects the degree of conflict between indicators and corrects the defect that the original correlation coefficient cannot reflect the same correlation when the positive and negative correlations have the same absolute values; 3) redundancy information entropy (Iuculano et al., 2007) is introduced to reflect the dispersion of indicators so that the empowerment process integrates contrasting strength, conflict degree, and dispersion. The model of the improved CRITIC method based on the objective weighting calculation is

$$\begin{cases} s_j = \dfrac{1}{\bar{c}_j}\sqrt{\dfrac{1}{p}\displaystyle\sum_{i=1}^{p}\left(c_{ij} - \bar{c}_j\right)^2} \\ r_{jj'} = \dfrac{\dfrac{1}{\bar{c}_j\bar{c}_{j'}}\displaystyle\sum_{i=1}^{p}\left(c_{ij} - \bar{c}_j\right)\left(c_{ij'} - \bar{c}_{j'}\right)}{s_j s_{j'}} \\ \rho_j = 1 + \dfrac{1}{\ln p}\displaystyle\sum_{i=1}^{p}\left(z_{ij}\ln z_{ij}\right), z_{ij} = c_{ij}\Big/\sum_{i=1}^{p} c_{ij} \\ M_j = \left(s_j + \rho_j\right)\displaystyle\sum_{j'=1}^{q}\left(1 - \left|r_{jj'}\right|\right) \\ v_j = M_j\Big/\displaystyle\sum_{j=1}^{q} M_j \\ j, j' = 1, 2, \cdots, q;\ j \ne j' \end{cases} \tag{12}$$

In this formula, s_j and $s_{j'}$ are the variation coefficients of indexes I_j and $I_{j'}$, respectively; $\bar{c}_j$ and $\bar{c}_{j'}$ are the mean values of normalized index value; $r_{jj'}$ is the correlation coefficient of indexes j and j'; $c_{ij'}$ is the normalized index value of index $I_{j'}$ of object S_i; ρ_j is the redundant information entropy of index I_j; z_{ij} is the proportion of normalized index value; M_j is the information contained in index I_j (the larger M_j, the greater the amount of information contained in index I_j and the more important I_j); and v_j is the weights for index I_j by the improved CRITIC method. According to the improved CRITIC method, the final objective weight vector $\boldsymbol{V} = [v_j]_{1\times q}$ can be obtained.

3.1.4 Comprehensive Weight

According to the principle of Kullback relative entropy derived from probability measures and considering the consistency requirement of information contained in the subjective weight vector acquired from the G2 method, the objective weight vector obtained by the improved CRITIC method, and the real weight vector, this study establishes a comprehensive weight optimization model based on relative entropy and solves the comprehensive weight w_j which has the best consistency with subjective and objective weight. The optimization model is

$$\begin{cases} \min E(\lambda) = \displaystyle\sum_{\eta=u,v}\sum_{j=1}^{q} w_j \ln\left(\frac{w_j}{\eta_j}\right) \\ \text{s.t.} \displaystyle\sum_{\eta=u,v}\lambda_\eta = 1, w_j = \sum_{\eta=u,v}\lambda_\eta \eta_j \end{cases} \tag{13}$$

In the formula, the decision variable is $\lambda = (\lambda_u, \lambda_v)$, by minimizing the relative entropy, obtain the optimal solution λ^*, and then the comprehensive weight vector $\boldsymbol{W} = [w_j]_{1\times q}$ can be solved.

3.2 Decision Model

3.2.1 Double-Base Point Method

According to the obtained comprehensive weight vector and the standardized attribute decision-making matrix, the weighted decision-making matrix $\boldsymbol{Y} = [y_{ij}]_{p\times q}$ is calculated, where

$$y_{ij} = w_j c_{ij} \tag{14}$$

By taking the optimal value and the worst value of each evaluation index as the double-base points, the optimal and the worst base point vectors are introduced. The optimal base point vector of the weighted decision-making matrix is $\boldsymbol{Y}^+ = [y_j^+]_{1\times q}$, and the worst base point vector is $\boldsymbol{Y}^- = [y_j^-]_{1\times q}$. Among them, $y_j^+ = \max\{y_{ij}\}$ and $y_j^- = \min\{y_{ij}\}$.

The optimal and the worst base point vectors are used as the reference standards of the optimal and the worst transformation objects, respectively. The closeness degree between the selected object and the optimal reference standard is calculated by the double-base point method. The smaller the closeness degree is, the closer the evaluation object is to the optimal transformation object. The closeness degree is

$$\varphi_i = \frac{(Y^+ - Y_i)(Y^+ - Y^-)^{\mathrm{T}}}{\|Y^+ - Y^-\|^2}, i = 1, 2, \cdots, p \tag{15}$$

The comprehensive evaluation value of the DC transformation object is

$$f_i = (1 - \varphi_i) \times 100\%, i = 1, 2, \cdots, p \tag{16}$$

The larger the comprehensive evaluation value is, the higher the planning investment benefit of the DC transformation of the evaluated object is. When formulating the planning scheme, the investment objects of the DC transformation should be selected according to the evaluation value from high to low.

3.2.2 Scheme Selection Model

By taking the maximum overall evaluation value of the scheme as the goal and the total annual investment and industry benchmark of economic indexes as the constraint, the final scheme is determined, namely,

$$F = \max\left\{\sum_{k=1}^{K} f_k \middle| K = 1, 2, \cdots, p\right\} \tag{17}$$

In the formula, F is the objective function of the scheme selection model; K is the number of distribution networks selected for the DC transformation in turn; and f_k is the comprehensive evaluation value of the evaluation object at the k of investment priority:

$$\begin{cases} \text{s.t. } I_{14}^{\mathrm{B}} \geq \min\{I_{14k} | k = 1, 2, \cdots, K\} \\ I_{13}^{\mathrm{B}} \leq \min\{I_{13k} | k = 1, 2, \cdots, K\} \\ G \geq \sum_{k=1}^{K} I_{12k} \end{cases} \tag{18}$$

In this formula, I_{12k}, I_{13k}, and I_{14k} are the investment cost, investment payback period, and internal rate of return of the DC transformation object k of the priority level, respectively. G is the total annual investment. I_{13}^B and I_{14}^B are the industry benchmark investment payback period and benchmark yield, respectively.

4 EXAMPLE ANALYSIS

Based on the above comprehensive decision-making method for the DC transformation of urban distribution network, seven 10 kV urban distribution networks in a southern province of China are selected and recorded as S_1~S_7, respectively, to verify the feasibility of the proposed method.

The indexes of seven distribution networks are shown in **Table 1**. Due to the lack of data, indexes I_8, I_{10}, and I_{11} (bold type) in **Table 1** are transformed from qualitative value information to quantitative score by the Delphi-gold segmentation cloud generation method (Zhu et al., 2020; Han et al., 2020).

4.1 Analysis of Evaluation Results

The comprehensive evaluation values of seven distribution networks are shown in **Table 2**. It can be seen that the comprehensive evaluation value of S_3 is the highest among the seven urban distribution networks (S_1~S_7) to be DC retrofitted, which means the comprehensive benefit of S_3's DC transformation is the best. When upgrading the urban distribution network, S_3 should be the preferred DC transformation object.

In order to analyze the transformation demand and transformation economy of urban distribution network S_1~S_7 in more detail, the radar chart for index evaluation of criteria level is analyzed by evaluating the indexes in the criterion layer, and the radar chart for index evaluation of criteria level is shown in **Figure 3**.

Further, as shown in **Figure 3**, the demands for the upgrade and transformation of S_1 in all the aspects are large and the transformation economical efficiency is also good. **Table 2** shows that the comprehensive evaluation value is second only to S_3. Therefore, the DC transformation of S_1 is further carried out when the investment after S_3 is still sufficient.

Overall, considering the investment cost constraints, the project should prioritize the DC transformation of the distribution network with a larger comprehensive evaluation value.

4.2 Comparative Analysis of Evaluation Methods

In order to further illustrate the rationality of the comprehensive weight proposed by this study, the improved G2 method, the improved CRITIC method, the method proposed by Xie et al. (2010) (G2—entropy weight method), and the comprehensive

TABLE 1 | Index data of each distribution network.

Objects	R_{ASAI-1}/%	R_{ASAI-T}/%	I_1/%	$R_{SAIFI-1}$/(times/a)	$R_{SAIFI-T}$/(times/a)	I_2/%	R_{VQR-1}/%	R_{VQR-T}/%	I_3/%	I_4/%
S_1	99.9932	99.9990	99.9942	0.3682	0.1000	27.1592	99.87	99.99	99.88	16.90
S_2	99.9927	99.9990	99.9937	0.3728	0.1000	26.8240	99.89	99.99	99.90	12.20
S_3	99.9801	99.9901	99.9900	0.3998	0.2000	50.0250	99.82	99.97	99.85	18.40
S_4	99.9789	99.9901	99.9888	0.4092	0.2000	48.8759	99.88	99.97	99.91	10.93
S_5	99.9645	99.9658	99.9987	0.4669	0.3000	64.2536	99.82	99.95	99.87	11.18
S_6	99.9556	99.9658	99.9898	0.4275	0.3000	70.1754	99.79	99.95	99.84	16.92
S_7	99.8512	99.8630	99.9882	0.4012	0.5000	124.6261	98.80	98.79	100.01	14.92

Objects	I_5/%	I_6/%	I_7	I_8	I_9/(RMB/kWh)	I_{10}	I_{11}	I_{12}/ten thousand yuan	I_{13}/a	I_{14}/%
S_1	8.36	5.60	0.0321	0.848	26.3	0.8501	0.7526	6,550	9.62	12.56
S_2	5.79	5.40	0.0075	0.810	24.7	0.6278	0.7705	7,010	9.75	12.33
S_3	9.98	4.50	0.0559	0.790	20.8	0.8091	0.8171	6,420	9.65	12.08
S_4	8.71	9.35	0.0103	0.642	17.3	0.5963	0.5481	6,530	11.37	10.67
S_5	10.93	17.90	0.0641	0.463	14.4	0.4743	0.7152	6,910	11.22	10.82
S_6	6.47	5.35	0.0185	0.333	13.9	0.6582	0.6953	6,380	12.58	10.41
S_7	2.13	18.95	0.0469	0.134	8.3	0.5897	0.4743	6,540	14.62	9.01

TABLE 2 | Comprehensive evaluation value of different objects.

Objects	Comprehensive evaluation value
S_1	75.11
S_2	49.83
S_3	89.05
S_4	51.00
S_5	42.98
S_6	63.76
S_7	35.30

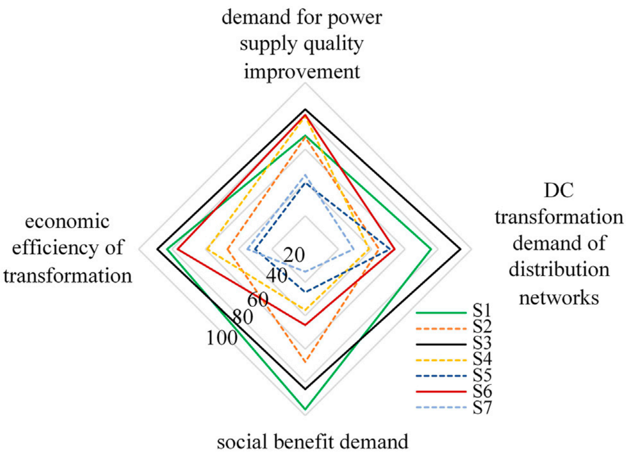

FIGURE 3 | Radar chart for index evaluation of criteria level.

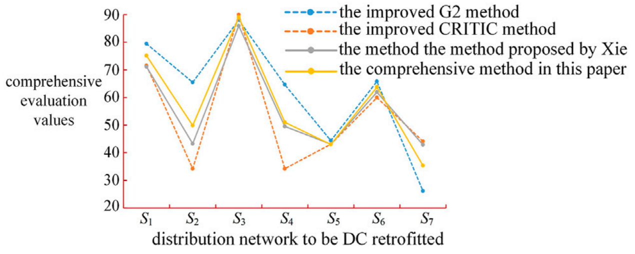

FIGURE 4 | Comparison of comprehensive evaluation results.

TABLE 3 | Evaluation results under five principles.

Principles	S_1	S_2	S_3	S_4	S_5	S_6	S_7
A	0.00	0.35	9.23	10.07	20.21	26.48	100.00
B	0.00	1.81	16.94	20.72	47.21	37.85	77.47
C	68.05	67.07	83.99	79.83	39.86	80.61	44.51
D	75.55	44.40	93.30	38.32	50.98	53.77	29.10
E	75.11	49.83	89.05	51.00	42.98	63.76	35.30

method in this study are used to evaluate seven distribution networks comprehensively. The evaluation results are shown in **Figure 4**.

Through the intuitive comparison in **Figure 4**, it can be seen that the differences in the evaluation results are mainly reflected in the distribution network S_2, S_4, S_5, and S_7. The evaluation results of the improved G2 method and improved CRITIC method are S_2>S_4>S_5>S_7 and S_7>S_5>S_2>S_4, respectively. This is mainly because the index weight of the improved G2 method is only determined subjectively by decision-makers, ignoring the objective information of the index. Similarly, the improved CRITIC method focuses on objective information and ignores the importance of expert opinions in decision-making, which will also lead to deviation in evaluation results. Although the evaluation results obtained by the method proposed by Xie et al. (2010) are consistent with those in this study, compared with Xie et al. (2010), the comprehensive method in this study introduces the analytical theory in the process of expert decision-making. In the process of handling objective information, the comparative strength, conflict degree, and discreteness of the index data are comprehensively considered. In summary, the evaluation results in this study will be more reasonable and

TABLE 4 | Optimization results under five principles.

Principles	The investment priority	Preferred objects	Investment cost
A	$S_7 > S_6 > S_5 > S_4 > S_3 > S_2 > S_1$	X_7, X_6, X_5	19,770
B	$S_7 > S_5 > S_6 > S_4 > S_3 > S_2 > S_1$	X_7, X_5, X_6	19,770
C	$S_3 > S_6 > S_4 > S_1 > S_2 > S_7 > S_5$	X_3, X_6, X_4	19,420
D	$S_3 > S_1 > S_6 > S_5 > S_2 > S_4 > S_7$	X_3, X_1, X_6	19,290
E	$S_3 > S_1 > S_6 > S_4 > S_2 > S_5 > S_7$	X_3, X_1, X_6	19,290

accurate. In addition, the sensitivity of the evaluation results obtained by this method is 152.24%, which is also significantly better than 100.59% of the method proposed by Xie et al. (2010).

In summary, the evaluation results obtained by the method in this study are more reasonable, accurate, and with greater identification, which can be well applied to the optimization of DC transformation objects of urban distribution networks in this study.

4.3 Analysis of Decision Results

In order to illustrate the correctness of the comprehensive decision-making results in this study, the decision-making results under five selection principles are compared and analyzed. Principle A is the low average reliability of power supply; principle B is the low reliability of traditional power supply; principle C is the high demand for power supply quality improvement; principle D is the high demand for DC distribution network; and principle E is the comprehensive evaluation value of this study that is high. The comprehensive evaluation results under the five principles are shown in **Table 3**.

Assume that the total annual investment is 20 million yuan, the industry benchmark investment payback period is 16 years, and the benchmark yield is 8%. The investment priorities, selected distribution network, and total investment costs of the five principles are shown in **Table 4**. Because the investment payback period and internal rate of return of the seven distribution networks meet the financial and economic constraints, **Table 4** only shows the total investment cost of the preferred object under investment cost constraints.

(1) Principle A takes the low average power supply reliability as the basis for the optimization of the transformation objects. As shown in **Tables 3**, **4**, the preferred objects are S_7, S_6, and S_5. However, with the continuous improvement of users' demand for uninterrupted power supply, the interruption frequency will become the main factor affecting users' electricity experience at a high level of power supply reliability. Therefore, in principle B, the traditional power supply reliability is comprehensively reflected by two indicators: power supply reliability rate and system average interruption frequency. Although the optimization objects are still S_7, S_5, and S_6, the order of optimization has changed. This is mainly because the average interruption frequency of S_5 is 0.4669, which is significantly higher than the 0.4275 of S_6. The optimization of the transformation objects through method B has the significance of improving power supply reliability but does not consider the differentiated demand of distribution networks.

(2) Principle C is based on the improvement of power supply quality. According to **Tables 3**, **4**, the selected objects are S_3, S_6, and S_4, which are different from principle B. This is mainly because principle C considers the different requirements of distribution networks for power supply quality. **Table 1** shows that compared with S_7 and S_6, although S_3 and S_4 have higher power supply reliability, their gap with the target level is larger than that of S_7 and S_6. In addition, principle C also reflects the demand for the improvement of power availability of distribution networks through the voltage qualification rate. In general, the optimization of the transformation objects through principle C has the significance of improving the differentiated power supply quality level. However, the direct and indirect demand for the DC transformation of urban distribution networks is not considered.

(3) Although the principle D effectively considers the DC transformation demand of distribution networks, it abandons the demand for the improvement of power supply quality without considering the social benefit and the economical efficiency, which is not comprehensive enough. However, principle E considers the differentiated demand of distribution networks and fully considers the direct and indirect demand of DC transformation, which can effectively bring into play the comprehensive benefits of DC transformation. As shown in **Tables 3**, **4**, the optimization objects and method D are the same as S_3, S_1, and S_6. This is because of the highest importance of the DC transformation demand of distribution networks under the indexes in the four-criterion layer, the large demand for upgrading and transformation in all aspects of S_3, S_1, and S_6, and the good economic efficiency of transformation. It can be analyzed in detail through the radar diagram in **Figure 2**, which is not repeated here.

It can be seen that the comprehensive decision results in this study can effectively reflect the comprehensive benefits of DC transformation of urban distribution networks, which can guide the distribution network planning department to arrange the priority scheme of DC transformation objects reasonably.

5 CONCLUSION

Aiming at the problem that there is no quantitative decision-making method for DC transformation priority of multiple distribution networks in urban distribution network upgrading, this study carried out the following work:

(1) Starting from the demand and economy of urban distribution network upgrading and transformation, considering the differentiated demand for power supply quality of distribution network transformation, and taking the direct demand of DC transformation driven by the restrictive DC transformation of AC transformation and the indirect demand of DC transformation driven by social development as the starting point, a comprehensive evaluation index system for DC transformation objects is designed, which comprehensively considers the demand for power supply quality improvement, DC transformation demand of distribution networks, social benefit demand, and transformation economical efficiency.

(2) The G2 method is improved by introducing the principle of the analytic hierarchy process to determine the subjective weight of the index, which can comprehensively consider the fuzziness of expert experience and the risk state of expert individuals. At the same time, the improved CRITIC method is used to determine the objective weight, which can comprehensively consider the contrast strength, conflict degree, and discreteness between indicators so that the weight is objective and accurate. The comprehensive weight optimization model based on relative entropy is established to make the evaluation results more reasonable, accurate, and identifiable. The example shows that the sensitivity of evaluation results is increased by about 50%.

(3) Based on the double-base point method and scheme selection model, a comprehensive decision model for the DC transformation of the urban distribution network is established. The example shows that the model can comprehensively consider the power supply quality improvement demand, DC transformation demand, social benefit demand, and transformation economical efficiency demand; maximize the comprehensive benefits in many aspects; arrange investment priorities to form transformation schemes; and prioritize the transformation of urban distribution network with the optimal comprehensive benefits.

China is vigorously promoting distributed renewable energy, electric vehicles, and energy storage, including distributed the photovoltaic, distributed energy storage system, microgrid, and electric vehicle cluster. Among them, there are many demands for DC transformation of the existing AC distribution network and for fine planning considering electric vehicles, renewable energy, and energy storage on the basis of DC transformation.

In this paper, the comprehensive decision of the DC transformation object is preliminarily made. However, the concrete DC transformation scheme has not been discussed. Therefore, after selecting the DC transformation object, designing the refined DC transformation scheme, which needs to consider the global optimization/sub-optimization that meets the multi-objectives of reliability, economy, power quality, safety, and flexibility of the transformation distribution network, and considering the optimal allocation of distributed renewable energy in time and space, such electric vehicles and energy storage, is the next need for further research.

DATA AVAILABILITY STATEMENT

The raw data supporting the conclusion of this article will be made available by the authors without undue reservation.

AUTHOR CONTRIBUTIONS

YO proposed the technical ideas and key formula derivation of the full text and presided over the content of the example design. XX mainly provided great support for simulation calculation and verification of results. MY put forward many positive suggestions on the technical content of the manuscript. FW was responsible for writing this manuscript.

FUNDING

This study received funding from the science and technology project of China Southern Power Grid, project number GDKJXM20173253. The funder was not involved in the study design, collection, analysis, interpretation of data, the writing of this article, or the decision to submit it for publication.

ACKNOWLEDGMENTS

The authors thank the planning center of Guangdong Power Grid Co., Ltd. for its financial and technical support. The discussion with the personnel of the organization enables the authors to understand the application demand and development trend of the distribution network in China.

SUPPLEMENTARY MATERIAL

The Supplementary Material for this article can be found online at: https://www.frontiersin.org/articles/10.3389/fenrg.2022.906047/full#supplementary-material

REFERENCES

Chen, X., Han, J., Zhang, Q., and Wang, Q. (2019). "Economic Comparison of AC and DC Distribution System," in IEEE 8th International Conference on Advanced Power System Automation and Protection (APAP), Xi'an, China, 21-24 Oct. 2019 (IEEE), 769–774. doi:10.1109/APAP47170.2019.9225098

Chen, Y., Li, J., Sheng, K., Yang, T., Xu, X., Han, Z., et al. (2020). Many-criteria Evaluation of Infrastructure Investment Priorities for Distribution Network Planning. *IEEE Access* 8, 221111–221118. doi:10.1109/ACCESS.2020.3043248

Cui, S., Lee, J.-H., Hu, J., De Doncker, R. W., and Sul, S.-K. (2019). A Modular Multilevel Converter with a Zigzag Transformer for Bipolar MVDC Distribution Systems. *IEEE Trans. Power Electron.* 34 (2), 1038–1043. doi:10.1109/TPEL.2018.2855082

De Miguel, L., Bustince, H., Pekala, B., Bentkowska, U., Da Silva, I., Bedregal, B., et al. (2016). Interval-Valued Atanassov Intuitionistic OWA Aggregations Using Admissible Linear Orders and Their Application to Decision Making. *IEEE Trans. Fuzzy Syst.* 24 (6), 1586–1597. doi:10.1109/TFUZZ.2016.2543744

Han, W., Lu, X. S., Zhou, M., Shen, X., Wang, J., and Xu, J. (2020). An Evaluation and Optimization Methodology for Efficient Power Plant Programs. *IEEE Trans. Syst. Man. Cybern. Syst.* 50 (2), 707–716. doi:10.1109/TSMC.2017.2714198

Hu, W., Guo, Q., Zhou, Y., Kang, Y., Bing, H., and Bao, D. (2019). Dynamic Comprehensive Methodology for Assessing Power Development Level Based on Provincial Data. *Csee Jpes* 6 (3), 672. doi:10.17775/CSEEJPES.2018.00910

Huang, C., Zhu, Z., Cao, Y., Liu, Z., and Shi, J. (2021). "Comprehensive Evaluation of Wiring Mode of Distribution Network in Large Overseas Cities," in The 16th IET International Conference on AC and DC Power Transmission (ACDC 2020) (IEEE), 1024. doi:10.1049/icp.2020.0276

Iuculano, G., Nielsen, L., Zanobini, A., and Pellegrini, G. (2007). The Principle of Maximum Entropy Applied in the Evaluation of the Measurement Uncertainty. *IEEE Trans. Instrum. Meas.* 56 (3), 717–722. doi:10.1109/TIM.2007.894915

Li, H., Yi, B., Li, Q., Ming, J., and Zhao, Z. (2020). Evaluation of DC Power Quality Based on Empirical Mode Decomposition and One-Dimensional Convolutional Neural Network. *IEEE Access* 8, 34339–34349. doi:10.1109/ACCESS.2020.2974571

Liao, S., Xu, J., Sun, Y., Gao, W., Ma, X.-Y., Zhou, M., et al. (2016). Load-Damping Characteristic Control Method in an Isolated Power System with Industrial Voltage-Sensitive Load. *IEEE Trans. Power Syst.* 31 (2), 1118–1128. doi:10.1109/TPWRS.2015.2424240

Lin, Z., Wen, F., Wang, H., Lin, G., Mo, T., and Ye, X. (2018). CRITIC-based Node Importance Evaluation in Skeleton-Network Reconfiguration of Power Grids. *IEEE Trans. Circuits Syst. II* 65 (2), 206–210. doi:10.1109/TCSII.2017.2703989

Liu, X., Liu, Y., Liu, Y., Xiang, Y., and Yuan, X. (2019). Optimal Planning of AC-DC Hybrid Transmission and Distributed Energy Resource System: Review and Prospects. *Csee Jpes* 5 (3), 409. doi:10.17775/CSEEJPES.2019.00540

Ma, L., and Zhang, X. (20202020). Economic Operation Evaluation of Active Distribution Network Based on Fuzzy Borda Method. *IEEE Access* 8, 29508–29517. doi:10.1109/ACCESS.2020.2972015

Ministry of Construction of the People's Republic of China (2007). *General Administration of Quality Supervision, Inspection and Quarantine of the People's Republic of China. GB 50217-2007 Code for Design of Cables of Electric Engineering*. Beijing: China Electric Power Press.

Okoli, C., and Pawlowski, S. D. (2004). The Delphi Method as a Research Tool: An Example, Design Considerations and Applications. *Inf. Manag.* 42 (1), 15–29. doi:10.1016/j.im.2003.11.002

Rentschler, A., Kuhn, G., Delzenne, M., and Kuhn, O. (2018). "Medium Voltage DC, Challenges Related to the Building of Long Overhead Lines," in IEEE/PES Transmission and Distribution Conference and Exposition (T&D), Denver, CO, USA, 16-19 April 2018 (IEEE), 1–5. doi:10.1109/TDC.2018.8440219

Shen, Y., Chen, Y., Zhang, J., Sang, Z., and Zhou, Q. (2019). Self-Healing Evaluation of Smart Distribution Network Based on Uncertainty Theory. *IEEE Access* 7, 140022–140029. doi:10.1109/ACCESS.2019.2939537

State Grid Corporation of China (2017). *Q/GDW 11723-2017 the Guidelines of Comprehensive Evaluation on AC/DC Hybrid Power Distribution Network*. Beijing: China Electric Power Press.

Wang, J., Liu, S., Wang, S., Liu, Q., Liu, H., Zhou, H., et al. (2021). Multiple Indicators-Based Health Diagnostics and Prognostics for Energy Storage Technologies Using Fuzzy Comprehensive Evaluation and Improved Multivariate Grey Model. *IEEE Trans. Power Electron.* 36 (11), 12309–12320. doi:10.1109/TPEL.2021.3075517

Wang, J., Pang, W., Pang, W., Wang, L., Pang, X., and Yokoyama, R. (2017). Synthetic Evaluation of Steady-State Power Quality Based on Combination Weighting and Principal Component Projection Method. *Csee Jpes* 3 (2), 160–166. doi:10.17775/CSEEJPES.2017.0020

Wang, Y., Chen, S.-Z., Wang, Y., Zhu, L., Guan, Y., Zhang, G., et al. (2020). A Multiple Modular Isolated DC/DC Converter with Bidirectional Fault Handling and Efficient Energy Conversion for DC Distribution Network. *IEEE Trans. Power Electron.* 35 (11), 11502–11517. doi:10.1109/TPEL.2020.2985232

Xie, J., Qin, Y., Xu, J., Wang, L., and Meng, X. (2010). "Study on the Fuzzy Comprehensive Evaluation of the Railway Emergency Plan Based on G2 Method," in 5th International Conference on Computer Science & Education, 1254–1257. doi:10.1109/ICCSE.2010.5593722

Zhao, H., and Li, J. (2021). Energy Efficiency Evaluation and Optimization of Industrial Park Customers Based on PSR Model and Improved Grey-TOPSIS Method. *IEEE Access* 9, 76423–76432. doi:10.1109/ACCESS.2021.3081142

Zhu, S., Ma, Y., Li, X., Yang, J., Lin, J., and Jing, J. (2020). On the Analysis and Improvement of Min-Entropy Estimation on Time-Varying Data. *IEEE Trans.Inform.Forensic Secur.* 15, 1696–1708. doi:10.1109/TIFS.2019.2947871

Conflict of Interest: The authors declare that the research was conducted in the absence of any commercial or financial relationships that could be construed as a potential conflict of interest.

frontiers | Frontiers in Energy Research

METHODS
published: 31 May 2022
doi: 10.3389/fenrg.2022.919842

A Method of Power Flow Database Generation Base on Weighted Sample Elimination Algorithm

*Xianbo Meng**[1], *Yalou Li*[1], *Dongyu Shi*[1], *Shanhua Hu*[1] *and Fei Zhao*[1]

[1]*China Electric Power Research Institute, Beijing, China*

With the rapid development of urban power grids, distributed renewable energy sources and adjustable loads have increased significantly, resulting in more complex operation conditions, increasing the difficulty of power flow calculations. The usage of artificial intelligence technology to assist in calculating power flows for large-scale urban grids has a wide range of application prospects. It is currently difficult to generate enough grid operation database with controlled distribution for artificial intelligence (AI) method research. Data is one of the important factors affecting the performance of deep learning algorithms, and the lack of research on data distribution characteristics also hinders the performance of deep learning algorithms. The distributional characteristics of data sets in high-dimensional feature spaces are difficult to represent and measure, and the algorithm design process is prone to encounter curse of dimensionality. This paper proposed a novel method for generating databases to improve the solving efficiency of data-driven power flow calculation problems. The proposed method removes samples based on the characteristics of data distribution. It constructs two databases, namely the blue noise distribution database and the variable density boundary enhanced distribution database. Compared with the classical stochastic sampling database, the proposed boundary-enhanced variable density (BEVD) database has significantly improved the judgment accuracy of power flow convergence. Finally, the China Electric Power Research Institute-36 (CEPRI-36) bus system is used to verify the effectiveness of the proposed method. The judgment accuracy was improved by 2.91%–9.5%.

Keywords: High-dimensional space, blue noise distribution, boundaryenhanced variable density (BEVD) distribution, Power flow calculation, Database construction

Edited by:
Shutang You,
The University of Tennessee,
Knoxville, United States

Reviewed by:
Lipeng Zhu,
Hunan University, China
Jingbo Wang,
Kunming University of Science and
Technology, China

Correspondence:
Xianbo Meng
mengxianyang1990@163.com

Specialty section:
This article was submitted to
Smart Grids,
a section of the journal
Frontiers in Energy Research

Received: *14 April 2022*
Accepted: *09 May 2022*
Published: *31 May 2022*

Citation:
Meng X, Li Y, Shi D, Hu S and Zhao F
(2022) A Method of Power Flow
Database Generation Base on
Weighted Sample
Elimination Algorithm.
Front. Energy Res. 10:919842.
doi: 10.3389/fenrg.2022.919842

1 INTRODUCTION

As the complexity of power grid operation increases, new power systems' safe and stable operation is facing severe challenges. Traditional state sensing and operation control technologies are challenging. Artificial intelligence (AI) technology is increasingly required to participate in power grid security and stability analysis. At present, the application research of artificial intelligence technology in power system analysis has been gradually carried out (Shi et al., 2020; Wang et al., 2021), and it has become an inevitable trend to use big data and deep learning technology to assist and supplement traditional time-domain simulation methods. The training and prediction effects of deep learning are highly dependent on sufficient and reasonable datasets (Sun et al., 2017). Among them, supervised learning, as the most mature research branch, is highly dependent on large-scale labelled datasets and requires that each sample contains labelled information. In power systems, the research of database distribution and generation methods have always been a relatively weak link in related research. When migrating deep models and learning algorithms that have performed well in other fields to the power system analysis, the primary problem is the data problem (Zhang et al., 2021).

The scope of application of data problem-solving methods is affected by data acquisition, which can be divided into actual acquisition and simulation. In some tasks, acquisition can only obtain samples, and adjusted or synthesized samples are primarily meaningless. Such tasks can only maximize the sample capacity to improve the generalization ability of the depth model, but the marginal benefit of its enhancement gradually decreases (Joulin et al., 2016) and the enhancement efficiency is low, and it is prone to the class imbalance problem (Japkowicz and Stephen, 2002; He and Garcia, 2009), which also leads to the decrease of the generalization ability of the deep model. In some other tasks, samples can only be supplemented by minor adjustments of a single sample, such as in the image field. Adjustments to databases in the image domain are called data augmentation techniques (Cubuk et al., 2018), including rotation, translation, cropping, and fine-tuning of colours for a single image sample.

More general approaches include simple resampling techniques, such as undersampling and random over-sampling (ROS) (Batista et al., 2004), which do not add new samples to the database. Still, other tasks, where the simulation samples are valid in a particular area, can apply some data synthesis methods, such as the SMOTE (Synthetic Minority Oversampling Technique) (Chawla et al., 2002) algorithm, the ADASYN (Adaptive synthetic sampling) (He et al., 2008) algorithm, and the mixup algorithm (Zhang et al., 2017). Reference (Tan et al., 2019) uses the Generative Adversarial Networks (GAN) method to generate a database with a similar distribution to the original data and extract unstable samples to supplement the original sample set, which can quickly adjust the class ratio. However, the above sample supplementation methods are all based on existing samples, and the reconstructed database does not change the cover but only changes the class ratio. In the literature (Chen et al., 2019), a grid simulation sample generation method based on the LSTM (Long short-term memory) algorithm was proposed, which achieved good results in automatic sample generation and improved the efficiency of simulation sample generation but did not consider the sample distribution characteristics, which made it difficult to evaluate the generated sample set.

For power systems, data can be obtained either through measurement or simulation. The continuous power flow method (Chiang et al.) shows that samples extending continuously beyond the acquisition range are also meaningful in power grid analysis. Therefore, the collected data can be effectively supplemented with simulation-generated data for grid analysis applications. The calm conditions allow more operation space when constructing the database, and the room for improving the quality of the database is also larger. For such tasks, improving the performance of machine learning algorithms by tuning databases rather than tuning model parameters has become a new research direction known as “data-centric machine learning” (Alvarez-Melis and Fusi, 2020). Research has been carried out on the problem of solving partial differential equations satisfying the conditions for sampling methods to improve the generalization ability of the model (Tang et al., 2021). However, in power grid applications, research on high-quality database generation methods is still very rare. The research on data problems has become a critical technical problem restricting the application of deep learning methods in power grid analysis, which needs to be improved and solved urgently. Because of this, the blue noise sampling in computer graphics (Dippé and Wold, 1985; Cook, 1986; Yuksel, 2015) is borrowed in this paper to enhance the quality of the database from the perspective of its distributional characteristics, and a sample generation method that considers distributional characteristics in a high-dimensional feature space is implemented using a weighted sample elimination method. For deep learning methods, whether the database distribution characteristics are better or worse is reflected in the model’s generalization performance after training. The task selected in this paper is convergence discrimination of power flow calculation. Using deep learning to judge the convergence of power flow calculation is a classification process. The trained deep model classifies the grid operation samples as feasible or not. The model can be regarded as an implicit representation of the boundary of the feasible region of power flow (Hu et al., 2017). Fitting the boundary of the feasible region is the basis for subsequent power system analysis and planning.

In this paper, for the first time, the distribution characteristics of the database suitable for the task of convergence discrimination of grid tide calculation are analyzed, the sampling rules of high-dimensional blue noise and BEVD under the framework of the elimination method are proposed, and sampling in high-dimensional feature space considering the distribution properties is realized. Finally, the CEPRI36 node model is used to verify the effectiveness of the database generation method and the correlation between the database distribution characteristics and the generalization performance of the deep learning method. The experiments specifically verify two conclusions.

1) The distribution characteristics of the dataset do have an impact on the generalization performance of the deep learning algorithm, and that the randomly generated database with the lowest generation cost is not the optimal distribution characteristic, so it is meaningful to investigate the distribution characteristics of the database.
2) It is verified that the BEVD distribution characteristics proposed for the classification problem with attention to boundaries have a positive impact on the generalization performance of deep learning algorithms.

2 DISTRIBUTION CHARACTERISTICS OF EXISTING DATABASES AND TARGET DISTRIBUTION CHARACTERISTICS

The database required for artificial intelligence methods is composed of samples, which are a collection of features that have been quantified. These features are collected from some objects or tasks that need to be processed. The sample is usually represented as a vector $x \in \mathbb{R}^n$, where each entry x_i of the vector is another feature. For the task of power flow convergence discrimination, the samples need to contain all the information that can be used for power flow calculation. The result of the power flow calculation is the power flow operating point, which is the combination of the power and voltage of all nodes in the system.

$$\{\{\boldsymbol{P}_i, \boldsymbol{Q}_i, \boldsymbol{V}_i, \boldsymbol{\theta}_i\} | \boldsymbol{i} = \boldsymbol{0}, \boldsymbol{1}, \ldots, \boldsymbol{N}\} \tag{1}$$

where N is the number of nodes in the system. The power flow calculation process is to specify one part of the features and find another part of the features through the power flow equations. Usually, the input features are the node injection power, that is, the active power and reactive power of the PQ node, and the active power and voltage of the PV node. Therefore, the number of feature values, i.e., the dimensionality of the feature space, is two times the number of nodes. Whether the power flow calculation can converge to a feasible solution is the label of this task, and the label and feature together constitute a sample required for supervised learning. Specifically, the sample is labelled as convergent if the remaining values can be obtained by computing the power flow equations, and conversely, the sample is labelled as non-convergent if the power flow equations cannot be solved by the computational program.

From a geometric point of view, a sample can be regarded as a data point in a high-dimensional feature space, and a sample set is a point cloud in a high-dimensional feature space. The distribution characteristic of the database is the distribution characteristic of the sample point cloud. This paper's research on distributional properties aims to improve the generalization ability of deep learning methods. In the task of convergence discrimination of power flow calculation, the generalization ability is reflected in the discrimination accuracy of the model to the test set. In the following, the distribution characteristics of the existing database are analyzed from a specific task. Based on this, a potentially better distribution characteristic is proposed as the goal of the generation method in this paper.

2.1 Analysis of the Distribution Characteristics of Existing Databases

The existing power system operation data are mainly obtained based on offline simulation or online collection. The original online and offline databases cannot meet the requirements of deep learning. Specifically, the online analysis data are collected under the actual operation condition, which constitutes a large amount of sample data but is unevenly distributed, thus showing the characteristics of many similar samples with low importance; the offline analysis data are obtained under the manually adjusted extreme operation mode, which constitutes a sample with solid typicality. However, the data volume is small, and it is challenging to cover all the typical working conditions of the grid. The distribution of samples consisting of two types of data in the operational feature space is shown in **Figure 1**.

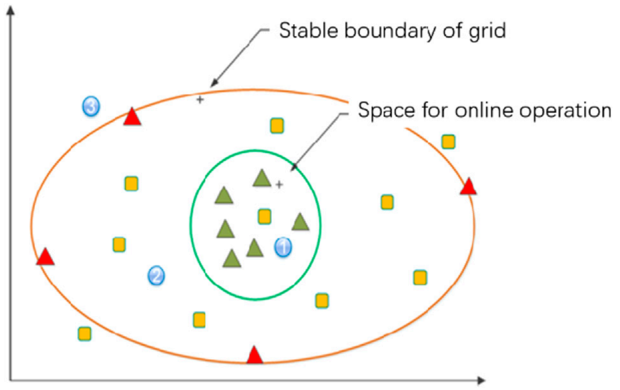

FIGURE 1 | illustration on grid operation sample sets.

The red triangle represents the offline analysis sample, the green triangle represents the online analysis sample, and the yellow squares represent samples that need replenishment. The operation space is divided into three regions by two lines: the green line indicates the boundary of online operation, and the resulting region one is the online operation region; the red line shows the boundary of stable operation of the grid, and the region three outside the boundary indicates the characteristic region of infeasibility or fault instability; the middle region two indicates the characteristic region where online operation does not occur, but the stable operation is possible. The samples in region two and region three provide critical information in the tasks related to the stability boundary, so the corresponding sample supplement operations need to be done.

2.2 Blue Noise Distribution

In computer graphics, the blue noise distribution is recognized as the best distribution property.

As shown in **Figure 2**, the left figure shows the point set formed by blue noise sampling, and the right figure shows the point set formed by random sampling. Many researchers default to random sampling as a form of uniform sampling; in fact, pure randomness does not give the desired results, and points tend to clutter the region and leave blank space, while blue-noise sampling makes the sample points uniform as possible. Assuming that each sample point can represent the information in a certain range, the blue noise distribution can cover a larger feature space. In contrast, the distribution formed by random sampling shows the characteristics of some regions are blank while some other regions are denser in points. The online data of the power grid presents a more heterogeneous distribution characteristic. Many duplicate samples are represented in the feature space as a dense cloud of points in a region. At the same time, there are no non-converging samples in the online data, so the region of non-convergence in the feature space is blank. In this paper, the blue noise distribution characteristic refers to the distribution characteristic in the high-dimensional space. Since the configurable number of samples in the feature space is much larger than the usually used sample set capacity as the

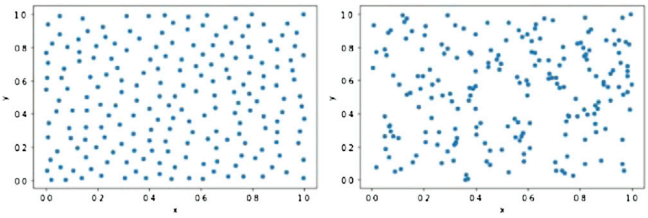

FIGURE 2 | Blue noise sampling and stochastic sampling in the two-dimensional plane.

dimensionality grows, forming a significant sparsity, the blue noise characteristic referred to in this paper cannot cover the entire feature space uniformly but can only ensure that no two sample points are too close to each other. Under the above assumptions, the blue noise distribution is still a distribution characteristic covering the largest feature space range with the same sample size.

2.3 Boundary-Enhanced Variable Density Distribution

Unlike the classical classification problem in computer vision, this task is more concerned with the situation near the boundary between classes. Specifically, the task of power flow solvable discrimination is consistent with the definition of a binary classification problem. The input feature x of the database is the node injected power of the grid. The class label y of the output is the presence or absence of a solution. And the performance metric is the accuracy of the discrimination, where the DL model classifies the input represented by x to the output represented by y.

However, unlike the classical binary classification problem, in the task of power flow solvable discrimination, the input features x moves continuously toward another class without passing through the other class, and there is a clear boundary between the two classes. In contrast, in the classical classification problem of computer vision, input features x belonging to one class movecontinuously toward another class, usually passing through a region that belongs to neither class 1 nor class 2, and the samples in this region are also considered as invalid samples and discarded. For example, identify whether the picture is of a “cat” or a “dog”. The input feature X moves from the “cat” class to the “dog” class, passing through the “non-cat” and “non-dog” classes, which do not usually appear in the database either. Thus, a more precise interpretation of the physical meaning of the task is formed: fitting the viable domain boundary.

The deep learning model makes sense of the task from the data and acquires knowledge. A database that better meets the requirements of this task should provide more boundary information. There should be more sample points near the boundary, fewer samples far from the boundary, and the distribution characteristics of this database are referred to as BEVD.

3 DATABASE GENERATION METHODS CONSIDER-ING DISTRIBUTION CHARACTERISTICS

This paper implements the database generation method considering the distribution characteristics by the weighted sample elimination method. This section introduces the definition and algorithmic process of the weighted sample elimination method. Then the rules for implementing each of the two distributions proposed in the previous section in the framework of the elimination method, i.e., the weight calculation formula, are designed.

3.1 Weighted Sample Elimination Algorithm

The algorithm that takes a set of samples as input and selects a subset as output is sample elimination. The method of assigning weights to all samples and eliminating the samples with the highest weights until the target number of samples is reached is called weighted sample elimination. The weighted sample rejection method is an algorithmic framework that can generate databases with different distribution characteristics by replacing the core rules. In other words, for sampling tasks targeting different distribution characteristics, the workflow of the elimination method is the same, and the only difference is the design of the weighting formula that determines the elimination order. The core idea of the algorithm is to guarantee the overall distribution characteristics of the sample point set by ensuring its local characteristics so that the elimination rule only needs to consider the nearby region of each sample point, which means that the weight calculation is only relevant to the sample points in its nearby region. Therefore, an efficient algorithm implementation requires two relatively common data structures: a spatial division structure for quickly finding the neighboring samples and a priority queue for selecting the sample with the highest weight. In the implementation of this paper, the kd-tree and the heap are used, respectively, and the detailed steps of the algorithm are shown in the following **Figure 3**. The first three operations are preparing the input terms of the algorithm, including the generation of the original database and the calculation of the parameters, the former of which requires the use of a power system simulation program. The middle two operations are the preparation of the algorithm and, finally, the loop operation of eliminating samples. The weight value of each sample is formed by the joint contribution of other points in the range, which is calculated as follows.

$$\boldsymbol{w_i} = \sum_{\boldsymbol{j=0}}^{\boldsymbol{n}} \boldsymbol{w_{ij}} \tag{2}$$

where w_i denotes the weight of sample i, w_{ij} denotes the weight contributed by each sample in the range to sample i, and the search range is a spherical region with sample point s_i as the center and radius r, and n is the number of other sample points in this range. The formula for w_{ij} reflects the elimination rule and is given in the next section.

When a sample is eliminated, only the weights of a few samples within its search range need to be adjusted, which means that the weights w_{ij} contributed by two sample points to each other are subtracted, so the computational complexity is significantly reduced. To further optimize the algorithm execution speed, the hardware parallel acceleration method provided by the tbb library is introduced in the kd-tree construction process. The various data structures and hardware accelerations mentioned above allow the algorithm to be practically applied in a limited high-dimensional space without suffering the curse of dimensionality.

3.2 Design of Weighting Formula for Blue Noise Sampling

The blue noise distribution in the high-dimensional feature space is a distribution that keeps no two sample points too close to each other, such that duplicate or similar samples can be eliminated under such a rule. The blue noise database covers the largest range in the feature space or has the largest amount of information for the same sample size. Here, the sample point distance represents the similarity between two samples, which is the similarity between two operation methods for the grid operation sample. The distance between two sample input features is in vector form in practical calculation, such as the distance between sample X_i $[x_{i1},x_{i2},...,x_{in}]$ and sample $X_j[x_{j1},x_{j2},...,x_{jn}]$ is calculated by the formula

$$d_{ij}\sqrt{\sum_{k=0}^{n}\left(x_{ik}-x_{jk}\right)^2} \tag{3}$$

The formula for calculating the weight function w_{ij} can be expressed as

$$w_{ij} = \left(1-\frac{\widehat{d}_{ij}}{2r_{max}}\right)\alpha \tag{4}$$

Where, $\widehat{d}_{ij} = min(d_{ij}, 2r_{\max})$. α is the parameter that indicates the strength of the influence of d_{ij} on w_{ij}. d_{ij} can be the Euclidian distance as well as the geodesic distance on a surface or any other function. The value of $r_{\max}$ depends on the sampling domain and the number of target samples. In 2D and 3D,

$$r_{\max,2} = \sqrt{\frac{A_2}{2\sqrt{3}N}} \tag{5}$$

$$r_{\max,3} = \sqrt{\frac{A_3}{4\sqrt{2}N}} \tag{6}$$

where A2 and A3 are the area and volume of the sampling domain, N is the number of target samples.

In higher dimensions we use a conservative estimate for $r_{\max,d}$ with $d > 3$, assuming that the hypervolume of the domain A_d can be completely filled with hyperspheres with no overlap. Note that this assumption causes overestimation of the $r_{\max}$ values. The hypervolume V_d of a hypersphere with radius r is $V_d = C_d r^d$, where C_d is a constant such that $C_d = C_{d-2}(2\pi/d)$ with $C_1 = 2$ and $C_2 = \pi$, resulting

$$r_{\max,d} \cong \sqrt[d]{\frac{A_d}{C_d N}} \tag{7}$$

The above scanning radius is also referred to as the maximum Poisson disc radius in Poisson disc sampling.

3.3 Design of Weighting Formula for Boundary-Enhanced Variable Density Sampling.

Traditional variable density sampling requires specifying the interval location and density. In contrast, the location is the area near the boundary in this task. The explicit representation of the boundary is the result of power flow calculation convergence discrimination, which cannot be known in advance. Obtaining a more accurate representation of the boundary requires a higher density of sampling near the boundary, and sampling near the boundary requires information about the location of the boundary, which is the main difficulty of the problem. In this paper, we use the label information and the distance information between sample points to make a judgment on the location of the sample points where the distance between sample points represents the similarity between two samples, and for grid operation samples, it can represent the similarity between two operation states. The distance of two samples in this paper is calculated using vector operation representation form, such as sample $X_i = [x_{i1},x_{i2},...,x_{in}]$ and sample $X_j = [x_{j1},x_{j2},...,x_{jn}]$ are calculated as

$$d_{ij} = \sqrt{\sum_{k=0}^{n}\left(x_{ik}-x_{ik}\right)^2} \tag{8}$$

The weight of the mutual contribution between the two samples is calculated by the formula：

$$w_{ij} = \begin{cases} 0 & y_i = y_j \\ -\left(1-\frac{\widehat{d}_{ij}}{2r}\right)^{\beta} & y_i \neq y_j \end{cases} \tag{9}$$

where y_i and y_j are the label value of the samples and $\widehat{d}_{ij} = \min(d_{ij}, 2r)$. β is the parameter indicating the strength of d_{ij}'s effect on w_{ij}. There are two cases according to whether the label information is the same or not, the samples in the range with the same class do not contribute to the weight value, while the samples in the range with different classes contribute a negative value to it.

The purpose of this is to make the effect of samples with different classes tend to retain the sample more, and the more samples with different classes in the range and the closer the distance, the more that sample point should be retained. As shown in **Figure 4** below, the dot's color indicates the class, and the circle indicates the scanned area of the three sample points, where the same class surrounds the sample point s1, and its weight value w1 is the maximum value of 0. s2 and s3 sample points contain sample points of different classes within the scanned area. The sample points of different classes around s2

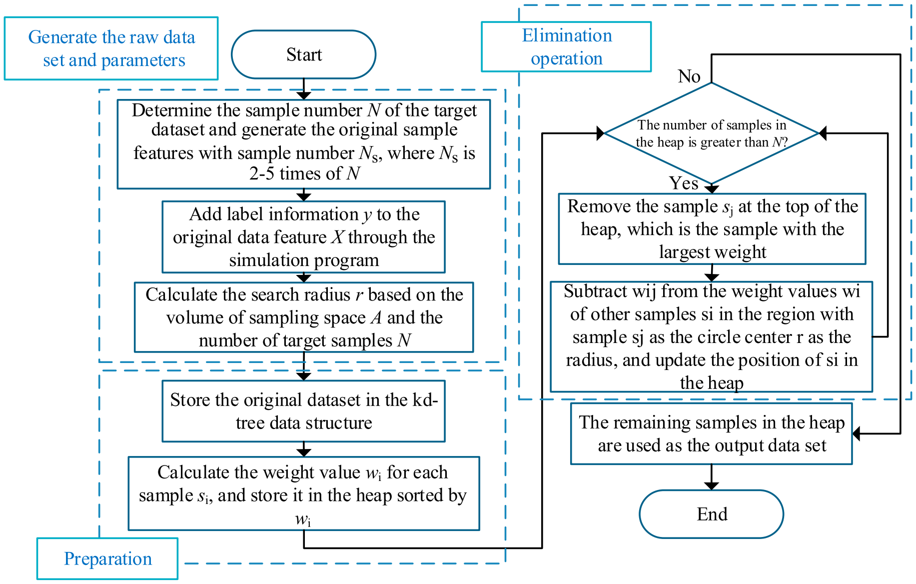

FIGURE 3 | Algorithm flow chart of weighted sample elimination.

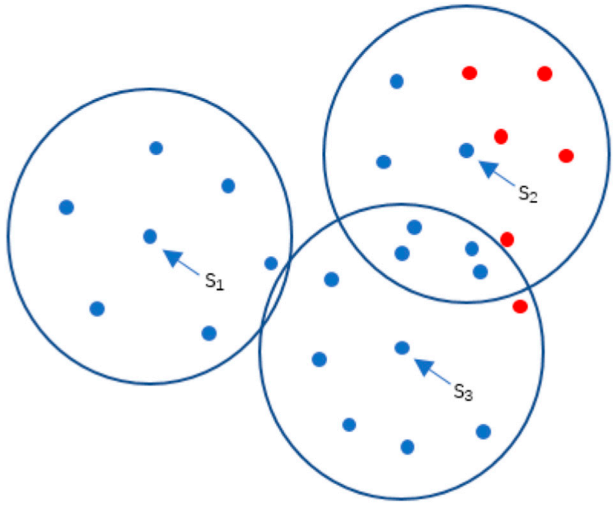

FIGURE 4 | Schematic of the rule of BEVD sampling.

are more and closer, so their weight values will be smaller, which means that they are retained with the highest priority.

Since it is difficult to visualize the high-dimensional feature sample set, the morphology of the variable density distribution characteristics is demonstrated here by a 2-dimensional arithmetic example, as shown in **Figure 5**. The two images to the left of the arrow are the algorithm's input database and output database, respectively. The color is the label information, which indicates the class to which the samples belong. The algorithm prioritizes eliminating sample points far from the boundary, thus forming BEVD distribution characteristic, which characterizes the data as more sample points near the boundary and a smaller number of sample points in the region far from the boundary. The right side of the arrow is the probability density heat map of the output database, which can reflect the target distribution characteristics more intuitively. The color scale on the right side indicates the number of samples in the region. The brighter it is, the more samples there are, and the distribution characteristics show a higher density near the boundary between classes.

4 DATABASES QUALITY COMPARISON METHOD

In this paper, the study of database distribution characteristics aims to improve the performance of deep models, so the quality of databases cannot be compared only from some statistical characteristics of databases but needs to be put into the complete training-testing process of deep learning. The ability to train a model with higher discriminative accuracy is the indicator to evaluate the database distribution characteristics.

The specific comparison method is shown in **Figure 6** below. The databases to be compared are used as training sets. The same deep network structure is trained. The same learning algorithm is used to update the parameters in the network. The training result models corresponding to the training set are obtained, and then the same test set is evaluated to obtain the discrimination accuracy of each model. The difference in database quality in this paper is only reflected in the distribution characteristics of the database, so the sample size should be kept consistent when used as the training set.

The confusion matrix generally represents the test results of the binary classification problem, as shown in **Table 1**, where m, n represents the true number of samples in category one and category 2, respectively, and s, t represents the number of

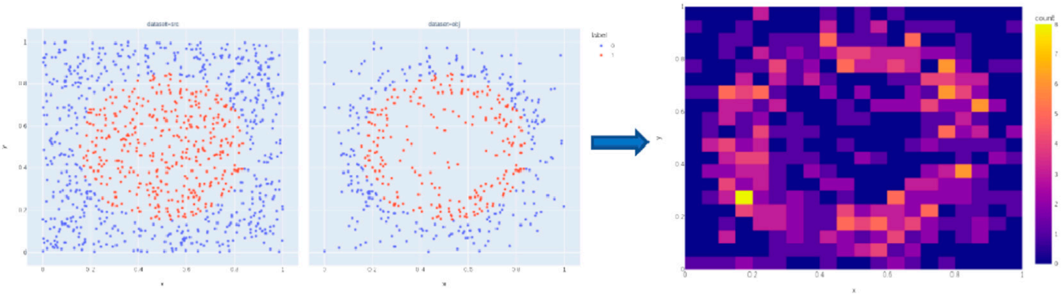

FIGURE 5 | Input/output of the algorithm in 2D arithmetic and Density heat map of BEVD sampling results.

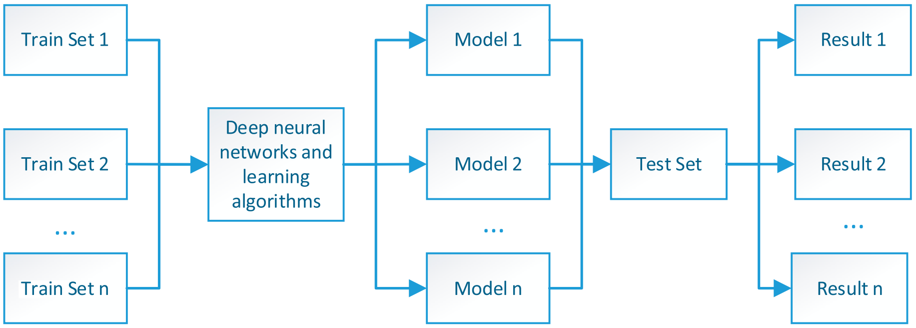

FIGURE 6 | Overall diagram of database comparison method.

TABLE 1 | Confusion matrix of the two-category task.

		Classification results		
		Class 1	**Class 2**	**Total**
Real Label	Class 1	*a*	*c*	*m*
	Class 2	*d*	*b*	*n*
	Total	*s*	*t*	*w*

samples predicted to be in two categories in the test classification; w is the sum of all samples; a, b represent the number of samples correctly classified and c, d represent the number of samples incorrectly classified. From the confusion matrix, it can be directly observed which class of samples the problem occurs in the discriminations.

A more detailed analysis is possible from the confusion matrix, which is divided into the following three indicators.

Accuracy is the proportion of correct predictions among the total number of cases examined. The formula for quantifying binary accuracy is:

$$ACC = \frac{a+b}{w} \tag{10}$$

Precision is for classification results and is defined as the probability that all samples predicted to be of a certain class have a real label of that class.

$$PREC_{class1} = \frac{a}{s} \tag{11}$$

$$PREC_{class2} = \frac{c}{t} \tag{12}$$

Recall is for real labels and is defined as the probability that all samples that are actually of a class are classified as samples of that class.

$$REC_{class1} = \frac{a}{m} \tag{13}$$

$$REC_{class2} = \frac{b}{n} \tag{14}$$

5 EXPERIMENTAL VERIFICATION

5.1 Case Introduction

The grid model used in this paper is CEPRI36, and the specific structure is shown in **Figure 7**, in which some nodes are connected to capacitors or reactors not involved in regulation. There are 18 nodes involved in the regulation of generating units or loads. The nodes inject power as input feature values, for a total of 36 variables, i.e., the sample contains a feature dimension of 36 dimensions.

The original database generation method required for the weighted sample rejection method: The feature values are formed by randomly specifying the nodes to inject power and dynamic balance pre-processing. The power flow calculation

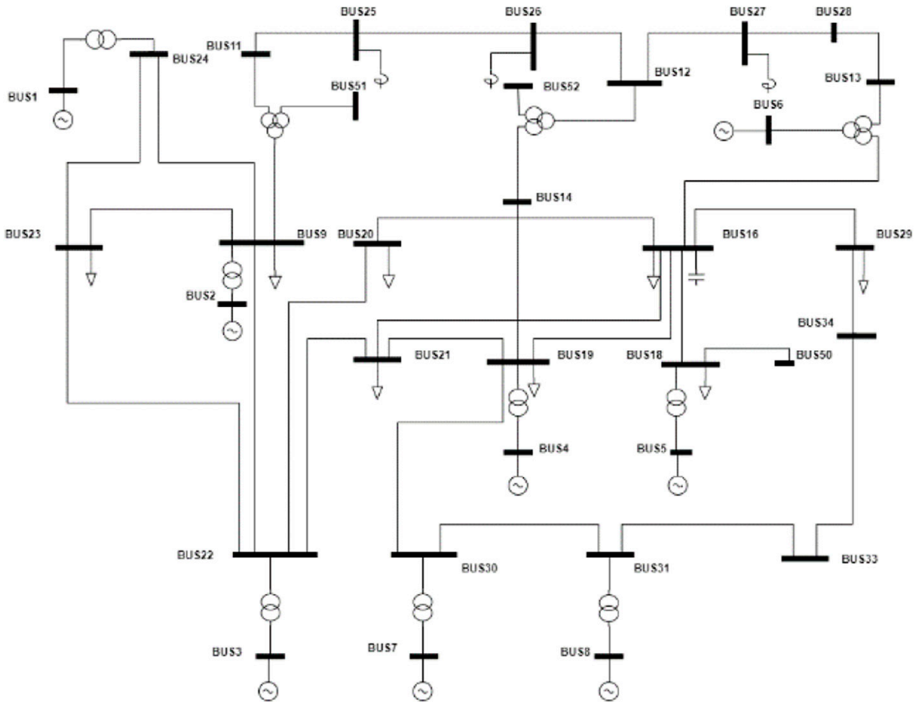

FIGURE 7 | CEPRI36 grid model topology connection diagram.

program automatically generates the label information based on the feature values. The resulting original database contains 15,000 samples. THE WEIGHTED ELIMINATION METHOD GENERATED a BEVD database of 5000 samples and a blue noise database of 5000 samples, respectively; the comparison group randomly sampled 5000 samples from the original database. The above three subsets of the original database are used as the train set in the experiment. The test set contains 2000 samples different from the original database, of which 1000 samples each for the two classes of convergence and non-convergence. Two types of deep learning models are selected.

Model 1: Multilayer Perceptron Model (MLP). The MLP is a forward-structured artificial neural network that maps a set of input vectors to output vectors and consists of multiple layers of nodes, each fully connected to the next layer. In addition to the input nodes, each node is a processing unit with a nonlinear activation function.

Model 2: Convolutional neural network (CNN). CNN contains two convolutional layers and two fully connected layers. Each node is a processing unit with a nonlinear activation function except the input node.

The experimental environment of the database generation program is 3.30Gis Hz, the CPU is AMD Ryzen9 5900 HS, and the kd-tree construction process calls tbb to achieve 8-core parallel acceleration, which takes less than 1 min to generate 5000 samples from 15000 samples elimination, which can meet the practical application.

The weighted elimination algorithm is implemented in C++ to ensure the performance; the deep learning algorithm is implemented through the pytorch framework.

5.2 RESULTS AND DISCUSSION

The confusion matrix of the experimental results is shown in **Figure 8**. Combining different databases and deep models forms six confusion matrixes of model test results. According to the combination of different databases and depth models to form six sets of confusion matrices of model test results, where the column direction of each confusion matrix represents the model's predicted class, and the row direction represents the real class to which the samples belong. Class 0 in the figure is convergence, and class 1 is non-convergence. The color shade of each cell of the matrix indicates the number of samples. The discrimination accuracy of the deep model trained by the BEVD database is significantly higher than the other two in the non-convergence class. And the case of the blue-noise database compared with the random sampling database is that the blue-noise database is better under the MLP model and the random sampling database is better under the CNN model.

The collated 2-level metrics are shown in **Table 2**, where P_0 and P_1 denote the precision of converged and non-converged samples, R_0 and R_1 denote the recall of converged and non-converged samples, and A denotes the accuracy. In terms of accuracy A, the combination of the variable density boundary

FIGURE 8 | Confusion matrix for the results of experiment.

TABLE 2 | Level 2 indicator for the results of experiment.

Train set	Deep model	P_0/%	P_1/%	R_0/%	R_1/%	A/%
BEVD database	MLP	88.7	98.3	98.5	87.4	92.95
	CNN	87.3	98.3	98.6	85.7	92.15
random sampling database	MLP	75.6	99.4	99.6	67.9	83.75
	CNN	82.8	98.9	99.1	79.5	89.3
blue noise database	MLP	84.2	98.6	98.9	81.5	90.2
	CNN	78.1	98.6	99	72.4	85.7

enhancement database with both depth models is the highest; while the blue noise database and the random sampling database present performance related to the deep model, with the blue noise database performing better under the MLP model and the random sampling database performing better under the CNN model. In terms of precision and recall, the error in discrimination mainly occurs in the error of discriminating non-converging samples as converging samples.

The above experimental results show that the generalization performance of the deep learning algorithm has the following relationship with the database.

1) The generalization performance of deep learning algorithms is determined by the database together with the model and algorithm. The discriminative accuracy of the BEVD database with the combination of both models is the highest and has similar values, while the accuracy of the other two datasets with the combination of different deep models are significantly different, with a difference of 5.55% and 4.5%, respectively
2) For the class boundary fitting task like convergence discrimination of power flow calculation, the database with BEVD distribution is more suitable for the demand.
3) The uniformity of the database distribution has no significant effect on the generalization performance of this task. The blue-noise database is more uniform than the random sampled database, The blue-noise database is more uniform than the random sampled database, and the discriminative accuracy of the MLP combined with the former is 6.45% higher than that of the combination with the latter, while the CNN with both has the opposite result of 3.6% lower.

Among the above three conclusions, the third one is inconsistent with intuition. This phenomenon can be understood as follows: if the labels of the database are continuously changing in the feature space, then a more uniformly distributed database should have a positive impact on the generalization performance of the deep model, while the labels in the trend convergence discrimination task are step-changing at the boundaries, and the positions of the samples in the feature space have different levels of importance. Therefore, the uniformity of the database distribution does not show a significant relationship with the model generalization performance.

The weighted sample elimination algorithm has the following features:

1) It Allows specifying the number of samples in the target database, and the termination condition of the algorithm can be controlled.
2) Good scalability to generate databases with different distribution characteristics by designing different sample weight calculation formulas.
3) It Supports the sampling domain as an arbitrary stream shape, which can meet the pre-processing operations such as the active balance of the original data.
4) The computational complexity of the algorithm is $O(N\log N)$ and the storage complexity is $O(N)$, which can be applied in high-dimensional feature space.

6 CONCLUSION

In order that the application of artificial intelligence in grid analysis can be further developed and model algorithms can be compared and optimized in a unified database, this paper researches the impact of the distribution characteristics of power flow database on the performance of deep learning generalization, and the methods for generating database considering the distribution characteristics, with the following contributions**:**

1) A database generation method T considering distribution characteristics in high-dimensional feature space is proposed, which can effectively reduce the computational complexity and storage complexity by typical data structure design and parallel acceleration of hardware.
2) The sample weight calculation rules for blue noise distribution and BEVD distribution in high-dimensional feature space are proposed and applied in the framework of the weighted elimination method, which can realize blue noise sampling and BEVD sampling in high-dimensional feature space.
3) The requirements of the power flow convergence discrimination problem on the database distribution characteristics are analyzed, and it is verified that the deep model trained by the variable density boundary-enhanced distribution database has apparent advantages in handling this task. The judgment accuracy was improved by 2.91%–9.5%.

Improving the generalization performance of learning models from the perspective of improving the quality of databases belongs to the field of data-centered machine learning. The research results of this paper can lay the foundation for the study of database distribution characteristics of classification problems focusing on boundaries.

DATA AVAILABILITY STATEMENT

The raw data supporting the conclusions of this article will be made available by the authors, without undue reservation.

AUTHOR CONTRIBUTIONS

XM: conceptualization, methodology, software, writing—original draft. YL: validation, writing—review and; editing. DS: resources, project administration, investigation. SH: data curation, supervision, software. FZ: visualization.

FUNDING

This work was supported by State Grid Corporation of China Science and Technology Project—Research on Evaluation and Verification Technology of Artificial Intelligence Model for Power Flow Adjustment and Stability Discrimination of Large Power Grid—under Grant 5100-202155343A-0-0-00.

REFERENCES

Alvarez-Melis, D., and Fusi, N. (2020), Database Dynamics via Gradient Flows in Probability Space. 12. doi:10.13334/j.0258-8013.pcsee.181622

Batista, G. E. A. P. A., Prati, R. C., and Monard, M. C. (2004). A Study of the Behavior of Several Methods for Balancing Machine Learning Training Data. *SIGKDD Explor. Newsl.* 6, 20–29. doi:10.1145/1007730.1007735

Chawla, N. V., Bowyer, K. W., Hall, L. O., and Kegelmeyer, W. P. (2002). SMOTE: Synthetic Minority Over-sampling Technique. *jair* 16, 321–357. doi:10.1613/jair.953

Chen, J., Chen, Y., Tian, F., Guo, Z., and Li, T. (2019). The Method of Sample Generation for Power Grid Simulation Based on LSTM. *Proc. CSEE* 39, 4129–4134. (in Chinese).

Chiang, H.-D., Flueck, A. J., Shah, K. S., and Balu, N. C. P. F. L. O. W. A Practical Tool for Tracing Power System Steady-State Stationary Behavior Due to Load and Generation Variations.10(2):623-634. doi:10.1109/59.387897

Cook, R. L. (1986). Stochastic Sampling in Computer Graphics. *ACM Trans. Graph.* 5, 51–72. doi:10.1145/7529.8927

Cubuk, E. D., Zoph, B., Mane, D., Vasudevan, V., and Le, Q. V. (2018). Autoaugment: Learning Augmentation Policies from Data. 2019 IEEE/CVF Conference on Computer Vision and Pattern Recognition (CVPR), *arXiv preprint arXiv:1805.09501.*

Dippé, M. A., and Wold, E. H. (1985). Antialiasing through Stochastic Sampling. *Proc. 12th Annu. Conf. Comput. Graph. Interact. Tech.*, 69–78. doi:10.1145/325334.325182

Haibo He, H., and Garcia, E. A. (2009). Learning from Imbalanced Data. *IEEE Trans. Knowl. Data Eng.* 21, 1263–1284. doi:10.1109/tkde.2008.239

He, H., Bai, Y., Garcia, E. A., and Li, S. (2008).ADASYN: Adaptive Synthetic Sampling Approach for Imbalanced Learning. 2008 IEEE international joint conference on neural networks. IEEE, 1322–1328. doi:10.1109/ijcnn.2008.4633969

Hu, W., Zheng, L., Min, Y., Dong, Y., Yu, R., and Wang, L. (2017). Research on Power System Transient Stability Assessment Based on Deep Learning of Big Data Technique. *Power Syst. Technol.* 41 (10), 3140–3146. (in Chinese). doi:10.13335/j.1000-3673.pst.2017.1889

Japkowicz, N., and Stephen, S. (2002). The Class Imbalance Problem: A Systematic Study1. *Ida* 6, 429–449. doi:10.3233/ida-2002-6504

Joulin, A., Van Der Maaten, L., Jabri, A., and Vasilache, N. (2016).Learning Visual Features from Large Weakly Supervised Data. European Conference on Computer Vision. Springer, 67–84. doi:10.1007/978-3-319-46478-7_5

Shi, Z., Yao, W., Zeng, L., Wen, J., Fang, J., Ai, X., et al. (2020). Convolutional Neural Network-Based Power System Transient Stability Assessment and Instability Mode Prediction. *Appl. Energy* 263, 114586. doi:10.1016/j.apenergy.2020.114586

Sun, C., Shrivastava, A., Singh, S., and Gupta, A. (2017). Revisiting Unreasonable Effectiveness of Data in Deep Learning Era. in Proceedings of the IEEE international conference on computer vision, 843–852.doi:10.1109/iccv.2017.97

Tan, Bendong., Yang, Jun., Lai, Qiupin., Xie, Peiyuan., Li, Jun., and Xu, Jian. (2019). Data Augment Method for Power System Transient Stability Assessment Based on Improved Conditional Generative Adversarial Network. *Automation Electr. Power Syst.* 43 (1), 149–157. (in Chinese). doi:10.7500/AEPS20180522004

Tang, K., Wan, X., and Yang, C. (2021). DAS: A Deep Adaptive Sampling Method for Solving Partial Differential Equations. *arXiv preprint arXiv:2112.14038*. doi:10.48550/arXiv.2112.14038

Wang, Zhengcheng., Zhou, Yanzhen., Guo, Qinglai., and Sun, Hongbin. (2021). Transient Stability Assessment of Power System Considering Topological Change: a Message Passing Neural Network-Based Approach. *Proc. CSEE* 44 (07), 2341–2350. (in Chinese).

Yuksel, C. (2015). "Sample Elimination for Generating Poisson Disk Sample Sets," *Comput. Graph. Forum.*, 34, 25–32. doi:10.1111/cgf.12538

Zhang, H., Cisse, M., Dauphin, Y. N., and Lopez-Paz, D. (2017). Mixup: Beyond Empirical Risk Minimization. *arXiv preprint arXiv:1710.09412*.

Zhang, Y., Zhang, H., Li, C., and Pu, T. (2021). Review on Deep Learning Applications in Power System Frequency Analysis and Control. *Proc. CSEE* 4110, 3392–3406+3665. (in Chinese).

Conflict of Interest: The authors declare that the research was conducted in the absence of any commercial or financial relationships that could be construed as a potential conflict of interest.

frontiers | Frontiers in Energy Research

ORIGINAL RESEARCH
published: 14 July 2022
doi: 10.3389/fenrg.2022.909611

Probabilistic Optimal Power Flow-Based Spectral Clustering Method Considering Variable Renewable Energy Sources

Juhwan Kim [1]***, Jaehyeong Lee*** [2]***, Sungwoo Kang*** [1]***, Sungchul Hwang*** [3]***, Minhan Yoon*** [4]*** and Gilsoo Jang*** [1]*

[1]*School of Electrical Engineering, Korea University, Seoul, South Korea,* [2]*Power System Planning Department, Korea Electric Power Corporation, Naju, South Korea,* [3]*Department of Electrical Engineering, Sunchon National University, Suncheon, South Korea,* [4]*Department of Electrical Engineering, Kwangwoon University, Seoul, South Korea*

OPEN ACCESS

Edited by:
Xingpeng Li,
University of Houston, United States

Reviewed by:
Maneesh Kumar,
Yeshwantrao Chavan College of Engineering (YCCE), India
Martin P. Calasan,
University of Montenegro, Montenegro

****Correspondence:***
Minhan Yoon
myoon@kw.ac.kr
Gilsoo Jang
gjang@korea.ac.kr

Specialty section:
This article was submitted to Smart Grids, a section of the journal Frontiers in Energy Research

Received: *31 March 2022*
Accepted: *30 May 2022*
Published: *14 July 2022*

Citation:
Kim J, Lee J, Kang S, Hwang S, Yoon M and Jang G (2022) Probabilistic Optimal Power Flow-Based Spectral Clustering Method Considering Variable Renewable Energy Sources. Front. Energy Res. 10:909611. doi: 10.3389/fenrg.2022.909611

Power system clustering is an effective method for realizing voltage control and preventing failure propagation. Various approaches are used for power system clustering. Graph-theory-based spectral clustering methods are widely used because they follow a simple approach with a short calculation time. However, spectral clustering methods can only be applied in system environments for which the power generation amount and load are known. Moreover, it is often impossible to sufficiently reflect the influence of volatile power sources (e.g., renewable energy sources) in the clustering. To this end, this study proposes a probabilistic spectral clustering algorithm applicable to a power system, including a photovoltaic (PV) model (for volatile energy sources) and a classification method (for neutral buses). The algorithm applies a clustering method that reflects the random outputs of PV sources, and the neutral buses can be reclassified via clustering to obtain optimal clustering results. The algorithm is verified through an IEEE 118-bus test system, including PV sources.

Keywords: hierarchical spectral clustering, electric power system, photovolataics, power system analysis, expansion

1 INTRODUCTION

New and renewable energy resources have been increasingly used worldwide owing to energy policies aimed at achieving carbon neutrality (Cauz et al., 2020; Li et al., 2021). From a numerical perspective, the accumulated capacity of global wind power increased by a factor of 36.7 (from 16.9 to 621.6 GW) between 2000 and 2019. Within the same time frame, photovoltaic (PV) capacity increased by a factor of 480.8, from 1.2 GW in 2000 to 590.3 GW in 2019 (IRENA, 2021). Owing to the variability in wind and PV generation, wind and PV are treated as variable renewable energy (VRE) sources. In one instance in Denmark (where high renewable penetration has been achieved), VRE generation exceeded demand for 845 h and recorded a high demand of 213%. Such situations have become more frequent since the first occurrence in 2015 (Holttinen et al., 2021). Increases in the uncertainty and variability of VRE sources are expected to pose challenges to the secure operation of modern power systems. Accordingly, probability analyses have been applied to incorporate the uncertainties from VRE sources and converter-interfaced generation (Wiget et al., 2014; Leeuwen and Moser, 2017). Novel

TABLE 1 | Comparison of clustering references.

Paper	Advantages	Disadvantages
Sarajpoor et al. (2021)	Proposes a time aggregation framework for choosing representative periods for studies that include both wind and load data	Inapplicable to clustering content for network segmentation
Chai et al. (2018)	1) Novel index based on electrical distance and voltage capability 2) Network partition based on Tabu search	Local voltage regulations are required in applications
Cao et al. (2021)	Undertakes network partitioning considering the voltage sensitivity (based on electrical distance) to achieve decentralized control	Cannot guarantee application in transmission system because of its application in the distribution system
Ma et al. (2021)	Proposes graph-theory-based network partitioning algorithm to realize decentralized detection with a faster response	Numerous grouping steps for network partitioning
Si et al. (2021)	Summarizes the concepts and general process in electric load clustering for smart grids	Does not cover specific application cases
von Luxburg, (2007)	Presents the most common spectral clustering algorithms and derives them from scratch via several different approaches	Does not cover the application of the power system
Sánchez-García et al. (2014)	Provides a thorough theoretical justification of the use of spectral clustering in power systems, including the results of our methodology for several test systems	Clustering process considering the variability of VRE sources is neglected
Tyuryukanov et al. (2018)	Proposes an approach based on the orthogonal transformation of spectral clustering to closely fit the axes of the canonical coordinate system	Clustering process considering the variability of VRE sources is neglected
Amini et al. (2020)	Improves hierarchical clustering such that the generator coherency constraint can be included in the clustering process	Clustering process considering the variability of VRE sources is neglected
Bialek and Vahidinasab, (2022)	Offers a graph-theoretic justification for tree-partitioning based on spectral clustering	Does not include the system dynamics simulation when tree-partitioning

approaches are required to handle the corresponding challenges in power system operation, planning, and control.

The clustering (i.e., partitioning, islanding, and splitting) of electric power systems is a concept that emerges especially frequently in control and protection technologies (Park and Kim, 2006; Sarajpoor et al., 2021). In power systems, clustering methods are used in various ways and for various purposes. Chai et al. proposed a double-layer voltage control strategy to solve the voltage violation problem in a distribution system. The proposed method was aimed at minimizing the PV active power curtailment and network power loss of each cluster. In this case, the process of dividing clusters was based on a clustering method that operated according to electrical distance, thus facilitating rapid optimization. In general, following the high penetration of PV power, numerous approaches have been proposed based on the corresponding voltage (for example, to avoid voltage violations). In this context, decentralized or distributed control based on power network clustering offers an advantage over centralized control (Cao et al., 2021). The clustering method can be applied not only to system control but also to event detection (Ma et al., 2021). Nevertheless, in the case of a large existing system, it is difficult to search for events owing to the large quantities of measured data. A graph-theory-based network partitioning algorithm has been proposed to address this problem and accelerate the system response.

The clustering algorithms used in several of the papers cited herein can be classified into different categories (Si et al., 2021). Among these algorithms, hierarchical spectral clustering is an important clustering method and is widely used for the partitioning of electric power systems. Owing to its strong theoretical basis (von Luxburg, 2007; Lee et al., 2014), this method has been used in various power system studies. This spectral clustering technique can be applied using the electrical parameters (e.g., the topology, admittance, and power flow) of a power system alongside hierarchical clustering, where the preferred number of clusters is considered the input. Consequently, hierarchical clustering can be obtained for the connection strength determined by the chosen electrical weighting (Sánchez-García et al., 2014). This method has been studied from various perspectives, such as to improve the calculation efficiency and partition quality through orthogonal conversion (Tyuryukanov et al., 2018), to island power systems according to the minimum active flow disruptions (Amini et al., 2020), and to prevent cascading failures through tree partitioning (Bialek and Vahidinasab, 2022). As described above, numerous studies have focused on clustering; these studies and their findings are summarized and compared in **Table 1**.

However, methods for clustering in power transmission systems that incorporate variable power sources (e.g., renewable generation) have not been fully discussed. This is because when applying power flow-based clustering, the results can differ in response to variations in power generation. Clustering according to topology or admittance can be considered; however, this leads to further issues that cannot be addressed (e.g., those concerning a branch list with an overload risk, maximum overload rates, and overload probabilities). Accordingly, a probabilistic flow analysis method has been proposed to address these issues (Zhu et al., 2020; Wang et al., 2021; Lin et al., 2022). It is necessary to discuss clustering based on a consideration of a probabilistic interpretation of renewable power generation sources (e.g., PV sources). Therefore, in this paper, we propose a probabilistic clustering methodology for power systems operating with a high penetration of VRE sources.

The main contributions of this paper are as follows:

- A probabilistic spectral clustering methodology based on the Monte Carlo method: This method can be applied to power systems by considering the characteristics of VRE

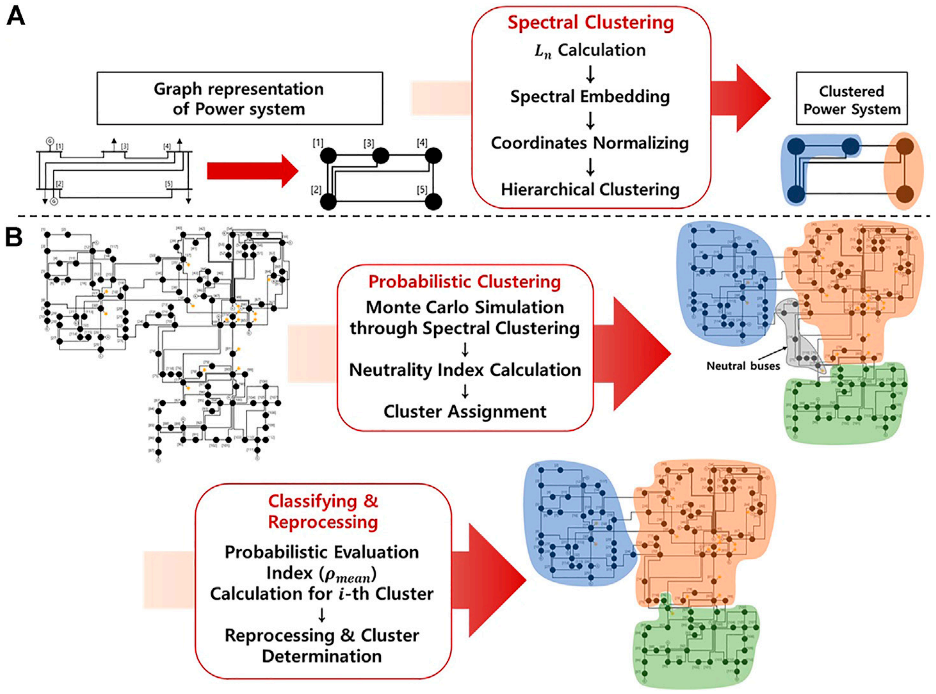

FIGURE 1 | Clustering process. **(A)** Hierarchical spectral clustering method. **(B)** Probabilistic spectral clustering and classification of neutral buses.

sources whilst applying the hierarchical spectral clustering method in the existing power system network.

- The classification and reprocessing of neutral buses: Neutral buses are generated as a result of the proposed probabilistic clustering method and the change in power flow. By reprocessing such buses using neutrality and probabilistic evaluation index, optimal clustering results can be derived.
- The definition of new evaluation indices for probabilistic clustering: The probabilistic expansion index is discussed anew, allowing the expansion to be used as a clustering evaluation index for application under probabilistic conditions. As a result, a more appropriate clustering can be derived.

The remainder of this paper is organized as follows: In **Section 2**, the essential preliminaries are introduced, and the spectral clustering method and related contents are summarized. **Section 3** describes the proposed probabilistic spectral clustering method, PV modeling, and neutral bus classification. In **Section 4**, the results of the method applied to an IEEE 118-bus test system are verified. Finally, the discussion and conclusion are presented in **Section 5** and **Section 6**.

2 HIERARCHICAL SPECTRAL CLUSTERING OF POWER SYSTEM

A power system can be partitioned via hierarchical spectral clustering, as shown in **Figure 1A**; the proposed probabilistic spectral clustering is shown in **Figure 1B**. The spectral clustering algorithm consists of four steps, as illustrated in **Figure 1**.

2.1 Graph Representation of Network

2.1.1 Terminology

For graph-theory-based network partitioning, power systems with N buses are represented as a graph G = (V, E) with a vertex set V and edge set E. The buses and transmission lines (or transformers) in power grids can be denoted as vertices (nodes) and edges (links), as follows:

$$v_i \in V, \qquad i = 1, 2, \ldots, N, \tag{1}$$

$$e_{ij} \in E \subset V \times V, \qquad i, j = 1, 2, \ldots, N. \tag{2}$$

This graph is only considered a simple graph (i.e., no loops or multiple edges are allowed). Multiple edges are replaced by equivalent single edges. All graphs are undirected.

2.1.2 Edge Weights Reflecting Power System

The topological structure of the graph does not include the electrical information of the power system. Therefore, the edge weights should be used. Edge weight is a function $w: E \rightarrow \mathbb{R}$ such that the weight is calculated as follows:

1) $w(e_{ij}) = w(e_{ji})$ for all e_{ij},
2) $w(e_{ij}) = 0$ if $e_{ij} \notin E$,
3) $w(e_{ii}) = \sum_{j=1, j \neq i}^{N} w(e_{ij})$.

In this study, we adopt the notation that $w(e_{ij}) = w_{ij}$ if $i \neq j$, and $d_i = w(e_{ii})$ for the weighted vertex degree. In a purely

TABLE 2 | Characteristics of the photovoltaic (PV) module.

PV module characteristic	Value
Current at maximum power point, I_{MPP} (A)	7.76
Voltage at maximum power point, V_{MPP} (V)	28.36
Short circuit current, I_{SC} (A)	8.38
Open circuit voltage, V_{oc} (V)	36.96
Current temperature coefficients, K_i (A/°C)	0.00545
Voltage temperature coefficients, K_v (V/°C)	0.1278

topological structure, all edges have unit weights. To represent power grids, we can use the values of the power flows as edge weights. When P_{ij} denotes an active power flow from buses i to j, the corresponding edge weight is defined as follows:

$$w_{ij} = \frac{|P_{ij}|+|P_{ji}|}{2}. \tag{3}$$

The power-flow-based weight depends on the operating point and denotes the importance of a branch. Thus, a branch with a small flow is more likely to be removed. In contrast, a branch with a large flow exhibits a strong connection between each vertex and is more likely to be grouped together with other elements.

2.1.3 Graph Laplacian Matrix

Laplacian matrices are used in the spectral clustering method for efficient graph partitioning. The method uses the eigenvector and eigenvalues of two types of Laplacian matrices, which are related to the undirected weighted simple graph G = (V, E, *w*).

The Laplacian matrix L of G is an $N \times N$ matrix, where N is the number of vertices.

$$[L]_{ij} = \begin{cases} d_i, & if\ i = j \\ -w_{ij}, & if\ i \neq j\ and\ e_{ij} \in E \\ 0, & otherwise. \end{cases} \tag{4}$$

The normalized Laplacian matrix is calculated using a diagonal matrix D with nonzero elements d_i.

$$L_{nor} = D^{-1/2} L D^{1/2}, \tag{5}$$

$$[L_n]_{ij} = [L_n]_{ij} = \begin{cases} 1, & if\ i = j \\ \dfrac{-w_{ij}}{\sqrt{d_i}\sqrt{d_j}}, & if\ i \neq j\ and\ e_{ij} \in E \\ 0, & otherwise. \end{cases} \tag{6}$$

The normalized Laplacian matrix is scale-independent and more suitable for clustering.

The eigenvalues of the Laplacian matrix are non-negative real numbers, and the number of zero eigenvalues is equal to the number of connected components in the graph. For the normalized Laplacian matrix of a connected graph with N vertices, the eigenvalues can be written as follows (von Luxburg et al., 2008):

$$0 = \lambda_1 \leq \lambda_2 \leq \ldots \leq \lambda_k \leq \ldots \leq \lambda_N \leq 2, \tag{7}$$

$$\lambda_2 > 0. \tag{8}$$

By taking the k smallest eigenvalues together with their respective eigenvectors $(\nu_1, \nu_2, \ldots, \nu_k, \ldots, \nu_N)$ of the normalized Laplacian matrix, we can partition the power system using a spectral clustering method. This method is described in the next section.

2.2 Spectral Clustering

Clustering refers to the classification of the vertices in a graph into several groups (clusters) such that vertices in the same cluster are highly interconnected but are weakly connected to vertices in other clusters. Among the clustering methods, spectral clustering uses normalized Laplacian eigenvalues and eigenvectors. The concept applies the first k eigenvectors corresponding to the smallest k eigenvalues (called spectral k-embedding) and identifies the geometric coordinates that match the N vertices. These coordinates form the N rows of the $N \times k$ matrix, consisting of k eigenvectors. The resulting points are clustered using a spectral clustering algorithm, as discussed below.

2.2.1 Laplacian Matrix Calculation

The Laplacian and normalized Laplacian matrix are calculated for graph G using **Eqs (4)–(6)**, as described in the previous section. At this time, the edge weight is calculated as a power flow using **Eq. (3)**. The latter of the two calculated matrices is used in this study. The eigenvectors of this matrix provide the coordinates representing each bus in the space $\mathbb{R}^k$. The constant k can be determined using the spectral embedding process described in the next section.

2.2.2 Spectral Embedding

Spectral embedding is an important process in spectral clustering. This process employs the first k eigenvectors of the Laplacian matrix, that is, it reduces the dimensions of the matrix from the $N \times N$ Laplacian graph to the $N \times k$ $(k \ll N)$ matrix X, which consists of the chosen eigenvectors. In other words, the dimensions to be analyzed are reduced from $\mathbb{R}^N$ to $\mathbb{R}^k$. This makes it possible to increase the quality of the resulting clusters whilst reducing the computation time.

The criterion for determining the embedding space k is based on the eigengaps (i.e., the differences between two sequential eigenvalues). However, in general, we can obtain a better k -partition with smaller eigenvalues (Sánchez-García et al., 2014). Hence, we use a relative eigengap, as follows:

$$\gamma_k = \frac{\lambda_{k+1} - \lambda_k}{\lambda_k} \qquad (k \geq 2). \tag{9}$$

When the value of the eigengap is large, we obtain a better network partition with at least k clusters. Therefore, in the following simulation, the value of k that maximizes the eigengap value is set as the embedding space.

2.2.3 Coordinate Normalization

After spectral embedding, the coordinates of the N vertices are represented in space $\mathbb{R}^k$. However, the magnitudes of coordinates differ; hence, the results from the clustering may be distorted.

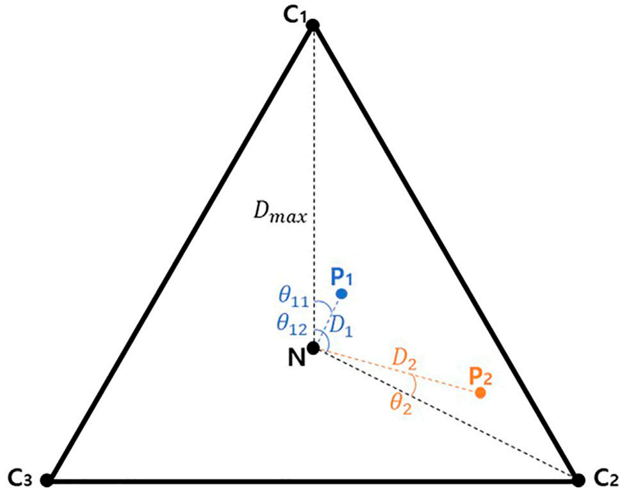

FIGURE 2 | Graphical example of neutrality index (cluster number = 3).

Therefore, spectral clustering is performed once each coordinate value has been normalized to norm 1. This process involves projecting each coordinate into a hypersphere, i.e., a (k -1)-sphere (depending on the embedding space k). The value of each coordinate can be normalized as follows:

$$u_i = \frac{x_i}{\|x_i\|} \quad (1 \le i \le N). \tag{10}$$

2.2.4 Hierarchical Clustering

Through the clustering process described above, we express each bus as a coordinate in space $\mathbb{R}^k$, and we perform clustering by classifying the coordinates. Several methods are available for grouping each bus, including k-means, k-medoid, and hierarchical clustering (Sarajpoor et al., 2021). The k-means and k-medoid methods are frequently used for grouping, but they have several disadvantages. First, the clusters must be determined before clustering. Moreover, the connections between buses in the graph are neglected. Thus, the hierarchical clustering method is applied in this study.

Hierarchical clustering offers several advantages over other clustering methods. It identifies the hierarchy of clusters, which we represent as dendrograms. A dendrogram is a tree diagram that visualizes the hierarchical spectral structure of a power system. This method employs a bottom-up process applied for power system clustering. In N buses, the two most similar buses are merged into a cluster. Here, similarity refers to the distance between buses or clusters. This distance indicates the Euclidian distance between buses i and j.

$$similarity_{ij} = \left\|u_i - u_j\right\| \quad \left(u_i,\ u_j \in \mathbb{R}^k\right). \tag{11}$$

After the buses are chosen, a new graph with N-1 buses is formed. In the new graph, the two closest buses are merged into a new cluster again, and this process is repeated until the desired number of clusters is obtained. This procedure helps grasp the hierarchical structure immediately, and the number of clusters can be adjusted without additional calculations.

2.3 Clustering Evaluation

Through the hierarchical spectral clustering described thus far, the desired number of clusters can be obtained from graph G. The purpose of clustering is to identify a cluster in which the buses in the cluster are strongly connected to each other and weakly connected to buses in other clusters. To evaluate the quality of a cluster, two quantities are defined to evaluate the connectivity described above. First, boundary (∂) is defined as the sum of the edge weights of buses within a specific cluster C and those of the buses within other clusters. It can be used to evaluate the connectivity between different clusters.

$$\partial(C) = \sum\nolimits_{i\in C,\ j\notin C} w_{ij}. \tag{12}$$

Second, the volume (vol) of cluster C is defined as the sum of the degrees of cluster C. It can be used to evaluate the connectivity of the buses within a specific cluster:

$$vol(C) = \sum\nolimits_{i\in C} d_i. \tag{13}$$

For the abovementioned purposes, the quality evaluation metric for a cluster can be defined as the value obtained by dividing the boundary by the volume. It is denoted as the expansion (ϕ) (Sarajpoor et al., 2021).

$$\phi(C) = \frac{\partial(C)}{vol(C)}. \tag{14}$$

The smaller the value of the expansion for the network partition, the better the clustering (i.e., strong connections between buses included in a specific cluster, and weak connections between buses outside thereof). When partitioning the power system into k clusters, we use the maximum expansion value to evaluate the quality of the clustering method (Sánchez-García et al., 2014):

$$\phi_{max}(C_1, \ldots, C_k) = \max_{1\le i\le k} \phi(C_i). \tag{15}$$

It is possible to evaluate whether clustering has been well executed by using a normalized cut (i.e., the arithmetic mean of all clusters' expansions) (von Luxburg, 2007). This method is widely used in the evaluation of graph clustering because the average quality of all clusters can be evaluated.

$$\phi_{mean}(C_1, \ldots, C_k) = \frac{1}{k}\sum\nolimits_{i=1}^{k} \phi(C_i). \tag{16}$$

In this study, in view of the expansion of renewable energy sources in power systems, a metaheuristic approach is applied for probabilistic interpretation. To this end, numerous clustering results must be analyzed for various cases. For this purpose, the above two objective function equations are used to efficiently optimize and evaluate the results. In contrast, several more complex objective functions were required for the method proposed by Cotilla-Sanchez et al. (2013).

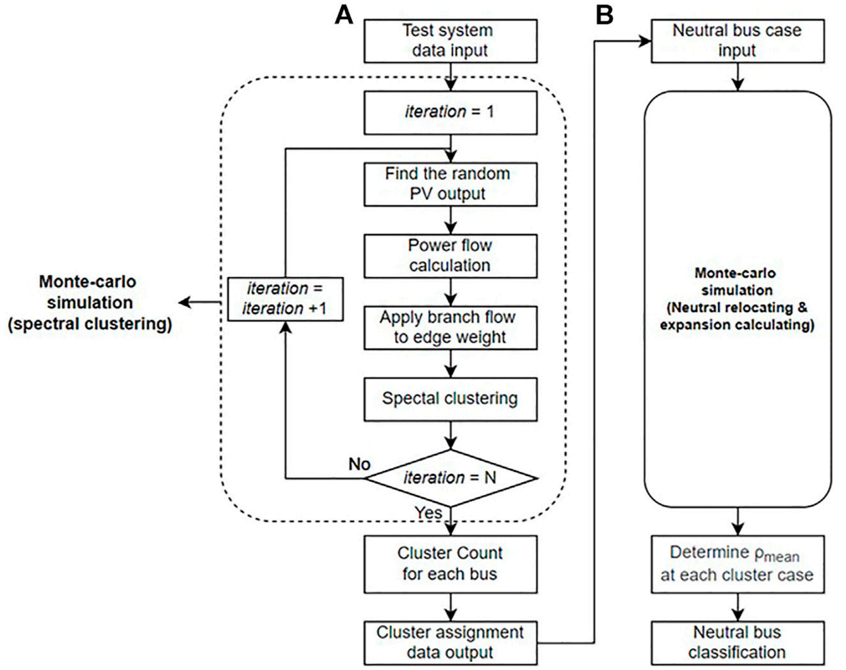

FIGURE 3 | Proposed methodology. **(A)** Probabilistic spectral clustering algorithm. **(B)** Neutral bus classification.

3 PROBABILISTIC SPECTRAL CLUSTERING METHODOLOGY

In this section, we propose a probabilistic spectral clustering method applicable to power systems containing variable sources (e.g., renewable energy sources). In addition, we explain the process of optimizing the neutral buses that may arise in the process of probabilistic analysis by using an evaluation index (i.e., the expansion described in the previous section). To this end, a model is required for the PV output power and its corresponding variability.

3.1 Modeling of Variable Renewable Energy Source: Photovoltaic (PV)

In this study, assuming a situation in which PV sources are expanded in a power system, we repeatedly perform the clustering process for a power flow with an intermittent PV output. The output power of the PV is affected by the random phenomenon of solar irradiance, which changes the power flows of the branches in the power system. Generally, it is more efficient to model irradiance using a beta probability density function than other probability density functions (Teng et al., 2013). Accordingly, the solar irradiance can be expressed as follows:

$$f_{beta}(s) = \begin{cases} \dfrac{\Gamma(\alpha+\beta)}{\Gamma(\alpha)\Gamma(\beta)} s^{\alpha-1}(1-s)^{\beta-1} & (0 \le s \le 1, \quad \alpha, \beta \ge 0) \\ 0 & otherwise \end{cases}, \tag{17}$$

$$\beta = (1-\mu)\left(\frac{\mu(1-\mu)}{\sigma^2} - 1\right), \tag{18}$$

$$\alpha = \frac{\mu\beta}{1-\mu}. \tag{19}$$

In the above, $f_{beta}(s)$ denotes the beta distribution function for solar irradiance, where s is a random variable characterizing the solar irradiance (kW/m^2); Γ is a gamma function comprising the beta distribution function; and α and β are the parameters of the beta distribution function, where both must be positive. μ and σ denote the mean and standard deviation of s, respectively, and these values are used to calculate the parameters. The values of the mean and standard deviation of s for a specified time period are 0.657 kW/m^2 and 0.284 kW/m^2, respectively (Hung et al., 2014).

The output power of the PV module depends on the solar irradiance, ambient temperature, and parameters of the PV module. When the PV module operates at the maximum power point and at a solar irradiance s, the output power can be calculated as a function of s as follows (Sehsalar et al., 2019):

$$P_{PV}(s) = N \times FF \times V(s) \times I(s), \tag{20}$$

$$FF = \frac{V_{MPP} I_{MPP}}{V_{oc} I_{SC}}, \tag{21}$$

$$V(s) = V_{oc} - K_V \times T_C, \tag{22}$$

$$T_C = T_a + s \times \frac{T_n - 20\ (℃)}{0.8}, \tag{23}$$

$$I(s) = s \times (I_{SC} + K_i \times (T_C - 25\ (℃)). \tag{24}$$

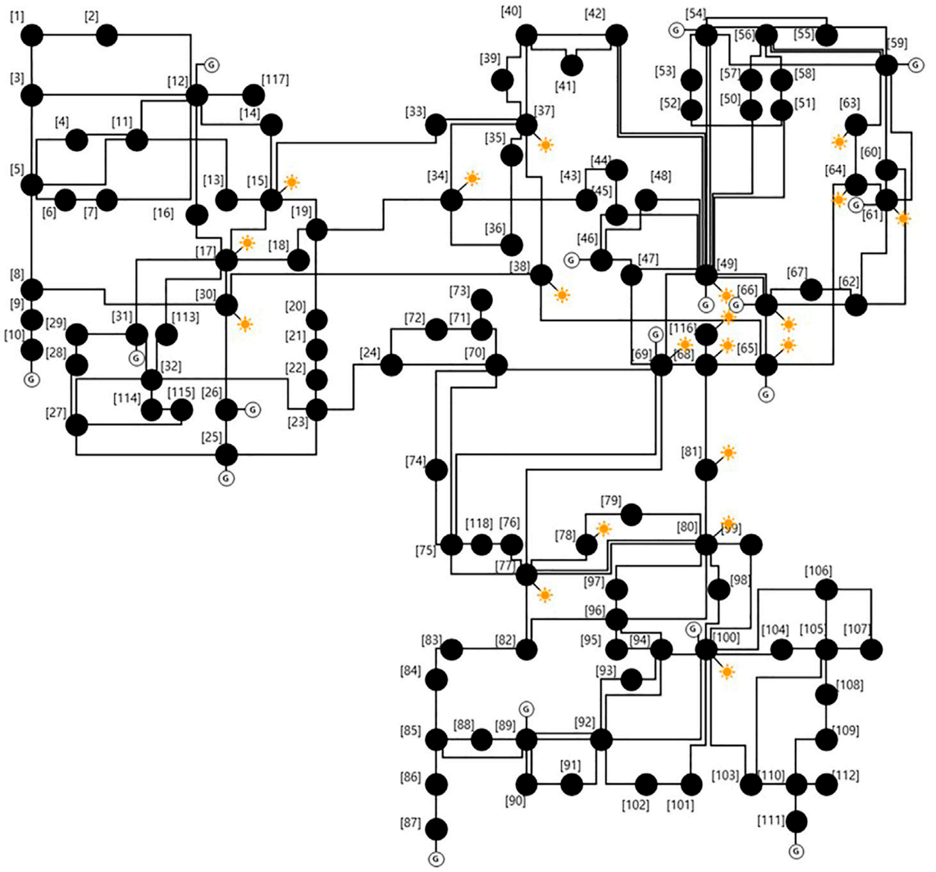

FIGURE 4 | IEEE 118-bus system with photovoltaic (PV) integration.

Here, N denotes the number of PV modules, and FF is the fill factor obtained from **Eq. (22)**; V_{MPP} and I_{MPP} are the voltage and current at the maximum power point in V and A, respectively; V_{oc} and I_{SC} are the open-circuit voltage and short-circuit current, respectively; T_C, T_a, and T_n are the cell, ambient, and nominal operating temperatures of the PV cell, respectively (in °C); and K_V and K_i are the voltage and current temperature coefficients, respectively (in V/°C and A/°C, respectively). The output power of the PV system installed on the buses in the power system can be determined using **Eq. (20)**. The parameters of the PV module in **Table 2** also reflect the values reported in the study by Hung et al. (2014).

3.2 Probabilistic Optimal Power Flow Algorithm

The PV output varies depending on the changes in the solar irradiance over time; accordingly, the value of the power flow in the power system also varies. Owing to this randomness, the results from the power-flow-based spectral clustering vary continuously. The power generation of the existing turn-on generators should be readjusted to match the PV output. The total power generation of conventional generators is adjusted via the total load, PV generation, and power loss parameters, as follows:

$$\sum\nolimits_{i=1}^{n_g} P_{Gi} = \sum\nolimits_{j=1}^{n_l} P_{Lj} - \sum\nolimits_{k=1}^{n_{PV}} P_{PVk} + P_{loss}. \tag{25}$$

In the above, P_{Gi} denotes the active power generation at the generator bus i; P_{Lj} is the load at the bus j; P_{PVk} denotes the PV generation at bus k; n_g, n_l, and n_{PV} denote the total number of generator buses, load buses, and buses connected to PV, respectively; and P_{loss} is the power loss in the network.

In this study, the problem regarding the re-dispatching of generators is solved using an optimal power flow (OPF) calculation, and the objective function is the total fuel cost, as represented by the generator output active power (Chayakulkheeree, 2014; Shaheen et al., 2019).

$$\min_{P_{Gi}} FC = \sum\nolimits_{i=1}^{n_g} cost\,(P_{Gi}). \tag{26}$$

In the above, FC denotes the total cost of the conventional generator connected to bus i, n_g is the total number of generator buses and P_{Gi} denotes the active power generated at generator bus i.

The constraints of the OPF problem are the power-balance equation and variable limits.

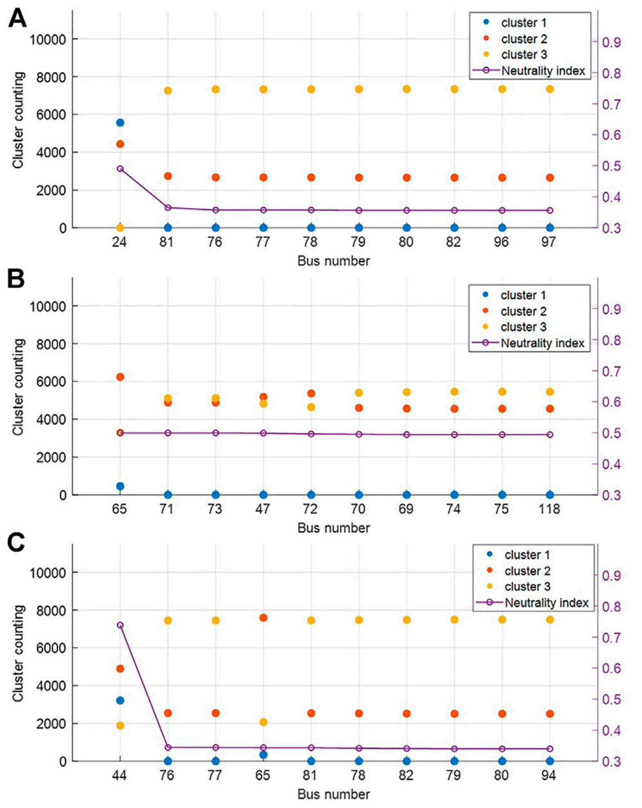

FIGURE 5 | Simulation result at **(A)** 20%, **(B)** 50%, **(C)** 80% penetration level.

$$P_{inj,k} - \sum_{l=1}^{N} V_k V_l \left[G_{kl} \cos(\delta_l - \delta_k) + B_{kl} \sin(\delta_l - \delta_k)\right] = 0, \quad (27)$$

$$Q_{inj,k} - \sum_{l=1}^{N} V_k V_l \left[G_{kl} \sin(\delta_l - \delta_k) - B_{kl} \cos(\delta_l - \delta_k)\right] = 0. \quad (28)$$

Here, $P_{inj,k}$ is the total active power injected into bus k, and $Q_{inj,k}$ is the total reactive power injected into bus k. G_{kl} and B_{kl} are the conductance and susceptance of the admittance Y_{kl} (an element of the admittance matrix), respectively; δ_l and δ_k are the voltage angles at buses k and l, respectively; and N is the total number of buses. Thus,

$$P_{Gi,min} \le P_{Gi} \le P_{Gi,max}, \qquad i = 1, 2, \ldots, n_g, \quad (29)$$

$$Q_{Gi,min} \le Q_{Gi} \le Q_{Gi,max}, \qquad i = 1, 2, \ldots, n_g, \quad (30)$$

$$V_{i,min} \le V_i \le V_{i,max}, \qquad i = 1, 2, \ldots, n, \quad (31)$$

$$V_k V_l \left[G_{kl} \cos(\delta_l - \delta_k) + B_{kl} \sin(\delta_l - \delta_k)\right] \le flow_{\lim,kl}, \quad k, l = 1, 2, \ldots, n. \quad (32)$$

In the above equation, $flow_{lim,kl}$ is the branch flow limit of the line that connects buses k and l.

The clustering considering the random variable should be performed by aggregating the repeated results obtained from the power-flow-based clustering affected by the random PV output. To this end, we propose a probabilistic spectral clustering algorithm. This algorithm repeats the spectral clustering process described in the previous chapter (**Figure 1**) by reflecting the power flow determined from the power flow calculations considering the variable PV output. This algorithm is summarized as follows.

1) Employ test power system data for the probabilistic spectral clustering algorithm.
2) Determine the random PV output calculated through **Eq. (20)**. The solar irradiance follows the beta distribution function; hence, the value of the PV output is randomly determined, changing the value of the power flow.
3) Calculate the power flow in the power system whilst considering the PV output as a negative load. The power flow may vary depending on the random PV output at each moment.
4) Apply each branch's flow to the corresponding edge weight. In this study, the weight is based on the active power flow, and the value of the edge weight depends on the PV output.
5) Perform the spectral clustering shown in **Figure 1**. This process involves calculating the Laplacian matrix, spectral embedding, and hierarchical clustering.
6) Repeat Steps 2–5 N times (i.e., the maximum iteration number). The PV output varies at each iteration; hence, the clustering results from the test power system also vary.
7) Count the number of clusters in which each bus is included after the N iterations.
8) Assign buses to each cluster. In this process, non-neutral buses can be easily allocated, though some neutral buses are not. Hence, it is necessary to classify the neutral buses. This is described in the next section.

3.3 Neutral Buses and Classification

3.3.1 Definition of Neutral Buses

Under a probabilistic condition, the clustering result varies according to the variable generation source. This is because the change in PV generation affects the power flow in the power system. As a result, certain buses are grouped into clusters; however, it remains difficult to identify which buses are classified into which clusters. These buses can be referred to as neutral buses. The neutral buses can also be treated as having an almost equal probability of being assigned to each cluster. To define neutrality in this study, the distance between two points is used [i.e., from the most neutral case and from the counting number (in which each bus is grouped in each cluster) represented in the coordinates]. It is possible to identify which cluster has a high grouping probability for each bus by using the angle between the cases grouped into only one cluster and the coordinates of each case. Using these two elements, the neutrality index (NI) at each bus can be defined as follows:

$$D = \left(\sum_{i=1}^{k} |n_i - p_i|^2\right)^{1/2}, \quad (33)$$

$$NI = \left(\frac{D_{max} - D}{D_{max}}\right)_i. \quad (34)$$

In the above, D denotes the distance between the coordinates P (consisting of the counting number in which

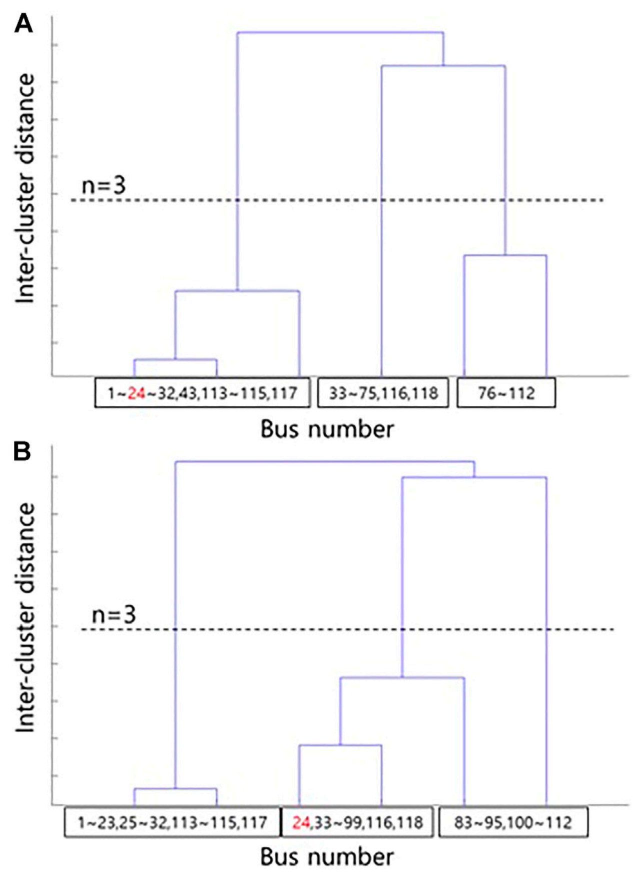

FIGURE 6 | Hierarchical structure at 20% penetration level with respect to PV output. **(A)** Bus 24 belongs to Cluster 1. **(B)** Bus 24 belongs to Cluster 2.

each bus is grouped into each cluster) and the coordinates for the most neutral coordinate N. The distance between the two points N and P is given by the Euclidean distance. If the number of clusters is k for $N(n_1, n_2, \ldots, n_k)$ and $P(p_1, p_2, \ldots, p_k)$, then the distance in k dimensions is defined as shown above.

i indicates the cluster to which each bus belongs with a higher probability. As shown in **Figure 2**, i can be obtained from the angles between the vector NP (formed by the most neutral coordinate N and the coordinates for the bus to be obtained) and the vectors $\mathrm{NC_i}$ [formed by N and the least neutral coordinates C_i (i = 1, 2, . . ., k)]. For example, if the cluster number is three, the coordinate of the most neutral case is N (3,333.33, 3,333.33, 3,333.33) when the number of iterations is 1×10^4. Moreover, D_{max} denotes the distance between the least neutral case [C_1 (10,000, 0, 0), C_2 (0, 10,000, 0), or C_3 (0, 0, 10,000)] and the most neutral coordinates. The case of P_1 case has a smaller distance D_1 than that of P_2. Therefore, it can be said that the NI value of P_1 is larger and more neutral. Indicator i can be obtained from the case with the smallest value between the angles θ formed by the two vectors NP_m ($m = 1, 2$) and NC_n ($n = 1, 2, 3$). For the coordinate P_1, an angle θ_{11} formed with NC_1 is less than an angle θ_{12} formed with NC_2; thus, the value of i is 1. For this reason, it may be seen that the value of i for P_2 is 2.

For neutral buses with high NI values, a reclassification process and a verification process are required. These processes refer to the evaluation of a neutral bus using an index appropriate for the probabilistic environment, as described in the next section.

3.3.2 Classification and Reprocessing Based on Probabilistic Evaluation Index

To evaluate clustering results (as described in the previous section), we calculate the expansion [**Eq. (14)**] of each cluster and use their maximum (**Eq. (15)**) or average (**Eq. (16)**) expansion values. However, this method can only evaluate the results when clustering the power system in each iteration: it is impossible to evaluate the overall results of the probabilistic clustering (i.e., those reflecting the changing power flow with respect to the variable PV power output). Therefore, a novel method is needed to evaluate the clustering results whilst reflecting random renewable generation during iteration. This method can also be used to determine the clusters into which the neutral buses should be classified.

To evaluate the clustering results from N iterations, the representative index (based on expansion) must be determined in the evaluation. We can consider the maximum and average values of expansion as the index, as described in the previous section (**Eq. 15** and **Eq. 16**). There are N iterations after setting the representative value at each iteration; hence, the probabilistic clustering quality should be evaluated using N data elements. In this study, we use the maximum value amongst the N representatives as a probabilistic clustering evaluation index to conservatively judge the clustering quality when the PV output drastically changes the power current in the system. Therefore, the indices for evaluating the probabilistic clustering results can be defined using the following two equations (with reference to **Eq. 15** and **Eq. 16**):

$$\rho_{max} = \max_{1 \le j \le N} \phi_{max.j}, \tag{35}$$

$$\rho_{mean} = \max_{1 \le j \le N} \phi_{mean.j}. \tag{36}$$

Here, ρ_{max} and ρ_{mean} are the probabilistic clustering evaluation indices based on the expansion maximum (ϕ_{max}) and mean (ϕ_{mean}), respectively. Because the two indices take the maximum value of the expansion in the overall iteration, we can see that even when the PV output has the worst effect on power system clustering, the indices indicate whether the cluster is well established and determine the average cluster quality of all clusters. However, in this study, we did not use the index ρ_{max} to classify neutral buses; instead, we used ρ_{mean}. The evaluation index was defined using the mean expansion value because if the maximum expansion value is used, the expansion value of the worst cluster will take this same maximum value, resulting in a probabilistic index overlap.

The aforementioned index can be used to determine which cluster is the most appropriate for a neutral bus to be grouped into. To this end, the neutral buses are first relocated to each cluster, and the expansion values (which vary depending on the PV output) are aggregated. By calculating the probabilistic

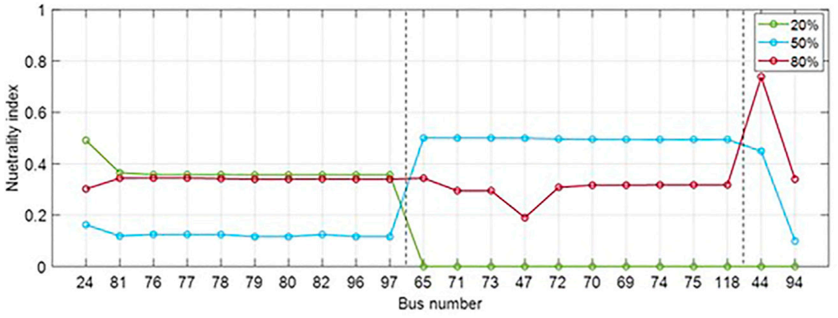

FIGURE 7 | Neutrality index results at each penetration level.

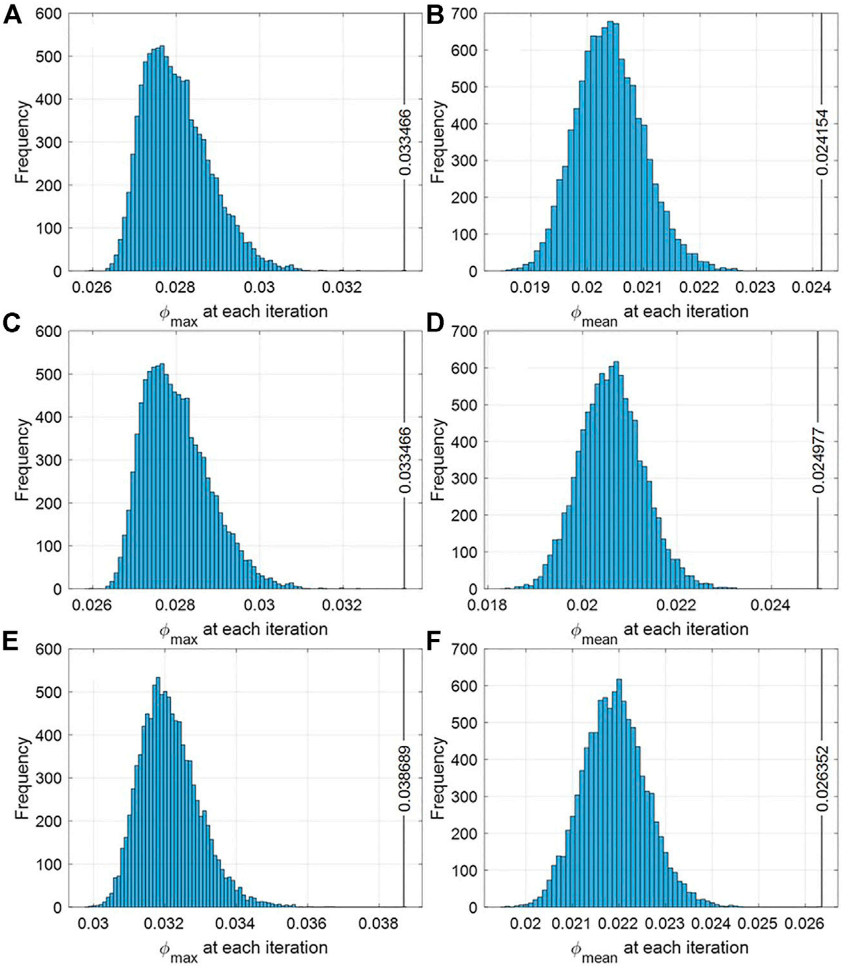

FIGURE 8 | Histogram of probabilistic clustering evaluation indices for each cluster at a 20% penetration level. **(A–C)** ρ_{max} of Clusters 1, 2, and 3, respectively **(D–F)** ρ_{mean} of Clusters 1, 2, and 3, respectively.

clustering evaluation index when placing the neutral buses in each cluster, we can determine in which cluster the value of the index is minimized when placing the neutral buses. At this time, the neutral buses can be classified into their corresponding clusters. That is, the neutral buses can be further classified using the mean index (ρ_{mean}). The flowchart in **Figure 3** summarizes this process and the probabilistic spectral clustering algorithm discussed in the previous section.

TABLE 3 | List of buses connected to PV model.

Bus numbers
15, 17, 30, 34, 37, 38, 49, 61, 63, 64, 65, 66, 68, 69, 77, 78, 80, 81, 100, 116

4 CASE STUDY

As described in this section, the proposed probabilistic spectral clustering algorithm and neutral bus classification were tested using an IEEE 118-bus test system (as shown in **Figure 4**). This system approximates the American Electric Power system and contains 19 generators, 35 synchronous condensers, 177 lines, nine transformers, and 91 loads. The total generator output and load consumption of the test system were 4,374.5 MW and 4,242.0 MW, respectively. To reflect the random outputs of PV generation, the PV models described in the previous section were connected to 20 buses in the power system as shown in **Table 3**. By varying the rating of the PV power to 42.42, 106.05, and 169.68 MW, we tested the probabilistic spectral clustering algorithm for system penetration levels of 20, 50, and 80%, respectively. A penetration level means the ratio of the sum of PV ratings to the total load. Depending on the output of the PV system, the outputs of the generators that were turned on were re-dispatched for the OPF calculations. All numerical calculations (e.g., the power flow calculations) were implemented using MATLAB software (Zimmerman and Murillo-Sanchez, 2020).

We first performed the proposed probabilistic spectral clustering (described in the previous section) based on the power flow Laplacian. Owing to the variable generation source (here, the PV source), the power flow in the test system differed for each iteration. Consequently, the coordinates of each bus differed for each iteration, producing different clustering results. In this simulation, the 118-bus system with PV integration was divided into three clusters. As shown in **Table 4-1**, **Table 4-2**, and **Table 4-3**, we observed the number of times each bus was partitioned into clusters during the 10,000 iterations. Referring to the tables, **Figure 5** shows the graphs for the cluster counting number and the NI [**Eq. (33)**] for the 10 most neutral buses.

Each table summarizes the results from the probabilistic spectral clustering after 10,000 repetitions, and buses with the same counting number were grouped and displayed in ascending order. Therefore, when the count number was divided by 10,000, the probability of the buses belonging to each cluster could be calculated. This shows the number of times each bus is grouped into each cluster in the 118-bus system incorporating a variable PV power output.

From **Table 4-1**, it can be seen that certain buses can be reliably classified into each cluster; however, in the case of Bus 24, the counting numbers grouped into two clusters are similar; hence, it can be considered as a neutral bus. Furthermore, **Figure 6** shows snapshots in which Bus 24 is grouped differently into Clusters 1 and 2 according to the variability of PV; here, the hierarchical structure of the buses (as analyzed by spectral clustering) is shown. The similarity of the buses varies owing to PV variability, which changes the cluster to which Bus 24 is assigned.

Next, the counting numbers in which the buses are clearly classified in **Table 4-1** decreased as shown in **Table 4-2** to **Table 4-3** furthermore, when the penetration level of PV sources increased, reliable clustering became more difficult. In particular, in the case of a 20% penetration level, Buses 44 and 65 were reliably clustered; however, when the penetration level increased to 50 and 80%, the buses become neutral and clustering them presented ambiguity.

The simulation results at each penetration level suggest that different neutral buses appear in each case. The most neutral buses for each case were obtained from the maximum NI. Accordingly, the NIs grouped into the clusters for the buses described in **Figure 5** at each penetration level are summarized in **Figure 7**. Among the three clusters, the values of the maximum cluster probability and NIs for most neutral buses at each penetration level are listed in **Table 5**.

As shown in **Figure 7**, the NIs for neutral buses varied according to the penetration level. In particular, when the penetration level increased, the NI value of the most neutral bus likewise increased. The result of the clustering was not ensured, owing to the variable power generation (e.g., with PV sources). In addition, in **Table 5**, by observing the number of buses exhibiting the maximum probability for each penetration level, we see that buses were most neutral at penetration levels of 20 and 80%. At a penetration level of 50%, the probability of the most neutral bus (Bus 65, which had the largest NI value) was not the smallest value. This is because the counting number of Bus 65 was grouped into Cluster 1, and the value of NI also increased.

At a penetration level of 20% or 80%, the probability of each bus being grouped into a specific cluster was less than or approximately equal to 50%. Furthermore, the higher the penetration level, the lower the probability. A low clustering

TABLE 4-1 | Simulation results at 20% penetration level.

Bus number	Cluster 1	Cluster 2	Cluster 3	Bus number	Cluster 1	Cluster 2	Cluster 3
1–23	10,000	0	0	83–95	0	0	10,000
24	5,564	4,436	0	96–99	0	2,657	7,343
34–75	0	10,000	0	100–112	0	0	10,000
76–78	0	2,668	7,332	113–115	10,000	0	0
79–80	0	2,657	7,343	116	0	10,000	0
81	0	2,739	7,261	117	10,000	0	0
82	0	2,657	7,343	118	0	10,000	0

TABLE 4-2 | Simulation results at 50% penetration level.

Bus number	Cluster 1	Cluster 2	Cluster 3	Bus number	Cluster 1	Cluster 2	Cluster 3
1–13	10,000	0	0	66–67	0	6,338	3,662
14–18	9,997	3	0	68	0	6,245	3,755
19	9,992	8	0	69	0	4,562	5,438
20–23	9,997	3	0	70	0	4,599	5,401
24	1,117	8,883	0	71	0	4,884	5,116
25–32	9,997	3	0	72	1	5,363	4,636
33	1,665	7,542	793	73	0	4,884	5,116
34	1,665	7,548	787	74–75	0	4,550	5,450
35	1,665	7,533	802	76–77	0	849	9,151
36	1,665	7,548	787	78	0	846	9,154
37–40	1,665	7,533	802	79–80	0	788	9,212
41	1,502	7,618	880	81	0	807	9,193
42	0	6,338	3,662	82	0	848	9,152
43	1,664	7,547	789	83	0	788	9,212
44	0	6,340	3,660	84–94	0	671	9,329
45	0	6,338	3,662	95–99	0	788	9,212
46	0	6,023	3,977	100–112	0	671	9,329
47	0	5,181	4,819	113–115	9,997	3	0
48–63	0	6,338	3,662	116	0	6,245	3,755
64	17	6,328	3,655	117	10,000	0	0
65	461	6,237	3,302	118	0	4,550	5,450

TABLE 4-3 | Simulation results at 80% penetration level.

Bus number	Cluster 1	Cluster 2	Cluster 3	Bus number	Cluster 1	Cluster 2	Cluster 3
1–23	10,000	0	0	73	2	7,873	2,125
24	2,185	7,815	0	74–75	2	7,683	2,315
25–32	10,000	0	0	76–77	2	2,546	7,452
33–40	9,928	70	2	78	1	2,527	7,472
41	9,818	178	4	79e80	1	2,509	7,490
42	181	7,733	2086	81	1	2,541	7,458
43	9,927	71	2	82	2	2,517	7,481
44	3,213	4,901	1886	83–84	0	2079	7,921
45	181	7,733	2086	85–92	0	2078	7,922
46	89	8,593	1,318	93	0	2,104	7,896
47	5	8,682	1,313	94–99	0	2078	7,922
48–64	181	7,733	2086	100	0	2,508	7,492
65	337	7,594	2069	101	0	2,500	7,500
66–67	181	7,733	2086	102	0	2078	7,922
68	11	7,830	2,159	103–112	0	2,508	7,492
69	2	7,691	2,307	113–115	10,000	0	0
70	2	7,692	2,306	116	11	7,830	2,159
71	2	7,873	2,125	117	10,000	0	0
72	123	7,809	2068	118	2	7,682	2,316

probability does not guarantee that the buses grouped into a specific cluster represent the optimal clustering results. Therefore, when neutral buses are assigned to three clusters, it is necessary to determine which cluster is most appropriate for grouping, by considering the variable PV power output. To this end, the expansion-based evaluation process described in **Figure 3** is required. In this example, the classification process was applied to Buses 24, 65, and 44, and the index ρ_{mean} was calculated. The smaller the value of each index, the smaller the value of the expansion, indicating a more optimal clustering result. In **Figure 8** (below), histograms of the values ϕ_{max} and ϕ_{mean} (as calculated using the Monte Carlo procedure) are shown. The maximum values for each index (i.e., the values of ρ_{max} and ρ_{mean}) are also shown in the figure.

Neutral bus classification is the process of obtaining the expansion value for each cluster when placing neutral buses into Clusters 1–3 (for each penetration level) and repeating this process 10,000 times by considering the random output of the PV power. As a result, when each neutral bus was assigned to Clusters 1 and 2, the evaluation index value was minimized; that is, optimal clustering was achieved. **Figure 8A** and **Figure 8B** show the same histogram for the penetration

TABLE 5 | Most neutral buses in each penetration level case.

Penetration level (%)	Neutral buses	Probability	Neutrality index
20	24	55.64% (cluster 1)	0.4905_1
50	65	62.37% (cluster 2)	0.4998_2
80	44	49.01% (cluster 2)	0.7383_2

TABLE 6 | Probabilistic clustering evaluation index in each penetration level case. The minimum value for the evaluation index ρmean. Since the cluster with the minimum ρmean is the optimal cluster, we emphasized this with bold fonts.

Penetration level	20 (%)		50 (%)		80%	
Evaluation index	$\rho_{\max}$	ρ_{mean}	$\rho_{\max}$	ρ_{mean}	$\rho_{\max}$	ρ_{mean}
Cluster 1	3.3466	**2.4154%**	10.8802	7.1623%	7.6356%	5.1725%
Cluster 2	3.3466	2.4977%	4.6483	**3.2697%**	7.4233%	**5.1259%**
Cluster 3	3.8689	2.6325%	10.8802	7.2417%	7.6356%	5.2654%

level of 20% (shown in **Figure 7**). It can be seen that when ϕ_{max} used, the distribution of the expansion values is completely consistent, making it impossible to classify neutral buses using ρ_{max}. In addition, because the shapes and maximum values of ρ_{mean} in **Figures 8D, E**, and **Figure 8F** differ from each other, it is necessary to check the value of ρ_{mean} and classify the neutral buses.

In the analysis results, the optimal cluster for each neutral bus was found to be the cluster with the highest probability in **Table 5**. The optimal cluster can be obtained using this value because the value of indicator i matches the cluster with the highest probability.

5 DISCUSSION

In this simulation, when the penetration level increased, the probability that most buses were grouped into a specific cluster also decreased. Thus, as the penetration level of PV power increased, the clustering results changed more frequently, and the number of buses that were difficult to classify increased. The NI value for each bus also increased. Therefore, the most neutral buses can be found using the NI values, and such buses should be classified.

The most neutral buses for each penetration level can be organized as shown in **Table 5**. As a result, at penetration levels of 20 and 80%, the probability of an optimal cluster is low (~50%), and the NI is high. This is because differences between the probabilistic evaluation index values for each cluster in **Table 6** are very small; thus, each clustering result has a similar effect. For this reason, to obtain the most optimal case among similar clustering results, it is necessary to group the clusters with the highest clustering probability among the neutral buses, as well as to verify the results using the probabilistic clustering evaluation index.

In the case of a penetration level of 50%, the NI value was high; however, the maximum probability was also high. When applying the neutral bus classification process in this case, the differences in the values of the probability evaluation index between Cluster 2 and other clusters were found to be large. Therefore, classification should be first performed on the most neutral buses (with the smallest maximum probability), before proceeding to the next-most neutral buses. Thus. buses will be grouped into clusters with the highest probability, similar to the results mentioned above.

6 CONCLUSION

This paper introduces a novel method for performing spectral clustering in power systems with variable sources (e.g., renewable energy sources). Because the output of a renewable energy source is variable, it is necessary to consider variable generation at every moment when clustering. To this end, we propose a probabilistic approach based on a widely adopted graph-theory-based spectral clustering method. The conventional spectral clustering method is limited in that it can only be used in power systems for which the power generation and load can be determined. To overcome this problem and reflect the effects of variable power sources, we developed the probabilistic spectral clustering method to group buses into clusters with the highest grouping probability. The results from the probabilistic clustering can be further optimized by classifying neutral buses. The proposed method was applied to an IEEE 118-bus system with PV integration to confirm the clustering results, which varied depending on the PV penetration level. In addition, the neutral buses for each case generated by the probabilistic spectral clustering method were classified to calculate the probabilistic evaluation index for each cluster and to verify which cluster yielded the optimal clustering.

This method can be applied to power system clustering under conditions of variable renewable energy sources, and it is expected to be implemented in power system planning and operation in the future for net-zero establishment. The probabilistic clustering methodology applied in this study synthesizes the expansion value, which depends on the variability of VRE, via the Monte Carlo procedure and identifies the optimal clustering point. This probabilistic analysis method can help determine an optimal operation plan in environments where the penetration of renewable energy is high. In particular, from the perspective of system planning and operation, improvements in system reliability and stability can be expected in environments with high renewable energy penetration. This can be achieved through the installation and control of high-voltage direct current across the interfaces between clusters determined using the probabilistic clustering methodology.

DATA AVAILABILITY STATEMENT

The original contributions presented in the study are included in the article/Supplementary Material; further inquiries can be directed to the corresponding authors.

AUTHOR CONTRIBUTIONS

JK put forward the main research points and mathematical analysis and wrote the manuscript. SK, JL, and SH conceived the idea and contributed to data interpretation. MY led the experiments. MY and GJ gave guidance on the study and wrote the manuscript.

FUNDING

This research was supported by the Basic Research Program through the National Research Foundation of Korea (NRF), funded by the MSIT (No. 2020R1A4A1019405), as well as a Korea Institute of Energy Technology Evaluation and Planning (KETEP) grant funded by the Korean Government (MOTIE) (No. 20191210301890).

REFERENCES

Amini, M., Samet, H., Seifi, A. R., Al-Dhaifallah, M., and Ali, Z. M. (2020). An Effective Multi-Solution Approach for Power System Islanding. *IEEE Access* 8, 93200–93210. doi:10.1109/ACCESS.2020.2995085

Bialek, J. W., and Vahidinasab, V. (2022). Tree-partitioning as an Emergency Measure to Contain Cascading Line Failures. *IEEE Trans. Power Syst.* 37, 467–475. doi:10.1109/TPWRS.2021.3087601

Cao, D., Zhao, J., Hu, W., Ding, F., Huang, Q., Chen, Z., et al. (2021). Data-driven Multi-Agent Deep Reinforcement Learning for Distribution System Decentralized Voltage Control with High Penetration of PVs. *IEEE Trans. Smart Grid* 12, 4137–4150. doi:10.1109/TSG.2021.3072251

Cauz, M., Bloch, L., Rod, C., Perret, L., Ballif, C., and Wyrsch, N. (2020). Benefits of a Diversified Energy Mix for Islanded Systems. *Front. Energy Res.* 8, 147. doi:10.3389/fenrg.2020.00147

Chai, Y., Guo, L., Wang, C., Zhao, Z., Du, X., and Pan, J. (2018). Network Partition and Voltage Coordination Control for Distribution Networks with High Penetration of Distributed PV Units. *IEEE Trans. Power Syst.* 33, 3396–3407. doi:10.1109/TPWRS.2018.2813400

Chayakulkheeree, K. (2014). "Probabilistic Optimal Power Flow: An Alternative Solution for Emerging High Uncertain Power Systems," in 2014 International Electrical Engineering Congress (iEECON), Pattaya, Thailand, March 19–21, 2014, 1–4. doi:10.1109/iEECON.2014.6925970

Cotilla-Sanchez, E., Hines, P. D. H., Barrows, C., Blumsack, S., and Patel, M. (2013). Multi-attribute Partitioning of Power Networks Based on Electrical Distance. *IEEE Trans. Power Syst.* 28, 4979–4987. doi:10.1109/TPWRS.2013.2263886

Holttinen, H., Groom, A., Kennedy, E., Woodfin, D., Barroso, L., Orths, A., et al. (2021). Variable Renewable Energy Integration: Status Around the World. *IEEE Power Energy Mag.* 19, 86–96. doi:10.1109/MPE.2021.3104156

Hung, D. Q., Mithulananthan, N., and Lee, K. Y. (2014). Determining PV Penetration for Distribution Systems with Time-Varying Load Models. *IEEE Trans. Power Syst.* 29, 3048–3057. doi:10.1109/TPWRS.2014.2314133

Lee, J. R., Gharan, S. O., and Trevisan, L. (2014). Multiway Spectral Partitioning and Higher-Order Cheeger Inequalities. *J. ACM* 61, 1–30. doi:10.1145/2665063

Leeuwen, T. v., and Moser, A. (2017). "Impact of Flexible Transmission Assets on Day-To-Day Transmission Grid Operation under Uncertainties," in International ETG Congress 2017, Bonn, Germany, November 28–29, 2017, 1–6.

Li, Z., Cheng, Z., Si, J., Zhang, S., Dong, L., Li, S., et al. (2021). Adaptive Power Point Tracking Control of PV System for Primary Frequency Regulation of AC Microgrid with High PV Integration. *IEEE Trans. Power Syst.* 36, 3129–3141. doi:10.1109/TPWRS.2021.3049616

Lin, X., Shu, T., Tang, J., Ponci, F., Monti, A., and Li, W. (2022). Application of Joint Raw Moments-Based Probabilistic Power Flow Analysis for Hybrid AC/VSC-MTDC Power Systems. *IEEE Trans. Power Syst.* 37, 1399–1412. doi:10.1109/TPWRS.2021.3104664

Ma, D., Hu, X., Zhang, H., Sun, Q., and Xie, X. (2021). A Hierarchical Event Detection Method Based on Spectral Theory of Multidimensional Matrix for Power System. *IEEE Trans. Syst. Man. Cybern. Syst.* 51, 2173–2186. doi:10.1109/TSMC.2019.2931316

Park, Y., and Kim, J. (2006). A Survey on the Power System Modeling Using a Clustering Algorithm. *Proc. KIEE Conf.*, 410–411.

Sanchez-Garcia, R. J., Fennelly, M., Norris, S., Wright, N., Niblo, G., Brodzki, J., et al. (2014). Hierarchical Spectral Clustering of Power Grids. *IEEE Trans. Power Syst.* 29, 2229–2237. doi:10.1109/TPWRS.2014.2306756

Sarajpoor, N., Rakai, L., Arteaga, J., and Zareipour, H. (2021). A Shape-Based Clustering Framework for Time Aggregation in the Presence of Variable Generation and Energy Storage. *IEEE Open J. Power Energy* 8, 448–459. doi:10.1109/OAJPE.2021.3097366

Sehsalar, O. Z., Galvani, S., and Farsadi, M. (2019). New Approach for the Probabilistic Power Flow of Distribution Systems Based on Data Clustering. *IET Renew. Power Gener.* 13, 2531–2540. doi:10.1049/iet-rpg.2018.6264

Shaheen, M. A. M., Hasanien, H. M., Mekhamer, S. F., and Talaat, H. E. A. (2019). Optimal Power Flow of Power Systems Including Distributed Generation Units Using Sunflower Optimization Algorithm. *IEEE Access* 7, 109289–109300. doi:10.1109/ACCESS.2019.2933489

Si, C., Xu, S., Wan, C., Chen, D., Cui, W., and Zhao, J. (2021). Electric Load Clustering in Smart Grid: Methodologies, Applications, and Future Trends. *J. Mod. Power Syst. Clean. Energy* 9, 237–252. doi:10.35833/MPCE.2020.000472

Teng, J.-H., Luan, S.-W., Lee, D.-J., and Huang, Y.-Q. (2013). Optimal Charging/discharging Scheduling of Battery Storage Systems for Distribution Systems Interconnected with Sizeable PV Generation Systems. *IEEE Trans. Power Syst.* 28, 1425–1433. doi:10.1109/TPWRS.2012.2230276

The International Renewable Energy Agency (2021). Available at: https://www.irena.org/Statistics/View-Data-by-Topic/Capacity-and-Generation/Statistics-Time-Series (Accessed March 22, 2022).

Tyuryukanov, I., Popov, M., van der Meijden, M. A. M. M., and Terzija, V. (2018). Discovering Clusters in Power Networks from Orthogonal Structure of Spectral Embedding. *IEEE Trans. Power Syst.* 33, 6441–6451. doi:10.1109/TPWRS.2018.2854962

von Luxburg, U. (2007). A Tutorial on Spectral Clustering. *Stat. Comput.* 17, 395–416. doi:10.1007/s11222-007-9033-z

von Luxburg, U., Belkin, M., and Bousquet, O. (2008). Consistency of Spectral Clustering. *Ann. Stat.* 36. doi:10.1214/009053607000000640

Wang, S., Su, H., and Zhang, Z. (2021). "Probabilistic Power Flow Calculation Considering the Correlation of Distributed Power Sources," in 2021 IEEE

International Conference on Advances in Electrical Engineering and Computer Applications (AEECA), Dialan, China, August 27–28, 2021, 53–58. doi:10.1109/AEECA52519.2021.9574164

Wiget, R., Vrakopoulou, M., and Andersson, G. (2014). "Probabilistic Security Constrained Optimal Power Flow for a Mixed HVAC and HVDC Grid with Stochastic Infeed," in 2014 Power Systems Computation Conference, Wroclaw, Poland, August 18–22, 2014, 1–7. doi:10.1109/PSCC.2014.7038408

Zhu, X., Liu, C., Su, C., and Liu, J. (2020). Learning-based Probabilistic Power Flow Calculation Considering the Correlation Among Multiple Wind Farms. *IEEE Access* 8, 136782–136793. doi:10.1109/ACCESS.2020.3011511

Zimmerman, R. D., and Murillo-Sanchez, C. E. (2020). *MATPOWER User's Manual Version 7.1*. Madison, WI: Power Systems Engineering Research Center.

Conflict of Interest: JL was employed by the company Korea Electric Power Corporation.

The remaining authors declare that the research was conducted in the absence of any commercial or financial relationships that could be construed as a potential conflict of interest.

NOMENCLATURE

Abbreviations

PV Photovoltaic

VRE Variable renewable energy

Symbols

$\partial(C)$ Boundary of cluster C

γ Eigengap

λ Eigenvalue

$\phi(C)$ Expansion of cluster C

ϕ_{max} Maximum expansion of clusters

e Mean expansion of clusters

μ Mean of random variable

α, β Parameter of f_{beta}

ρ_{max} Probabilistic clustering evaluation index based on expansion max

ρ_{mean} Probabilistic clustering evaluation index based on expansion mean

σ Standard deviation of random variable

δ_l Voltage angle at bus k

$vol(C)$ Volume of cluster C

$\mathbf{B_{kl}}$ Susceptance of the admittance Y_{kl}

$\mathbf{E}$ Edge set

$\boldsymbol{e}$ Normalized coordinates of bus i

$\boldsymbol{f_{beta}}$ Beta probability density function

FC Total fuel cost

FF Fill factor

$\mathbf{G}$ Graph

$\mathbf{G_{kl}}$ Conductance of the admittance Y_{kl}

$\mathbf{I_{SC}}$ Short-circuit current

$\mathbf{K_c}$ Voltage temperature coefficients

$\mathbf{K_i}$ Current temperature coefficients

$\mathbf{L}$ Laplacian matrix

$\mathbf{L_n}$ Normalized Laplacian matrix

$\mathbf{n_g}$ Total number of generator buses

NI Neutrality index

$\mathbf{n_l}$ Total number of load buses

$\mathbf{n_{PV}}$ Total number of PV buses

$\mathbf{P_{G\boldsymbol{e}}}$ Active power generation at generation bus i

$\mathbf{P_{inj,k}}$ Active power injected into bus k

$\mathbf{P_{L\boldsymbol{j}}}$ Active power consumption at load bus j

$\mathbf{P_{loss}}$ Power loss in the network

$\mathbf{P_{PV\boldsymbol{k}}}$ PV generation at PV bus k

$\mathbf{Q_{inj,k}}$ Reactive power injected into bus k

$\mathbf{s}$ Random variable of solar irradiance

$\mathbf{T_a}$ Ambient temperature of PV cell

$\mathbf{T_c}$ Cell temperature of PV cell

$\mathbf{T_n}$ Nominal operating temperature of PV cell

$\boldsymbol{v}$ Eigenvector

$\mathbf{V}$ Vertex set

$\mathbf{V_{oc}}$ Open-circuit voltage

$\boldsymbol{x_i}$ Coordinates of bus i

$\mathbf{Y_{kl}}$ Admittance of branch from buses from i to j

Advantages of publishing in Frontiers

OPEN ACCESS
Articles are free to read
for greatest visibility
and readership

FAST PUBLICATION
Around 90 days
from submission
to decision

HIGH QUALITY PEER-REVIEW
Rigorous, collaborative,
and constructive
peer-review

TRANSPARENT PEER-REVIEW
Editors and reviewers
acknowledged by name
on published articles

Frontiers
Avenue du Tribunal-Fédéral 34
1005 Lausanne | Switzerland

Visit us: www.frontiersin.org
Contact us: frontiersin.org/about/contact

REPRODUCIBILITY OF RESEARCH
Support open data
and methods to enhance
research reproducibility

DIGITAL PUBLISHING
Articles designed
for optimal readership
across devices

FOLLOW US
@frontiersin

IMPACT METRICS
Advanced article metrics
track visibility across
digital media

EXTENSIVE PROMOTION
Marketing
and promotion
of impactful research

LOOP RESEARCH NETWORK
Our network
increases your
article's readership